pharmaceutics

Special Issue Reprint

Advanced Pharmaceutical Science and Technology in Israel

Edited by
Arik Dahan

mdpi.com/journal/pharmaceutics

MDPI

Advanced Pharmaceutical Science and Technology in Israel

Advanced Pharmaceutical Science and Technology in Israel

Guest Editor

Arik Dahan

MDPI

Basel • Beijing • Wuhan • Barcelona • Belgrade • Novi Sad • Cluj • Manchester

Guest Editor
Arik Dahan
Department of Clinical
Pharmacology
Ben-Gurion University of the
Negev
Beer-Sheva
Israel

Editorial Office
MDPI AG
Grosspeteranlage 5
4052 Basel, Switzerland

This is a reprint of the Special Issue, published open access by the journal *Pharmaceutics* (ISSN 1999-4923), freely accessible at: https://www.mdpi.com/journal/pharmaceutics/special_issues/HTX7S57746.

For citation purposes, cite each article independently as indicated on the article page online and as indicated below:

Lastname, A.A.; Lastname, B.B. Article Title. *Journal Name* **Year**, *Volume Number*, Page Range.

ISBN 978-3-7258-4773-0 (Hbk)
ISBN 978-3-7258-4774-7 (PDF)
https://doi.org/10.3390/books978-3-7258-4774-7

Cover image courtesy of Arik Dahan

Contents

About the Editor

Arik Dahan

Arik Dahan is a Professor of Pharmaceutics and Biopharmaceutics at the Department of Clinical Pharmacology and the School of Pharmacy, Ben-Gurion University of the Negev in Beer-Sheva, Israel. He is also an Adjunct Professor of Pharmaceutical Sciences at the College of Pharmacy, University of Michigan, USA. Dr Dahan received his PhD (2007) from the Hebrew University of Jerusalem, Israel. From 2007 until 2009 he was a post-doctoral research fellow at the University of Michigan College of Pharmacy with Professor Gordon L. Amidon. Dr Dahan's research interest is the integration of up-to-date molecular and cellular mechanistic investigations of drug disposition in the context of the human body in order to enable successful drug delivery and therapy. In implementing this molecular biopharmaceutical approach to ADME research, Dr Dahan is seeking to enable mechanistic-based successful solutions to drug delivery, especially (but not only) oral, in challenging scenarios, e.g., low-solubility, low-permeability, efflux transport, extensive metabolism, poor site targeting, various pathophysiological conditions (e.g., obesity, poat-bariatric surgery, inflammatory bowel disease), and pediatrics patient care. He has published over 150 highly regarded journal papers, and contributed chapters to numerous books.

pharmaceutics

MDPI

Editorial

Advanced Pharmaceutical Science and Technology in Israel

Arik Dahan

Department of Clinical Pharmacology, School of Pharmacy, Faculty of Health Sciences, Ben-Gurion University of the Negev, Beer-Sheva 8410501, Israel; arikd@bgu.ac.il; Tel.: +972-8-647-9483

1. Introduction

Israel has a significant and diverse history of ground-breaking research and development in pharmaceutical sciences and technology within academic settings, pharma/biopharma companies, and the biotechnology community [1].

This Special Issue of *Pharmaceutics*, entitled "Advanced Pharmaceutical Science and Technology in Israel", was put together to highlight the exceptional achievements and significant international impact of pharmaceutical research performed in Israel in celebration of the country's 75th diamond anniversary of growth and prosperity.

In recent decades, the fields of pharmaceutical science and engineering have undergone rapid growth and development, both globally and in Israel alone [2]. To reflect this growth, we invited contributions on all aspects of pharmaceutical sciences and technology, including drug delivery, drug targeting, preformulation/formulation, biopharmaceutics/pharmacokinetics, nanopharmaceutics, pharmaceutics biotechnology, personalized medicine, and other related topics. We hoped that our Special Issue would contribute to multidisciplinary discussions on these exciting topics and prompt new scientific collaborations, further advancing pharmaceutical sciences and engineering in Israel and globally. In the next paragraphs, we summarize the contributions accepted for publication in Pharmaceutics under our Special Issue.

2. An Overview of Published Articles

In their article, Eydelman et al. developed a novel starch-based nanoparticle system that delivers cannabidiol (CBD) directly to the brain via intranasal administration. Compared to the CBD solution, the CBD-loaded nanoparticles achieved higher brain concentrations and showed strong anti-inflammatory effects in microglial cells, with low toxicity. These findings suggest that this system could be an effective method for targeting CBD treatment to the central nervous system (contribution 1).

The article by Bornstein et al. introduces melt-jet printing as a novel, solvent-free method of engineering active pharmaceutical ingredient (API) particles. Using paracetamol as a model, the researchers demonstrated how various substrates affect particle shape, with aluminum producing highly spherical microparticles due to its thermal and surface properties. The particles maintained their chemical integrity and exhibited minimal degradation. This method has also been successfully applied to other APIs, highlighting melt-jet printing's potential for precise and reproducible pharmaceutical particle design (contribution 2).

The article by Ifrah et al. presents a novel oral drug delivery approach for the poorly absorbed antiviral drug zanamivir orally using self-double nanoemulsifying Winsor delivery systems (SDNE-WDS). Two formulations (SDNE-WDS1 and SDNE-WDS2) produced nanoemulsions that significantly enhanced zanamivir's intestinal permeability, with particle sizes of 542.1 nm and 174.4 nm, respectively. Both systems increased drug transport

across artificial membranes and in rat intestines, achieving permeability levels 3.5–5.5 times higher than the standard reference. These results highlight SDNE-WDSs as a promising strategy for improving the oral bioavailability of low-permeability, BCS class III drugs (contribution 3).

The article by Zinger et al. analyzed mechanical processing methods for extracting regenerative cells from lipoaspirate, aiming to identify the optimal technique without using enzymes. After reviewing 10,000 titles and selecting six relevant studies involving 117 patients, the researchers used multivariate meta-analysis to identify key factors affecting cell yield. Optimal conditions included a centrifuge force of 2000$\times$ *g* for 10 min, a cannula diameter of 2 mm, and 30 intra-syringe passes. Patient factors such as higher BMI and younger age were also associated with higher yield. The study highlights a novel statistical approach to optimizing mechanical lipoaspirate processing (contribution 4).

The article by Ramot et al. evaluated the Bioprotect biodegradable fillable balloon as a rectal spacer for prostate cancer radiotherapy using a rat model. Tissue responses at 4, 26, and 52 weeks post-implantation showed mild to moderate fibrosis and encapsulation, indicating good biocompatibility and safety. No adverse effects were observed, and all animals remained healthy. These results support the balloon's potential for clinical use to reduce radiation-related complications and improve outcomes in prostate cancer treatment (contribution 5).

The article by Porat et al. investigated how bariatric surgery impacts the solubility, dissolution, and pharmacokinetics of sildenafil, the first-line drug to treat erectile dysfunction. Solubility tests showed a strong pH dependence, with significantly reduced solubility at the higher pH levels seen after gastric bypass surgery (especially post-OAGB). Dissolution and PBPK modeling revealed impaired absorption, delayed drug onset, and reduced peak concentrations (C_{max}) in postbariatric patients, particularly after OAGB. These findings highlight the unpredictable and procedure-specific effects of bariatric surgery on sildenafil's effectiveness, suggesting potential challenges in managing erectile dysfunction in this patient population (contribution 6).

The article by Ankri et al. evaluated the safety of Allocetra-OTS, a cell-based therapy using apoptotic cells, in a preclinical toxicology model with Sprague Dawley rats. Following three intravenous doses, no adverse effects were observed across key health indicators. Although temporary changes in immune cell and mild splenomegaly with extramedullary hematopoiesis occurred, these were expected and resolved during recovery. The highest tested dose was identified as the NOAEL. Overall, Allocetra-OTS was well tolerated, supporting its suitability for future clinical development (contribution 7).

The article by Merzbach et al. presents Clarstatin, a novel thiourea-bridged cyclic peptidomimetic designed to mimic a specific motif of the HLA-DRB1 gene's shared epitope (SE). Clarstatin targets the proline-rich domain of cell surface calreticulin (CS-CRT), implicated in triggering autoimmune inflammation. Synthesized using Fmoc-SPPS and confirmed by LC-MS, Clarstatin demonstrated the ability to reduce calcium levels in Jurkat T cells and significantly alleviated symptoms in a mouse model of autoimmune uveitis. It was also found to be safe in acute toxicity tests, highlighting its potential as a therapeutic agent for treating inflammatory autoimmune diseases such as uveitis (contribution 8).

The article by Tepper-Shimshon et al. investigated how simulated microgravity (SMG) influences the cellular uptake of small molecules, reflecting microgravity-induced changes in membrane function. Using a random-positioning machine, researchers found that SMG increased uptake of efflux transporter substrates by up to 60% and reduced the uptake of a glucose transporter substrate by 20%. The uptake of a large cathepsin probe (MW 1198 g/mol) also increased, whereas the emission of molecules >3000 g/mol decreased by

50%. These results suggest that SMG can alter membrane transport differentially, potentially impacting drug distribution during spaceflight (contribution 9).

The article by Milošević et al. explored the use of a synthetic polymer (P-Esbp), presenting multiple E-selectin-binding peptides to inhibit leukocyte infiltration and reduce kidney inflammation. In acute kidney injury (AKI), P-Esbp effectively suppressed E-selectin expression and mitigated inflammation. However, in a chronic kidney disease (CKD) model, P-Esbp had a limited effect due to the compensatory actions of other adhesion molecules (P-selectin and VCAM-1). The findings highlight the complexity of cell adhesion mechanisms in kidney injury and suggest that targeting multiple CAMs could be a more effective strategy for controlling inflammation in both AKI and CKD (contribution 10).

3. Conclusions

Naturally, the articles published in this Special Issue represent only a small fraction of the top-notch pharmaceutical research and development taking place in Israel [3,4]. That being said, this collection of articles does serve as a unique example of the outstanding and diverse contributions Israel has made to the global pharmaceutical arena [5]. The Special Issue covers many hot topics in the pharmaceutical sciences, including gene therapy [6], cell-based therapy [7], nanomedicine [8], new drug delivery systems [9], 3D printing [10], space medicine [11], personalized medicine [12], and advanced PBPK modeling [13]. Looking to the future, Israel will undoubtedly continue to be a significant pioneer in the global pharmaceutical science and technology arenas.

Conflicts of Interest: The author declares no conflicts of interest.

List of Contributions

1. Eydelman, I.; Zehavi, N.; Feinshtein, V.; Kumar, D.; Ben-Shabat, S.; Sintov, A.C. Cannabidiol-Loaded Nanoparticles Based on Crosslinked Starch: Anti-Inflammatory Activity and Improved Nose-to-Brain Delivery. *Pharmaceutics* **2023**, *15*, 1803.
2. Bornstein, S.; Uziel, A.; Lewitus, D.Y. Controlling Microparticle Morphology in Melt-Jet Printing of Active Pharmaceutical Ingredients through Surface Phenomena. *Pharmaceutics* **2023**, *15*, 2026.
3. Ifrah, S.; Dahan, A.; Debotton, N. Towards Effective Antiviral Oral Therapy: Development of a Novel Self-Double Emulsifying Drug Delivery System for Improved Zanamivir Intestinal Permeability. *Pharmaceutics* **2023**, *15*, 2518.
4. Zinger, G.; Kepes, N.; Kenett, R.; Peyser, A.; Sharon-Gabbay, R. A Multivariate Meta-Analysis for Optimizing Cell Counts When Using the Mechanical Processing of Lipoaspirate for Regenerative Applications. *Pharmaceutics* **2023**, *15*, 2737.
5. Ramot, Y.; Levin-Harrus, T.; Ezratty, A.; Steiner, M.; Ezov, N.; Domb, A.J.; Abdel-Haq, M.; Shohat, S.; Aperman, L.; Adler, L.; et al. Assessment of Bioprotect's Biodegradable Balloon System as a Rectal Spacer in Radiotherapy: An Animal Study on Tissue Response and Biocompatibility. *Pharmaceutics* **2023**, *15*, 2744.
6. Porat, D.; Dukhno, O.; Cvijić, S.; Dahan, A. The Complexity of Bariatric Patient's Pharmacotherapy: Sildenafil Biopharmaceutics and Pharmacokinetics before vs. after Gastric Sleeve/Bypass. *Pharmaceutics* **2023**, *15*, 2795.
7. Ankri, C.; Hershkovitz, O.; Hershkovitz, L.; Brami, M.; Levy, R.; Sarig, H.; Souli, E.; Reicher, B.; Amor-Baroukh, V.; Mevorach, D.; et al. Safety of Repeated Administration of Xenogeneic Human Apoptotic State (Allocetra-OTS) in Sprague Dawley Rats. *Pharmaceutics* **2024**, *16*, 426.

8. Merzbach, S.; Hoffman, A.; Lazarovici, P.; Gilon, C.; Amer, R. Development of Clarstatin, a Novel Drug Lead for the Therapy of Autoimmune Uveitis. *Pharmaceutics* **2024**, *16*, 723.
9. Tepper-Shimshon, O.; Tetro, N.; Hamed, R.; Erenburg, N.; Merquiol, E.; Dey, G.; Haim, A.; Dee, T.; Duvdevani, N.; Kevorkian, T.; et al. Differential Effect of Simulated Microgravity on the Cellular Uptake of Small Molecules. *Pharmaceutics* **2024**, *16*, 1211.
10. Milošević, N.; Rütter, M.; Ventura, Y.; Feinshtein, V.; David, A. Targeted Polymer–Peptide Conjugates for E-Selectin Blockade in Renal Injury. *Pharmaceutics* **2025**, *17*, 82.

References

1. Beyar, R.; Zeevi, B.; Rechavi, G. Israel: A start-up life science nation. *Lancet* **2017**, *389*, 2563–2569. [CrossRef] [PubMed]
2. Van Noorden, R. Israel edges out South Korea for top spot in research investment. *Nature* **2017**. [CrossRef]
3. Arunachalam, S.; Doss, M.J. Science in a small country at a time of globalisation: Domestic and international collaboration in new biology research in Israel. *J. Inf. Sci.* **2000**, *26*, 39–49. [CrossRef]
4. Breznitz, S.M. Cluster Sustainability: The Israeli Life Sciences Industry. *Econ. Dev. Q.* **2013**, *27*, 29–39. [CrossRef]
5. Senor, D.; Singer, S. *Start-Up Nation: The Story of Israel's Economic Miracle*; McClelland & Stewart: Toronto, ON, Canada, 2011.
6. Gao, J.; Gunasekar, S.; Xia, Z.J.; Shalin, K.; Jiang, C.; Chen, H.; Lee, D.; Lee, S.; Pisal, N.D.; Luo, J.N.; et al. Gene therapy for CNS disorders: Modalities, delivery and translational challenges. *Nat. Rev. Neurosci.* **2024**, *25*, 553–572. [CrossRef] [PubMed]
7. Li, Y.-R.; Dunn, Z.S.; Yu, Y.; Li, M.; Wang, P.; Yang, L. Advancing cell-based cancer immunotherapy through stem cell engineering. *Cell Stem Cell* **2023**, *30*, 592–610. [CrossRef] [PubMed]
8. Mitchell, M.J.; Billingsley, M.M.; Haley, R.M.; Wechsler, M.E.; Peppas, N.A.; Langer, R. Engineering precision nanoparticles for drug delivery. *Nat. Rev. Drug Discov.* **2021**, *20*, 101–124. [CrossRef] [PubMed]
9. Vargason, A.M.; Anselmo, A.C.; Mitragotri, S. The evolution of commercial drug delivery technologies. *Nat. Biomed. Eng.* **2021**, *5*, 951–967. [CrossRef] [PubMed]
10. Murugan, M.; Ramasamy, S.K.; Venkatesan, G.; Lee, J.; Barathi, S.; Kandasamy, S.; Sarangi, P.K. The comprehensive review on 3D printing- pharmaceutical drug delivery and personalized food and nutrition. *Food Chem.* **2024**, *459*, 140348. [CrossRef] [PubMed]
11. Eyal, S.; Derendorf, H. Medications in Space: In Search of a Pharmacologist's Guide to the Galaxy. *Pharm. Res.* **2019**, *36*, 148. [CrossRef] [PubMed]
12. Ratiner, K.; Ciocan, D.; Abdeen, S.K.; Elinav, E. Utilization of the microbiome in personalized medicine. *Nat. Rev. Microbiol.* **2024**, *22*, 291–308. [CrossRef] [PubMed]
13. Isoherranen, N. Physiologically based pharmacokinetic modeling of small molecules: How much progress have we made? *Drug Metab. Dispos.* **2025**, *53*, 100013. [CrossRef] [PubMed]

pharmaceutics

MDPI

Article

Cannabidiol-Loaded Nanoparticles Based on Crosslinked Starch: Anti-Inflammatory Activity and Improved Nose-to-Brain Delivery

Ilya Eydelman [1,†], Na'ama Zehavi [2], Valeria Feinshtein [1], Dinesh Kumar [1,3], Shimon Ben-Shabat [1,*] and Amnon C. Sintov [2,4,*]

[1] Department of Clinical Biochemistry and Pharmacology, Ben-Gurion University of the Negev, Be'er Sheva 8410501, Israel; eydelman@bgu.ac.il (I.E.); shteiman@bgu.ac.il (V.F.); dineshbarbola@cuh.ac.in (D.K.)
[2] Laboratory for Biopharmaceutics, E.D. Bergmann Campus, Ben-Gurion University of the Negev, Be'er Sheva 8410501, Israel; naamaz1974@gmail.com
[3] Department of Pharmaceutical Sciences, Central University of Haryana, Mahendragarh 123031, Haryana, India
[4] Department of Biomedical Engineering, Ben Gurion University of the Negev, Be'er Sheva 8410501, Israel
* Correspondence: sbs@bgu.ac.il (S.B.-S.); asintov@bgu.ac.il (A.C.S.); Tel.: +972-8-646-1976 (S.B.-S.); +972-8-647-2709 (A.C.S.)
† This work was performed in partial fulfillment of the requirements for the Ph.D. degree of I.E.

Abstract: Cannabidiol (CBD) has previously been shown to inhibit inflammatory cytokine production in both in vitro and in vivo studies of neurodegenerative diseases. To date, the CBD treatment of these diseases by quantitative targeting directly to the brain is one of the greatest challenges. In this paper, we present a new particulate system capable of delivering CBD into the brain via the intranasal route. Intranasal administration of CBD-loaded starch nanoparticles resulted in higher levels of cannabidiol in the brain compared to an identically administered cannabidiol solution. The production and the characterization of starch-based nanoparticles was reported, as well as the evaluation of their penetration and anti-inflammatory activity in cells. Cannabidiol-loaded starch nanoparticles were prepared by crosslinking with divanillin, using the nanoprecipitation method. Evaluation of the anti-inflammatory activity in vitro was performed using the BV2 microglia cell line. The starch nanoparticles appeared under electron microscopy in clusters sized approximately 200 nm in diameter. In cultures of lipopolysaccharide-induced inflamed BV2 cells, the cannabidiol-loaded starch nanoparticles demonstrated low toxicity while effectively reducing nitric oxide production and IL-6 levels. The anti-inflammatory effect was comparable to that of a glucocorticoid. Starch-based nanoparticle formulations combined with intranasal administration may provide a suitable platform for efficacious cannabidiol delivery and activity in the central nervous system.

Keywords: cannabidiol nanoparticles; intranasal delivery; inflammation; microglia cells; nitric oxide; interleukin-6

1. Introduction

Neurological dysfunctions in the central nervous system (CNS) disrupt memory, speech, and sensorimotor and autonomic performance, with different degrees of severity. Although neurological disorders can be caused by degeneration, trauma, infection, neoplasm, or autoimmune condition [1], neuroinflammation is common in most disorders [2]. Therefore, inhibition of CNS inflammation is optional for many of these conditions. Indeed, this strategy produced a neuroprotective effect in various studies [3,4]. Neuroinflammation is a term that describes several cellular and molecular pathologies that result from the activation of resident CNS cells, and infiltration of CNS by leukocytes or by inflammatory mediators within the CNS. The principal CNS cell types involved in the inflammatory

processes are microglia and astrocytes. Lymphocytes, neutrophils, and monocytes from peripheral blood can infiltrate CNS and escalate neuroinflammation. Both resident and infiltrating cells produce inflammatory mediators, particularly cytokines, which are crucial in the inflammation processes [5]. Transient or moderate inflammation can be beneficial, but prolonged or excessive microglia activation may result in pathologic inflammation and contribute to neurodegenerative and neoplastic diseases [6]. Although drug-targeting various inflamed tissues in the CNS has been demonstrated as a treatment option, the delivery of therapeutic substances to the brain is not an easy task. Due to low drug permeability and cellular uptake, new methods have been sought to effectively deliver active agents, such as cannabidiol, to the CNS tissues without causing undesired consequences. Cannabidiol (CBD) is one of the important phytocannabinoids isolated from the plant *Cannabis sativa*. It lacks psychoactive effects and has a good safety profile [7]. Cannabidiol has been reported to have pharmacological effects in several pathology models, ranging from inflammatory and neurodegenerative diseases to epilepsy, autoimmune disorders, arthritis, schizophrenia, and cancer [8]. Various in vitro and in vivo evidence supports the role of CBD in treating degenerative inflammatory diseases. It can strongly inhibit the production of inflammatory cytokines, including IL-1β, IL-6, and interferon β in LPS-stimulated murine microglial cells [9]. Despite its therapeutic potential, the successful delivery of CBD remains a significant challenge. After an oral administration and a first-pass effect, the bioavailability of CBD is between 13% and 19% [8]. Therefore, an effective delivery platform based on nanotechnology can significantly increase the CBD quantities delivered into the CNS. Intranasal administration of nanoparticulate systems is an alternative solution to the conventional delivery of CNS-targeted drugs. The nasal cavity can be divided into respiratory and olfactory regions. In the respiratory region, drugs can enter systemic circulation or be directly transported to the brain tissue through the trigeminal nerve pathway. In the olfactory region, drugs can be transported or diffused directly to the brain through the olfactory mucosa pathway, considered the most important direct pathway [10]. The use of various drugs delivered through nanoparticulate platforms via the intranasal route has been described as a potential strategy for overcoming the challenges of drug delivery to the brain [10–12].

In the present study, we have demonstrated that nanoparticles based on crosslinked starch (starch nanoparticles, SNPs) are capable of delivering relatively high quantities of CBD into the brain via the intranasal route compared to an intranasal non-particulate CBD. We manufactured CBD-loaded SNPs by a nanoprecipitation technique [13–15], during which crosslinking of starch by divanillin (DV) took place [15]. After characterization of these SNPs, we evaluated their intracellular uptake, cell viability, and the anti-inflammatory effect in an LPS-induced inflammation model of microglia cells.

2. Materials and Methods

2.1. Materials

Maize (corn) starch was obtained from Hopkin & Williams Ltd. (Chadwell Heath, Essex, England). Divanillin (DV) was prepared by an enzymatic reaction of vanillin (Sigma-Aldrich Israel Ltd., Rehovot, Israel) in the presence of horseradish peroxidase and hydrogen peroxide. Mannitol and Triton X-100 were obtained from Sigma-Aldrich, and urea from E. Merck (Darmstadt, Germany). Sodium hydroxide AR, hydrochloric acid 32% AR, and ethyl alcohol AR were purchased from BioLab Ltd. (Jerusalem, Israel). High-performance liquid chromatography (HPLC)-grade solvents were obtained from J.T. Baker (Mallinckrodt Baker, Inc., Phillipsburg, NJ, USA).

2.2. Preparation of Starch Nanoparticles

Starch slurry was prepared using corn starch (1 g), sodium hydroxide (0.8 g), urea (1 g), and double-distilled water (50 mL). All components were stirred until complete dissolution (1-2 h, at room temperature). Prior to particle preparation, starch slurry was acidified to pH 3 by a concentrated HCl solution (32%). An aliquot of the acid-

ified starch slurry containing 20 mg of starch was then diluted with purified water, and appropriate volumes of divanillin suspension (5 mg/mL) were added. Using the "non-solvent dropping" technique, ethanolic solution of CBD (2mg or 5mg/15.4 mL) was dripped into an aqueous mixture of starch and divanillin using a syringe pump (NE-300, New Era Pump Systems, Farmingdale, NY, USA) at a rate of 0.2 mL/min (20 mL syringe with 23G needle). The mixture was constantly stirred at 700 rpm by a magnetic bar in a 40 °C heated bath. At the completion of the non-solvent dripping, the mixture was stirred for an additional hour (500 rpm) and then the remaining ethanol was evaporated by a rotary evaporator (R-205 Rotavapor, Büchi Labortechnik AG, Switzerland). Purified water was added (ad 45 mL) and the starch nanoparticles dispersion was centrifuged (250 rcf, 8 °C, 4 min). The supernatant was carefully collected (40 mL) and 20 mL of mannitol solution (0.1% *w*/*v*) was added. The SNP dispersion was then lyophilized.

2.3. Determination of CBD Content in SNPs

Accurately weighed (3–4 mg) lyophilized CBD-loaded SNP powder was dispersed in water/methanol (1:1), sonicated for 8 min, and centrifuged at 16,000 rcf for 12 min. The supernatant was collected (800 µL) and analyzed by HPLC. The extract was injected into a HPLC system (1260 Infinity II, Agilent Technologies Inc., Santa Clara, CA, USA) equipped with a prepacked column (ReproSil-Pur 300 ODS-3, 5 µm, 250 mm 4.6 mm, Dr. Maisch, Ammerbuch, Germany). The samples were chromatographed using a mobile phase consisting of acetonitrile/acetic acid 0.1% (80:20) at a flow rate of 1 mL/min. Calibration curves—peak areas measured at 208 nm for CBD versus drug concentration—were constructed by running standard drug solutions in methanol for each series of chromatographed samples. The limit of detection (LOD) was 0.01 µg/mL and limit of quantification (LOQ) was 0.05 µg/mL. The entrapment efficiency percentage (EE%) was calculated according to the following equation:

$$\text{EE\%} = \frac{Mass\ of\ CBD\ in\ formulation}{Total\ mass\ of\ CBD\ used\ in\ formulation} \times 100$$

Nanoparticle tracking analysis (NTA): Measurements were performed using a NanoSight NS300 instrument (Malvern Instruments Ltd., Worcestershire, UK), equipped with a 642 nm red laser module and 450 nm long-pass filter, and a camera operating at 25 frames per second, which captured a video file of the particles moving at a constant flow rate from a syringe on a syringe pump. The software for capturing and analyzing the data (NTA 2.3 and 3.4) calculated the hydrodynamic diameters of the particles by using the Stokes–Einstein equation.

2.4. Transmission Electron Microscopy (TEM)

TEM images were recorded with FEI Tecnai T12 G2 TWIN transmission electron microscope operating at 120 kV. Samples of SNPs dispersions were deposited on a copper 300 mesh grid, coated with Formvar and carbon (Electron Microscopy Sciences, Fort Washington, PA, USA) and dried for 5 min. Samples were then stained with 1% uranyl acetate solution. Images were taken using TemCam—F214 (Gauting, Germany).

2.5. Cell Culture Assays

BV-2 cells were maintained in RPMI 1640 medium supplemented with 10% fetal bovine serum (FBS) and antibiotics (penicillin 100 U/mL, streptomycin 100 µg/mL) at 37 °C in a humidified incubator under 5% CO_2.

2.6. Cell Viability Assay

BV2 cells were seeded in a 96-well plate at 1×10^4 cells/well for normal growing conditions, and at 2×10^4 cells/well for LPS-induced inflammation conditions. After 24 h, the cells were treated either with unloaded or with CBD-loaded SNPs. SNPs were dispersed in RPMI. After an additional 24 h, the medium was removed and, CellTiter 96® Aque-

ous One Solution reagent [3-(4,5-dimethylthiazol-2-yl)-5-(3-carboxymethoxyphenyl)-2-(4-sulfophenyl)-2H-tetrazolium, inner salt; MTS] and an electron coupling reagent (phenazine ethosulfate; PES)–20 µL of reagent in 100 µL of fresh medium were added to each well. After 1 h of development, the plate was scanned by a microplate reader (iMark, Bio-Rad) at 490 nm. For viability determination in NO examination (Section 2.9), cells were seeded in 24-well plates at 2×10^5 cells/well; following the induction of inflammation and treatment for 22 h, the medium was removed for examination from each well and immediately replaced with 360 µL of fresh medium containing 60 µL of solution reagent as mentioned previously. After 30 min of development, a total volume of 240 µL from each well was transferred to a 96-well plate where it was equally divided among two wells (120 µL each) and scanned by a microplate reader. An average reading was used for calculation of viability.

2.7. Cannabidiol Release from SNPs in Culture Medium

Two aliquots of SNP powder containing 112 µg of CBD were placed in two glass beakers, each containing 50 mL of culture growth medium. The content of one container was allowed to be unstirred whereas the other was continuously stirred at 150 rpm with a magnetic bar. Both containers were kept at 37 °C during the experiment. Samples of 5 mL were taken from each container at 2 h, 6 h, and 24 h after application. The samples were ultracentrifuged at 30,000 rcf for 12 min at a temperature of 8 °C, and the supernatant from each sample was analyzed by HPLC.

2.8. Cellular Uptake of Nanoparticles

BV2 cells were seeded in 6-well plates at 5×10^5 cells/well. After 24 h incubation, the cells were treated with CBD-loaded SNPs dispersed in RPMI and incubated for an additional 24 h. Cell viability was determined by trypan blue staining and the concentration of cells was measured by a cell counter (Countess™ 3 Automated Cell Counter, Invitrogen). The culture medium was removed, and the cells were washed twice with phosphate-buffered saline solution (PBS). Further, the cells were dissociated from the plate by a rubber scraper. The collected cells were dispersed in PBS and divided into three equal fractions which were treated separately with PBSx1, Triton-X 100 1%, and methanol 100% to evaluate CBD in the cell surface, cytosol only, and the whole cell, respectively. The fractions were shaken for 1 h at 30 rpm using a vertical shaker (Rotamix RM1, Elmi), then centrifuged at 750 rcf for 5 min, and the supernatant was collected and analyzed for CBD content by HPLC.

2.9. Nitric Oxide (NO) Formation

Cells were seeded in 24-well plates at 2×10^5 cells/well. Following 24 h of incubation, the cells were treated with FBS-free medium for 4 h, referred as a "starvation period". Then, this medium was removed, and inflammation was induced by 7 ng/mL lipopolysaccharide (LPS) in a growth medium containing 1% FBS, 1% HEPES buffer, and 0.1% bovine serum albumin (BSA). The effect of various treatments—which were administered concomitantly—on NO formation was studied after 22 h of treatment using Griess reagent. Duplicates of 100 µL medium were loaded on 96-well plate together with preprepared nitrite standards ($NaNO_2$). The experimental medium was used as "standard zero". Aliquots (100 µL) of Griess reagent were added to each well. After 15 min of settling in the dark, the plate was scanned by a microplate reader (iMark, Bio-Rad) at 540 nm.

2.10. IL-6 Determination

The experiment was conducted as described in Section 2.9. The medium was either examined immediately at the end of the experiment or was kept at −80 °C until examination. A mouse IL-6 ELISA MAX set (BioLegend, San-Diego, CA, USA) was used to determine IL-6 levels. Standards and samples were treated according to manufacturer's protocol.

2.11. Animals

All animal treatments followed protocols reviewed and approved by the Institutional & Use Committee, Ben-Gurion University of the Negev, which complies with the Israeli Law of Human Care and Use of Laboratory Animals. Sprague Dawley rats (male, 200–300 g body weight, Envigo RMS, Ein Karem, Jerusalem, Israel) were used in this study. All animals were housed in polycarbonate cages and maintained on a 12/12 h light/dark cycle under controlled temperature and humidity conditions. The rats had ad libitum access to food and water.

2.12. Intranasal Administration (IN)

Animals were randomly divided into groups for each formulation or post-administration period. The IN-administered dose used for each animal was 100 μg CBD in nanoparticles, which accounted for approximately 0.4 mg/kg body weight. SNP powder was suspended in water immediately before nasal installation. The applied volume was 20 μL/nostril (total of 40 μL containing 100 μg CBD). As a non-particulate control, CBD was dissolved in 50:35:15 (*v*/*v*) PEG 400:saline 0.9%:ethanol as described by Paudel et al. [16]. Similar to the SNP-administered group, the applied volume was 20 μL/nostril, which corresponded to a total dose of 100 μg CBD. The animals were sedated with isoflurane vapor just before administration. After a predetermined period from administration (5, 10, and 15 min for SNPs administration; 10 min for dissolved CBD), the animals were euthanized by CO_2 aspiration. The brain was carefully excised, frozen at −80 °C, lyophilized overnight, and kept at −20 °C. Just before analysis, the dry brain tissue was crushed, extracted with 2 mL methanol, sonicated for 8 min, centrifuged at 17,000 rcf for 12 min, and the separated supernatant was analyzed by HPLC.

2.13. Statistical Analysis

Data were derived from at least two independent experiments performed in triplicate and expressed as mean values (±SD). The statistical differences between mean values were assessed by using the Student's *t*-test at $p < 0.05$.

3. Results and Discussion

3.1. Production and Size Characterization of Nanoparticles

Based on a previous study in our group [15], we set out to develop a starch-based nanoparticulate system loaded with cannabidiol (CBD). As mentioned previously, CBD possesses anti-inflammatory and neuroprotective effects which are highly relevant for the treatment of neurodegenerative diseases [8,9,17]. Starch was chosen as a particle-forming polymer because it is a natural, renewable, and biodegradable substance, and is widely used in various pharmaceutical applications [14,18,19]. Following SNP production, we first characterized these nanoparticles by analyzing particle size, showing that the initial process yielded nanoparticles larger than 200 nm. Interestingly, by decreasing starch concentration in the aqueous solution before nanoprecipitation from 1.7 mg/mL to 1mg/mL, the average size was reduced (Table 1). Table 1 summarizes the size measurements of nanoparticles crosslinked by divanillin (DV) at two concentrations, demonstrating that size reduction was affected by decreasing the starch concentration only, and was not dependent on the crosslinkage degree. However, the use of 20% crosslinker on a starch basis at 1.7 mg/mL of starch concentration (in the aqueous solution prior to the nanoprecipitation) produced an average particle size of >300 nm and this formulation was not examined further. This phenomenon of reduction in particle size while the starch concentration decreased is in agreement with previous publications [20,21]. Hedayati et al. [20] suggested that the high viscosity of a highly concentrated starch gel solution hinders the dispersion of starch slurry toward the non-solvent, leading to the formation of larger particles. Saari et al. [21] attributed this phenomenon not to the particle size, but to an aggregation of smaller nanoparticles, suggesting that at higher concentrations, more particles of a similar size are formed and aggregated to produce clusters. In the present study, we have shown by using

TEM imaging that the nanoparticle size measured by NTA is indeed related to a cluster of aggregated small nanoparticles (Figure 1). As shown, the crosslinking did not significantly change the size of the SNP clusters, however: as evidenced by TEM images, it formed denser cluster structures compared to the non-crosslinked SNPs.

Table 1. Summary of the mean particle size of CBD-loaded starch nanoparticles manufactured at two starch concentrations and several crosslinking degrees. (* statistically significant, $p < 0.05$; ^{NS} not statistically significant).

Formulation	Aqueous Starch Concentration, mg/mL	Divanillin Concentration on Starch Basis, %*w*/*w*	Mean Particle Size ± SD (in Diameter), nm	Polydispersity Index
SNP0-1	1.7	0	274.0 ± 75.2	0.11 ± 0.03
SNP0-2	1.0	0	* 187.4 ± 19.3	0.19 ± 0.03
SNP5-1	1.7	5.0	260.5 ± 16.1	0.15 ± 0.07
SNP5-2	1.0	5.0	* 206.1 ± 21.0	0.13 ± 0.02
SNP10-1	1.7	10.0	248.6 ± 11.8	0.16 ± 0.07
SNP10-2	1.0	10.0	^{NS} 205.8 ± 44.4	0.17 ± 0.06
SNP15-1	1.7	15.0	297.0 ± 14.8	0.16 ± 0.02
SNP15-2	1.0	15.0	* 206.7 ± 43.6	0.21 ± 0.07

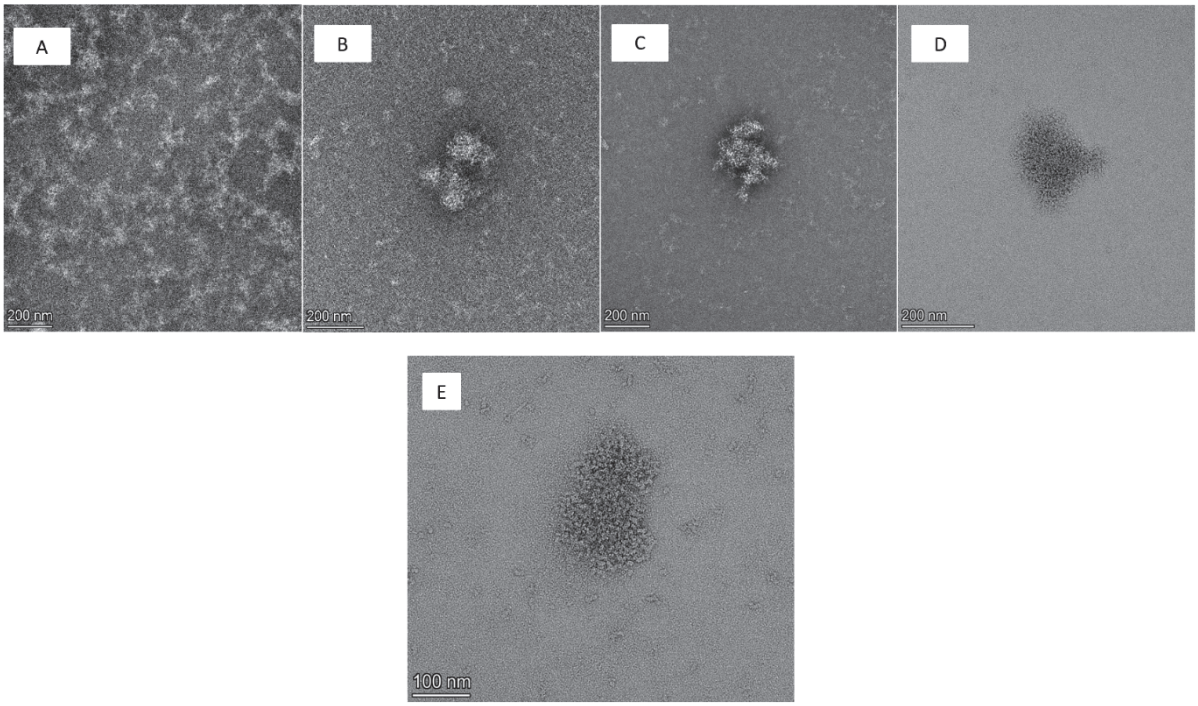

Figure 1. TEM images of CBD-loaded starch nanoparticles, non-crosslinked (**A**), and crosslinked with 5% DV (**B**), 10% DV (**C**), 15% DV (**D**) at ×45,000 magnification. Starch nanoparticles crosslinked with 10% DV (**E**) are also shown at ×92,000 magnification, demonstrating a cluster composed of smaller nanoparticles.

We chose a formulation that was produced with an initial starch concentration of 1 mg/mL for all our subsequent experiments, since the mean particle size was smaller compared to the formulation with a higher initial starch concentration. Crosslinking agents can enhance the stability of the formulation. They can also influence the size of the

nanoparticles that are formed [22]. Crosslinker presence can also change the nanoparticle morphology [23]. Since these factors can have an influence on tissue penetration or biodegradation, we have decided to explore both the non-crosslinked and crosslinked formulations. The uploading of CBD to the nanoparticles was monitored using an extraction technique involving a mixture of equal volumes of water and methanol. It was realized that the extraction of CBD from the dried SNP powder was more efficient using this technique than by using 1% Triton-X 100, N-methyl-2-pyrrolidone (Pharmasolve™), methanol only, or even 9:1 methanol-water. The entrapment efficiency (EE%) of CBD in the nanoparticles was determined, and the values were 39.4% ± 13.9, 29.5% ± 5.08, 29.2% ± 10.6, and 32.5% ± 8.2 for SNPs crosslinked with 0%, 5%, 10%, and 15% DV, respectively. It was also found that the EE% was higher when the nanoprecipitation process was performed at pH 3. Starch solutions with a pH lower or higher than 3 resulted in a decrease in the CBD loading (30% reduction in the crosslinked SNPs and 25% in the non-crosslinked SNPs). These data were obtained during a preliminary evaluation where one batch preparation was performed for each of four formulations (1 mg/mL initial starch; 0%, 5%, 10% and 15% DV) at 4 different pH conditions (pH = 2.3, 2.5, 3, 4.4). As a result of this experiment, the EE was consistently higher at pH 3 for all formulations. Such influence of pH on nanoprecipitation processes was also reported by Podaralla and Perumal [24]. As shown above, the EE values of the crosslinked SNPs were lower than the non-crosslinked SNPs (29.2–32.5% vs. 39.4%). This expected finding indicates that the crosslinking of starch by divanillin decreased the intermolecular space of the amorphous regions in the polysaccharidic structure.

3.2. CBD Penetration to the Brain after Intranasal Administration

It was hypothesized that a nanoparticulate system is more advantageous than a solution in delivering a drug to the brain following intranasal administration (IN). Preliminary data obtained by brain CBD analyses following IN administration of SNPs and a CBD solution to rats (Section 2.12) supported this hypothesis. Figure 2 presents the results of the preliminary pharmacokinetic study of brain CBD after IN administration of CBD-loaded crosslinked SNPs (5% DV) in rats (100 μg CBD dose, n = 6). The peak brain concentration (C_{max} = 5.22 μg/g tissue) was determined 10 min after administration. In contrast, the concentrations of brain CBD after IN administration of non-particulate CBD, which had been dissolved in PEG 400: saline: ethanol (100 μg dose of CBD in solution, n = 3) at the same time points, were under the limit of detection of the HPLC method, namely, less than 10 nanograms/mL. Conventional formulations administered intranasally rely on absorption through the nasal epithelium into the blood circulation. This may allow us to avoid the hepatic first pass effect [25], yet the delivery into the brain is dependent on the brain blood vessels that create the blood brain barrier. As a consequence of this systemic route, plasma t_{max} following IN administration of CBD solution in rats and dogs was detected at approximately 30 min [16,25]. In contrast, when nanoparticulate-aided administration is employed, the major anticipated route is through the olfactory nerves directly into the brain [10]. This faster and more efficient penetration into the brain is due to the circumvention of the systemic circulation by direct trafficking into the CNS. Extensive pharmacokinetic studies, which are beyond the scope of this report, are needed to elaborate and establish the mechanism in which SNPs target the brain following IN administration. These studies will be separately published.

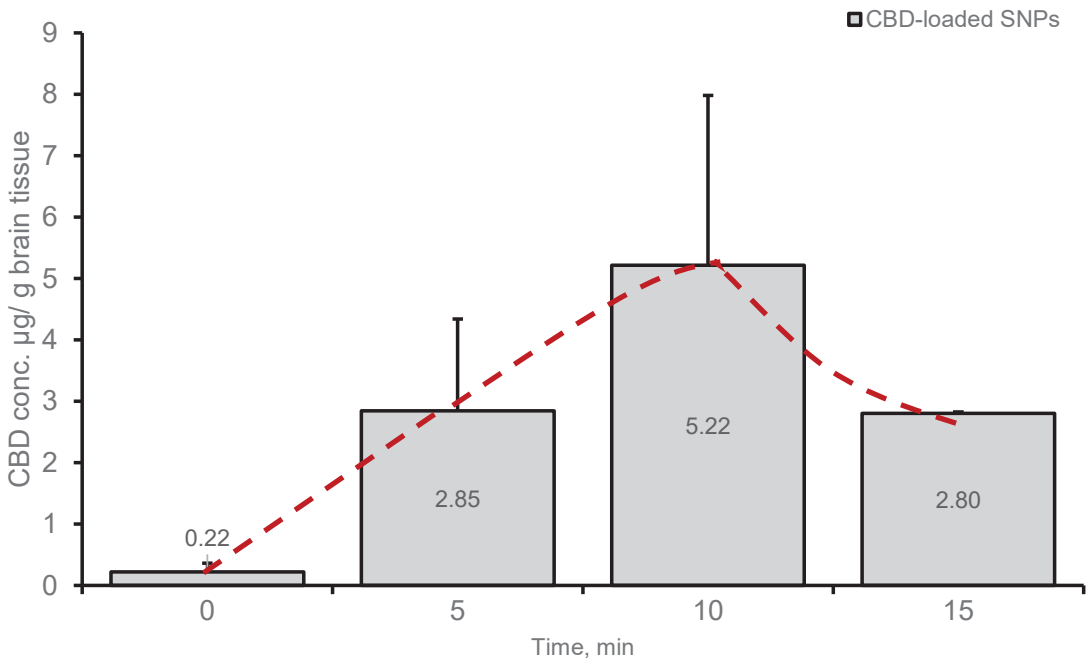

Figure 2. Brain levels of CBD after IN administration of CBD-loaded SNPs 5% DV—100 µg dose, 0.4 mg/kg body weight. Mean (±SD) measured in methanolic brain extracts, n = 2 for 0 and 15 min, n = 3 for 5 min, n = 6 for 10 min. Animals were randomly assigned to each group.

3.3. CBD Release from SNPs

The release of CBD from SNPs was monitored in a culture growth medium without dissolution excipients such as bovine serum albumin. Cumulative released concentrations of CBD were measured at various periods of time after dispersion of CBD-loaded SNPs in the medium, with and without stirring. The measurements revealed that the release of CBD from the SNPs was incomplete while the concentration of CBD released to the medium accounted for 44% and 38% of total applied CBD in stirred and unstirred samples, respectively (at a peak reached after 2 h). A total of 40% and 31% of the applied CBD in the SNPs were obtained immediately upon the application of stirred and unstirred samples, respectively. After two hours of release study, the CBD concentration in the medium slowly declined. This phenomenon may result from a two-way process, dissociation of CBD from the SNPs and its precipitation, or reattachment to the available SNPs in the media. The dissociation is initially dominant, followed by an equilibrium state. A graphical description of the experiment is found in Supplementary Materials, Figure S1.

3.4. Cellular Uptake of CBD-SNPs

The experimental procedure for the evaluation of nanoparticle entry into cells has previously been described by Zamansky et al. [26]. In these experiments we used BV2 cells in culture and CBD-loaded SNPs which had been crosslinked with 15% DV. Briefly, after 24 h treatment, the BV2 cells in each well were washed, detached from the wells, counted, and divided into three equal fractions treated with either PBS×1, Triton-X 100 1%, or methanol 100%. The purpose of the treatments was to retrieve CBD from separate parts of the cells: (a) PBS to recover CBD from the cell surface ("ExCell" fraction), (b) Triton X-100 to recover CBD from the cell surface and cytosol (CBD within cells, but not in the nucleus), and (c) methanol to extract total CBD. By subtracting the CBD quantity found in the ExCell fraction from the amount found by Triton X-100, the amount within the cytosol ("InCytosol") is determined. By extracting the CBD quantity found in ExCell fraction from the total CBD quantity as analyzed in the methanol extract, the amount within the cells ("InCell"; cytosol + nucleus) is determined. Cell viability was examined using trypan blue staining. The obtained viability data were 83.5% ± 4.9, 88.5% ± 12.0, and

69% ± 1 for untreated control, 5 μM CBD and 10 μM CBD concentrations in SNP dispersion, respectively (n = 3). There was a statistically significant difference between the control cells and the cells treated with 10 μM CBD concentration in SNPs as well as between cells treated with 5 μM and 10 μM CBD concentrations in SNPs. No significant difference between the control and 5 μM treatment groups was discovered. The lower viability obtained in the 10 μM CBD-SNP treated cells as determined by trypan blue staining (18% reduction) was different from the results acquired by the MTT viability test which demonstrated viability reduction only at 15 μM CBD in SNPs, probably because the trypan blue viability values were not calculated relative to the control cells. As shown in Table 2, the quantity of CBD found in the "ExCell" fraction was, as expected, similar in all experiments, as the concentrations of nanoparticles were approximately the same. This supports previous studies showing that CBD exhibits some of its effects through interactions with the cell membrane receptors, such as the CB1, CB2, TRP receptors, GPR receptors, 5-HT_{1A} receptor, and A_{2A} receptor [8,27]. Furthermore, it may indicate that there was an interaction between CBD-loaded SNPs and the surface layer of the cells. When the low concentration of CBD in SNPs dispersion (5 μM) was applied to cells, "InCell" and "InCytosol" CBD fractions decreased significantly compared to the higher concentration of CBD in SNPs. However, no differences between "InCell" and "InCytosol" CBD fractions were found, suggesting that CBD entering the cytoplasm did not cross the nuclear membrane. CBD in the cytosol can influence NADPH oxidase, NF-kB and STAT3 pathways, or act as an agonist on the PPARγ receptor on the nuclear membrane [27,28].

Table 2. Cellular uptake of CBD from CBD-loaded SNPs (15% DV) in BV2 cell culture, 24 h after treatment (values presented as mean ± SD).

	10 μM CBD 2.67×10^9 SNPs/mL	**5 μM CBD 1.33×10^9 SNPs/mL**
"ExCell" CBD, μg	0.15 (±0.002)	0.15 (±0.008)
"InCell" CBD, μg	0.21 (±0.05)	0.12 (±0.02)
"InCytosol" CBD, μg	0.22 (±0.04)	0.12 (±0.04)
% of administered CBD found in cells	1.4	1.6

3.5. Effect of CBD-Loaded SNPs Treatment on Cell Viability and Nitric Oxide (NO) Formation in BV2 Cells

Concurrently with neuroprotective and anti-inflammatory effects, there are also a few reports indicating that CBD has a cytotoxic effect on cancer and normal cell lines [29–31]. The effect on the viability of microglial BV2 cells in normal growth conditions was evaluated for CBD-loaded SNPs and for matching numbers of unloaded SNPs. We found a significant reduction in viability at concentrations of ≥15 μM CBD in SNPs with more than a 50% reduction in viability at a concentration of 25 μM of CBD in SNPs. This effect is in accordance with a report describing a reduction in the viability of normal human cells following a treatment with CBD at concentrations greater than 10 μM [32]. Unloaded SNPs caused a certain growth inhibition (15–20%) only with a particle concentration of 4×10^9 nanoparticles per milliliter, which corresponded to the concentration of particles for 25 μM CBD treatment. In contrast, the viability of LPS-inflamed cells was significantly reduced at a concentration of 10 μM CBD in SNPs, that is, 53% ± 20.7, $p < 0.02$ and 55% ± 12.8, $p < 0.004$ (mean ± SD; n = 9; three independent experiments) relative to untreated control of LPS-induced cells ('LPS control') for non-crosslinked (0% DV) and crosslinked (15% DV) starch formulations, respectively. This can be attributed to an increase in cytotoxic effect of CBD under conditions of a reduced serum in the growth medium as described by Sainz-Cort et al. [31]. We further conducted experiments using 5 μM and 7 μM of CBD in SNP dispersion and matching numbers of unloaded nanoparticles of the same formulations (0% and 15% DV). After treatment of LPS-induced cells with CBD-loaded SNPs we found no significant reduction in viability; however, reduced viability was noted

only after treatment with non-crosslinked SNPs loaded with 7 μM CBD concentration, 73.2% ± 15.9, $p < 0.05$ (mean ± SD; n = 9; 3 independent experiments), relative to "LPS control". This reduction, which was related to the absence of crosslinker in the formulation, may be due to a higher release of CBD to the medium and to a more prominent cytotoxic effect. A slight elevation in viability (3–5%, $p < 0.05$) was recorded for 2 out of 4 groups of unloaded SNPs, while the other groups were not statistically different from the "LPS control". There are inconsistent data regarding the cytotoxic concentration of CBD in microglia cells under inflammatory conditions. Dos-Santos-Pereira et al. [33] mentioned a successful use of CBD at concentrations up to 10 μM in primary microglia cells for the prevention of LPS-induced inflammation, while Kozela et al. [9] showed only a slight reduction in viability when applying 10 μM CBD to LPS-inflamed BV2 cells. On the other hand, a report by Wang et al. [34] demonstrated around a 60% reduction in viability of microglia BV2 cells occurred using the same CBD concentration and same time frame of treatment as in the study of Dos-Santos-Pereira et al. [33]. Nonetheless, it is difficult to utterly compare these reports since some experimental conditions, such as the LPS concentration and the time of LPS and CBD treatment, were different. In addition, no direct comparison can be made between the current use of CBD-loaded SNPs and the CBD-containing solutions that were used in the published experiments. Detailed information regarding viability experiments is found in Supplementary Materials, Figures S2–S4.

Under consideration based on the cell viability testing, the nitric oxide (NO) formation was evaluated in inflamed (LPS-induced) BV2 cells treated with either unloaded or CBD-loaded SNPs (with 0% or 15% DV). CBD-loaded SNPs were compared to unloaded SNPs (set to contain a matching number of nanoparticles per milliliter), in LPS-induced (7 ng/mL) cells and non-inflamed control cells (treated with a medium without LPS). SNPs unloaded with CBD did not affect NO secretion (Figure 3), whereas a concentration-dependent reduction in NO production was observed with non-crosslinked SNPs (0% DV) containing 10, 15, and 20 μM CBD, resulting in 58.7% (±9.0%), 34.7% (±13.0%), and 14.6% (±9.0%) of released NO (n = 9) relative to the NO formed by the LPS-inflamed control cells, respectively (Figure 3). However, as mentioned earlier, cell viability was compromised at these CBD concentrations, and therefore further cell inflammation experiments were conducted using lower CBD concentrations. Figure 4 presents an experiment with two SNP formulations (0% and 15% DV) containing CBD at a concentration of 7 μM. The reduction in NO production was approximately 35% for both formulations compared to NO release from untreated LPS-induced control cells (Figure 4). The use of 5 μM CBD in SNPs at the same conditions in three independent experiments has also resulted in a statistically significant reduction of NO formation (obtained values of 84.1% ± 9.3, $p < 0.03$ and 86.3% ± 5.6, $p < 0.01$ for 0% DV and 15% DV, respectively) relative to NO release from LPS-induced control cells (n = 9).

3.6. Effect of Treatment with CBD-Loaded SNPs on IL-6 Levels in BV2 Cells

The secreted levels of IL-6 were also monitored. IL-6 is an interleukin produced throughout the inflammation process in the medium of BV2 cells and used as an additional marker of inflammation level. As expected, a significant elevation in the level of IL-6 was noted as compared to the untreated control 22 h after LPS stimulation (7 ng/mL) which had been preceded by a 4 h "starvation period" (see Materials and Methods section). The glucocorticoid dexamethasone (2.5 μM) was used as a positive control for anti-inflammatory effect [33]. The utilization of SNP formulations containing 5 μM CBD without crosslinker resulted in the reduction of IL-6 levels by approximately 50% as compared to LPS-treated control cells ("LPS control") using an experimental procedure identical to that of NO experiments (Figure 5A). Although there was an apparent reduction in IL-6 when crosslinked (15% DV) SNPs were applied to the cells at the same CBD concentration (83.4 ± 25% relative to "LPS control"), this reduction was not statistically significant. However, it was noted that unloaded nanoparticles of this formulation (SNPs with 15% DV) caused an elevation in IL-6 (126.9% ± 31) compared to the "LPS control". Two additional controls, CBD solution in DMSO diluted with experimental medium ("free CBD"; 0.18% final DMSO

concentration) and dexamethasone, were also examined. Interestingly, we did not observe any effect of the "free CBD" on IL-6, although it was used at the same concentration as in the SNP formulations. CBD is practically insoluble in water but it is solubilized in BSA-supplemented growth medium (up to 8–10 μM), and the solubility can be further increased with additional BSA supplementation [35]. The experimental medium used in the present study contained 0.1% w/v BSA. We assumed that the reason for the lack of effect of 15% DV formulation as well as the "free CBD" was a relatively lower availability of CBD to the cells, either by immediate precipitation of the "free CBD" or by the slow rate of release of CBD from the crosslinked SNPs. As was demonstrated by Zamansky et al. [35], the addition of BSA can increase the release of CBD from nanoparticles and improve its solubility. We further confirmed that the CBD release from SNPs dispersed in water supplemented with BSA was improved. CBD release in purified water with 0.25% w/v BSA was increased by 64%, 90%, and 111% as compared to 0.1% w/v BSA at 0, 60, and 120 min, respectively. Therefore, we conducted a further series of experiments with 0.25% w/v BSA in the experimental medium (Sections 2.9 and 2.10). This addition resulted in a significant reduction of IL-6 after the "free CBD" treatment, but not after treatment with the crosslinked SNPs. We hypothesized that the possible cause of this phenomenon is related to the increase in IL-6 caused by unloaded crosslinked SNPs. Treatment with unloaded SNPs at a concentration of 1.34×10^9 nanoparticles per milliliter (which was approximately equal to the concentration of nanoparticles of a similar formulation loaded with 5 μM CBD) resulted in IL-6 values of 138% ± 34 of the untreated control (LPS-induced cells). This finding is in accordance with the result mentioned earlier (126%). However, treatment of LPS-induced cells with a crosslinked starch formulation in which the nanoparticle concentration was reduced by half resulted in a reduction of IL-6 to levels compared to the LPS-treated control. It should be noted that the treatment of non-LPS-induced cells with a crosslinked starch formulation, even at an increased nanoparticle concentration (×2), did not cause IL-6 elevation. We, therefore, produced SNPs (15% DV) using an increased *in-process* CBD quantity (×2.5). Although the EE of the formulation decreased to 23%, this resulted in a higher CBD concentration (in μg CBD/mg SNPs) and enabled treatment with the same concentration of CBD as in the previous assays, but with a reduced nanoparticle concentration (in units/mL). Figure 5B summarizes these experiments. As shown, the use of 15% DV in CBD-loaded SNP formulation resulted in a reduction of IL-6 by approximately 30%, compared to the untreated control of LPS-induced cells ("LPS control"). A similar reduction was noted in the "free CBD" group. The use of 5% DV containing formulation exhibited comparable results to 15% DV containing formulation and "free CBD". There was no significant difference between "LPS control" and the unloaded SNP formulations ($p = 0.94$ and $p = 0.34$ for 5% and 15% DV-containing formulations, respectively). Viability was not compromised in any of the groups represented in Figure 5.

It was previously demonstrated that IL-6 levels in BV2 cells started to rise approximately 2 h after LPS stimulation, continued to rise and remained at high levels 24 h after stimulation [36]. In the present study, we examined both the post-treatment effect of SNPs at 22 h after LPS stimulation (Figure 5), and 6 h after the stimulation (Figure 6). As evident from Figure 6, the anti-inflammatory effect is also noted at 6 h after treatment. A decrease of approximately 45% in IL-6 formation was observed after treatment with CBD-loaded non-crosslinked SNPs, which was comparable to the effect of "free CBD". A reduction of more than 25% was noted for CBD-loaded crosslinked SNPs (15% DV). The 15% reduction in IL-6 after treatment with unloaded non-crosslinked SNPs was found not to be statistically significant ($p = 0.09$); however, a significant increase ($p = 0.02$) in IL-6 formation was measured after treatment with unloaded crosslinked SNPs at this time point. This 18% increase may explicate the relatively lower reduction in IL-6 level after treatment with the CBD-loaded crosslinked (15% DV) SNPs in this experiment.

Muñoz et al. [37] reported that size-dependent inflammation was initiated by nanoparticles due to the interaction with cell membranes. The inflammation was attributed to smaller-sized (10–40 nm) particles while larger particles (100–1000 nm) behaved rather

inertly [37]. As reported in the present study (Table 1 and Figure 1), all SNP types were structured in clusters of a similar size; however, the crosslinked SNPs created a denser cluster of nanoparticles compared to the loosely connected clusters created by the non-crosslinked SNPs. The denser structures of the crosslinked SNPs may imply a general tendency of these nanoparticles to pursue interfacial reactions with interactive surfaces such as cell membranes, which resulted in increased IL-6 release.

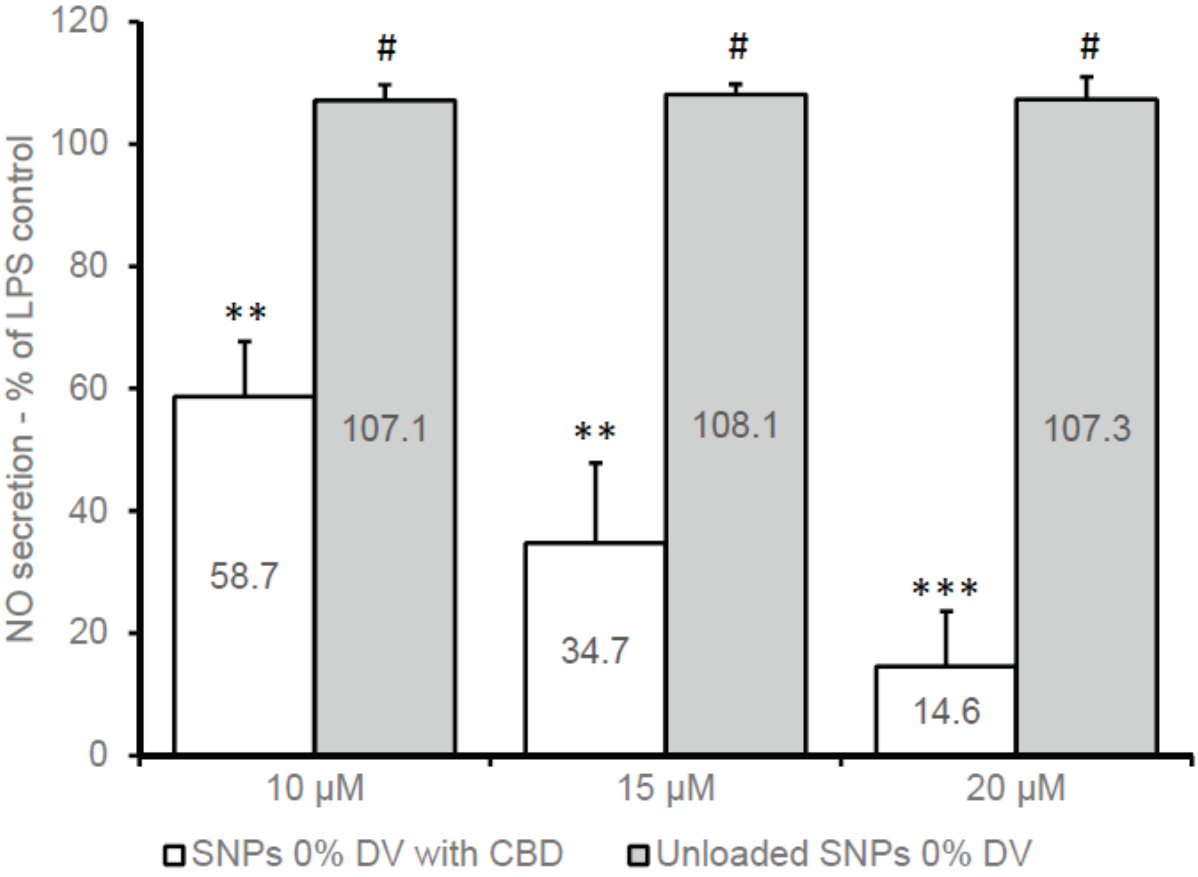

Figure 3. Nitric oxide secretion in BV2 cells 22 h after treatment with CBD-loaded and unloaded SNPs in medium with 1% FCS and LPS (7 ng/mL). Mean (±SD) of three independent experiments (n = 9). ** $p < 0.005$ against LPS control; *** $p < 0.0002$ against LPS control; # not significant against LPS control.

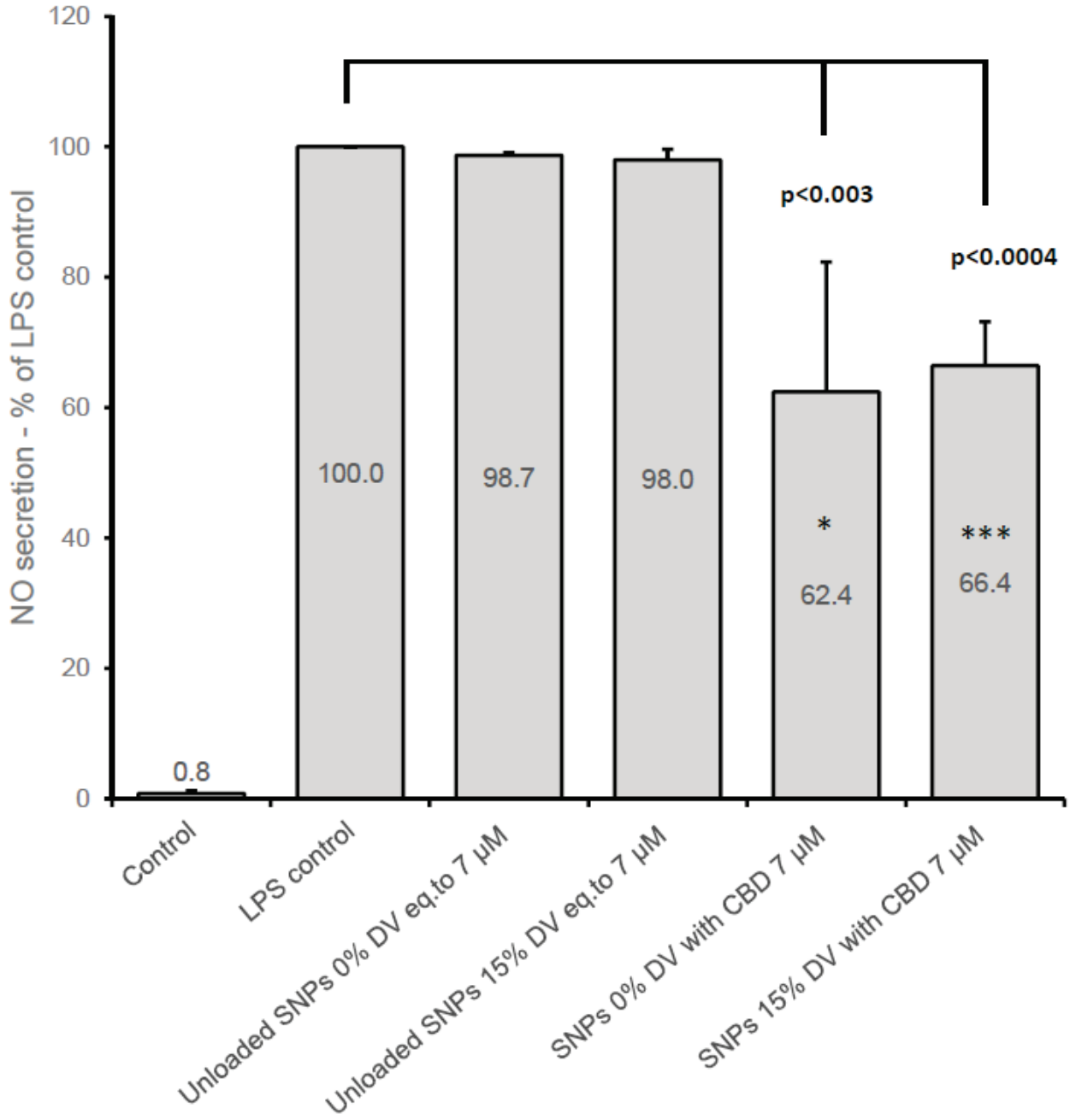

Figure 4. Nitric oxide secretion in BV2 cells 22 h after treatment with CBD-loaded and unloaded SNPs (two formulations)in medium with 1% FCS and LPS (7 ng/mL). Mean (±SD) of three independent experiments (n = 6 for control, LPS control, and unloaded SNPs; n = 9 for CBD-loaded SNPs). * $p < 0.03$ against matching blank SNPs; *** $p < 0.0006$ against matching blank SNPs. Values were adjusted for cell viability in case the viability was lower than 95% of LPS control group.

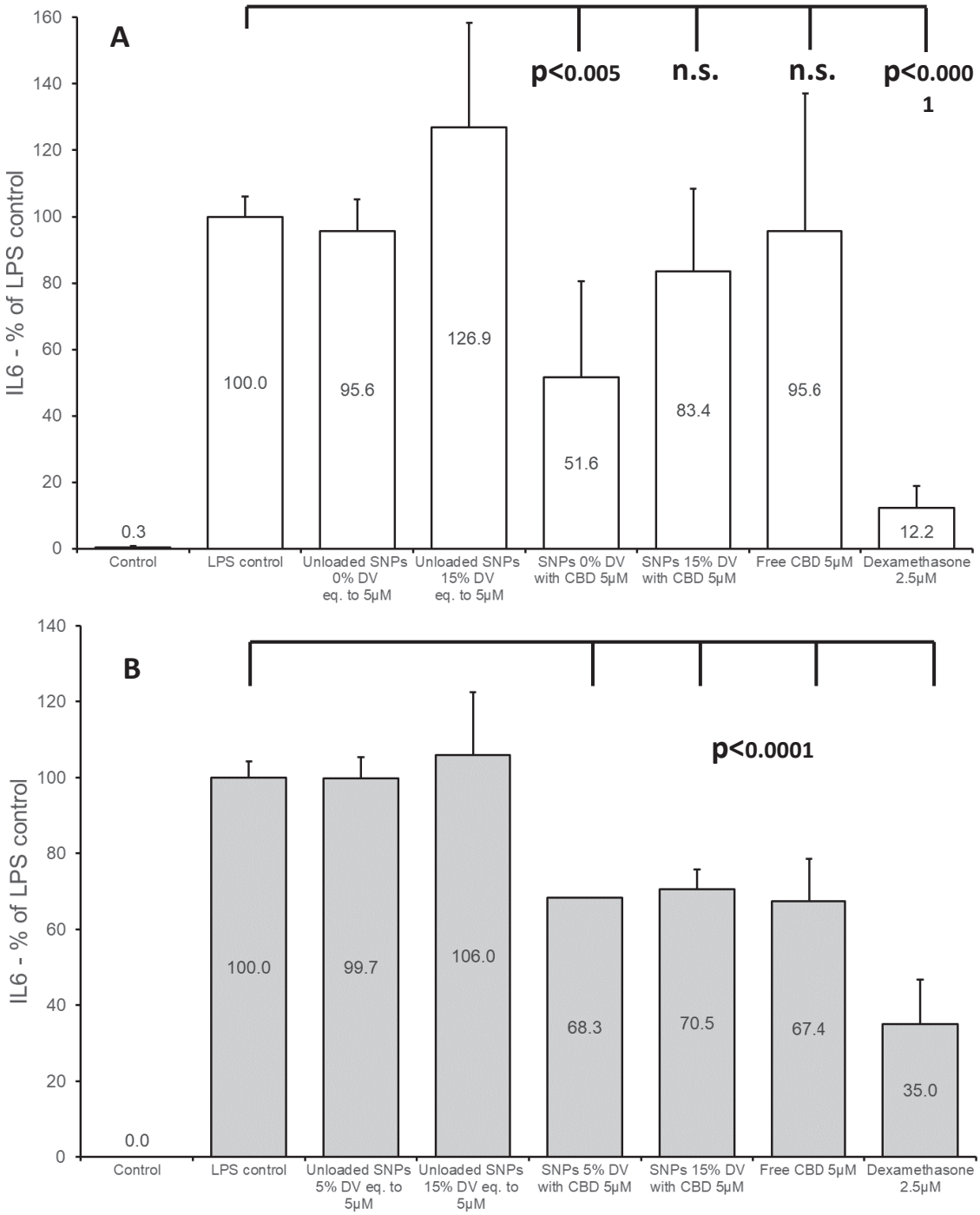

Figure 5. IL-6 production in BV2 cells 22 h after treatment with CBD-loaded and unloaded SNPs. The medium was prepared with 1% FCS, LPS (7 ng/mL), and 0.1% BSA (**A**) or 0.25% BSA (**B**). Mean (±SD) of two or three independent experiments (n = 6).

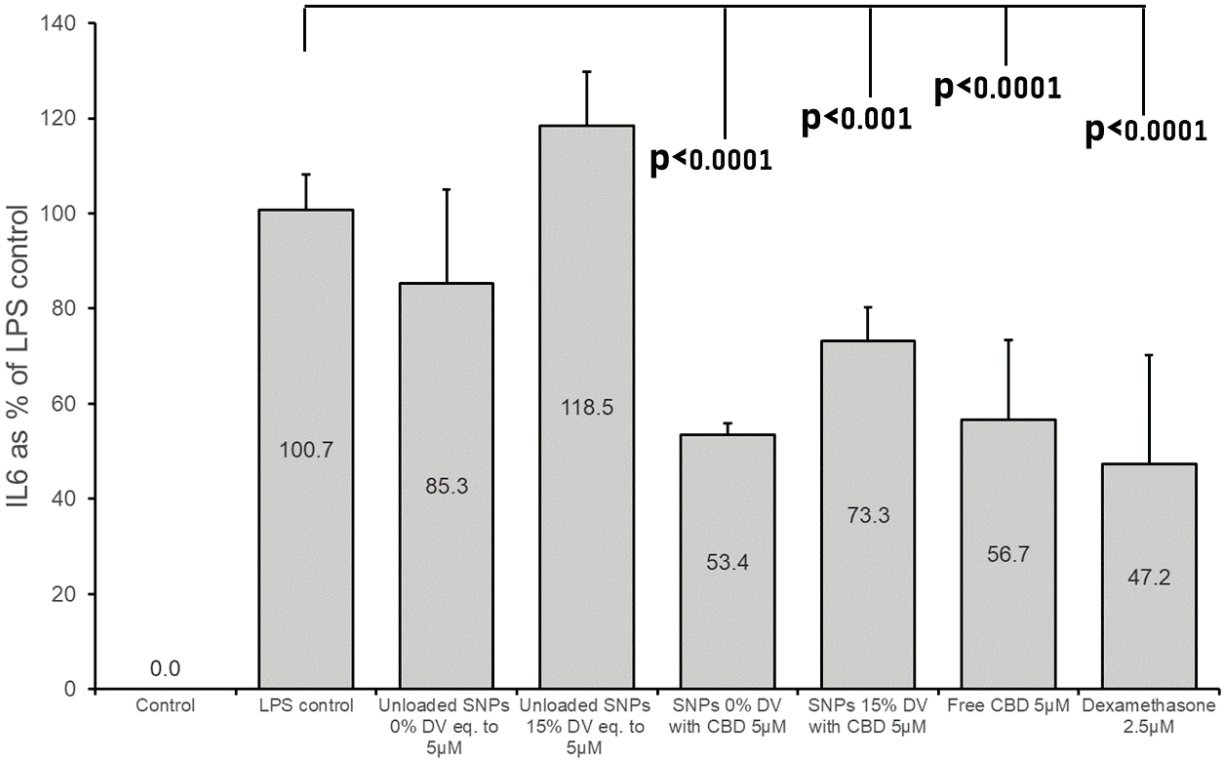

Figure 6. IL-6 production in BV2 cells 6 h after treatment with CBD-loaded and unloaded SNPs. The medium was prepared with 1% FCS, LPS (7 ng/mL) and 0.25% BSA. Mean (±SD) of two or three independent experiments (n = 6 for control, unloaded SNPs, CBD-loaded SNPs, and dexamethasone; n = 8 for LPS control and free CBD).

4. Conclusions

Cannabinoids, including cannabidiol (CBD), are potential active agents for the treatment of inflammation-related conditions, with an emphasis on neuroinflammation. In this study, starch-based CBD-containing nanoparticles were produced with and without the addition of a crosslinker. The adjustments of several parameters during production resulted in improved particle characteristics in the size and entrapment of CBD. A preliminary in vivo study indicates an advantage of intranasal CBD-loaded SNPs over intranasal CBD in solution regarding brain penetration. Additional examination has demonstrated the ability of these SNPs to deliver entrapped CBD into microglia cells. This action resulted in a reduction of NO production and IL-6 levels indicating an anti-inflammatory activity without a decrease in viability.

Supplementary Materials: The following supporting information can be downloaded at: https://www.mdpi.com/article/10.3390/pharmaceutics15071803/s1, Figure S1: Time dependent CBD release from SNPs in growth medium. One sample at each time point was analyzed, without and with stirring. CBD-loaded SNPs 15% DV. Expected CBD concentration in case of total release of SNPs-loaded CBD–2.3 μg/ml; Figure S2: BV2 cells viability 22 h after treatment with CBD-loaded SNPs (two formulations and various CBD concentrations) in normal growth conditions. Mean (±SD) of three independent experiments (n = 30 for control (not presented); n = 15 for each CBD-loaded SNPs group). *—$p < 0.01$ against untreated control; **—$p < 0.002$ against untreated control; ***—$p < 0.0009$ against untreated control; Figure S3: BV2 cells viability 22 h after treatment with CBD-loaded and unloaded SNPs (two formulations)—medium with 1% FCS and LPS (7 ng/mL). Mean (SD) of three independent experiments (n = 6 for control, LPS control (not presented) and unloaded SNPs; n = 9 for CBD-loaded SNPs). *—$p < 0.05$ against LPS control; #—nonsignificant against LPS control; Figure S4: BV2 cells viability 22 h after treatment with CBD-loaded and unloaded (blank) SNPs (two formulations)—medium with 1% FCS and LPS (7 ng/mL). Mean (±SD) of three independent experiments (n = 18 for control and LPS control; n = 9 for each treatment group).

*—$p < 0.02$ against LPS control; **—$p < 0.006$ against LPS control; ***—$p < 0.0009$ against LPS control; #—nonsignificant against LPS control.

Author Contributions: Experimentation, investigation, writing—first draft, I.E.; experimentation, analysis, N.Z.; supervision, writing—review and editing, V.F.; conceptualization, D.K. conceptualization, writing—review and editing, S.B.-S. and A.C.S. All authors have read and agreed to the published version of the manuscript.

Funding: This research received no external funding.

Institutional Review Board Statement: The animal treatments were performed in accordance with a protocol reviewed and approved by the Institutional Committee for the Ethical Care and Use of Animals in Experiments, Ben-Gurion University of the Negev, which complies with the Israeli Law of Human Care and Use of Laboratory Animals. Authorization number: IL-30-06-2020(C).

Informed Consent Statement: Not applicable.

Data Availability Statement: Data can be available under request.

Acknowledgments: The authors are grateful for the professional assistance and technical support of the staff at Ilze Katz Institute for Nanoscale Science & Technology.

Conflicts of Interest: The authors declare that they have no known competing financial interests or personal relationships that could have appeared to influence the work reported in this paper.

References

1. GBD 2016 Neurology Collaborators. Global, Regional, and National Burden of Neurological Disorders, 1990–2016: A Systematic Analysis for the Global Burden of Disease Study 2016. *Lancet Neurol.* **2019**, *18*, 459–480. [CrossRef] [PubMed]
2. Gilhus, N.E.; Deuschl, G. Neuroinflammation—A Common Thread in Neurological Disorders. *Nat. Rev. Neurol.* **2019**, *15*, 429–430. [CrossRef] [PubMed]
3. Azodi, S.; Jacobson, S. Cytokine Therapies in Neurological Disease. *Neurother. J. Am. Soc. Exp. Neurother.* **2016**, *13*, 555–561. [CrossRef] [PubMed]
4. Mansur, R.B.; Delgado-Peraza, F.; Subramaniapillai, M.; Lee, Y.; Iacobucci, M.; Rodrigues, N.; Rosenblat, J.D.; Brietzke, E.; Cosgrove, V.E.; Kramer, N.E.; et al. Extracellular Vesicle Biomarkers Reveal Inhibition of Neuroinflammation by Infliximab in Association with Antidepressant Response in Adults with Bipolar Depression. *Cells* **2020**, *9*, E895. [CrossRef]
5. Cerqueira, S.R.; Ayad, N.G.; Lee, J.K. Neuroinflammation Treatment via Targeted Delivery of Nanoparticles. *Front. Cell. Neurosci.* **2020**, *14*, 576037. [CrossRef]
6. Saijo, K.; Glass, C.K. Microglial Cell Origin and Phenotypes in Health and Disease. *Nat. Rev. Immunol.* **2011**, *11*, 775–787. [CrossRef]
7. Kosović, E.; Sýkora, D.; Kuchař, M. Stability Study of Cannabidiol in the Form of Solid Powder and Sunflower Oil Solution. *Pharmaceutics* **2021**, *13*, 412. [CrossRef]
8. Pisanti, S.; Malfitano, A.M.; Ciaglia, E.; Lamberti, A.; Ranieri, R.; Cuomo, G.; Abate, M.; Faggiana, G.; Proto, M.C.; Fiore, D.; et al. Cannabidiol: State of the Art and New Challenges for Therapeutic Applications. *Pharmacol. Ther.* **2017**, *175*, 133–150. [CrossRef]
9. Kozela, E.; Pietr, M.; Juknat, A.; Rimmerman, N.; Levy, R.; Vogel, Z. Cannabinoids Delta(9)-Tetrahydrocannabinol and Cannabidiol Differentially Inhibit the Lipopolysaccharide-Activated NF-KappaB and Interferon-Beta/STAT Proinflammatory Pathways in BV-2 Microglial Cells. *J. Biol. Chem.* **2010**, *285*, 1616–1626. [CrossRef]
10. Pires, P.C.; Santos, A.O. Nanosystems in Nose-to-Brain Drug Delivery: A Review of Non-Clinical Brain Targeting Studies. *J. Control. Release Off. J. Control. Release Soc.* **2018**, *270*, 89–100. [CrossRef]
11. Battaglia, L.; Panciani, P.P.; Muntoni, E.; Capucchio, M.T.; Biasibetti, E.; De Bonis, P.; Mioletti, S.; Fontanella, M.; Swaminathan, S. Lipid Nanoparticles for Intranasal Administration: Application to Nose-to-Brain Delivery. *Expert Opin. Drug Deliv.* **2018**, *15*, 369–378. [CrossRef] [PubMed]
12. Zhang, F.; Lin, Y.-A.; Kannan, S.; Kannan, R.M. Targeting Specific Cells in the Brain with Nanomedicines for CNS Therapies. *J. Control. Release Off. J. Control. Release Soc.* **2016**, *240*, 212–226. [CrossRef] [PubMed]
13. Hornig, S.; Heinze, T.; Becer, C.R.; Schubert, U.S. Synthetic Polymeric Nanoparticles by Nanoprecipitation. *J. Mater. Chem.* **2009**, *19*, 3838. [CrossRef]
14. Morán, D.; Gutiérrez, G.; Blanco-López, M.C.; Marefati, A.; Rayner, M.; Matos, M. Synthesis of Starch Nanoparticles and Their Applications for Bioactive Compound Encapsulation. *Appl. Sci.* **2021**, *11*, 4547. [CrossRef]
15. Sintov, A.C.; Yariv, D. A New Nanoparticulate System Based on Divanillin-Crosslinked Starch: Mode of Manufacturing and In-Vitro Evaluation of Skin Penetration. *Starch-Stärke* **2022**, *74*, 2100172. [CrossRef]
16. Paudel, K.S.; Hammell, D.C.; Agu, R.U.; Valiveti, S.; Stinchcomb, A.L. Cannabidiol Bioavailability after Nasal and Transdermal Application: Effect of Permeation Enhancers. *Drug Dev. Ind. Pharm.* **2010**, *36*, 1088–1097. [CrossRef]

17. Watt, G.; Karl, T. In Vivo Evidence for Therapeutic Properties of Cannabidiol (CBD) for Alzheimer's Disease. *Front. Pharmacol.* **2017**, *8*, 20. [CrossRef]
18. Builders, P.F.; Arhewoh, M.I. Pharmaceutical Applications of Native Starch in Conventional Drug Delivery: Pharmaceutical Applications of Native Starch. *Starch-Stärke* **2016**, *68*, 864–873. [CrossRef]
19. Rodrigues, A.; Emeje, M. Recent Applications of Starch Derivatives in Nanodrug Delivery. *Carbohydr. Polym.* **2012**, *87*, 987–994. [CrossRef]
20. Hedayati, S.; Niakousari, M.; Mohsenpour, Z. Production of Tapioca Starch Nanoparticles by Nanoprecipitation-Sonication Treatment. *Int. J. Biol. Macromol.* **2020**, *143*, 136–142. [CrossRef]
21. Saari, H.; Fuentes, C.; Sjöö, M.; Rayner, M.; Wahlgren, M. Production of Starch Nanoparticles by Dissolution and Non-Solvent Precipitation for Use in Food-Grade Pickering Emulsions. *Carbohydr. Polym.* **2017**, *157*, 558–566. [CrossRef] [PubMed]
22. El-Naggar, M.E.; El-Rafie, M.H.; El-sheikh, M.A.; El-Feky, G.S.; Hebeish, A. Synthesis, Characterization, Release Kinetics and Toxicity Profile of Drug-Loaded Starch Nanoparticles. *Int. J. Biol. Macromol.* **2015**, *81*, 718–729. [CrossRef] [PubMed]
23. Lee, E.J.; Khan, S.A.; Park, J.K.; Lim, K.-H. Studies on the Characteristics of Drug-Loaded Gelatin Nanoparticles Prepared by Nanoprecipitation. *Bioprocess Biosyst. Eng.* **2012**, *35*, 297–307. [CrossRef] [PubMed]
24. Podaralla, S.; Perumal, O. Influence of Formulation Factors on the Preparation of Zein Nanoparticles. *AAPS PharmSciTech* **2012**, *13*, 919–927. [CrossRef]
25. Polidoro, D.; Temmerman, R.; Devreese, M.; Charalambous, M.; Ham, L.V.; Cornelis, I.; Broeckx, B.J.G.; Mandigers, P.J.J.; Fischer, A.; Storch, J.; et al. Pharmacokinetics of Cannabidiol Following Intranasal, Intrarectal, and Oral Administration in Healthy Dogs. *Front. Vet. Sci.* **2022**, *9*, 899940. [CrossRef]
26. Zamansky, M.; Zehavi, N.; Ben-Shabat, S.; Sintov, A.C. Characterization of Nanoparticles Made of Ethyl Cellulose and Stabilizing Lipids: Mode of Manufacturing, Size Modulation, and Study of Their Effect on Keratinocytes. *Int. J. Pharm.* **2021**, *607*, 121003. [CrossRef]
27. Atalay, S.; Jarocka-Karpowicz, I.; Skrzydlewska, E. Antioxidative and Anti-Inflammatory Properties of Cannabidiol. *Antioxidants* **2019**, *9*, 21. [CrossRef]
28. Yousaf, M.; Chang, D.; Liu, Y.; Liu, T.; Zhou, X. Neuroprotection of Cannabidiol, Its Synthetic Derivatives and Combination Preparations against Microglia-Mediated Neuroinflammation in Neurological Disorders. *Mol. Basel Switz.* **2022**, *27*, 4961. [CrossRef]
29. ChoiPark, W.-H.-D.; Baek, S.-H.; Chu, J.-P.; Kang, M.-H.; Mi, Y.-J. Cannabidiol Induces Cytotoxicity and Cell Death via Apoptotic Pathway in Cancer Cell Lines. *Biomol. Ther.* **2008**, *16*, 87–94. [CrossRef]
30. Russo, C.; Lavorgna, M.; Nugnes, R.; Orlo, E.; Isidori, M. Comparative Assessment of Antimicrobial, Antiradical and Cytotoxic Activities of Cannabidiol and Its Propyl Analogue Cannabidivarin. *Sci. Rep.* **2021**, *11*, 22494. [CrossRef]
31. Sainz-Cort, A.; Müller-Sánchez, C.; Espel, E. Anti-Proliferative and Cytotoxic Effect of Cannabidiol on Human Cancer Cell Lines in Presence of Serum. *BMC Res. Notes* **2020**, *13*, 389. [CrossRef]
32. Pagano, S.; Coniglio, M.; Valenti, C.; Federici, M.I.; Lombardo, G.; Cianetti, S.; Marinucci, L. Biological Effects of Cannabidiol on Normal Human Healthy Cell Populations: Systematic Review of the Literature. *Biomed. Pharmacother. Biomed. Pharmacother.* **2020**, *132*, 110728. [CrossRef] [PubMed]
33. Dos-Santos-Pereira, M.; Guimarães, F.S.; Del-Bel, E.; Raisman-Vozari, R.; Michel, P.P. Cannabidiol Prevents LPS-Induced Microglial Inflammation by Inhibiting ROS/NF-KB-Dependent Signaling and Glucose Consumption. *Glia* **2020**, *68*, 561–573. [CrossRef] [PubMed]
34. Wang, F.; Li, M.; Lin, C.; Jin, S.; Li, H.; Lu, Y.; Wang, H.; Wang, H.; Wang, X. Cannabidiol-Dihydroartemisinin Conjugates for Ameliorating Neuroinflammation with Reduced Cytotoxicity. *Bioorg. Med. Chem.* **2021**, *39*, 116131. [CrossRef] [PubMed]
35. Zamansky, M.; Zehavi, N.; Sintov, A.C.; Ben-Shabat, S. The Fundamental Role of Lipids in Polymeric Nanoparticles: Dermal Delivery and Anti-Inflammatory Activity of Cannabidiol. *Molecules* **2023**, *28*, 1774. [CrossRef]
36. Borgonetti, V.; Benatti, C.; Governa, P.; Isoldi, G.; Pellati, F.; Alboni, S.; Tascedda, F.; Montopoli, M.; Galeotti, N.; Manetti, F.; et al. Non-Psychotropic *Cannabis sativa* L. Phytocomplex Modulates Microglial Inflammatory Response through CB2 Receptors-, Endocannabinoids-, and NF-KB-Mediated Signaling. *Phytother. Res. PTR* **2022**, *36*, 2246–2263. [CrossRef]
37. Muñoz, L.E.; Bilyy, R.; Biermann, M.H.C.; Kienhöfer, D.; Maueröder, C.; Hahn, J.; Brauner, J.M.; Weidner, D.; Chen, J.; Scharin-Mehlmann, M.; et al. Nanoparticles Size-Dependently Initiate Self-Limiting NETosis-Driven Inflammation. *Proc. Natl. Acad. Sci. USA* **2016**, *113*, E5856–E5865. [CrossRef]

pharmaceutics

MDPI

Article

Controlling Microparticle Morphology in Melt-Jet Printing of Active Pharmaceutical Ingredients through Surface Phenomena

Shachar Bornstein, Almog Uziel and Dan Y. Lewitus *

Department of Polymer Materials Engineering, Shenkar College of Engineering, Design and Art, Ramat Gan 5252626, Israel; shacharb550@gmail.com (S.B.); almoguziel@gmail.com (A.U.)
* Correspondence: lewitus@shenkar.ac.il

Abstract: Achieving homogeneity and reproducibility in the size, shape, and morphology of active pharmaceutical ingredient (API) particles is crucial for their successful manufacturing and performance. Herein, we describe a new method for API particle engineering using melt-jet printing technology as an alternative to the current solvent-based particle engineering methods. Paracetamol, a widely used API, was melted and jetted as droplets onto various surfaces to solidify and form microparticles. The influence of different surfaces (glass, aluminum, polytetrafluoroethylene, and polyethylene) on particle shape was investigated, revealing a correlation between substrate properties (heat conduction, surface energy, and roughness) and particle sphericity. Higher thermal conductivity, surface roughness, and decreased surface energy contributed to larger contact angles and increased sphericity, reaching a near-perfect micro-spherical shape on an aluminum substrate. The integrity and polymorphic form of the printed particles were confirmed through differential scanning calorimetry and X-ray diffraction. Additionally, high-performance liquid chromatography analysis revealed minimal degradation products. The applicability of the printing process to other APIs was demonstrated by printing carbamazepine and indomethacin on aluminum surfaces, resulting in spherical microparticles. This study emphasizes the potential of melt-jet printing as a promising approach for the precise engineering of pharmaceutical particles, enabling effective control over their physiochemical properties.

Keywords: melt-jet printing; active pharmaceutical ingredients (APIs); particle engineering; microparticles; sphericity; surface properties

1. Introduction

The production of solid powders from synthesized APIs involves a series of steps aimed at obtaining high-quality particles with desired properties. One crucial aspect is the crystallization of the API in reactors to obtain a crystal slurry through cooling, evaporation, seeding, or antisolvent addition. This is followed by solid–liquid separation, washing, and drying field [1,2]. Each solid form of the API has unique properties that affect its solubility, bioavailability, hygroscopicity, melting point, stability, flowability, compressibility, and other performance characteristics [3]. Controlling these processes and understanding their impact on the resulting drug properties is crucial in the pharmaceutical industry as API particles' physicochemical properties and solid-state morphology directly affect their performance [2,3].

Various methods are utilized in the pharmaceutical industry to produce particulate materials, and new techniques are constantly being developed [4]. Most methods aim to manufacture drug delivery systems by combining the API with an excipient carrier [5]. Among these methods, spray drying is the most prevalent technique, particularly for generating inhalable particles using specialized excipients and isolating thermally labile products [6]. However, spray drying is rarely used to produce pure API particles due to the inherent challenges of partial dissolution, which can lead to uncontrolled recrystallization and chemical instability.

An alternative technique introduced recently is electro-spraying, which enables the production of pharmaceutical particles. This method involves the application of a high voltage (several kilovolts) to a microcapillary nozzle in a spraying system [5]. When used for producing drug particles or drugs combined with an excipient, a solution is first prepared in an appropriate organic solvent. Then, it is sprayed, frequently with the addition of an electrolyte, into a receiving solution containing additional stabilizers to prevent particle aggregating after formation; thus, the generated API particles are not pristine. Moreover, it has limitations in achieving precise control over particle size, size distribution, and morphology [5,7].

Another method employed for creating drug particles or delivery systems within the micrometer size range is spray cooling, also called spray congealing [8,9]. In this technique, the molten material is atomized into a cold, inert environment (usually nitrogen), causing the droplets to solidify and form spherical, free-flowing particles suitable for direct use in tableting or capsule filling. This eliminates the need for additional downstream processes such as secondary drying, milling, or granulation. However, spray congealing has certain drawbacks, including relatively high process temperatures, a narrow range of particle sizes, and high maintenance costs [9]. Moreover, spray congealing is rarely used to process the API alone and is usually accompanied by a molten excipient. Furthermore, the downscaling of the process, making it suitable for the spraying and generation of small amounts of API, or reproducing the process in a laboratory environment, poses challenges.

Printing technologies have emerged as a promising approach in pharmaceutical manufacturing, particularly for drug delivery systems. While there are numerous examples of digital manufacturing of dosage forms that include an API with an excipient [10,11], printing pure API particles is still rare, especially when aiming for the precise engineering of particle properties. Among these rare occasions of digital printing of API, inkjet printing (IJ) has demonstrated potential in producing drug-only systems by preparing ink by dissolving the API in an appropriate solvent. IJ is a non-contact approach that allows for the precise processing of liquid droplets on a substrate without contact with two-dimensional and three-dimensional structures [12,13]. Various dosage forms have been created using 2D and 3D IJ, generating API films for several applications, including localized or targeted action, improved efficacy, safety, reduced toxicity, and, consequently, improved patient compliance [14,15].

Recently, we have shown that melt droplet deposition (melt-jet printing) using a specialized valve allows for the fabrication of solid spherical particles from melts. This technique eliminates the need for organic solvents and surfactants, offering several advantages in the production of drug particles [16–18]. Melt-jet printing involves depositing a controlled amount of molten material onto a cold non-wetting surface, resulting in immediate solidification. Using this technique, polycaprolactone-based microspheres with varying amounts of ibuprofen as a model drug were produced. In vitro release studies revealed that one can control the crystal characteristics of both the excipient polycaprolactone and ibuprofen API, through the precise control of the printing parameters, with the substrate temperature being the most significant, resulting in tunable drug release rates over extended periods. The melt-jet printing approach offers several advantages: controlled particle size via nozzle diameter, controlled crystallization through the cooling rate, minimal material loss, and solvent-free processing, which are inherent to the melt-based process, and reproducibility. Additionally, we discovered that the interaction between the jetted-molten droplet and surface influences the resulting particle shape (sphericity). The substrate's roughness, surface energy, along with the surface tension of the melt have been found to be crucial factors affecting the shape of the solidified particle [16,19–22].

In this study, we evaluated the capacity to apply the melt-jet printing technique to produce pristine paracetamol raw material (powder) directly from crude while controlling several API properties in a single step, including shape, size, and polymorphism, thus deeming them suitable for use in the preparation of dosage forms. This was achieved by depositing paracetamol molten droplets onto different surfaces while elucidating whether

a relationship between melt printing parameters, including substrate properties, would affect the API microparticle shape and morphology. This was achieved through the melt deposition of the molten API onto various surfaces with a wide range of physio-chemico-thermo properties and the investigation of the potential correlations between these surface characteristics and the formed solid particle's shape and morphology. Factors such as surface energy, roughness, chemical composition, and thermal conductivity were considered. Thermal and chemical characterization methods were employed to evaluate whether the printing process itself resulted in changes to the integrity of the paracetamol, including HPLC, DSC, and XRD. Furthermore, the method's applicability to other APIs was demonstrated by printing both carbamazepine and indomethacin on chosen surfaces.

2. Results and Discussion

2.1. Melt-Jet Printing of Paracetamol Microparticles on Different Surfaces

Paracetamol microparticles were produced using a melt-jet printing technique, wherein the molten droplets were deposited onto various surfaces. Our previous research has indicated that the interaction between the surface and the molten droplets plays a crucial role in achieving spherical particle formation [16]. Hence, we selected four distinct surfaces for this study: two polymeric surfaces, polytetrafluoroethylene (PTFE) and polyethylene (PE); one ceramic surface, glass; and one metallic surface, aluminum. These surfaces vary in their surface energy (tension), surface roughness, thermal conductivity, and heat capacity. The objective was to investigate whether the substrate material would have an effect on the printing outcome in terms of the particle shape and morphology to allow better control over these parameters. Figure 1 shows representative scanning electron microscope (SEM) images that depict the paracetamol printed particle shape as a function of the varying printing substrate material. By keeping all other printing parameters the same, we observed that altering the substrate alone resulted in distinct differences in the particle shapes, particularly in terms of their sphericity [23]. Notably, the particles exhibited a flattened bottom on the PTFE, PE, and glass surfaces, while the particles printed on the aluminum surface exhibited a spherical shape. These findings suggest that the molten droplets reach the surfaces while they are still in a molten state (in contrast to spray congealing, where they solidify in the air). As result, the molten droplets are allowed to effectively wet the surface prior to solidifying into particles [16]. A notable difference observed among the particles was the measurement of their apparent contact angles obtained from the SEM images. These were determined to be 88.5 $\pm$ 4.1, 104.5 $\pm$ 1.5, 131.4 $\pm$ 15, and 180 $\pm$ 0 degrees for PTFE, glass, PE, and aluminum surfaces, respectively.

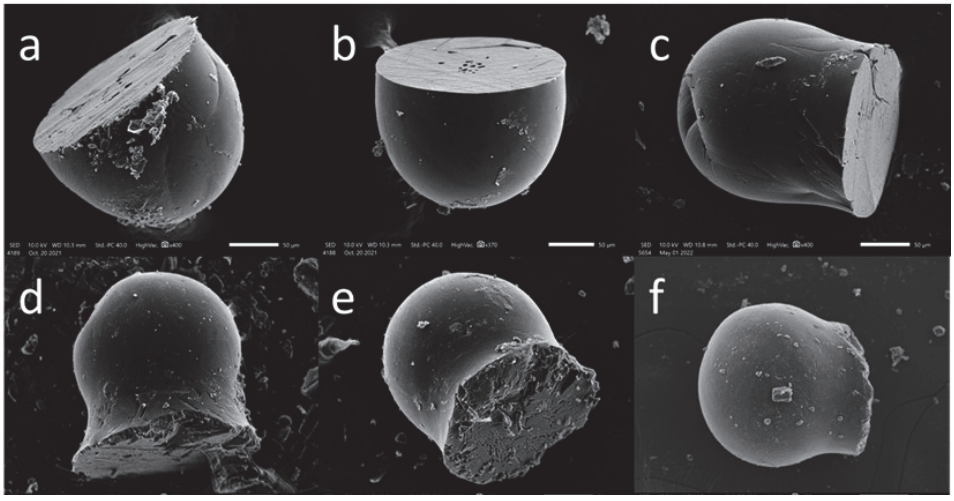

Figure 1. *Cont*.

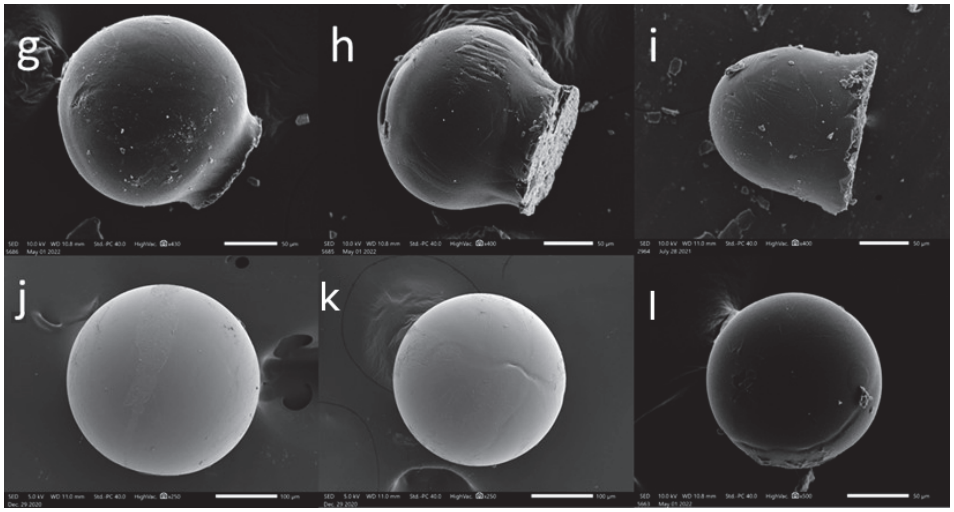

Figure 1. Melt-jet printing of paracetamol on different surfaces. SEM images of microparticles printed on (**a**–**c**) PTFE, (**d**–**f**) glass, (**g**–**i**) PE, and (**j**–**l**) aluminum surfaces; their measured apparent contact angles (sphericity) are detailed in the text. Scale bars: 50 μm.

2.2. Influence of Surface Properties on Paracetamol Microparticle Shape in Melt-Jet Printing

To further elucidate the relationship between melt-jet printing on different surfaces and the resulting microparticle shapes, an inquiry was conducted to identify potential correlations between surface structure and properties and the resulting form of the printed microparticles. Surface wetting, a phenomenon influenced by various surface factors such as surface energy, roughness, and chemical composition, plays a crucial role in determining the contact angle and, consequently, the wettability of the material surface [24]. The relationship between surface roughness (Ra) and wettability, as defined by Wenzel, suggests that surface roughness can improve wettability when combined with surface chemistry. For instance, a chemically hydrophobic surface becomes even more hydrophobic with the addition of surface roughness. High surface energy (HSE) results in strong molecular attractions and a lower contact angle between the surface and the microparticles. In contrast, low surface energy (LSE) results in weak molecular attraction, which makes bonding more challenging [25]. Thus, we attempted to correlate these aforementioned surface properties to the resulting particle shapes. The roughness of the surfaces was measured using atomic force microscopy (AFM). Representative AFM images of the four different surfaces (PTFE, PE, aluminum, and glass) are shown in Figure S1. The mean surface roughness values were found to be highest for the PE and lowest for the glass. The surface energy values of the substrates were found in the literature and were highest for aluminum and lowest for PTFE. Thus, no correlation between these two parameters and the particle's shape and sphericity was found (see table in Figure 2a). Consequently, an additional material property plays a role in determining the droplets interaction with the surface. Zitzenbacher et al. [26] explored the contact angles of molten polymers on different coating materials and observed a decrease in the contact angle between the melt and the surface with an increase in the surface energy of the coating. It was also noted that the contact angle of polymer melts on polished steel decreased as the surface temperature increased. These findings suggest that as the thermal conductivity of the substrate increases, leading to a higher cooling rate, the temperature of the melt decreases, resulting in larger contact angles and increased sphericity. In addition, Zhou et al. [21] found that increasing an aluminum substrate's temperature enhances the interaction between a polypropylene droplet and the substrate, resulting in an increased contact area between the PP droplet and the substrate, subsequently leading to a smaller contact angle. Materials with high thermal conductivity (K) can effectively transfer and dissipate heat [27], leading to faster cooling and the maintenance of spherical microparticles. Furthermore, Zitzenbacher et al. [20] measured the contact angle of polymer melts on polished steel, finding that the contact

angle decreases with increasing surface temperature due to the decrease in surface tension of the liquid polymer melt. Thus, in addition to the surface roughness and surface energy, the thermal conductivity of the four substrates was collected from the literature [28–31] to allow us to assess the parameters influencing the wetting phenomena on paracetamol particle formation. The properties of the surfaces and their corresponding apparent contact angles are detailed in Figure 2.

a)

	Aluminum	PTFE	PE	Glass
K (W/Mk)	234	0.25	0.42	1.37
Ra	118.9	24.6	218.1	13.6
SE (mJ/m^2)	50	18	25.9	36
Apparent contact angle (°)	180	88.5	131.4	104.5

b)

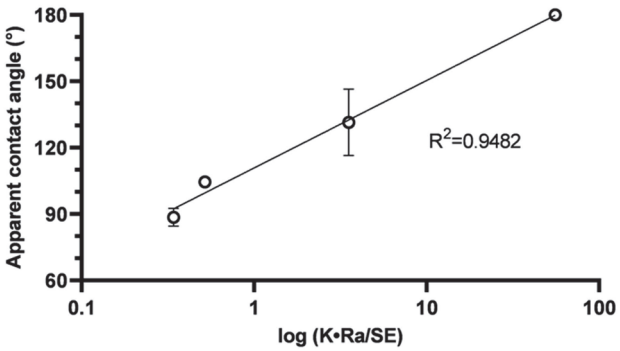

Figure 2. Surface properties and sphericity of paracetamol particles. (**a**) Thermal conductivity (K), roughness (Ra), and surface energy (SE) of aluminum, PTFE, PE, and glass surfaces and corresponding average apparent contact angle of printed paracetamol particles. (**b**) Relationship between the sphericity of paracetamol particles (apparent contact angle) and an expression incorporating surface properties (K, Ra, and SE).

These findings suggest that multiple surface factors come into play when a molten API droplet interacts with a surface. The contact angle and microparticle shape are influenced not only by surface roughness and surface tension, but by the substrate's thermal conductivity as well. As thermal conductivity increases, leading to a higher cooling rate, the melt temperature decreases, resulting in larger contact angles, in turn leading to an increase in sphericity. These observations demonstrate that greater thermal conductivity and surface roughness contribute to larger microparticle contact angles, yielding rounder-shaped particles. Conversely, higher substrate surface energy leads to smaller contact angles and flatter microparticles. This explains the variations in particle shape observed when printing on surfaces with different properties. Furthermore, these findings can be visualized by plotting the apparent contact angle against an expression of the thermal conductivity, surface roughness, and surface energy, as depicted in Figure 2b.

During the melt-jet printing process, a specialized inkjet-like device ejects a small portion of a molten API onto a surface. The device operates by applying pressure to the molten material, causing it to be expelled as a droplet. Initially, an ejected droplet with a following tail is formed [32]. Then, as the ejected droplet interacts with the surface, the tail merges with the main drop, leading to the spontaneous formation of a spherical shape on the surface. Figure 3 shows a sequence of images captured using a high-speed camera emphasizing the spontaneous formation of paracetamol microparticle upon the interaction of the molten jet with the aluminum surface.

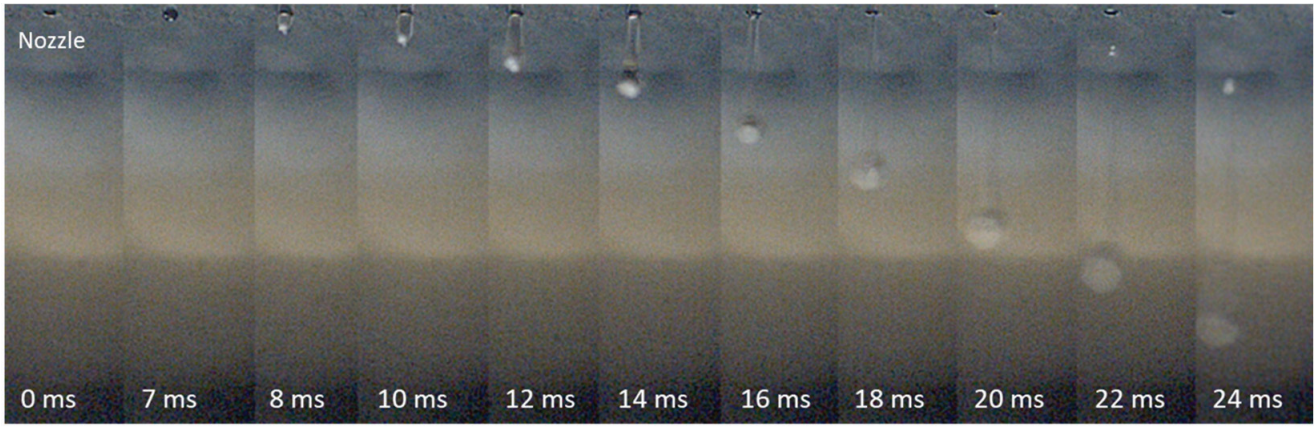

Figure 3. Melt-jet printing process paradigm: a sequence of images (**from left to right**) captured with a high-speed digital camera, showing the ejection of a molten paracetamol droplet from the nozzle (**top**) on an aluminum surface (**bottom**).

2.3. Characterization of Melt-Jet-Printed Paracetamol Microparticles

Spherical particles were successfully obtained exclusively on aluminum surfaces, leading us to further characterize them. Figure 1j–l shows the SEM images of paracetamol microparticles printed on an aluminum surface, revealing a smooth surface and a spherical shape with an average particle size of 207 ± 35 µm.

To analyze the polymorphism of the paracetamol and ensure that the microparticle production process did not induce polymorphic form changes, differential scanning calorimetry (DSC) measurements were conducted. DSC is a valuable technique for characterizing polymorphism in pharmaceutical materials, specifically for determining form I from form II in paracetamol [33]. Figure 4a,b present the DSC results obtained for the neat paracetamol powder and the printed paracetamol particles. Before processing, the neat paracetamol exhibited an endothermic peak at 171.2 °C with a melting enthalpy of 162.8 J/g. In comparison, the printed microparticles displayed an endothermic peak at 170.7 °C with a melting enthalpy of 169.8 J/g, with no apparent shoulder at 140 °C or skewing of the curve to lower temperatures, indicating that they retained the monoclinic form I of paracetamol without significant changes from the neat powder [33]. The polymorphic form of an API plays a critical role in determining its physical characteristics and subsequent therapeutic efficacy. The introduction of a new or unknown crystal form can have significant implications for product performance, occasionally leading to detrimental clinical outcomes [33]. Paracetamol exists in three polymorphic forms: two stable forms, monoclinic (form I) and orthorhombic (form II), along with one unstable form (form III). Understanding and controlling the polymorphic forms can influence factors such as dissolution rate, ease of consumption, and API release rate [34]. To further attest to the effect of the printing process on paracetamol's morphology, XRD analyses were performed. XRD results, presented in Figure 4c, reveal that the printed particles exhibit a pattern resembling those of the neat powder. The reflexes in the reference appear to be less broad compared to the printed material, which may be attributed to a smaller crystallite size in the printed material resulting from the rapid cooling during the printing process [35]. Additionally, relative reflex intensities differ between the two materials (e.g., near 20° 2θ) potentially due to preferred orientation and large crystals in the neat powder [36], while for the printed spherical particles, the presence of a preferred orientation is unlikely.

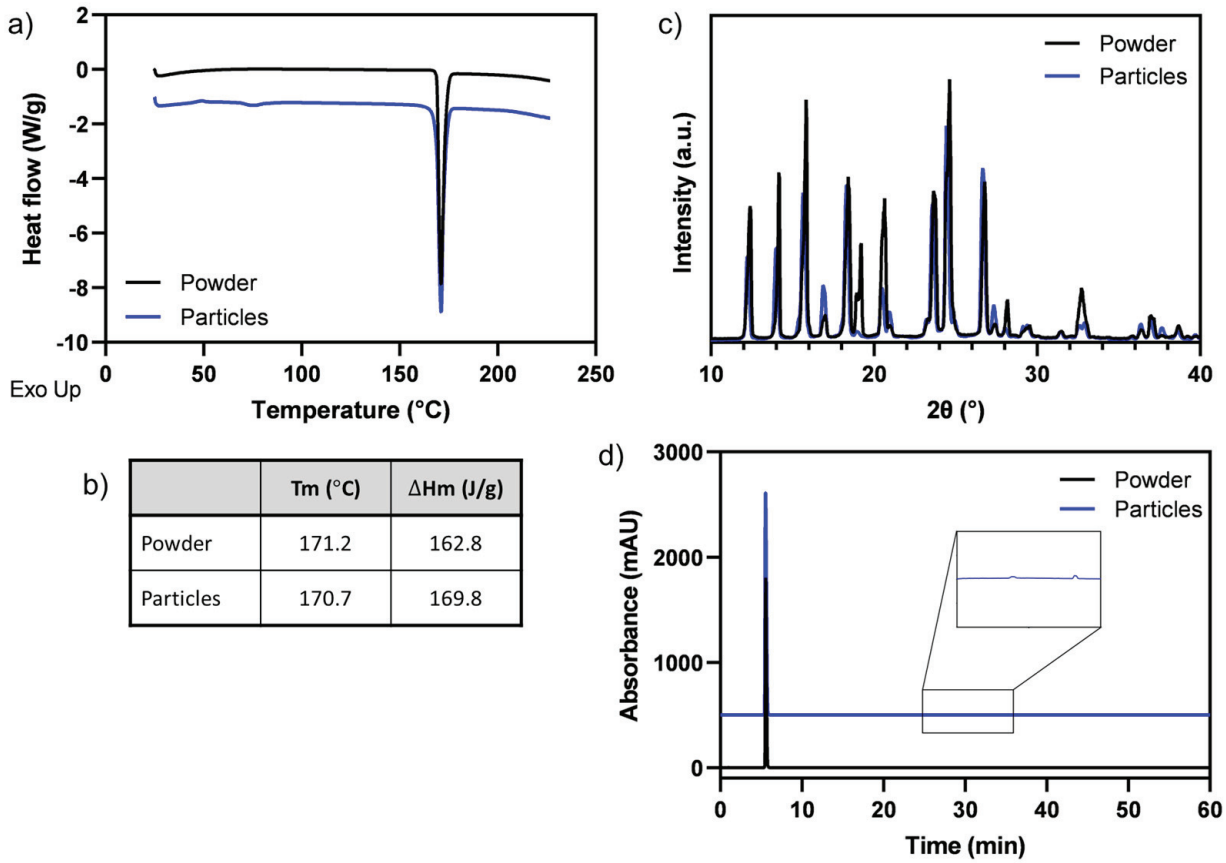

b)

	Tm (°C)	ΔHm (J/g)
Powder	171.2	162.8
Particles	170.7	169.8

Figure 4. Paracetamol microparticles characterization. (**a**) DSC thermograms, (**b**) melting temperatures (Tm) and enthalpies (ΔHm), (**c**) XRD patterns, and (**d**) HPLC chromatograms of neat powder (black) and printed particles (blue).

Paracetamol is a synthetic non-opiate derivative of the toxic 4-aminophenol, with 4-aminophenol being its primary hydrolytic product [37]. Various methods have been reported for assessing paracetamol's purity and detecting its main degradation products, including high-performance liquid chromatography (HPLC) [38]. Figure 4d displays HPLC chromatograms of the paracetamol powder and microparticles (shifted for clarity). In both chromatograms, a prominent paracetamol peak appears at 5.5 min. In the printed microparticles, two additional peaks are visible at 28.8 and 33.1 min. However, given that their measured quantities are less than 0.05% of the paracetamol peak, as per the European Pharmacopoeia [39], they are considered negligible, suggesting that no significant degradation products were generated during the particle production. It is possible that thermally sensitive APIs may exhibit more significant degradation products after the printing process. To evaluate their stability, printed particles were stored under various temperature and humidity conditions for 4 weeks. DSC curves of analyses performed at different storage conditions indicated that no major changes in the polymorphic structure of paracetamol were observed (Figure S2a). These findings are further corroborated by the XRD analyses (Figure S2b). Moreover, all the HPLC chromatograms (Figure S2c) showed a prominent paracetamol peak with no significant degradation products. Lastly, SEM images of the particles after 4 weeks are shown in Figure S2d. As observed, no major changes were seen, demonstrating that the particles retained their original morphology and structure.

To further demonstrate the method's applicability to other APIs, carbamazepine and indomethacin were also printed on aluminum surfaces. These materials exhibit different melting temperatures and were processed at a reservoir temperature of 165 °C for the indomethacin and 200 °C for the carbamazepine, compared to the paracetamol's processing temperature of 176 °C. Figure 5 shows the SEM images of near-perfect spherical micropar-

ticles of paracetamol, carbamazepine, and indomethacin printed on an aluminum surface, indicating that regardless of the API used, all particles exhibited consistent spherical shapes. This finding highlights the robustness and versatility of the melt-jet printing method in achieving uniform particle shapes among various APIs.

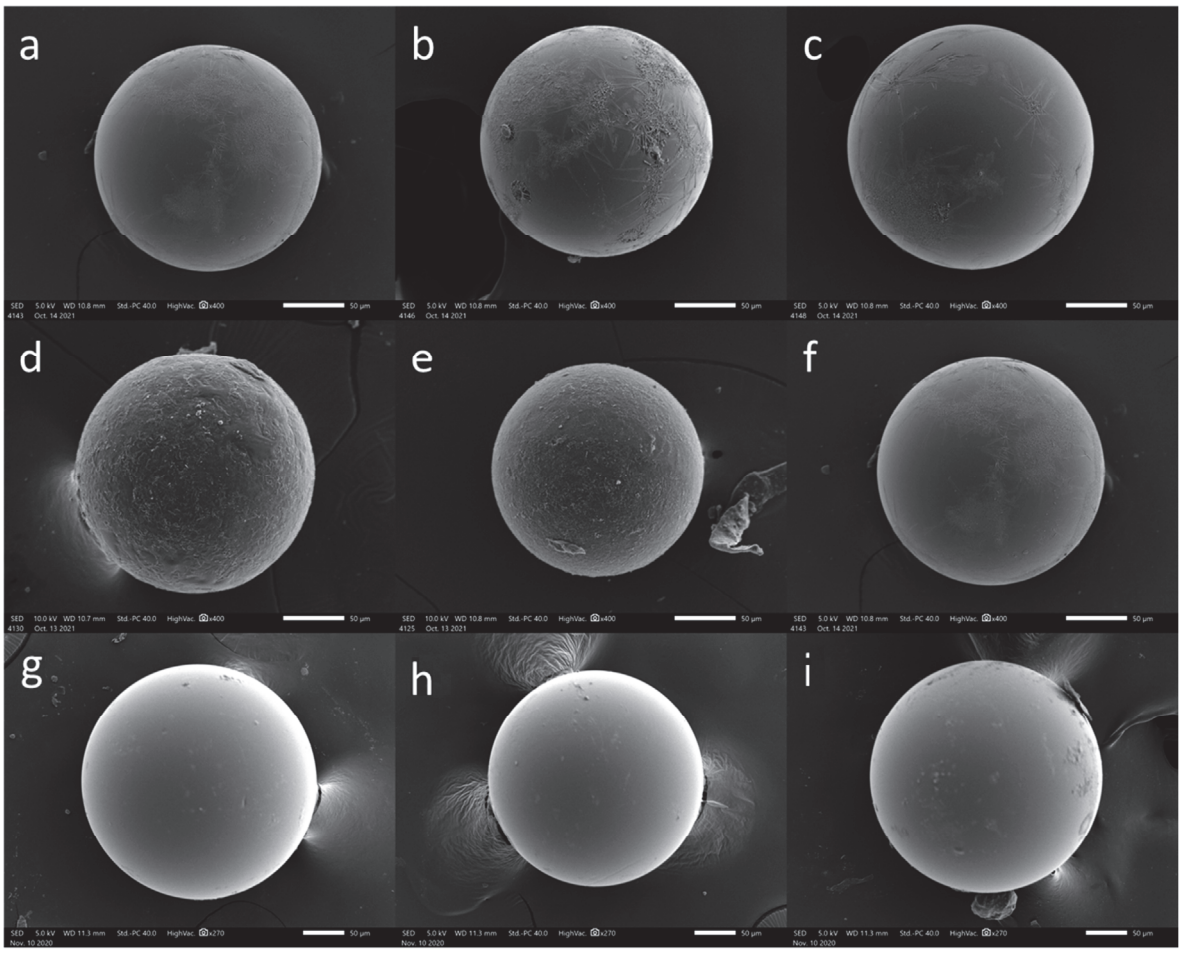

Figure 5. API particles printed on an aluminum surface. SEM images of (**a**–**c**) paracetamol, (**d**–**f**) carbamazepine, and (**g**–**i**) indomethacin microparticles. Scale bars: 50 μm.

3. Materials and Methods

3.1. Materials

Paracetamol, carbamazepine, and indomethacin were kindly provided by Merck KGaA, Darmstadt, Germany. N,N-Dimethylformamide, ethanol (HPLC grade), methanol (HPLC grade), acetone, and dimethyl sulfoxide (DMSO) (HPLC grade) were purchased from Bio-Lab Ltd., Jerusalem, Israel.

3.2. Preparation of Microparticles

API particles were prepared in a similar manner to polymeric micro-particles [16,18], with some modifications. API was inserted into a heated reservoir of a pneumatic jetting valve (P-Jet CT, Liquidyn® (Nordson EFD) Oberhaching, Germany). The following settings were used for paracetamol, indomethacin, and carbamazepine, respectively: reservoir temperature: 176 °C, 165 °C, and 200 °C; die temperature: 174 °C, 163 °C, and 198 °C; valve pressure: 0.85 bar, 1.8–1.9 bar, and 1–1.2 bar. The spring (tappet) tightness was 0.6–0.9 turns, and the distance between the nozzle and the surface was set at 30 cm. The temperature and pressure were controlled using a Liquidyn V100 controller. To generate micro-particles, droplets of the molten API were jetted through a 100 μm needle flat die

nozzle (Liquidyn®) onto an aluminum, PTFE, PE, or glass surface and subsequently cooled at room temperature.

3.3. Microparticle Characterization

Microparticle size, shape, surface morphology, and apparent contact angle were evaluated using scanning electron microscopy (SEM). The microparticles were coated with an Au-Pd mixture using a sputter coater unit (SC7620, Quorum, East Sussex, UK). Microparticle size and surface morphology were assessed using a JEOL JSM-IT200 SEM (JEOL, Tokyo, Japan) operated at an acceleration voltage of 5 kV. The microparticle size was measured using the SEM software (JSM-IT200 Operation software) roller. The apparent contact angle between the microparticles and the surface was determined using the SEM's angle measurement function. The measurements were conducted on 10 randomly selected particles, and the average and standard deviations were reported.

3.4. Thermal Analysis

Microparticles and neat powder of API (5–10 mg) were analyzed via differential scanning calorimetry (DSC) measurements (Q200, TA Instrument, New Castle, DE, USA). All experiments were performed from 25 to 230 °C at a scanning rate of 10 °C/min, with one heating run using closed crucibles.

3.5. HPLC Analysis of Paracetamol

HPLC analysis was carried out using a UHPLC system (Thermo Scientific, Bremen, Germany) fitted with a C18 core–shell column (2.6 μm, 150 mm × 2.1 mm i.d.) and a SecurityGuard Ultra column (2 mm × 2.1 mm i.d) (Phenomenex, Torrance, CA, USA). Chromatographic separation was achieved using a previously described method [39] with some adjustments. Separation was done with a solvent mixture of phosphate buffer (prepared by dissolving 1.7 g of potassium dihydrogen phosphate and 1.8 g of dipotassium hydrogen phosphate in HPLC-grade water and diluting to 1000 mL with water) (solvent A) and methanol (solvent B). The gradient profile started at 5% B for 1 min and was then raised to 10% over 9 min, held at 10% for 10 min, then raised to 34% over 20 min, and held at 34% for 10 min. At 50 min, the column was returned to 5% until 60 min for the re-equilibration of the system. The column temperature was 30 °C, the flow rate was 0.35 mL/min, and the injection volume was 5 μL. Quantitation of the paracetamol samples was performed using a diode-array detector (Diode RA, UltiMate 3000, Thermo-Scientific, Waltham, MA, USA), operated at a wavelength of 254 nm. Prior to analysis, samples of paracetamol powder and particles were dissolved in a mixture of water–methanol (85:15 v/v) at a concentration of 0.5 mg/mL, and then filtered through 0.22 μm PTFE filters.

3.6. Surface Roughness Measurements

A multi-mode atomic force microscope (AFM, Bruker Multimode AFM, Santa Barbara, CA, USA), operated in a contact mode, was used to obtain a quantitative and qualitative evaluation of the samples. In contact mode, the force between the AFM tip and the sample surface was kept constant by the microscope feedback system while the sample surface was scanned beneath the AFM tip, and the vertical piezoelectric ceramic movement was recorded. Images with 512 × 512 pixels were acquired with a scan size of 50 μm × 50 μm and a scan rate of 2.03 Hz. An NP-type V-shape Si3N4 cantilever (Bruker) with a normal bending constant of k = 0.06 N/m and a tip radius of approximately 0.6 μm was used. During imaging, the set point was chosen to be 2.0 V higher than the top–bottom laser photo detector output obtained when the tip was out of surface contact. AFM images were analyzed using specialized software (Gwyddion 2.54 software). The AFM obtained a 3-dimensional image of the surface of the samples. Eight different areas were measured in each sample at different sections, all located in the center of the samples. The mean roughness (Ra) was recorded after measurement.

3.7. Powder X-ray Diffraction (PXRD)

Powder X-ray diffraction analyses were performed using a Stoe StadiP 611 instrument (Stoe, Darmstadt, Germany) equipped with a Mythen1K Si-strip detector. Measurements were performed in transmission geometry with Cu-Kα1 radiation source generated at 40 kV and 40 mA. Samples were scanned with an angular resolution of 0.03° 2θ over a 2θ range from −36° 2θ to +36° 2θ with measurement times of 30 s/PSD-step and a PSD step width of 0.09° 2θ. After the measurements, the diffractograms were folded to range from 0° 2θ to 36° 2θ.

3.8. High-Speed Images

A digital high-speed camera (Phantom v12, Phantom High-Speed Cameras—Vision Research, Wayne, NJ, USA) equipped with a microscopic lens (Nikon 10 × CFI plan achromat) was used to observe and document the ejection, flight, impact, and stabilization of the droplet in detail, shooting at 27,000–43,000 fps.

3.9. Particle Stability Analysis

Printed paracetamol particles were immediately stored under various conditions and evaluated after 4 weeks to understand further whether the melt-based process affects the API's stability. Storage conditions of 2–8 °C, 25 °C/62% RH, 40 °C/0% RH, 40 °C/75% RH followed the guidelines of the European Medicine Agency (ICH Q1A (R2) Stability testing of new drug substances and drug products—Scientific guideline) [40]. Storage at 2–8 °C was achieved by storing the particles in an airtight scintillation vial inside a refrigerator. Then, 40/"0" was achieved using a vacuum oven set at 40 °C. Saturated salts were used for the 25/60 and 40/75 conditions. DSC, HPLC, XRD, and SEM analyses at each time point were performed as described above.

4. Conclusions

Melt-jet printing technology enabled the production of spherical paracetamol microparticles without the need for solvents or excipients. The printed particles maintained the polymorphic structure of paracetamol and exhibited minimal signs of degradation. The study provides valuable insights into the influence of the printing substrate properties on melt printing outcomes, highlighting the critical role of surface characteristics in achieving the desired API microparticle shapes. Notably, the aluminum substrate yielded near-perfect spherical particles. These findings may contribute to the development and optimization of effective melt printing techniques, especially for small-scale pharmaceutical applications. Using a single printhead, one can produce 1–1.5 mg of spherical particles per minute, multipliable as a function of the number of printing heads in the system.

Supplementary Materials: The following supporting information can be downloaded at: https://www.mdpi.com/article/10.3390/pharmaceutics15082026/s1, Figure S1: Three-dimensional AFM images of (a) PTFE, (b) aluminum, (c) PE, and (d) glass surfaces.; Figure S2. Paracetamol particle stability analysis after 4 weeks of storage. (a) DSC thermograms, (b) XRD patterns, (c) HPLC chromatograms, and (d) SEM images (Scale bars: 50 μm) of neat powder and printed particles stored under different conditions: 2–8 °C, 25 °C/62% RH, 40 °C/0% RH, and 40 °C/75% RH. Table S1: Surface roughness (Ra) measurements by AFM.

Author Contributions: Conceptualization, S.B. and D.Y.L.; formal analysis, S.B., A.U. and D.Y.L.; funding acquisition, D.Y.L.; writing—original draft, S.B., A.U. and D.Y.L. All authors have read and agreed to the published version of the manuscript.

Funding: This research was funded the Israeli Innovation Authority of the Israeli Ministry of Economy, grant number 70078, and partially supported by Merck Healthcare KGaA, Darmstadt, Germany.

Institutional Review Board Statement: Not applicable.

Informed Consent Statement: Not applicable.

Data Availability Statement: The data presented in this study are available in this article.

Conflicts of Interest: The authors declare no conflict of interest.

References

1. Rogers, L.; Briggs, N.; Achermann, R.; Adamo, A.; Azad, M.; Brancazio, D.; Capellades, G.; Hammersmith, G.; Hart, T.; Imbrogno, J.; et al. Continuous Production of Five Active Pharmaceutical Ingredients in Flexible Plug-and-Play Modules: A Demonstration Campaign. *Org. Process Res. Dev.* **2020**, *24*, 2183–2196. [CrossRef]
2. Wang, Z.; Solomos, M.; Axnanda, S.; Chen, C.; Figus, M.; Schenck, L.; Sun, C.C. Varied Bulk Powder Properties of Micro-Sized API within Size Specifications as a Result of Particle Engineering Methods. *Pharmaceutics* **2022**, *14*, 1901. [CrossRef]
3. Lu, J.; Rohani, S. Polymorphism and Crystallization of Active Pharmaceutical Ingredients (APIs). *Curr. Med. Chem.* **2009**, *16*, 884–905. [CrossRef] [PubMed]
4. Thassu, D.; Deleers, M.; Pathak, Y.V. *Nanoparticulate Drug Delivery Systems*; CRC Press: Boca Raton, FL, USA, 2007; 376p.
5. Peltonen, L.; Valo, H.; Kolakovic, R.; Laaksonen, T.; Hirvonen, J. Electrospraying, Spray Drying and Related Techniques for Production and Formulation of Drug Nanoparticles. *Expert Opin. Drug Deliv.* **2010**, *7*, 705–719. [CrossRef]
6. Ohtake, S.; Izutsu, K.I.; Lechuga-Ballesteros, D. *Drying Technologies for Biotechnology and Pharmaceutical Applications*; John Wiley & Sons: Hoboken, NJ, USA, 2020; ISBN 9783527341122.
7. Rasenack, N.; Müller, B.W. Micron-Size Drug Particles: Common and Novel Micronization Techniques. *Pharm. Dev. Technol.* **2004**, *9*, 1–13. [CrossRef]
8. Bertoni, S.; Dolci, L.S.; Albertini, B.; Passerini, N. Spray Congealing: A Versatile Technology for Advanced Drug-Delivery Systems. *Ther. Deliv.* **2018**, *9*, 833–845. [CrossRef]
9. Bertoni, S.; Albertini, B.; Passerini, N. Spray Congealing: An Emerging Technology to Prepare Solid Dispersions with Enhanced Oral Bioavailability of Poorly Water Soluble Drugs. *Molecules* **2019**, *24*, 3471. [CrossRef]
10. Uziel, A.; Shpigel, T.; Goldin, N.; Lewitus, D. Three-Dimensional Printing for Drug Delivery Devices: A State-of-the-Art Survey. *J. 3D Print. Med.* **2019**, *3*, 95–109. [CrossRef]
11. Wang, J.; Zhang, Y.; Aghda, N.H.; Pillai, A.R.; Thakkar, R.; Nokhodchi, A.; Maniruzzaman, M. Emerging 3D Printing Technologies for Drug Delivery Devices: Current Status and Future Perspective. *Adv. Drug Deliv. Rev.* **2021**, *174*, 294–316. [CrossRef]
12. Boehm, R.D.; Miller, P.R.; Daniels, J.; Stafslien, S.; Narayan, R.J. Inkjet Printing for Pharmaceutical Applications. *Biochem. Pharmacol.* **2014**, *17*, 247–252. [CrossRef]
13. Kollamaram, G.; Croker, D.M.; Walker, G.M.; Goyanes, A.; Basit, A.W.; Gaisford, S. Low Temperature Fused Deposition Modeling (FDM) 3D Printing of Thermolabile Drugs. *Int. J. Pharm.* **2018**, *545*, 144–152. [CrossRef]
14. Chou, W.-H.; Gamboa, A.; Morales, J.O. Inkjet Printing of Small Molecules, Biologics, and Nanoparticles. *Int. J. Pharm.* **2021**, *600*, 120462. [CrossRef]
15. Meléndez, P.A.; Kane, K.M.; Ashvar, C.S.; Albrecht, M.; Smith, P.A. Thermal Inkjet Application in the Preparation of Oral Dosage Forms: Dispensing of Prednisolone Solutions and Polymorphic Characterization by Solid-State Spectroscopic Techniques. *J. Pharm. Sci.* **2008**, *97*, 2619–2636. [CrossRef] [PubMed]
16. Shpigel, T.; Uziel, A.; Lewitus, D.Y. SPHRINT—Printing Drug Delivery Microspheres from Polymeric Melts. *Eur. J. Pharm. Biopharm.* **2018**, *127*, 398–406. [CrossRef] [PubMed]
17. Shpigel, T.; Cohen Taguri, G.; Lewitus, D.Y. Controlling Drug Delivery from Polymer Microspheres by Exploiting the Complex Interrelationship of Excipient and Drug Crystallization. *J. Appl. Polym. Sci.* **2018**, *136*, 47227.
18. Uziel, A.; Gelfand, A.; Amsalem, K.; Berman, P.; Lewitus, G.M.; Meiri, D.; Lewitus, D.Y. Full-Spectrum Cannabis Extract Microdepots Support Controlled Release of Multiple Phytocannabinoids for Extended Therapeutic Effect. *ACS Appl. Mater. Interfaces* **2020**, *12*, 23707–23716. [CrossRef] [PubMed]
19. Deng, X.; Paven, M.; Papadopoulos, P.; Ye, M.; Wu, S.; Schuster, T.; Klapper, M.; Vollmer, D.; Butt, H.J. Solvent-Free Synthesis of Microparticles on Superamphiphobic Surfaces. *Angew. Chem.* **2013**, *125*, 11496–11499. [CrossRef]
20. Zitzenbacher, G.; Dirnberger, H.; Längauer, M.; Holzer, C. Calculation of the Contact Angle of Polymer Melts on Tool Surfaces from Viscosity Parameters. *Polymers* **2017**, *10*, 38.
21. Zhou, M.; Fu, L.; Jiang, F.; Jiang, B.; Drummer, D. Atomistic Investigation on the Wetting Behavior and Interfacial Joining of Polymer-Metal Interface. *Polymers* **2020**, *12*, 1696. [CrossRef]
22. Prakash, C.G.J.; Prasanth, R. Approaches to Design a Surface with Tunable Wettability : A Review on Surface Properties. *J. Mater. Sci.* **2021**, *56*, 108–135. [CrossRef]
23. Cruz-Matías, I.; Ayala, D.; Hiller, D.; Gutsch, S.; Zacharias, M.; Estradé, S.; Peiró, F. Sphericity and Roundness Computation for Particles Using the Extreme Vertices Model. *J. Comput. Sci.* **2019**, *30*, 28–40. [CrossRef]
24. Aliofkhazraei, M. *Wetting and Wettability*; InTech: Rijeka, Croatia, 2015.
25. Packham, D.E. Surface Energy, Surface Topography and Adhesion. *Int. J. Adhes. Adhes.* **2003**, *23*, 437–448. [CrossRef]
26. Zitzenbacher, G.; Huang, Z.; Längauer, M.; Forsich, C.; Holzer, C. Wetting Behavior of Polymer Melts on Coated and Uncoated Tool Steel Surfaces. *J. Appl. Polym. Sci.* **2016**, *133*, 43469. [CrossRef]
27. Mokhena, T.C.; Mochane, M.J.; Sefadi, J.S.; Motloung, S.V.; Andala, D.M. Thermal Conductivity of Graphite-Based Polymer Composites. In *Impact of Thermal Conductivity on Energy Technologies*; IntechOpen: London, UK, 2018; Chapter 11; Volume 181.

28. Mark, J.E. *Physical Properties of Polymers Handbook*; Springer: New York, NY, USA, 2007; Volume 1076, p. 825.
29. Bansal, N.P.; Doremus, R.H. *Handbook of Glass Properties*; Elsevier: Amsterdam, The Netherlands, 2013; ISBN 0080523765.
30. Hu, G.; Kang, J.; Ng, L.W.T.; Zhu, X.; Howe, R.C.T.; Jones, C.G.; Hersam, M.C.; Hasan, T. Functional Inks and Printing of Two-Dimensional Materials. *Chem. Soc. Rev.* **2018**, *47*, 3265–3300. [CrossRef]
31. Fenouillot, F.; Cassagnau, P.; Majesté, J.-C. Uneven Distribution of Nanoparticles in Immiscible Fluids: Morphology Development in Polymer Blends. *Polymer* **2009**, *50*, 1333–1350.
32. Lee, J.H.; Kim, J.H.; Hwang, K.T.; Hwang, H.J.; Han, K.S. Formulation of a graft polymer-containing aqueous yellow ceramic ink for digital ink-jet printing. *RSC Adv.* **2020**, *10*, 2428–2436. [CrossRef]
33. Wang, I.-C.; Lee, M.-J.; Seo, D.-Y.; Lee, H.-E.; Choi, Y.; Kim, W.-S.; Kim, C.-S.; Jeong, M.-Y.; Choi, G.J. Polymorph Transformation in Paracetamol Monitored by In-Line NIR Spectroscopy during a Cooling Crystallization Process. *AAPS PharmSciTech* **2011**, *12*, 764–770. [CrossRef]
34. Grzesiak, A.L.; Lang, M.; Kim, K.; Matzger, A.J. Comparison of the Four Anhydrous Polymorphs of Carbamazepine and the Crystal Structure of Form I. *J. Pharm. Sci.* **2003**, *92*, 2260–2271. [CrossRef]
35. Shtukenberg, A.G.; Tan, M.; Vogt-Maranto, L.; Chan, E.J.; Xu, W.; Yang, J.; Tuckerman, M.E.; Hu, C.T.; Kahr, B. Melt Crystallization for Paracetamol Polymorphism. *Cryst. Growth Des.* **2019**, *19*, 4070–4080.
36. Jendrzejewska, I.; Goryczka, T.; Pietrasik, E.; Klimontko, J.; Jampilek, J. X-Ray and Thermal Analysis of Selected Drugs Containing Acetaminophen. *Molecules* **2020**, *25*, 5909. [CrossRef]
37. Feng, X.; Zhang, Q.; Cong, P.; Zhu, Z. Analytical Methods Determination of the Paracetamol Degradation Process with Online UV Spectroscopic and Multivariate Curve Resolution-Alternating Least Squares Methods: Comparative validation by HPLC. *Anal. Methods* **2013**, *5*, 5286–5293. [CrossRef]
38. Sornchaithawatwong, C.; Vorrarat, S.; Nunthanavanit, P. Simultaneous Determination of Paracetamol and Its Main Degradation Product in Generic Paracetamol Tablets Using Reverse-Phase HPLC. *J. Health Res.* **2010**, *24*, 103–106.
39. Aqeel, Z.; Hansen, D.; Behr, H. *European Pharmacopoeia Paracetamol Monograph Draft Method: Achieving Improved Sensitivity, Resolution, and Separation for Paracetamol and All 14 Related Impurities Using Kinetex®5 Mm C18 Core-Shell Columns*; Phenomenex Inc.: Torrance, CA, USA, 2020.
40. European Medicines Agency. *ICH Q1A (R2) Stability Testing of New Drug Substances and Drug Products—Scientific Guideline*; European Medicines Agency: Amsterdam, The Netherlands, 2003.

pharmaceutics

MDPI

Article

Towards Effective Antiviral Oral Therapy: Development of a Novel Self-Double Emulsifying Drug Delivery System for Improved Zanamivir Intestinal Permeability

Sapir Ifrah [1], Arik Dahan [1,*] and Nir Debotton [2,*]

[1] Department of Clinical Pharmacology, School of Pharmacy, Faculty of Health Sciences, Ben-Gurion University of the Negev, Beer-Sheva 84105, Israel; sapirgar@post.bgu.ac.il
[2] Department of Chemical Engineering, Shenkar College of Engineering and Design, Ramat-Gan 52526, Israel
* Correspondence: arikd@bgu.ac.il (A.D.); nird@shenkar.ac.il (N.D.); Tel.: +972-(8)-6479483 (A.D.); +972-(3)-6019320 (N.D.); Fax: +972-(3)-6479303 (A.D.); +972-(3)-60110175 (N.D.)

Abstract: Self-double emulsifying drug delivery systems have the potential to enhance the intestinal permeability of drugs classified under the Biopharmaceutics Classification System (BCS) class III. One such example is the antiviral agent zanamivir, exhibiting suboptimal oral absorption (with a bioavailability range of 1–5%). To address this challenge, we have developed an innovative oral formulation for zanamivir: a self-double nanoemulsifying Winsor delivery system (SDNE-WDS) consisting of the microemulsion, which subsequently yields final double nanoemulsion ($W_1/O/W_2$) upon interaction with water. Two distinct formulations were prepared: SDNE-WDS1, classified as a W/O microemulsion, and SDNE-WDS2, discovered to be a bicontinuous microemulsion. The inner microemulsions displayed a consistent radius of gyration, with an average size of 35.1 ± 2.1 nm. Following self-emulsification, the resultant zanamivir-loaded nanoemulsion droplets for zSDNE-WDS1 and zSDNE-WDS2 measured 542.1 ± 36.1 and 174.4 ± 3.4 nm, respectively. Both types of emulsions demonstrated the ability to enhance the transport of zanamivir across a parallel artificial membrane. Additionally, in situ rat intestinal perfusion studies involving drug-loaded SDNE-WDSs revealed a significantly increased permeability of zanamivir through the small intestinal wall. Notably, both SDNE-WDS formulations exhibited effective permeability (P_{eff}) values that were 3.5–5.5-fold higher than those of the low/high permeability boundary marker metoprolol. This research emphasizes the success of SDNE-WDSs in overcoming intestinal permeability barriers and enabling the effective oral administration of zanamivir. These findings hold promise for advancing the development of efficacious oral administration of BCS class III drugs.

Keywords: oral drug absorption; bioavailability; intestinal permeability; microemulsion; nanoemulsion; self-double emulsifying drug delivery system; zanamivir

1. Introduction

Nearly half of the antiviral drugs are classified under the biopharmaceutical classification system (BCS) as class III [1]. Active agents falling into this classification are characterized by high solubility but low permeability across the intestinal lumen, resulting in poor bioavailability [2]. Prominent antiviral drugs in BCS class III include abacavir, didanosine, maraviroc, and zidovudine, approved for the treatment of HIV (Human Immunodeficiency Virus). Additionally, ganciclovir and valganciclovir are prescribed for HCMV (human cytomegalovirus) infections, while trifluridine inhibits viral infections caused by HSV (herpes simplex virus) [3]. HBV (hepatitis B virus) and HCV (hepatitis C virus) are treated with adefovir dipivoxil and sofosbuvir, respectively. Furthermore, some of these agents are utilized in clinical practice to treat multiple human infectious diseases. For instance, lamivudine and tenofovir are indicated for the medical treatment of HIV and HBV. Acyclovir, valacyclovir, and vidarabine are used to treat various members of the

herpesviridae family, including HSV and VZV (Varicella–Zoster Virus) [3]. It is not surprising that viruses replicating through similar mechanisms (RNA, DNA, or retroviruses) are often susceptible to the same antiviral agents. For example, ribavirin efficiently inhibits HCV and RSV (Respiratory Syncytial Virus), both of which are RNA viruses. Consequently, with the emergence of new viral infections, such as Severe Acute Respiratory Syndrome Coronavirus 2 (SARS-CoV-2), some of these medications may prove effective if the viruses share similar replicating mechanisms. Regardless of the mechanism of action, improving the oral absorption of these antiviral drugs enhances compliance and hinders the further spread of viral diseases.

Influenza virus is one of the major viral diseases that can erupt into epidemics or even pandemics. In the United States, the average number of influenza patients over the past five years was 32 million, with an approximate 0.1% death rate. The appearance of SARS-CoV-2 led to a decrease in influenza virus incidence during the 2021–2022 season. However, in the subsequent 2022–2023 season, the number of infected individuals increased dramatically by 4.5-fold compared to the previous season [4].

The first-line treatment for the influenza virus typically involves the use of neuraminidase inhibitors, which target and inhibit the neuraminidase enzyme found on the viral envelope. By employing this mechanism of action, neuraminidase inhibitors effectively impede the release of new virions from infected cells, leading to a reduction in the severity and duration of influenza symptoms. Neuraminidase inhibitors, such as oseltamivir, peramivir, zanamivir, and laninamivir octanoate (currently only approved in Japan), are highly effective and widely used for the treatment of both influenza A and influenza B viruses [5]. However, all these drugs (except oseltamivir) fall under BCS class III, indicating challenges in their oral administration. Accordingly, they are administered through inhalation or intravenous routes [6–9]. Nevertheless, such non-oral administration methods can negatively impact patient compliance and increase the overall cost of the treatment. To address these limitations, it becomes crucial to enhance the intestinal permeability of peramivir, zanamivir, and laninamivir octanoate.

Zanamivir (MW 332.31 g/mol; Log P 4.13), the first discovered neuraminidase inhibitor, has demonstrated higher resistance to influenza mutations compared to oseltamivir [10]. This can be attributed to its hydrophilic nature, which is a result of the presence of a guanidino group and its structural similarity to sialic acid. The unique molecular structure of zanamivir facilitates stronger interactions with the active site of the influenza virus, thereby increasing its overall effectiveness [11]. Currently, zanamivir is administered via inhalation, with an absorption rate ranging from 4% to 17% [12]. Common side effects associated with zanamivir usage include sinusitis and dizziness, while more severe effects, such as bronchospasm (which can be fatal), allergic reactions, and neuropsychiatric events, are particularly observed in children [13,14]. By increasing its ability to be absorbed through the gastrointestinal (GI) tract, oral administration of zanamivir could become a viable option, offering a more convenient and cost-effective treatment approach for influenza.

Numerous drug-delivery emulsion systems have been developed to improve the bioavailability of drugs through the GI tract [15]. These systems not only improve drug solubility but also provide protection and prolong the stability of non-chemically stable drugs [16]. Upon reaching the target tissue, drug activity is enhanced while minimizing side effects. Additionally, drug-delivery emulsion systems have the potential to reduce treatment duration and frequency, which is particularly important in antiviral therapies that may require prolonged or high-dose regimens, resulting in increased treatment costs [17]. Moreover, since emulsions typically consist of an oil phase and an aqueous phase, they can be formulated and customized to accommodate both hydrophilic and lipophilic active substances [18]. Among these systems, oil-in-water (O/W) emulsions are the most commonly utilized in oral administration [19–21]. O/W emulsion systems are specifically beneficial for improving the solubility of drugs classified as Biopharmaceutics Classification System (BCS) class II (low solubility, high permeability) and class IV (low solubility, low permeability) [21]. On the other hand, double emulsion systems can augment the

permeability of drugs classified as BCS class III by dissolving the drug in the inner aqueous phase and increasing its lipophilicity through the oil phase. Nonetheless, double emulsion systems may suffer from thermodynamic instability over time, limiting their practical applications [22].

In our previous laboratory research, we investigated double emulsion systems encapsulating the active ingredient zanamivir [10]. In this present study, we developed a novel self-emulsifying double emulsion system that holds promise for enhanced intestinal permeability and ultimately improved effectiveness.

Self-double emulsifying drug delivery systems (SDEDDS) are assembled using two distinct primary emulsion types: water-in-oil (W_1/O) or oil-in-water (O_1/W). These primary emulsions are combined with an external continuous phase to produce final double emulsions, resulting in water-in-oil-in-water ($W_1/O/W_2$) and oil-in-oil-in-water ($O_1/W/O_2$) configurations, respectively. The former is the prevalent choice for oral administration since the external phase of the $W_1/O/W_2$ system consists of water. In this type of double emulsion, small aqueous droplets are encapsulated within oil droplets within the continuous water phase. The incorporation of hydrophilic emulgators within the oil phase of the primary W_1/O emulsions is responsible for enabling the self-emulsification process within these delivery systems. Consequently, when the primary emulsion encounters the aqueous environment under GI motility, it self-emulsifies into the final $W_1/O/W_2$ double emulsion structure [23,24]. Considering the inherent instability of double emulsions, the utilization of SDEDDSs, which undergo spontaneous emulsification facilitated by GI movements, proves to be a more effective approach. This is mainly owing to the superior stability achieved by the primary emulsions, transforming SDEDDS into an ideal choice for the delivery of BCS class III drugs [22,25–27]. Furthermore, the size of the final droplets of the emulsion systems is a critical factor that significantly influences their stability. Hence, the deliberate reduction in the final SDEDDS following self-emulsification to approximate the dimensions of a nanoemulsion becomes an intriguing strategy. This approach holds the potential to enhance not only the stability but also the permeability of zanamivir, potentially facilitating its absorption and bioavailability within the GI tract.

Microemulsions are a specialized class of emulsions characterized by droplet sizes typically ranging from 5 to 50 nm. These unique emulsions classically comprise water, oil, surfactants, and co-surfactants, while the specific composition and ratios of these components play a crucial role in determining their formation and stability [28]. Microemulsions exhibit distinct advantages, including thermodynamic stability and isotropic clarity [29]. Importantly, these emulsions possess the ability to spontaneously form without the need for vigorous mechanical energy processes such as sonication or homogenization, a feature not shared by nanoemulsions or macroemulsions [30].

Gordon Winsor introduced a classification system for microemulsions, categorizing them into four distinct types [31]: Type I microemulsion is characterized as an O/W microemulsion, where a portion of the oil component is solubilized by the emulsifier, and it achieves equilibrium with an excess of the oil phase. In contrast, Type II microemulsion is classified as a W/O microemulsion, where a fragment of the water component is solubilized by the emulsifier, and it reaches equilibrium with an excess of the aqueous phase. Type III microemulsion is unique in that it involves the solubilization of both oil and water constituents by the emulator. This type of emulsion is commonly named a bicontinuous microemulsion since it maintains an equilibrium state with an excess of the oil and water phases. Winsor Type IV is specifically referring to a single-phase micellar solution [28,32].

Our hypothesis employs the utilization of SDEDDSs, which involve the formulation of primary (W_1/O) microemulsions that transform into final $W_1/O/W_2$ double emulsions upon mixing with water. The incorporation of hydrophilic emulsifiers within the oil phase of the primary microemulsions facilitates the self-emulsification process within these delivery systems. Consequently, when these microemulsions encounter aqueous environments during GI motility, they culminate in the formation of final double nanoemulsions. This novel class of SDEDDS has been termed Self-Double Nanoemulsifying Winsor

Delivery System or SDNE-WDS. Our research focuses on exploring the potential of SDNE-WDSs to enhance the intestinal permeability of the antiviral drug zanamivir through oral administration.

2. Materials and Methods

2.1. Materials

All organic solvents were of HPLC grade and acquired from Carlo Erba (Milan, Italy). Polysorbate 80, 9,10-diphenyl anthracene, and sorbitan laurate were purchased from Merck KGaA (Darmstadt, Germany). Sucrose stearate was obtained from Sisterna (St. Paul, MN, USA), and zanamivir was obtained from Glentham Life Sciences (Corsham, UK). Rhodamine B, sodium lauryl sulfate (SLS), sodium phosphate dibasic dihydrate, sodium phosphate monobasic dehydrate, and uranyl acetate were acquired from Sigma Aldrich (St. Louis, MO, USA). Carboxymethyl cellulose (CMC) and mineral oil were purchased from Ziv Chemicals Ltd. (Holon, Israel).

2.2. Methods

2.2.1. Preparation of SDNE-WDSs with or without Drug Cargo

Two formulations were selected based on appropriate material ratios for creating SDNE-WDSs. The oil phase of the formulations was comprised of mineral oil and various surfactants, while the internal aqueous phase (W_1) contained carboxymethyl cellulose (CMC) as a gelling agent. The difference in the emulsions lies in the utilization of distinct emulgator systems: SDNE-WDS1 employed sorbitan laurate, whereas SDNE-WDS2 contained sucrose stearate. In the context of drug-loaded dispersed systems, a zanamivir solution was incorporated into the W_1 phase, yielding zanamivir-loaded systems referred to as zSDNE-WDSs. Following homogenization, the resulting primary W_1/O emulsions were rapidly cooled in an ice bath to room temperature. The self-emulsification process was carried out using a modified technique that was described in prior publications [33,34]. In brief, the final SDNE-WDSs were attained by adding 1 part of W_1/O emulsions to 6.67 parts of the continuous aqueous phases W_2, followed by stirring over 30 min at 1000 RPM (as depicted in Scheme 1).

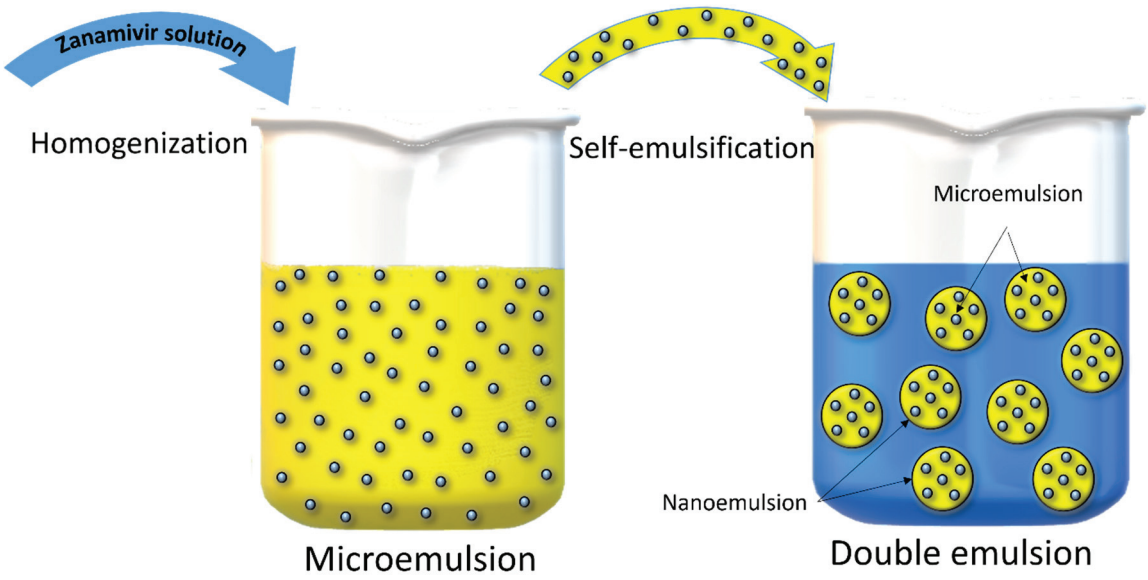

Scheme 1. Illustration depicting the preparation process of drug-loaded SDNE-WDSs.

2.2.2. Visualization by Electron Microscope

The morphological examinations of SDNE-WDS1 and SDNE-WDS2 were conducted using transmission electron microscopy (TEM) (Thermo Fisher Scientific (FEI) Talos F200C transmission electron microscope operating at 200 kV, San Jose, CA, USA). A droplet of the

specimen was deposited onto a copper grid coated with a carbon film, facilitating a thin film on the grid's surface. Subsequently, this film underwent negative staining through exposure to a 2% (w/v) uranyl acetate solution. After drying at ambient temperature, micrographs were captured using a Ceta 16M CMOS camera (Costa Mesa, CA, USA).

2.2.3. Confocal Laser Scanning Microscope (CLSM) Imaging

To visualize the inner aqueous phase in comparison to the outer aqueous phase, the hydrophilic fluorescent probe rhodamine B was dissolved in the W_1 of the emulsions as a probe for the inner aqueous droplets. Additionally, 9,10-Diphenyl anthracene (DPhA) was dissolved in the oil phase as a fluorescent marker for the oil phase. Fluorescent CLSM images of the double-labeled SDNE-WDSs were obtained using the Zeiss LSM META microscope (Jena, Germany), with rhodamine B parameters set at λ_{ex} 553 nm and λ_{em} 580 nm and DPhA parameters set at λ_{ex} 373 nm and λ_{em} 426 nm.

2.2.4. Analysis of Mean Droplet Size and Surface Charge

The mean droplet sizes and zeta potentials of freshly prepared $W_1/O/W_2$ emulsions derived from SDNE-WDSs were ascertained employing a dynamic light scattering instrument (Zetasizer Nano ZS by Malvern, UK). The particle size distribution of the double emulsions was evaluated subsequent to dilution with water.

2.2.5. Small-Angle X-ray Scattering (SAXS)

SAXS patterns of the mean particle size of the inner aqueous droplets in both SDNE-WDSs were obtained using a SAXSLAB GANESHA 300-XL instrument (Skovlunde, Denmark). The specimen preparation method was carried out according to a procedure detailed elsewhere [35]. The radius of gyration (R_g) was calculated from the Guinier plot using Equation (1).

$$\ln(I_0) = \ln(I) - \frac{1}{3}q^2{R_g}^2 \quad (1)$$

where I_0 represents the initial scattering intensity, I is the scattering intensity depending on the scatter vector (q) in cm^{-1}, and R_g is the radius of gyration in nm.

2.2.6. Determination of Winsor Emulsion Type Using Conductivity Investigation

We utilized conductivity measurements to determine the type of Winsor emulsion of the SDNE-WDS formulations. We employed the ExStik® EC500 instrument (Waltham, MA, USA), which features a stainless-steel electrode optimized for measurements across a wide conductivity range, from 0 to 2000 µs/cm. Additionally, this measurement was performed at a controlled temperature of 25 °C. To identify the type of microemulsion present in SDNE-WDS2, we introduced various concentrations of water into the formulations. A change in the slope of the conductivity measurement of each preparation was indicative of a transition in the microemulsion type, shifting from W/O to bicontinuous and subsequently to O/W [36].

2.2.7. High-Pressure Liquid Chromatography (HPLC) Analysis of Zanamivir

The analysis of zanamivir was conducted using High-Pressure Liquid Chromatography (HPLC) on a Waters 2695 HPLC system (Alliance, Milford, MA, USA). A Hypersil® BDS C18 column with dimensions of 150 mm × 4.6 mm and a particle size of 5 µm was used for chromatographic separation. Data analysis was performed using the Empower Pro software (EMP 2 Feature release 5, Built 2154).

A gradient elution method was applied to identify zanamivir, involving a transition from 10% acetonitrile (v/v) to 90% acetonitrile (v/v) in water over a 10-minute period. The flow rate was maintained at 0.5 mL/min, and 10 µL of the sample was injected for analysis. Zanamivir concentration was quantified at a wavelength of 242 nm using a UV detector. This HPLC analysis provided an accurate determination of zanamivir concentration [8].

2.2.8. Quantification of Encapsulation Efficiency

To calculate the entrapment efficiency (EE) of zanamivir within SDNE-WDSs, we employed an ultrafiltration technique. Following the self-emulsification process, 300 µL of the resulting double emulsions were mixed with 300 µL of a 10% SLS solution. Subsequently, these double emulsions were subjected to centrifugation at 14,000 RPM and 40 °C for 15 min to completely disrupt the formulations. The clarified solutions obtained post-centrifugation were subjected to HPLC analysis to quantify the quantity of free zanamivir. The calculation of entrapment efficiency involved determining the percentage (w/w) of the encapsulated drug relative to the total zanamivir content within the SDNE-WDSs, as per Equation (2) [37,38]. This entrapment efficiency assessment was conducted in triplicate for robust and accurate results.

$$\mathrm{EE}[\%] = \frac{\text{W initial amount of drug} - \text{W untrapped free drug}}{\text{W initial amount of drug}} \times 100\% \quad (2)$$

2.2.9. In Vitro Release Studies

Experiments evaluating the invitro release profiles of the self-emulsified SDNE-WDSs in comparison to the zanamivir solution were conducted in an aqueous buffer adjusted to match the pH of the small intestine. These experiments utilized dialysis bags with a molecular weight cut-off ranging from 12–14 kDa (Sigma Aldrich, St. Louis, MO, USA). Dialysis techniques are commonly employed for the examination of molecule release from a dispersed drug system due to their ability to isolate the droplets, enabling the active moiety to diffuse into the release medium through a membrane that does not restrict its passage. Accordingly, the pores of the membrane should possess a considerably greater size than that of the released substance. Next, 15 mL of the zanamivir-loaded SDNE-WDSs were placed within the dialysis bag and introduced into 200 mL of phosphate buffer solution (PBS) at pH 6.8, ensuring the presence of a significantly higher volume of media compared to the saturation point at which dissolution would slow (commonly referred to as "sink conditions"). Under continuous magnetic stirring, we extracted 150 µL samples from the dialysis bag at predetermined time intervals (0, 0.33, 0.67, 1, 2, 3, and 4 h). Subsequently, the drug concentration within these samples was determined using an HPLC method after disrupting the SDNE-WDSs [38].

2.2.10. Parallel Artificial Membrane Permeability Assay (PAMPA) for Assessing Passive Diffusion of Encapsulated Zanamivir

The evaluation of the in vitro passive diffusion of encapsulated zanamivir across artificial membranes was carried out using a Pre-coated PAMPA (BD Gentest™, San Jose, CA, USA) [39]. The donor wells were loaded with 300 µL of the respective test groups, which included the free drug, zSDNE-WDS1, and zSDNE-WDS2. The resulting PAMPA sandwich configuration was incubated at 25 °C, during which zanamivir concentrations in both the donor and acceptor plates were quantified using the HPLC technique. The calculation of the effective permeability coefficients, denoted as P_{app}, was performed according to Equation (3), which is adapted from the Corning® (Tewksbury, MA, USA) Gentest guidebook:

$$\mathrm{P}_{app} = \frac{-\ln\left[1 - C_A(t)/C_{equilibrium}\right]}{A \times (1/V_D + 1/V_A) \times \mathrm{T}} \quad (3)$$

where:

$C_D(t)$ represents the compound concentration in the donor well at time t [mM]; $C_A(t)$ denotes the compound concentration in the acceptor well at time t [mM]; V_D represents the volume of the donor well; V_A represents the volume of the acceptor well; $C_{equilibrium}$ is calculated as $[C_D(t) \times V_D + C_A(t) \times V_A]/(V_D + V_A)$; A signifies the filter area; T is the incubation time.

2.2.11. In Situ Single-Pass Intestinal Perfusion (SPIP) Studies

To assess the effective permeability coefficients of zanamivir-loaded zSDNE-WDSs within the proximal jejunal segment, we employed the in situ single-pass rat intestinal perfusion model. All animal procedures adhered to the guidelines set by the Ben-Gurion University of the Negev Animal Use and Care Committee (Protocol IL-30-04-2019). Male Sprague Dawley rats, approximately 300 g in weight (Harlan, Israel), were utilized in this study and were housed and managed in accordance with the Ben-Gurion University of the Negev Unit for Laboratory Animal Medicine Guidelines. The rats underwent an overnight fast (lasting 12–18 h) while having access to water. Random assignments to different experimental groups were produced for each animal. The procedure closely followed the established protocol, as was previously reported [8,39,40]. Briefly, the rats were anesthetized via intramuscular injection with 100 mg/kg of ketamine and 5 mg/kg of xylazine. A midline abdominal incision, approximately 3 cm in length, was made. Permeability measurements were focused on an 11 cm proximal jejunal segment, commencing 2 cm below the ligament of Treitz. The intestinal segment was cannulated at both ends, with an initial perfusion consisting of normal saline solution at 37 °C to establish a steady state, followed by subsequent perfusion involving the collection of samples at 8-min intervals. All perfusion solutions underwent incubation in a water bath at 37 °C and were subsequently pumped through the intestinal segment. Samples from the perfusate were immediately subjected to HPLC analysis. Upon the conclusion of the experiment, the exact length of each perfused jejunal segment was measured. The net water flux during the single-pass rat jejunal perfusion investigations, signifying water absorption within the intestinal segment, was calculated utilizing Equation (4).

$$C'_{out} = C_{out} \times \frac{V_{out}}{V_{outT}} \quad (4)$$

where C_{out} is the drug concentration experimental value in the outlet sample, while the calculated C'_{out} represents the corrected concentration of the drug. V_{out} is the volume of the outlet sample, and V_{outT} is the theoretical volume that was expected to emerge. The actual absorption rate coefficient across the rat gut wall in the SPIP studies was calculated using Equation (5).

$$P_{eff} = \frac{-Q\ln\left(C'_{out}/C_{in}\right)}{2\pi RL} \quad (5)$$

where Q signifies the perfusion buffer flow rate and C'_{out}/C_{in} denotes the ratio of the outlet concentration (as calculated by Equation (4)) to the inlet concentration of the test drug. R represents the radius of the intestinal segment (set at 0.2 cm), and L signifies the length of the intestinal segment.

2.2.12. Data and Statistical Analysis

Data are presented as means ± standard deviation (means ± SD) or means ± standard error (means ± SE). Statistical analysis to determine significant differences among the experimental groups involved a one-way ANOVA test, followed by Tukey's test for comparisons between all groups. For pairwise comparisons between the two groups, an unpaired *t*-test was conducted. Significance was established at $p < 0.05$.

3. Results

3.1. Preparation and Characterization of Stable Zanamivir-Loaded SDNE-WDSs

Numerous formulations were developed to determine the optimal experimental conditions for creating stable SDNE-WDSs. In an attempt to ensure the future feasibility of this delivery system, consideration was given to selecting components from materials already approved for oral administration. The composition of both the oil phase and the gelling agent were similar to those employed in double emulsions previously developed in our laboratory [10]. The choice of hydrophobic emulsifiers, specifically sucrose stearate

and sorbitan laurate, was predicated on their demonstrated ability to construct stable double emulsions [41,42]. Furthermore, owing to its favorable physicochemical properties enabling incorporation into the oil phase, polysorbate 80 was the obvious selection as the hydrophilic self-emulsifying agent. Ultimately, two formulations exhibiting robust stability were selected: SDNE-WDS1 and 2. Both primary systems initially existed as microemulsions and, upon dilution with water, transformed into nanoemulsions.

The CLSM images presented in Figure 1 provide a visual representation of freshly prepared SDNE-WDSs following spontaneous emulsification. Figure 1 (i) represents the inner W1 phase (blue channel), while Figure 1 (ii) depicts the oil phase of the nanoemulsions (red channel). The superimposed images in Figure 1 (iv) demonstrate the co-localization of the red and blue fluorescent signals, signifying the presence of inner aqueous droplets within the oil phase. Moreover, there was no significant detection of red or blue fluorescent signals in the external aqueous phase W2, underscoring the effective encapsulation of the hydrophilic cargo within the inner aqueous phase of the oil droplets.

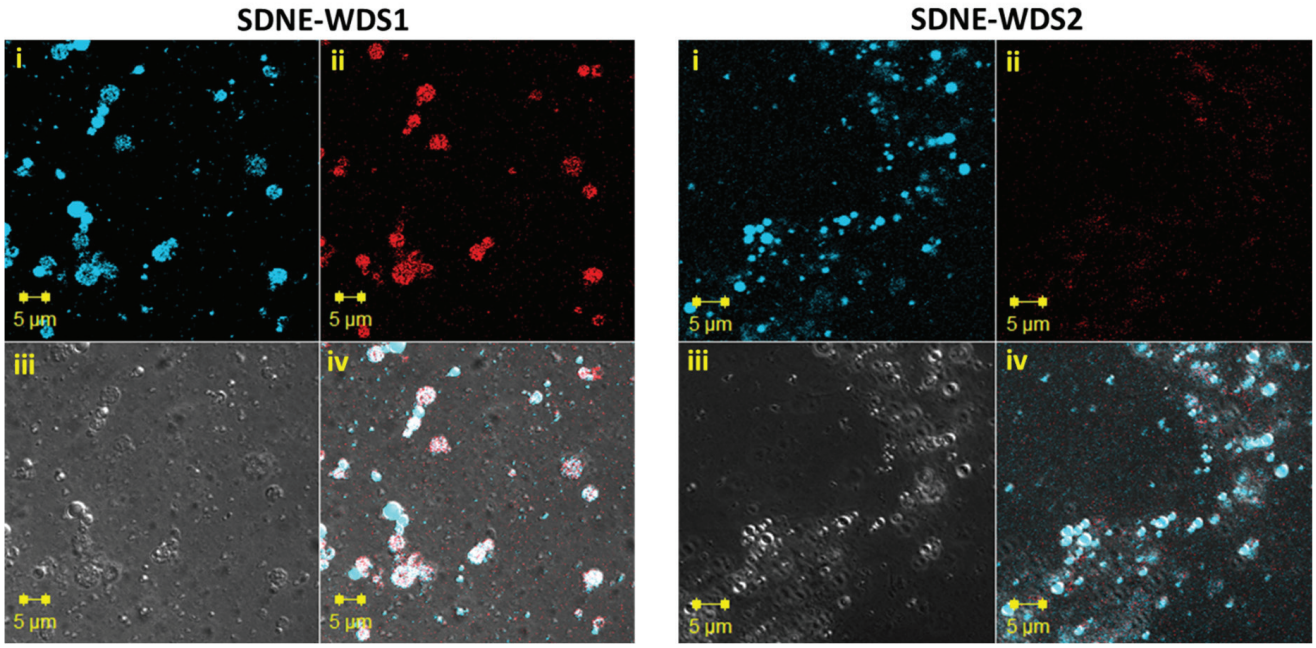

Figure 1. Confocal Laser Scanning Microscopy images of $W_1/O/W_2$ emulsions following self-emulsification of SDNE-WDS1 and SDNE-WDS2: (i) Blue marker DPhA in the oil phase; (ii) Red probe rhodamine B in W_1; (iii) Optical microscopy images; (iv) Superimposition of images (i,ii), illustrating merged fluorescent signals (blue and red). Magnification ×63.

Predominantly, SDNE-WDS1 yielded larger final nanodroplets compared to SDNE-WDS2. This difference in droplet size can be attributed to the distinct oil phase emulsifiers employed, as outlined above. The mean diameters of the $W_1/O/W_2$ droplets were 542.1 ± 36.1 nm and 623.9 ± 53.2 nm for SDNE-WDS1 with and without zanamivir, respectively. For SDNE-WDS2, the mean droplet size was 174.4 ± 3.4 nm, while that of zSDNE-WDS2 was 170 ± 2.3 nm. Remarkably, the presence of zanamivir in the inner aqueous phases of the systems did not result in a substantial difference in the size of the final double emulsion droplets. Additionally, the mean diameter measurements of the SDNE-WDSs aligned with the findings in Figure 2.

Both formulations exhibited a notable negative surface charge. Particularly, the zeta potential of SDNE-WDS1 was −43.9 ± 19.5 mV, while that of zSDNE-WDS1 was −56.93 ± 1.26 mV. For SDNE-WDS2, the zeta potential values were −62.43 ± 0.75 mV and −68.3 ± 17.5 mV, with and without zanamivir, respectively.

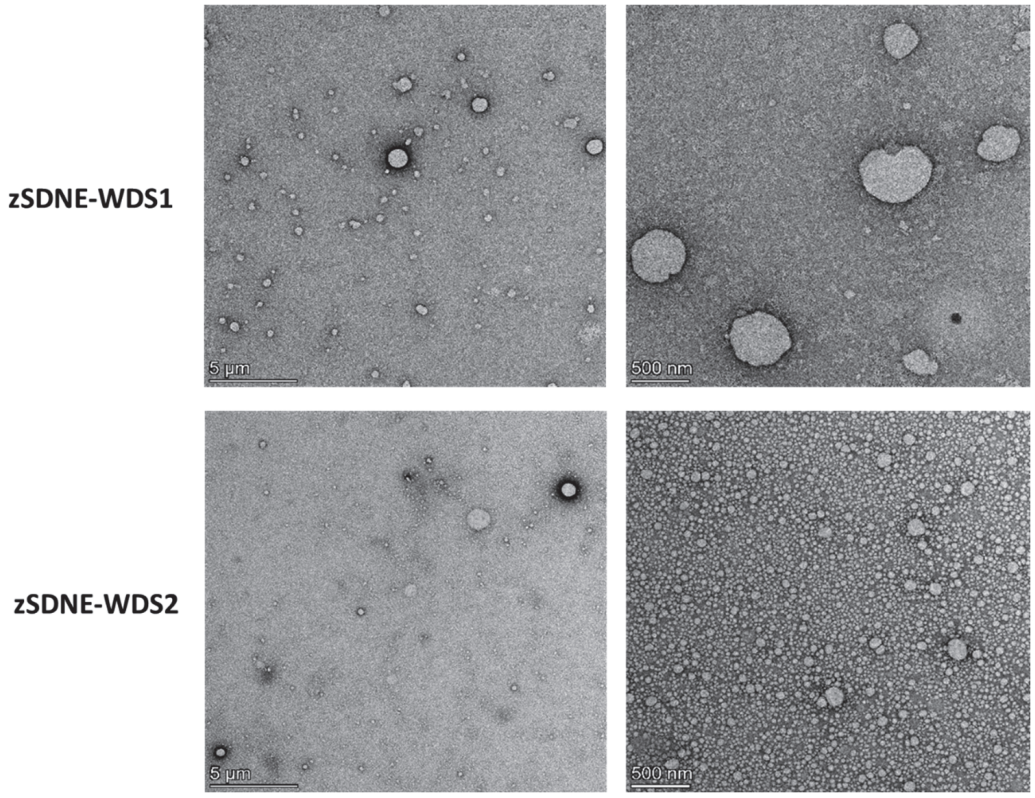

Figure 2. TEM images of $W_1/O/W_2$ emulsions following self-emulsification of zSDNE-WDS1 and zSDNE-WDS2. Specimens were negatively stained using a 2% uranyl acetate solution.

It is worth highlighting that comparable drug encapsulation efficiencies were achieved for the resultant diluted double emulsions despite their differences in droplet sizes and zeta potentials. In particular, the encapsulation efficiencies for zSDNE-WDS1 and zSDNE-WDS2 were found to be 77.12 $\pm$ 3.98% and 75.66 $\pm$ 3.79%, respectively.

Figure 2 depicts the TEM images of zSDNE-WDS1 and zSDNE-WDS2 subsequent to their emulsification, forming $W_1/O/W_2$ double nanoemulsions. Markedly, the outer oil droplets in the $W_1/O/W_2$ structure of zSDNE-WDS2 appeared visibly smaller compared to those in zSDNE-WDS1. Upon closer examination in higher magnification micrographs, zSDNE-WDS2 exhibited a more concentrated presence of smaller droplets, which might be attributed to its mean droplet size. These observations suggest that the choice of formulation and particularly emulsifying agents can influence the size and distribution of droplets within these drug carriers, stressing the importance of fine-tuning these parameters for specific drug delivery applications.

The average size of the inner aqueous phases within both Winsor systems was assessed by means of SAXS, as illustrated in Figure 3. Impressively, all the inner microemulsions exhibited a consistent radius of gyration, measuring at an average droplet size of 35.1 $\pm$ 2.1 nm. The size of these aqueous droplets remained distinctly stable, showing no considerable variation regardless of the type of oil phase emulsifier employed. Furthermore, the averaged radii of the microemulsions prepared with 60 µg/mL of active agent were comparable to those with zanamivir concentrations exceeding six-fold. This observation implies that the dosage of the active agent can be modified while preserving the structural integrity of the delivery system.

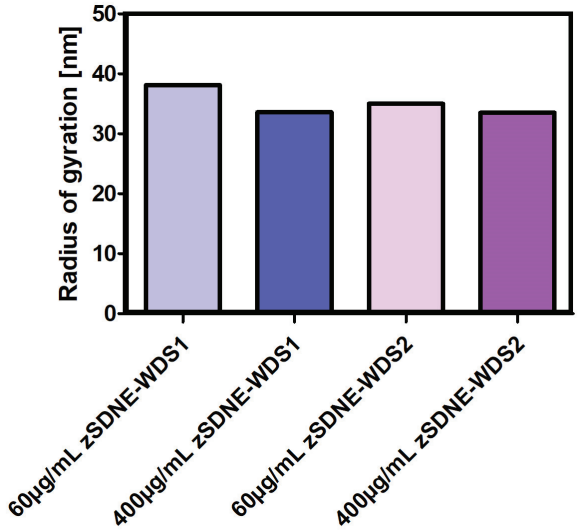

Figure 3. Radii of gyration of the inner aqueous droplets of SDNE-WDS1 and SDNE-WDS2 comprised varying zanamivir concentrations.

The primary microemulsion type was deduced from conductivity measurements of the continuous phase. SDNE-WDS1 exhibited negligible values, confirming its microemulsion type as W/O (Winsor system type II). Conversely, SDNE-WDS2 obtained a conductivity of 82 µs/cm, suggesting either an O/W or bicontinuous primary microemulsion. To clarify the exact nature of this Winsor system, conductivity measurements were conducted on a series of SDNE-WDS2-based formulations with increasing water content. In this experiment, a significant positive shift in the slope of the conductivity measurements indicates a transition from W/O to bicontinuous and subsequently to O/W [36]. In accordance with the conductivity study illustrated in Figure 4, three distinct slopes were identified, each indicative of a distinct Winsor system configuration (the initial slope corresponds to Type II, the middle slope to Type III, and the final slope to Type I). With a water content of 27%, SDNE-WDS2 clearly demonstrated a bicontinuous character (Winsor type III).

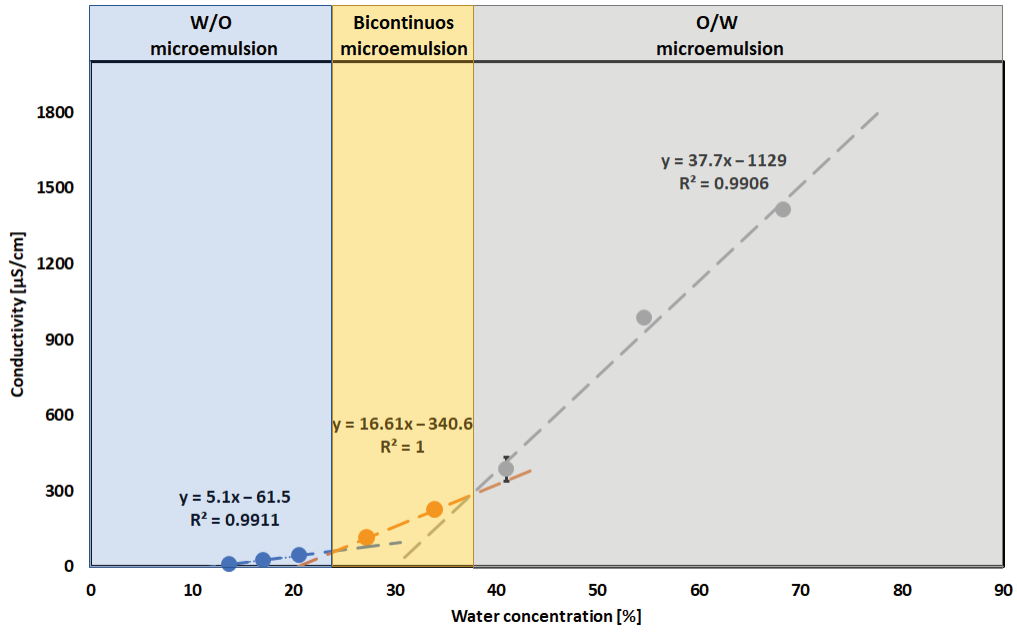

Figure 4. Conductivity values of the water-in-oil, bicontinuous, and oil-in-water microemulsions as a function of increasing water content in SDNE-WDS2-based formulations. The conductivity values are presented as means ± standard deviation (means ± SD); $n = 3$.

The mean diameters of the drug-loaded SDNE-WDSs were monitored over time, and the results are presented in Figure 5. Interestingly, SDNE-WDS1 exhibited instability at elevated temperatures. On the other hand, this formulation remained stable for at least 5 weeks at 4 °C, with slight fluctuations in averaged diameter following incubation at ambient temperature for 9 weeks (Figure 5A). Outstandingly, SDNE-WDS2 maintained long-term stability for a minimum of 10 weeks, following incubation at room temperature (RT), 4 and 40 °C (Figure 5B). The surface charge of colloidal carriers significantly influences their physicochemical stability. Overall, the zanamivir-loaded systems (excluding SDNE-WDS1 at 40 °C) consistently exhibited substantial and coherent negative zeta potential values throughout the study period, irrespective of incubation conditions (as shown in Figure 6).

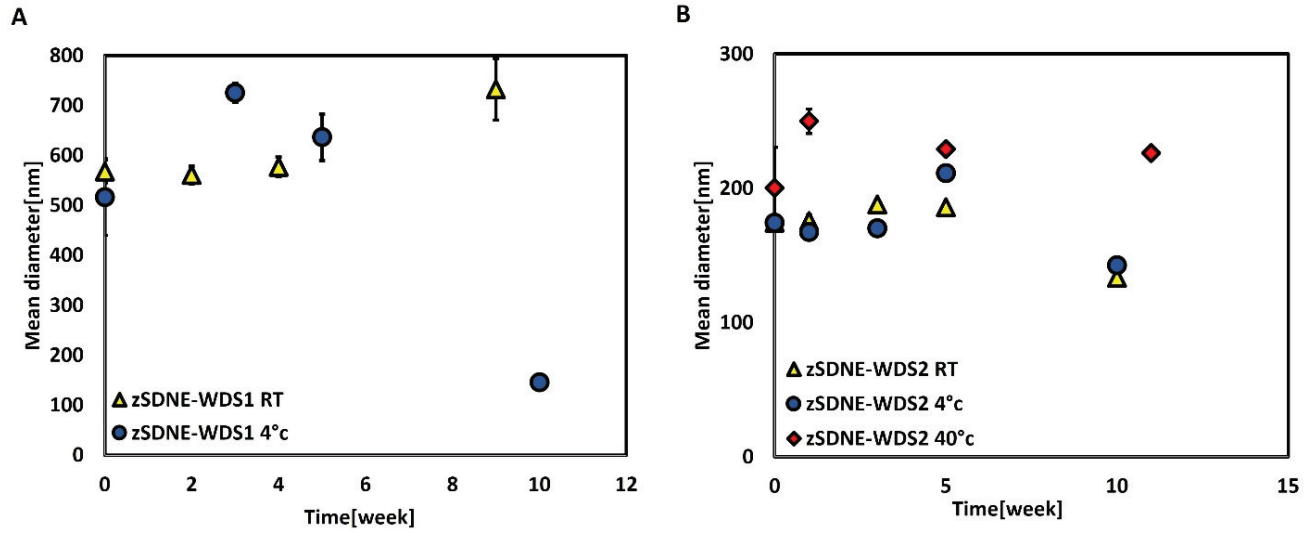

Figure 5. Mean droplet diameters of drug-loaded carriers over time following incubation at room temperature (RT), 4 and 40 °C. (**A**) Zanamivir-loaded SDNE-WDS1; (**B**) Zanamivir-loaded SDNE-WDS2. The results are represented as (means ± SD); $n = 3$.

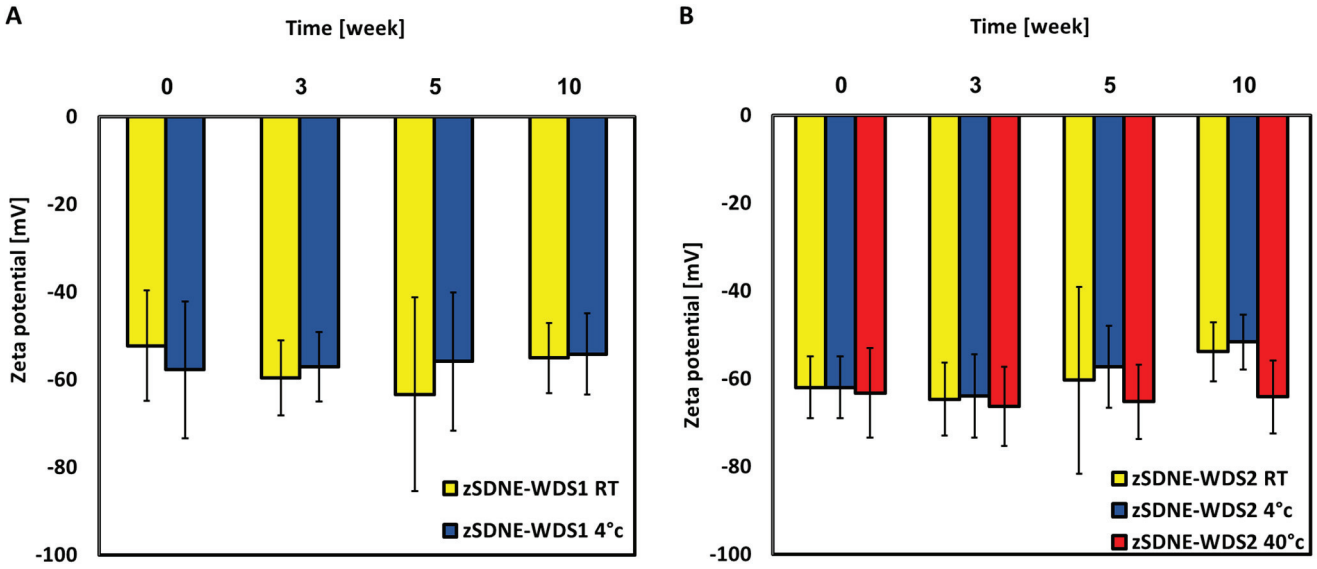

Figure 6. Surface charge assessment of drug-loaded carriers over time after incubation at RT, 4 and 40 °C. (**A**) Zanamivir-loaded SDNE-WDS1; (**B**) Zanamivir-loaded SDNE-WDS2. The zeta potential values are donated as (means ± SD); $n = 3$.

3.2. In Vitro Release Studies

Figure 7 explores the results of the in vitro release experiments involving zanamivir-loaded SDNE-WDSs conducted in a phosphate-buffered saline (PBS) solution at pH 6.8 and compares them to a solution of the free drug. When examining the initial 20-minute interval, unformulated zanamivir displayed an abrupt burst release, amounting to approximately 59% of the total payload, with the entire quantity being released within the first hour. In contrast, the two distinct types of zanamivir-loaded SDNE-WDSs exhibited a more controlled release pattern. After a duration of 4 h, the cumulative release of zanamivir from SDNE-WDS1 and SDNE-WDS2 reached 86.1% and 81.6%, respectively. These findings accentuate the potential of SDNE-WDSs to modulate the release kinetics of zanamivir, providing a more sustained delivery compared to the unformulated drug solution.

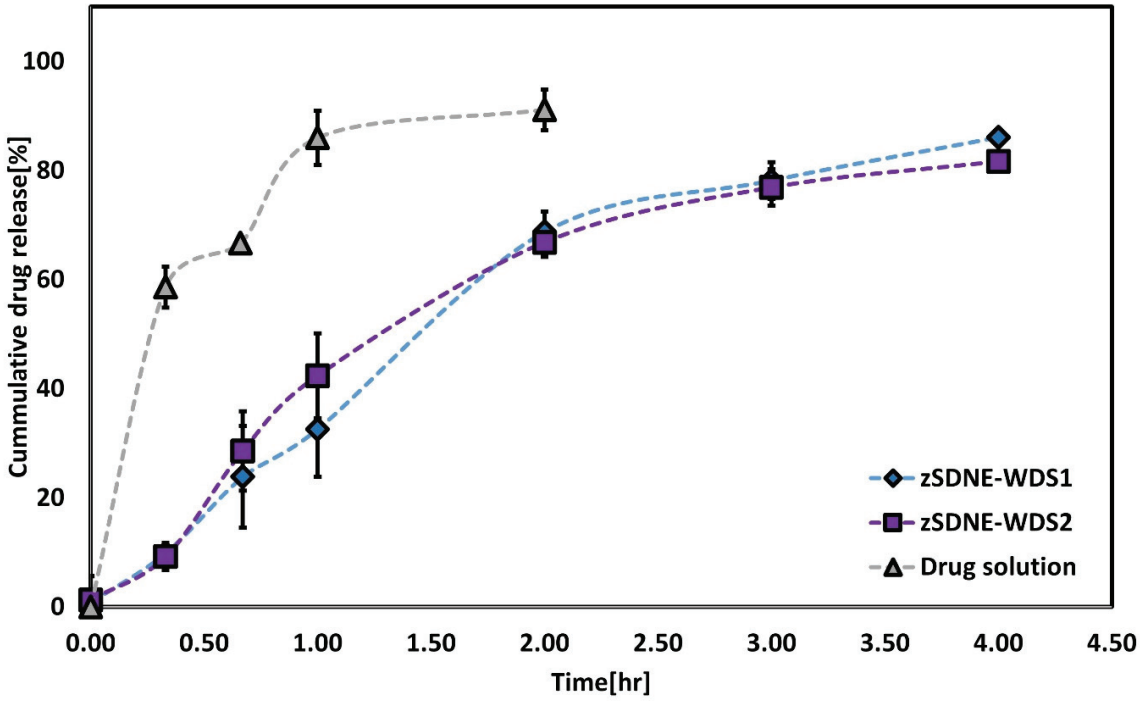

Figure 7. Release profiles of 400 μg/mL zanamivir from SDNE-WDS1, SDNE-WDS2, and a zanamivir solution. All formulations were tested in PBS at pH 6.8 while maintaining a temperature of 37 °C. The presented data represents the means ± SD; n = 9.

3.3. Parallel Artificial Membrane Permeability Assay

We conducted an in-depth investigation into the passive transport of zanamivir across an artificial membrane. Both unformulated and zanamivir-loaded double emulsions from SDNE-WDSs were subjected to this study. Following 24 h, zanamivir concentrations at the donor side were sampled, and the permeability was subsequently calculated using the acquired data (as shown in Figure 8). The results reveal the facilitated transport of encapsulated zanamivir across the artificial membrane, as demonstrated by the noticeable enhancement in the apparent permeability coefficients (P_{app}) of this antiviral agent. ZSDNE-WDS1 and zSDNE-WDS2 exhibited significantly increased P_{app} values, measuring at $5.14 \times 10^{-6} \pm 3.85 \times 10^{-7}$ and $9.63 \times 10^{-6} \pm 4.41 \times 10^{-6}$ cm/s, respectively. Remarkably, the permeability efficiency of these two formulations exhibited no marked statistical variation. These findings underline the efficacy of zanamivir-loaded SDNE-WDSs in promoting the permeation of the antiviral agent across the studied artificial membrane, potentially improving its bioavailability and therapeutic effectiveness.

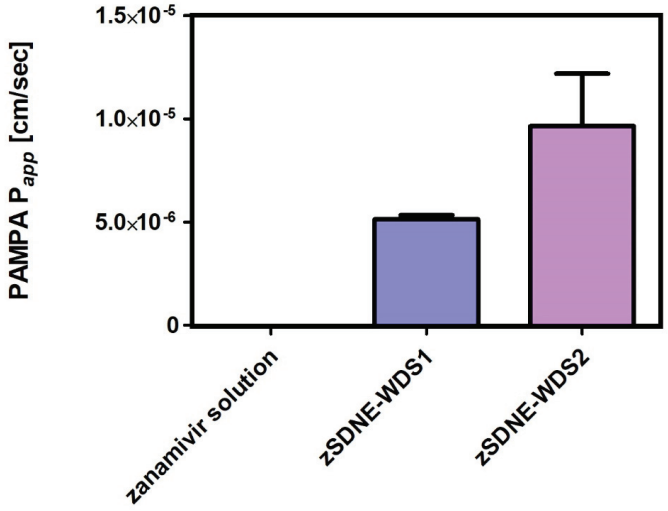

Figure 8. In vitro effective permeability values (P_{app}) of 400 µg/mL zanamivir loaded SDNE-WDSs following self-emulsification, as calculated from the results obtained through the PAMPA studies conducted at pH 7.4. The results are provided as means ± SE; $n = 4$.

3.4. In Situ *Single-Pass Intestinal Perfusion Studies*

We investigated the in situ effective permeability coefficients of free zanamivir, as well as when encapsulated within SDNE-WDSs by means of the single-pass intestinal perfusion rat model. This study was conducted within the proximal jejunum segment of the intestine and provided insights into the effective permeability coefficients of final nanoemulsions perfusate in comparison to those of the unformulated drug. The results presented in Figure 9 confirmed the inherently low permeability of zanamivir. Noticeably, the flux of zanamivir, when encapsulated within SDNE-WDSs, exhibited a significant increase in comparison to the free antiviral drug. The P_{eff} values for zSDNE-WDS1 and zSDNE-WDS2 were determined to be $2.19 \times 10^{-4} \pm 1.26 \times 10^{-4}$ and $1.40 \times 10^{-4} \pm 4.52 \times 10^{-5}$ [cm/s], respectively. This signifies that our emulsions displayed more than a 71-fold increase in permeability compared to the free drug ($p < 0.0004$). Remarkably, our in situ model did not discover any statistical difference in the effective permeability between these two SDNE-WDS formulations.

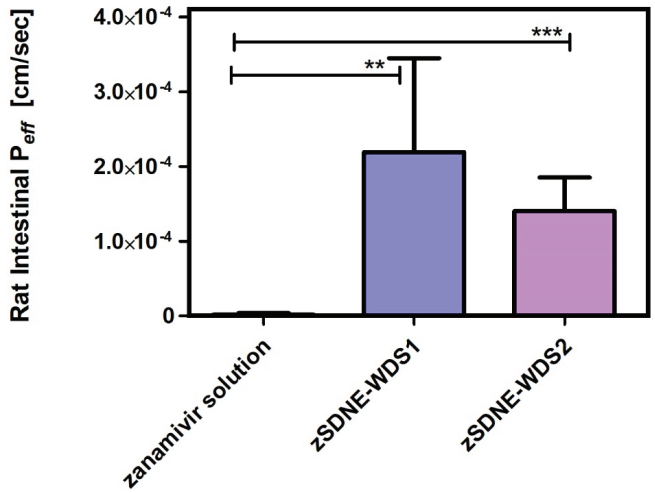

Figure 9. In situ effective permeability values (P_{eff}) of 400 µg/mL zanamivir solution and zanamivir encapsulated within SDNE-WDSs, determined by perfusion of emulsions in the jejunum of rats. The results are shown as means ± SD; $n = 6$ for the zanamivir solution and $n = 8$ for SDNE-WDSs. Statistical significance is indicated as follows: ** $p < 0.001$; *** $p < 0.0001$.

4. Discussion

BCS Class III compounds are characterized by their hydrophilic nature, which translates to high aqueous solubility, but they exhibit low permeability across biological membranes. Despite their pharmacological effectiveness, their poor absorption due to low permeability becomes the limiting factor in achieving sufficient bioavailability [43]. Notably, several antiviral agents, such as adefovir, lamivudine, ribavirin, zanamivir, and zidovudine, fall into this Class III category. While these agents effectively combat some of the most prevalent viruses known to afflict humans, unfortunately, their inherently low oral bioavailability of these agents restricts their administration via the oral route.

Prior research has highlighted that the bioavailability of Class III drugs can be enhanced through their encapsulation within drug delivery systems. In numerous instances, nanocarriers have demonstrated a remarkable ability to significantly improve the efficacy of these drugs [17]. For example, the utilization of a liposomal system for tenofovir led to a 10-fold increase in drug permeability compared to the free drug in Caco-2 cultures [44]. In another study, a self-nanoemulsifying drug delivery system (SNEDDS) that incorporated adefovir dipivoxil exhibited a considerable enhancement in the oral absorption of this drug when tested in rat models [45] These findings emphasize the potential of innovative drug delivery systems to overcome the challenges posed by Class III compounds and enhance their therapeutic impact.

In this study, our strategy involved encapsulating zanamivir within innovative colloidal carriers that integrate the distinctive characteristics of self-double emulsions, microemulsions, and nanoemulsions delivery systems. Consequently, we introduced two novel self-double nanoemulsifying Winsor delivery systems, namely SDNE-WDS1 and SDNE-WDS2. These systems vary in the composition of surfactants present in the oil phase, with SDNE-WDS1 containing sorbitan laurate and SDNE-WDS2 incorporating sucrose ester. When incorporating zanamivir into these SDNE-WDSs, we achieved the formation of microemulsions through conventional emulsion preparation methods, all while avoiding the necessity for high surfactant concentrations. In typical microemulsion preparations, surfactant concentrations often surpass nearly 50%; however, our innovative approach allowed us to create microemulsions with significantly lower surfactant concentrations [46].

While the inner aqueous droplets of the primary microemulsions remained unchanged (as illustrated in Figure 3), it is important to note that the choice of oil phase emulsifiers had a significant impact on the initial Winsor system (as depicted in Figure 4). It is particularly noteworthy that sorbitan laurate promoted the formation of a W/O microemulsion, whereas sucrose stearate resulted in a Winsor type III system, as demonstrated in Figure 4. This outcome is probably attributed to the differing Hydrophilic–Lipophilic Balance (HLB) values of these emulgators, which stand at 8.7 and 11, respectively. Considering that both of our formulations had an equal overall calculated HLB, this observation is uniquely intriguing.

As depicted in Figure 4, the water content range suitable for forming bicontinuous microemulsions with SDNE-WDS2 falls within the range of 24–37%. In a study by Tamhane et al., they explored the water content range required for bicontinuous microemulsions that encapsulated a plant protease inhibitor. In their research, the water content for their Winsor type III systems was determined to be in the range of 52–58% [36]. Predominantly to date, there have not been any investigations focusing on the use of bicontinuous microemulsions for oral administration, which could open promising approaches for potential pharmaceutical applications.

The selection of different emulsifiers incorporated within the oil phase of the microemulsions also had a considerable impact on the final average sizes of the double nanoemulsions obtained (as shown in Figure 5). In particular, the mean droplet size of zSDNE-WDS2 was three times smaller than that of zSDNE-WDS1 (as shown in Figure 5). This observation possibly contributes to the significantly enhanced stability of zSDNE-WDS2, incubated in RT, 4 and 40 °C over time.

Accelerated stability studies, which involve subjecting a pharmaceutical preparation to elevated temperatures for a specific duration, can provide insights into the preparation's shelf-life stability, often indicating a longer shelf life than the actual measured time [47]. As seen in Figure 5B, zSDNE-WDS2 demonstrated remarkable stability throughout the investigation, even under an elevated temperature environment. This extended stability can be attributed to the inherent thermodynamic stability of microemulsions, a characteristic that promotes their prolonged shelf life. The sustained long-term stability of the microemulsions developed in this study can be attributed to their small droplet size (Figure 3) and the relatively high surface charges of the final nanoemulsions (Figure 6) that collectively inhibit droplet coalescence [48].

SNEDDSs are initially composed of a single-phase oil that, upon exposure to gastric fluids and peristaltic movements, transforms into nanosized emulsion droplets. These minuscule droplets possess the capability to traverse the intestinal barrier, thereby enhancing the absorption of lipophilic drugs characterized by low bioavailability [45]. An illustrative instance involves chlorpromazine, classified as a BCS class II drug, which has been successfully loaded into SNEDDSs. The deployment of such systems has yielded a notable 2 to 6-fold increase in the area under the curve (AUC) values of chlorpromazine, surpassing the performance of the free drug in pharmacokinetic assessment [49]. However, while SNEDDSs are extensively employed for improving the bioavailability of predominantly lipophilic drugs, our investigation represents a pioneering effort. To the best of our knowledge, there has been no prior exploration into the utilization of self-emulsifying nanoemulsions for encapsulating hydrophilic drugs.

CLSM provides a powerful tool for visualizing fluorescently labeled compounds with exceptional optical microscopy resolution. In our study, we utilized rhodamine B to stain the internal aqueous phase and DPhA to stain the outer oil phase. This strategic staining allowed us to investigate whether the encapsulated hydrophilic fluorescent probe had permeated into the surrounding aqueous continuous phase or, more desirably, remained confined within the internal aqueous droplets. Figure 1 clearly indicates that rhodamine B resided within the oil droplets and exhibited no signs of leakage into the external aqueous phase. In another study, this phenomenon is further exemplified in self-double emulsions containing epigallocatechin-3-gallate (EGCG) [50].

The release profiles of zanamivir from SDNE-WDS1 and SDNE-WDS2 revealed a markedly slower release rate when compared to the rapid release observed with the free drug, as illustrated in Figure 7. Comparable release patterns have been reported in previous research involving other agents incorporated into SDEDDSs. For instance, an SDEDDS loaded with EGCG exhibited a release of approximately 30–55% of the active compound within 2 h, depending on the ratio between the oil and emulsifier used [50]. In our own investigations, both formulations exhibited nearly identical drug release profiles over time despite differences in their compositions. It is interesting to note that a similar phenomenon was observed in the release kinetics of several pidotimod SDEDDSs, where researchers explored varying phospholipid-to-cosurfactant ratios [24]. Nevertheless, Shi et al. explored Solid Lipid Nanoparticles (SLNs) as a potential formulation for zanamivir encapsulation with the aim of improving its oral delivery and enhancing its transport across the intestinal epithelial layer. Their study revealed an initial burst release effect of zanamivir from SLNs, with approximately 70% of the drug being released within the first 2 h. This burst release phenomenon is probably attributed to the presence of free drug within the system, which was not effectively encapsulated within the lipid nanoparticles [38]. The drug-loaded SLNs exhibited relatively low entrapment efficiencies for the antiviral agent, ranging from 35% to 56%, ultimately resulting in a significant amount of unformulated zanamivir being rapidly released [37,38]. A similar trend of relatively low encapsulation efficiency was observed in liposomal systems, where zanamivir entrapment ranged from 28% to 35% [51].

In contrast, previous work conducted in our laboratory demonstrated markedly higher encapsulation efficiencies for zanamivir in double emulsions, reaching levels of 96.6–98.9%, indicating a substantial degree of drug entrapment within these systems [10]. In this current

study, SDNE-WDSs achieved approximately 75% drug encapsulation. This high level of drug encapsulation indicates their potential as effective carriers for zanamivir. These results stress the promise of SDNE-WDSs as a robust platform for enhancing the delivery of various hydrophilic drugs, offering potential advantages in terms of drug stability and improved intestinal permeability.

To date and to the best of our knowledge, four publications have reported on in vitro and/or in vivo attempts to enhance the oral bioavailability of zanamivir. In our previous work, we widely discussed two of these publications that attained improved bioavailability by means of prodrugs [8,33]. The remaining two papers explored zanamivir encapsulation within drug delivery systems and examined permeation coefficients across Caco-2 monolayers. In one study, liposomal zanamivir increased drug permeation by 2.2 to 3.0-fold compared to the unformulated drug [51]. In contrast, another investigation found that zanamivir penetration was actually lower than that of the control solution when encapsulated within SLNs [38]. In addition to the aforementioned studies, our recently published research elucidated the superior apparent and effective permeability coefficients observed upon the incorporation of zanamivir into double emulsion systems [10].

In the present study, the results from in vitro PAMPA studies demonstrated a significant improvement in zanamivir membrane diffusion permeability upon emulsification of SDNE-WDSs, as depicted in Figure 8. To further explore the enhancement of oral zanamivir absorption facilitated by SDNE-WDSs, we conducted in situ studies utilizing the SPIP system in rats. Notably, the transport of encapsulated molecules across the jejunum of humans is remarkably predicted using this model [7]. Our findings, illustrated in Figure 9, revealed highly promising P_{eff} values, where SDNE-WDSs successfully converted zanamivir into a highly permeable compound, superior to the unformulated drug.

It is worth noting that the permeability values obtained in the rat model exceeded those observed in the in vitro studies. This observation is probably owing to the inherent differences between the two methods. PAMPA is a model for assessing the passive diffusion permeability across an artificial membrane. Conversely, the in situ SPIP system encompasses passive as well as active pathways involved in the permeation of a molecule through biological membranes [52–54].

Metoprolol offers a commonly accepted standard molecule for determining the BCS permeability classification of various compounds. In previous work, we established the permeability effective coefficient of metoprolol to be 4×10^{-5} cm/s, utilizing the SPIP model in rats [55]. It is particularly interesting that in the present study, under similar experimental conditions, the effective permeability values of zanamivir within SDNE-WDSs were approximately 3.5–5.5-fold higher than that of metoprolol. This outcome is particularly significant when considering the standard boundaries for low and high permeability classes. Our SDNE-WDSs have effectively masked the inherent poor permeability of zanamivir, successfully transforming this antiviral agent into a BCS class I compound characterized by high solubility and high permeability. Furthermore, in comparison to alternative carriers such as liposomes, SDNE-WDSs exhibit outstanding advantages due to their anticipated low production costs and high potential for efficient drug encapsulation [56,57].

5. Conclusions

The current study was undertaken to optimize the formulation of Self-Double Nanoemulsifying Winsor Delivery Systems (SDNE-WDSs) with the specific objective of augmenting the intestinal absorption of zanamivir, classified as a BCS class III compound. These SDNE-WDSs represent microemulsions that, upon emulsification, transform into colloidal carriers characterized by a high encapsulation efficacy. Results obtained from both in vitro permeability studies and in situ intestinal perfusion experiments reveal that zanamivir-loaded SDNE-WDSs exhibit enhanced intestinal membrane permeability compared to the unformulated drug. While these findings are promising, further comprehensive investigations are warranted to show pharmacokinetic analysis and to gain a deeper un-

derstanding of the precise absorption mechanisms underlying the enhanced absorption observed in the developed SDNE-WDSs.

Author Contributions: Conceptualization and methodology, N.D. and A.D.; investigation, S.I.; validation, A.D. and N.D.; data curation, S.I. and N.D. Writing—original draft preparation, S.I. All authors contributed to the writing—review and editing; visualization, S.I. and N.D.; supervision, A.D. and N.D. All authors have read and agreed to the published version of the manuscript.

Funding: This research received no external funding.

Institutional Review Board Statement: The animal study protocol was approved by the Animal Use and Care Committee of the Ben-Gurion University of the Negev (Protocol IL-30-04-2019, 30 April 2019).

Informed Consent Statement: Not applicable.

Data Availability Statement: Not applicable.

Conflicts of Interest: The authors declare no conflict of interest.

References

1. Chen, R.; Wang, T.; Song, J.; Pu, D.; He, D.; Li, J.; Yang, J.; Li, K.; Zhong, C.; Zhang, J. Antiviral Drug Delivery System for Enhanced Bioactivity, Better Metabolism and Pharmacokinetic Characteristics. *Int. J. Nanomed.* **2021**, *16*, 4959–4984. [CrossRef]
2. Dahan, A.; Miller, J.M.; Amidon, G.L. Prediction of solubility and permeability class membership: Provisional BCS classification of the world's top oral drugs. *AAPS J.* **2009**, *11*, 740–746. [CrossRef]
3. De Clercq, E.; Li, G. Approved Antiviral Drugs over the Past 50 Years. *Clin. Microbiol. Rev.* **2016**, *29*, 695–747. [CrossRef]
4. Center for Disease Control and Prevention. Available online: https://www.cdc.gov/flu/weekly/index.htm (accessed on 15 September 2023).
5. Samson, M.; Pizzorno, A.; Abed, Y.; Boivin, G. Influenza virus resistance to neuraminidase inhibitors. *Antivir. Res.* **2013**, *98*, 174–185. [CrossRef]
6. Holmes, E.H.; Devalapally, H.; Li, L.; Perdue, M.L.; Ostrander, G.K. Permeability enhancers dramatically increase zanamivir absolute bioavailability in rats: Implications for an orally bioavailable influenza treatment. *PLoS ONE* **2013**, *8*, e61853. [CrossRef] [PubMed]
7. Li, W.; Escarpe, P.A.; Eisenberg, E.J.; Cundy, K.C.; Sweet, C.; Jakeman, K.J.; Merson, J.; Lew, W.; Williams, M.; Zhang, L.; et al. Identification of GS 4104 as an orally bioavailable prodrug of the influenza virus neuraminidase inhibitor GS 4071. *Antimicrob. Agents Chemother.* **1998**, *42*, 647–653. [CrossRef]
8. Miller, J.M.; Dahan, A.; Gupta, D.; Varghese, S.; Amidon, G.L. Enabling the intestinal absorption of highly polar antiviral agents: Ion-pair facilitated membrane permeation of zanamivir heptyl ester and guanidino oseltamivir. *Mol. Pharm.* **2010**, *7*, 1223–1234. [CrossRef]
9. Ploger, G.F.; Hofsass, M.A.; Dressman, J.B. Solubility Determination of Active Pharmaceutical Ingredients Which Have Been Recently Added to the List of Essential Medicines in the Context of the Biopharmaceutics Classification System-Biowaiver. *J. Pharm. Sci.* **2018**, *107*, 1478–1488. [CrossRef]
10. Debotton, N.; Garsiani, S.; Cohen, Y.; Dahan, A. Enabling oral delivery of antiviral drugs: Double emulsion carriers to improve the intestinal absorption of zanamivir. *Int. J. Pharm.* **2022**, *629*, 122392. [CrossRef]
11. Colman, P.M. Zanamivir: An influenza virus neuraminidase inhibitor. *Expert. Rev. Anti Infect. Ther.* **2005**, *3*, 191–199. [CrossRef]
12. Food and Drug Administration. Available online: https://www.accessdata.fda.gov/drugsatfda_docs/label/2006/021036s008lbl.pdf#:~:text=Pharmacokinetics%3A%20Absorption%20and%20Bioavailability%3A%20Pharmacokinetic%20studies%20of%20orally,17%25%20of%20the%20inhaled%20dose%20is%20systemically%20absorbed (accessed on 19 September 2023).
13. Food and Drug Administration. Available online: https://www.accessdata.fda.gov/drugsatfda_docs/label/2018/021036s030lbl.pdf (accessed on 19 September 2023).
14. Palmer, R. Drugs: Lines of defence. *Nature* **2011**, *480*, S9–S10. [CrossRef]
15. Babadi, D.; Dadashzadeh, S.; Osouli, M.; Daryabari, M.S.; Haeri, A. Nanoformulation strategies for improving intestinal permeability of drugs: A more precise look at permeability assessment methods and pharmacokinetic properties changes. *J. Control. Release* **2020**, *321*, 669–709. [CrossRef] [PubMed]
16. Li, C.; Wang, J.; Wang, Y.; Gao, H.; Wei, G.; Huang, Y.; Yu, H.; Gan, Y.; Wang, Y.; Mei, L.; et al. Recent progress in drug delivery. *Acta Pharm. Sin. B* **2019**, *9*, 1145–1162. [CrossRef]
17. Lembo, D.; Cavalli, R. Nanoparticulate delivery systems for antiviral drugs. *Antivir. Chem. Chemother.* **2010**, *21*, 53–70. [CrossRef] [PubMed]
18. Nakano, M. Places of emulsions in drug delivery. *Adv. Drug Deliv. Rev.* **2000**, *45*, 1–4. [CrossRef] [PubMed]
19. Chaudhary, S.; Aqil, M.; Sultana, Y.; Kalam, M.A. Self-nanoemulsifying drug delivery system of nabumetone improved its oral bioavailability and anti-inflammatory effects in rat model. *J. Drug Deliv. Sci. Technol.* **2019**, *51*, 736–745. [CrossRef]

20. Ritschel, W.A. Microemulsion technology in the reformulation of cyclosporine: The reason behind the pharmacokinetic properties of Neoral. *Clin. Transplant.* **1996**, *10*, 364–373.
21. Shaikh, M.S.; Derle, N.D.; Bhamber, R. Permeability Enhancement Techniques for Poorly Permeable Drugs: A Review. *J. Appl. Pharm. Sci.* **2012**, *2*, 34–39. [CrossRef]
22. Lv, L.Z.; Tong, C.Q.; Lv, Q.; Tang, X.J.; Li, L.M.; Fang, Q.X.; Yu, J.; Han, M.; Gao, J.Q. Enhanced absorption of hydroxysafflor yellow A using a self-double-emulsifying drug delivery system: In vitro and in vivo studies. *Int. J. Nanomed.* **2012**, *7*, 4099–4107.
23. Padole, A.; Bodhankar, M. Self Double Emulsifying Drug Delivery System (Sdedds): A Review. *J. Drug Deliv. Ther.* **2012**, *2*, 124–127. [CrossRef]
24. Qi, X.; Wang, L.; Zhu, J.; Hu, Z.; Zhang, J. Self-double-emulsifying drug delivery system (SDEDDS): A new way for oral delivery of drugs with high solubility and low permeability. *Int. J. Pharm.* **2011**, *409*, 245–251. [CrossRef] [PubMed]
25. Akhtar, M.; Murray, B.S.; Afeisume, E.I.; Khew, S.H. Encapsulation of flavonoid in multiple emulsion using spinning disc reactor technology. *Food Hydrocoll.* **2014**, *34*, 62–67. [CrossRef]
26. Garti, N.; Bisperink, C. Double emulsions: Progress and applications. *Curr. Opin. Colloid. Interface Sci.* **1998**, *3*, 657–667. [CrossRef]
27. Sapei, L.; Naqvi, M.A.; Rousseau, D. Stability and release properties of double emulsions for food applications. *Food Hydrocoll.* **2012**, *27*, 316–323. [CrossRef]
28. Hashim, A.A. *Smart Nanoparticles Technology*; InTech: Rijeka, Croatia, 2012; pp. 195–220.
29. Li, Y.; Song, J.; Tian, N.; Cai, J.; Huang, M.; Xing, Q.; Wang, Y.; Wu, C.; Hu, H. Improving oral bioavailability of metformin hydrochloride using water-in-oil microemulsions and analysis of phase behavior after dilution. *Int. J. Pharm.* **2014**, *473*, 316–325. [CrossRef]
30. Kumar, S.H.; Singh, V. Nanoemulsification-a novel targeted drug delivery tool. *J. Drug Deliv. Ther.* **2012**, *2*, 40–45. [CrossRef]
31. Stauff, J. Solvent Properties of Amphiphilic Compounds, von P. A. Winsor. Butterworths Scientific Publ. Ltd.: London. 1954. 1. Aufl. IX, 270 S., gebd. 40 s. *Angew. Chem.* **1956**, *68*, 504. [CrossRef]
32. Healy, R.N.; Reed, R.L.; Stenmark, D.G. Multiphase Microemulsion Systems. *Soc. Pet. Eng. J.* **1976**, *16*, 147–160. [CrossRef]
33. Vasconcelos, T.; Marques, S.; Sarmento, B. Measuring the emulsification dynamics and stability of self-emulsifying drug delivery systems. *Eur. J. Pharm. Biopharm.* **2018**, *123*, 1–8. [CrossRef]
34. Williams, H.D.; Sassene, P.; Kleberg, K.; Bakala-N'Goma, J.C.; Calderone, M.; Jannin, V.; Igonin, A.; Partheil, A.; Marchaud, D.; Jule, E.; et al. Toward the establishment of standardized in vitro tests for lipid-based formulations, part 1: Method parameterization and comparison of in vitro digestion profiles across a range of representative formulations. *J. Pharm. Sci.* **2012**, *101*, 3360–3380. [CrossRef]
35. Netanel Liberman, G.; Ochbaum, G.; Malis Arad, S.; Bitton, R. The sulfated polysaccharide from a marine red microalga as a platform for the incorporation of zinc ions. *Carbohydr. Polym.* **2016**, *152*, 658–664. [CrossRef] [PubMed]
36. Tamhane, V.A.; Dhaware, D.G.; Khandelwal, N.; Giri, A.P.; Panchagnula, V. Enhanced permeation, leaf retention, and plant protease inhibitor activity with bicontinuous microemulsions. *J. Colloid Interface Sci.* **2012**, *383*, 177–183. [CrossRef]
37. Cao, Q.; Wu, H.; Zhu, L.; Wu, D.; Zhu, Y.; Zhu, Z.; Cui, J. Preparation and evaluation of zanamivir-loaded solid lipid nanoparticles. *J. Control. Release* **2011**, *152* (Suppl. S1), e2–e4. [CrossRef] [PubMed]
38. Shi, L.L.; Cao, Y.; Zhu, X.Y.; Cui, J.H.; Cao, Q.R. Optimization of process variables of zanamivir-loaded solid lipid nanoparticles and the prediction of their cellular transport in Caco-2 cell model. *Int. J. Pharm.* **2015**, *478*, 60–69. [CrossRef]
39. Miller, J.M.; Beig, A.; Carr, R.A.; Spence, J.K.; Dahan, A. A win-win solution in oral delivery of lipophilic drugs: Supersaturation via amorphous solid dispersions increases apparent solubility without sacrifice of intestinal membrane permeability. *Mol. Pharm.* **2012**, *9*, 2009–2016. [CrossRef]
40. Gupta, S.V.; Gupta, D.; Sun, J.; Dahan, A.; Tsume, Y.; Hilfinger, J.; Lee, K.D.; Amidon, G.L. Enhancing the intestinal membrane permeability of zanamivir: A carrier mediated prodrug approach. *Mol. Pharm.* **2011**, *8*, 2358–2367. [CrossRef] [PubMed]
41. Hoppel, M.; Reznicek, G.; Kählig, H.; Kotisch, H.; Resch, G.P.; Valenta, C. Topical delivery of acetyl hexapeptide-8 from different emulsions: Influence of emulsion composition and internal structure. *Eur. J. Pharm. Sci.* **2015**, *68*, 27–35. [CrossRef] [PubMed]
42. Shimanouchi, T.; Hayashi, T.; Toramoto, K.; Fukuma, S.; Hayashi, K.; Yasuhara, K.; Kimura, Y. Microfluidic and hydrothermal preparation of vesicles using sorbitan monolaurate/polyoxyethylene (20) sorbitan monolaurate (Span 20/Tween 20). *Colloids Surf. B Biointerfaces* **2021**, *205*, 111836. [CrossRef]
43. Dave, V.S.; Gupta, D.; Yu, M.; Nguyen, P.; Varghese Gupta, S. Current and evolving approaches for improving the oral permeability of BCS Class III or analogous molecules. *Drug Dev. Ind. Pharm.* **2017**, *43*, 177–189. [CrossRef]
44. Spinks, C.B.; Zidan, A.S.; Khan, M.A.; Habib, M.J.; Faustino, P.J. Pharmaceutical characterization of novel tenofovir liposomal formulations for enhanced oral drug delivery: In vitro pharmaceutics and Caco-2 permeability investigations. *Clin. Pharmacol. Adv. Appl.* **2017**, *9*, 29–38. [CrossRef]
45. Gupta, S.; Chavhan, S.; Sawant, K.K. Self-nanoemulsifying drug delivery system for adefovir dipivoxil: Design, characterization, in vitro and ex vivo evaluation. *Colloids Surf. A Physicochem. Eng. Asp.* **2011**, *392*, 145–155. [CrossRef]
46. Koneva, A.; Safonova, E.; Kondrakhina, P.; Vovk, M.; Lezov, A.; Chernyshev, Y.S.; Smirnova, N. Effect of water content on structural and phase behavior of water-in-oil (n-decane) microemulsion system stabilized by mixed nonionic surfactants SPAN 80/TWEEN 80. *Colloids Surf. A Physicochem. Eng. Asp.* **2017**, *518*, 273–282. [CrossRef]
47. World Health Organization. Available online: https://apps.who.int/iris/handle/10665/62169 (accessed on 15 September 2023).

48. Komatsu, H.; Kitajima, A.; Okada, S. Pharmaceutical characterization of commercially available intravenous fat emulsions: Estimation of average particle size, size distribution and surface potential using photon correlation spectroscopy. *Chem. Pharm. Bull.* **1995**, *43*, 1412–1415. [CrossRef] [PubMed]
49. Baloch, J.; Sohail, M.F.; Sarwar, H.S.; Kiani, M.H.; Khan, G.M.; Jahan, S.; Rafay, M.; Chaudhry, M.T.; Yasinzai, M.; Shahnaz, G. Self-nanoemulsifying drug delivery system (SNEDDS) for improved oral bioavailability of chlorpromazine: In vitro and in vivo evaluation. *Medicina* **2019**, *55*, 210. [CrossRef]
50. Hu, C.; Zhao, G.; Xia, Q.; Sun, R. Development and characterization of a self-double-emulsifying drug delivery system containing both epigallocatechin-3-gallate and α-lipoic acid. *J. Mater. Sci.* **2015**, *50*, 6567–6577. [CrossRef]
51. Boonyapiwat, B.; Sarisuta, N.; Kunastitchai, S. Characterization and in vitro evaluation of intestinal absorption of liposomes encapsulating zanamivir. *Curr. Drug Deliv.* **2011**, *8*, 392–397. [CrossRef]
52. Beig, A.; Fine-Shamir, N.; Lindley, D.; Miller, J.M.; Dahan, A. Advantageous solubility-permeability interplay when using amorphous solid dispersion (ASD) formulation for the BCS class IV P-gp substrate rifaximin: Simultaneous increase of both the solubility and the permeability. *AAPS J.* **2017**, *19*, 806–813. [CrossRef]
53. El-Kattan, A.; Varma, M. Oral absorption, intestinal metabolism and human oral bioavailability. *Top. Drug Metab.* **2012**, *10*, 31087.
54. Yu, H.; Wang, Q.; Sun, Y.; Shen, M.; Li, H.; Duan, Y. A new PAMPA model proposed on the basis of a synthetic phospholipid membrane. *PLoS ONE* **2015**, *10*, e0116502. [CrossRef]
55. Zur, M.; Cohen, N.; Agbaria, R.; Dahan, A. The biopharmaceutics of successful controlled release drug product: Segmental-dependent permeability of glipizide vs. metoprolol throughout the intestinal tract. *Int. J. Pharm.* **2015**, *489*, 304–310. [CrossRef]
56. Guo, S.; Huang, L. Nanoparticles containing insoluble drug for cancer therapy. *Biotechnol. Adv.* **2014**, *32*, 778–788. [CrossRef] [PubMed]
57. Hua, S. Lipid-based nano-delivery systems for skin delivery of drugs and bioactives. *Front. Pharmacol.* **2015**, *6*, 219. [CrossRef] [PubMed]

pharmaceutics

MDPI

Article

A Multivariate Meta-Analysis for Optimizing Cell Counts When Using the Mechanical Processing of Lipoaspirate for Regenerative Applications

Gershon Zinger [1,*,†], Nia Kepes [2], Ron Kenett [3,4], Amos Peyser [5] and Racheli Sharon-Gabbay [1,†]

[1] Hand Unit, Department of Orthopedic Surgery, Shaare Zedek Medical Center, Faculty of Medicine, Hebrew University of Jerusalem, Jerusalem 91120, Israel; rachelish@szmc.org.il
[2] Department of Neuroscience, Michigan State University Lyman Briggs College, East Lansing, MI 48824, USA; kepesnia@msu.edu
[3] The KPA Group, Ra'anana 4353701, Israel; ron@kpa-group.com
[4] The Samuel Neaman Institute, Technion, Haifa 3200003, Israel
[5] Department of Orthopedic Surgery, Shaare Zedek Medical Center, Faculty of Medicine, Hebrew University of Jerusalem, Jerusalem 91120, Israel; amosp@szmc.org.il
* Correspondence: gershonzinger@szmc.org.il
† These authors contributed equally to this work.

Abstract: Lipoaspirate has become the preferred source for regenerative cells. The mechanical processing of lipoaspirate has advantages over enzymatic processing but has a lower yield of regenerative cells. A review of the literature shows different techniques of extraction, but the ideal method or combination has not been determined. Methods: A comprehensive literature search was focused on the mechanical processing of lipoaspirate, without the use of enzymes. Data from the articles were integrated by utilizing a multivariate meta-analysis approach and used to create a statistical-based predictive model for a combination of multiple variables. Results: Starting with 10,000 titles, 159 articles were reviewed, and 6 met the criteria for inclusion and exclusion. The six studies included data on 117 patients. Sixteen factors were analyzed and six were identified as significant. The predictive profilers indicated that the optimal combination to maximize the cell yield was: a centrifuge force of 2000× *g*, a centrifuge time of 10 min, a cannula diameter of 2 mm, and an intra-syringe number of passes of 30. The optimal patient factors were a higher BMI and younger age. Conclusions: The novelty of the method used here was in combining data across different studies to understand the effect of the individual factors and in the optimization of their combination for mechanical lipoaspirate processing.

Keywords: lipoaspirate; mechanical processing; meta-analysis; multivariate; optimization; JMP®

1. Introduction

Adipose tissue is an abundant and easily accessible source of mesenchymal stem cells (MSCs) [1]. MSCs have the potential to differentiate into a variety of cell types and play a significant role in tissue regeneration [2]. The quality and quantity of MSCs obtained from lipoaspirate are highly dependent on the processing method used. Enzymatic methods using collagenase produce the greatest yield of regenerative cells [3]. However, enzymatic methods have disadvantages that include regulatory restrictions (FDA guidance, 2014b,c), the cost, and the time needed for processing [3]. Many mechanical methods have been proposed for lipoaspirate processing [4], but the optimal method or combination of methods remain unclear.

The yield of MSCs from lipoaspirate is affected by many processing factors. Understanding the effect of the different processing methods on the MSCs yield is crucial for the design of a multi-factor intervention technique. In this study, a set of statistical tools was used that combined evidence from published studies, in an approach that resembles a meta-analysis [5]. In general, a meta-analysis typically aims at deriving aggregate measures such as odds ratios, which is considered controversial by the medical community [6]. In a traditional meta-analysis,

effect sizes from studies that address the same research question are pooled together. Advances in multivariate meta-analysis can estimate outcome-specific effects for multiple outcomes [7] and for multiple factors that synthesize available factors simultaneously [8].

A multi-variate meta-analysis using JMP® software (Version 16 Pro) was used to create a model that predicts the ideal combination of methods to optimize the highest cell count for the mechanical processing of lipoaspirate.

2. Materials and Methods

2.1. Study Design

A comprehensive literature search was conducted using PRISMA guidelines [9] on PubMed, from 1 January 2000 to 26 April 2023. The search was performed using the search phrase: "isolation" or "method" or "mechanical" or "dissociation" AND ("lipoaspirate" or "adipose"). The inclusion criteria included studies published in English that evaluated mechanical methods of subcutaneous lipoaspirate processing and reported outcome data that included the nucleated cell count. The exclusion criteria included articles that evaluated enzymatic methods for either processing or for counting, review articles, primary animal studies, cell counts after culturing, sources other than subcutaneous, and those reporting only clinical outcomes (Scheme 1). The senior author (GZ) performed the initial title screening. Two investigators (RS and NK) independently reviewed all abstracts. The goal at this screening stage was to be inclusive of any potential studies that met the inclusion criteria. After removing studies that, from the abstracts, met the exclusion criteria, full texts of the remaining studies were retrieved. The full texts were assessed based on the same inclusion and exclusion criteria, but the detail allowed for a more accurate screening.

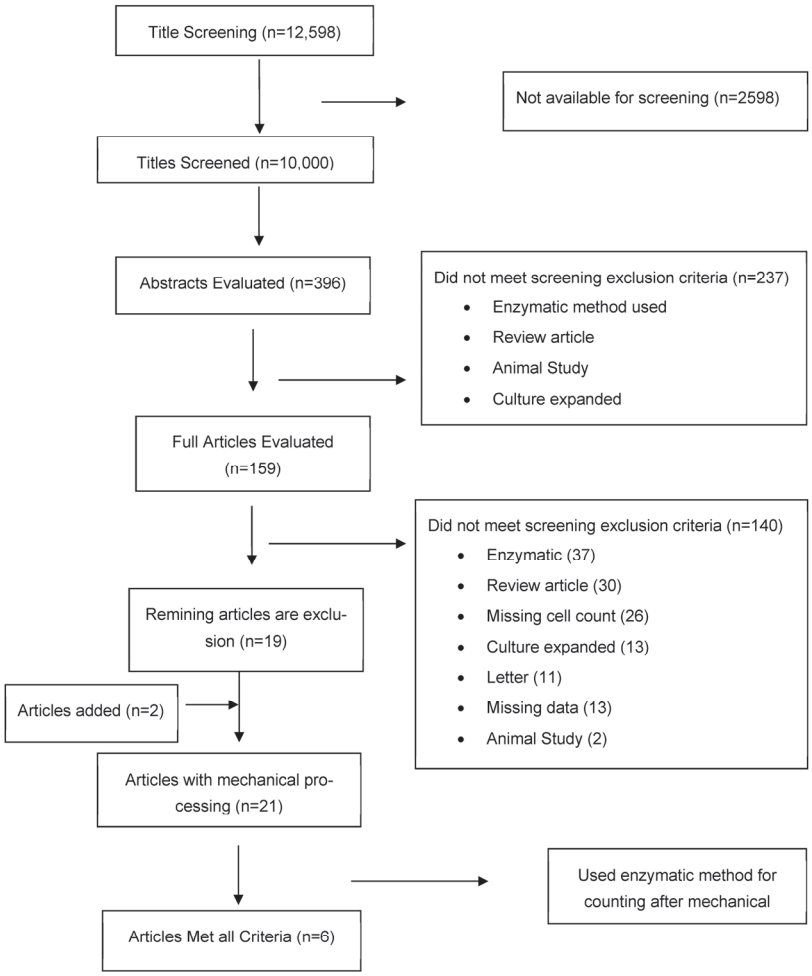

Scheme 1. Flow diagram.

2.2. Data Extraction and Outcome Normalization

The data were extracted into a spreadsheet, with the factors identified during the articles review (Table 1). This included patient characteristics such as age and sex (Table 2), surgeon-chosen factors such as the cannula size and liposuction site, and the methods used for mechanical processing (Table 3). The outcomes measure (response) was the nucleated cell count concentration. These data were independently extracted (RS and NK) and then compared. Disagreement was resolved by consensus. All data were then reviewed to confirm accuracy (RS and GZ).

Table 1. List of the six articles that were included in this review and analysis.

Article	Title	Reference
Cicione, 2016	In vitro validation of a closed device enabling the purification of the fluid portion of liposuction aspirates	[10]
Chaput, 2016	Mechanically Isolated Stromal Vascular Fraction Provides a Valid and Useful Collagenase-Free Alternative Technique: A Comparative Study	[11]
Mashiko, 2017	Mechanical Micronization of Lipoaspirates: Squeeze and Emulsification Techniques	[12]
Tiryaki & Cohen, 2020	In-Vitro Comparative Examination of the Effect of Stromal Vascular Fraction Isolated by Mechanical and Enzymatic Methods on Wound Healing	[13]
Busato, 2020	Simple and Rapid Non-Enzymatic Procedure Allows the Isolation of Structurally Preserved Connective Tissue Micro-Fragments Enriched with SVF	[14]
Tiryaki & Condé-Green, 2020	A 3-step Mechanical Digestion Method to Harvest Adipose-derived Stromal Vascular Fraction	[15]

Table 2. Patient characterization from the six articles.

Article	Donors	Gender	Average Age	Average BMI
Cicione, 2016 [10]	14	M/F	43	26.9
Chaput, 2016 [11]	21	M/F	37.8	26.5
Mashiko, 2017 [12]	10	F	41	21.8
Tiryaki & Cohen, 2020 [13]	10	F	39	26
Busato, 2020 [14]	27	F	55	28
Tiryaki & Condé-Green, 2020 [15]	35	F	39	26

Table 3. Mechanical factors summary for the aspiration and processing of the lipoaspirate.

Article	Setup	Lipo Site	Cannula Diameter	Device/Kit Name	Centrifuge Force (g)	Centrifuge Time (min)
Cicione, 2016 [10]	1	N/A *	N/A *	No	400	10
	2	N/A *	N/A *	MyStem	200	5
Chaput, 2016 [11]	1	Abdomen	4	No	558	10
	2	Abdomen	4	No	558	10
Mashiko, 2017 [12]	1	Thigh	3	No	1200	3
Tiryaki & Cohen, 2020 [13]	1	Hip	2	Lipocube	2000	10
Busato, 2020 [14]	1	Abdomen	2.38	Hy-Tissue SVF kit	400	10
Tiryaki & Condé-Green, 2020 [15]	1	Thigh	2	Lipocube	2000	10

* N/A data not available.

To enable the comparison between the different studies, the cell count results were normalized relative to the volume of the initial liposuction aspirate, as shown in Table 4. In some cases, this was calculated from the information provided in the text. If the starting lipoaspirate volume was unavailable, the corresponding author was contacted and in all cases was able to provide these critical data to allow for a comparison between the studies.

Table 4. Summary of cells count results and the normalization calculation.

Article	Setup	Lipoaspirate Volume (mL)	Cells Count as Published	Cells Count Unit	SVF Volume (mL)	Normalized (Cells/mL of Lipoaspirate)
Cicione, 2016 [10]	1	33.5 *	800,000	Cells	Not required	23,881
	2	33.5 *	2,200,000	Cells		65,672
Chaput, 2016 [11]	1	20 (the fat fraction was 50% of all Lipoaspirate)	90,000	Cells/mL of fat	Not required	45,000 **
	2	20	35,000	Cells/mL		17,500
Mashiko, 2017 [12]	1	59	150,000	Cells/mL	6.7	19,305
Tiryaki & Cohen, 2020 [13]	1	40	940,000	Cells/mL	5	117,500
Busato, 2020 [14]	1	30	41,000	Cells/mL of lipoaspirate	1	41,000
Tiryaki & Condé-Green, 2020 [15]	1	40	1,340,000	Cells/mL	5	167,500

* Average volume. ** Fat was 50% of the lipoaspirate.

In addition, the data included the statistical methods used to analyze the results, the sample size, the type and value of results, and the error and the *p*-values, which were extracted into the summary tables.

2.3. Multivariate Meta-Analysis Involving Multiple Factors

2.3.1. Impact of Missing Data

The presence of missing data negatively influences the fitting of statistical models. Corresponding authors were contacted to provide any missing data. For some factors, some information remained unavailable. Specifically, only one study exhibited some missing data, while five studies provided a complete set of the factors (Table 3). Prior to conducting the statistical analysis, we applied an "Automated Data Imputation" feature using JMP® software (version 16 Pro, SAS Institute (Cary, NC, USA) for the remaining missing data. This method utilized the mean values of the factors to impute the missing data points.

2.3.2. Result Standardization

In this study, the primary focus was on assessing and optimizing the yield of nucleated cells obtained through the mechanical processing of lipoaspirate, referred to here as the response variable (y). As demonstrated in Table 4, the reported results are presented in various units, making direct comparisons challenging. To facilitate the comparison of the cell count yields across different articles (Table 1) and to conduct statistical analyses, the data were standardized. The standardization process consisted of calculating normalized cell counts, which represent the nucleated cell count yield relative to the initial lipoaspirate volume (Table 4).

2.3.3. Multivariate Analysis

A multivariate regression analysis was conducted using JMP® software, with the response variable (y) representing the normalized yield of nucleated cells per mL of starting lipoaspirate obtained through the mechanical processing. The results obtained from the literature search were used as the experimental array. If, for example, two mechanical methods were used in the same article, these two methods were considered as separate in

the experimental array. The 16 experimental factors (x) are listed in Table 5. The sample size of each study was used in JMP® as the modeling frequency.

Table 5. The experimental factors.

Patient Characteristics:
1. Sex
2. Age
3. BMI
Factors under surgeon control:
4. Anesthesia volume
5. Cannula type (length, diameter)
6. Liposuction site
7. Lipoaspirate method
8. Wash fluid type
9. Wash volume
10. Decantation time
11. Centrifuge time and force
12. Intra-syringe number of passes
13. Processing method used first
14. Filtration method
Other factors:
15. Processing device or kit
16. Method used for cell count

Two distinct models, the Standard Least Squares and the Mixed models, were fitted and assessed for their goodness of fit. The Least Squares model is used to determine the best-fitting line or curve for a set of data points. The objective is to minimize the sum of the squared vertical distances between the actual data points and the corresponding points predicted by the model. This entails adjusting the parameters of a chosen model (such as the slope and intercept of a line) to minimize the sum of squared differences. Widely employed in regression analysis, this method is instrumental in revealing the most accurate relationship between variables, particularly when dealing with data variability or noise. The Least Squares model is limited by its sensitivity to outliers and the reliance on sufficient data [16].

A Mixed model, or mixed-effects model, is an extension of linear models that incorporates both fixed effects and random effects. The Mixed model is particularly useful when dealing with nested or repeated measurements. While Mixed models offer flexibility, they present challenges. They require a careful balance between fixed and random effects, and the estimation process can be computationally intensive. Additionally, assumptions about the random effects' distribution need consideration, and determining the appropriate level of complexity can require experience. Despite these challenges, mixed models are valuable for handling diverse data structures, providing a more realistic representation of complex relationships [17].

The Standard Least Squares model included variance analysis, an assessment of factors' importance, and the identification of critical factors. The Mixed model incorporates random effects to account for variability across the different studies and fixed effects related to the factors under investigation (Table 5). The Mixed model includes random effects covariance analysis with respect to the article name and fixed effects analysis for the factors: BMI, age, centrifuge time, centrifuge force, cannula diameter, and intra-syringe pass count.

When considering the effect of the study factor on the output variable, critical factors are defined as those that exhibited a p value < 0.001. Important factors are defined as those with $0.001 < p < 0.05$. Factors that exhibited an importance score with a p-value > 0.05 were considered as not important and excluded from the model.

For the Mixed model, a conditional residual quantile plot, a useful diagnostic tool in regression analysis, was generated for assessing the model's fit. In addition, an Actual by Predicted plot was also made to visually assess the performance of the predictive model. The visual assessment is an effective tool for comparing the actual (observed) values of the dependent variable with the predicted values generated by the model.

For both the Standard Least Squares and the Mixed models, the Prediction Profiler was used to predict the performance of factor combinations that were not used in any of the studies reviewed. The Predictive Profiler was used to identify the combination of factors that maximized the outcome measure—in this case, the nucleated cell count concentration. The JMP® Profiler enables the simultaneous optimization of multiple factors for the output variable while considering the impact of noise on the analysis [18].

2.3.4. Setup-Related Bias

The JMP® Design Evaluation is a tool that is used to determine whether the experiment is designed properly. This tool evaluates if there are sufficient data spread over the experimental array to build a reliable model [19]. In this study, the JMP® Design Evaluation tool was used to quantify the bias (percent error) after the model was created. To visualize the study performance (percent reliability), a Fraction of Design Space plot was employed. Furthermore, the models' performance was assessed through power and prediction variances [20]. These are post hoc evaluations and have limited interpretation.

3. Results

The systematic review yielded 12,598 references (Scheme 1). PubMed truncates after 10,000 titles. Therefore, only the first 10,000 titles were manually screened, and 396 abstracts were evaluated. None of the last 2800 titles of the 10,000 screened were already relevant. After a review of the complete abstracts, or if the abstract was unavailable, full articles were reviewed. Additional articles were identified during the review process. A total of 159 articles were chosen for full text review by two independent reviewers. From these, only six met the criteria and were included in this systematic review and analysis (Table 1). These six articles included data on 117 volunteers. These six articles were mined for data extraction and for subsequent analysis. Of the six articles, two articles, Cicione [10] and Chaput [11], each used two separate mechanical methods for processing. Therefore, these two articles were counted as four experiments in the array. Overall, the array included eight experiments used in the multivariate regression analysis. The patient characteristics are summarized in Table 2, and the mechanical factors are summarized in Table 3. A summary of the normalized cell counts is given in Table 4.

3.1. Multivariate Regression Analysis

In this study, 16 factors that could affect the nucleated cell count concentration were evaluated (Table 5). Multivariate regression analysis was used to study the association between the factors and the cell count. Two different models were fitted: Standard Least Squares and Mixed models. From the initial 16 factors, 6 were found to be significant ($p < 0.05$) and included in the regression analysis (Figure 1). In addition, all six factors were identified as critical ($p < 0.001$): two patient-related and four mechanical factors.

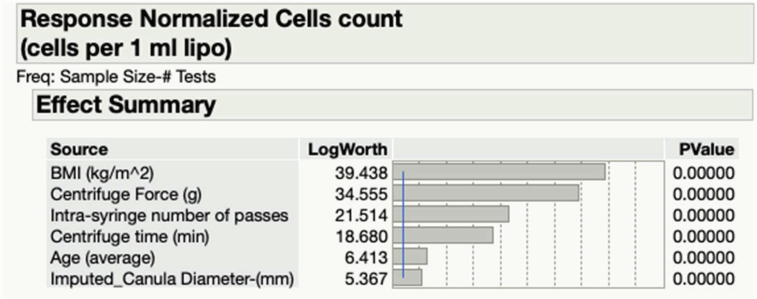

Figure 1. Effect summary report. Assessment of factors' importance by the Standard Least Squares model. # refers to number of tests performed. Blue vertical line denotes LogWorth = 2 = *p*-value 0.01.

Figures 2 and 3 are the Actual by Predicted plots that visually demonstrate the performance of both models, the Standard Least Squares and Mixed models, respectively. Each data point, on these plots, corresponds to an observation from the data presented in Tables 2 and 3. For the Standard Least Squares model (Figure 2), all the data points align along the 45-degree diagonal red line, signifying that the actual values match the predicted values, indicating a high model accuracy (R^2 = 0.97, *p* value < 0.001). For the Mixed model, the evaluation of the pattern and deviation of the data points in Figure 3 shows that the Mixed model's predictions do not align optimally with the actual outcomes. This departure from the diagonal line suggests the presence of potential systematic errors or biases in the model's predictions. These discrepancies may be linked to the limited dataset and random effects stemming from variations between articles.

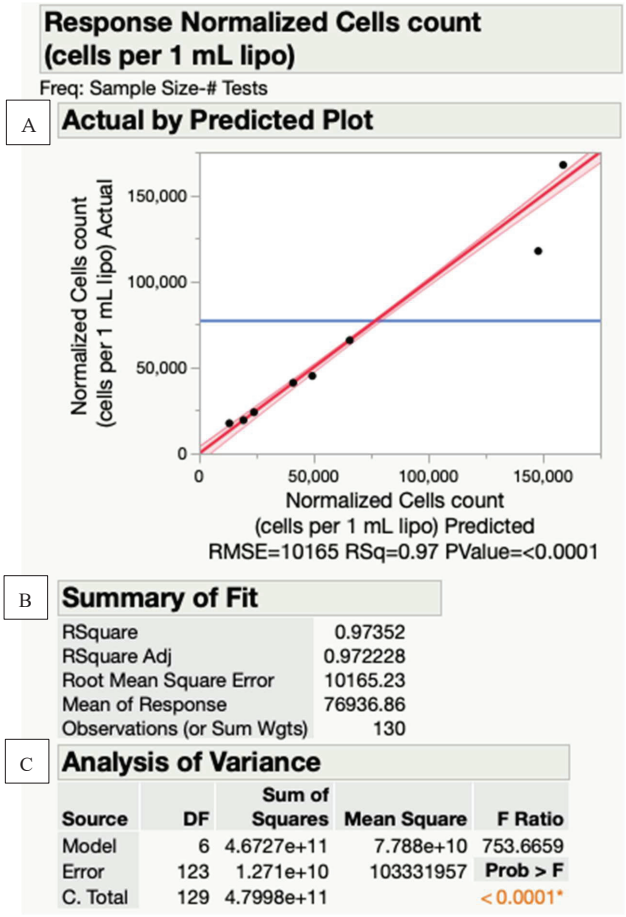

Figure 2. Assessment of the Least Squares model. Actual by Predicted plot (**A**), summary of fit (**B**), and analysis of variance (**C**). # refers to number of tests performed. * statistically significant.

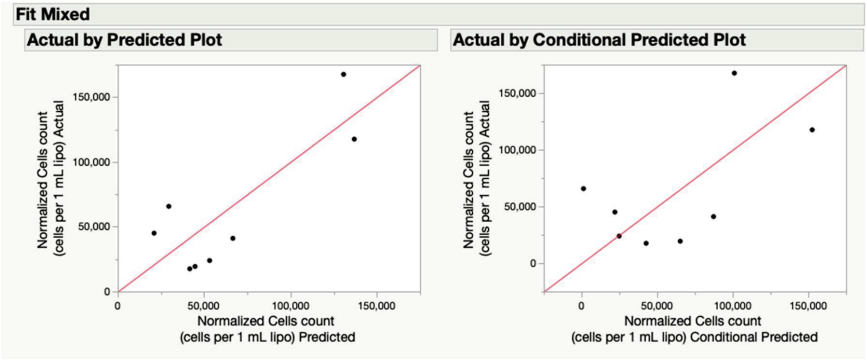

Figure 3. Actual by Predicted plot as generated by the Mixed model with (**right**) and without (**left**) the assumption of random effects.

In addition, the Mixed model's performance was also assessed through the distribution of the residuals (the difference between the actual and the predicted value; Figure 4), with constant variance across different levels of the factors. The residuals exhibited a consistent pattern across different factors. This suggests that the Mixed model adequately captured the relationship between the factors and the response variable for those conditions. The spread of residual points around the diagonal line was consistent along the line, confirming homoscedasticity (constant variance of residuals). These findings confirm that the Mixed model exhibited good suitability and effectiveness.

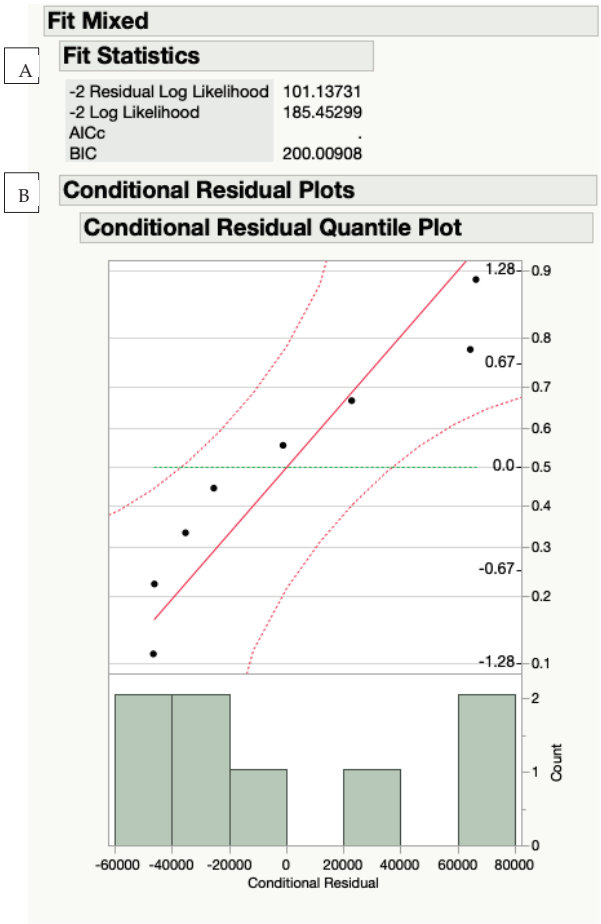

Figure 4. Assessment of the fit of a Mixed model regression. Summary of fit statistic (**A**) and conditional residual quantile plot (**B**) that investigate the distribution of the differences between observed and predicted values under different levels of factors.

3.2. Setup-Related Bias

While the Evaluation of Study Design is typically applied in the context of DOE ahead of the data collection, in this study, its purpose was to evaluate the viability of conducting this multivariate meta-analysis with just six articles (eight experiments). The power analysis yielded a *p*-value of less than 0.05, and the expected root mean squared error (RMSE) was estimated to be 1. When assessing the study design using the Fraction of Design Space plot (Figure 5), it revealed an 80% accuracy probability for the predictive models. In other words, there is a 20% chance that the model is biased and will not accurately predict the optimal mechanical combination.

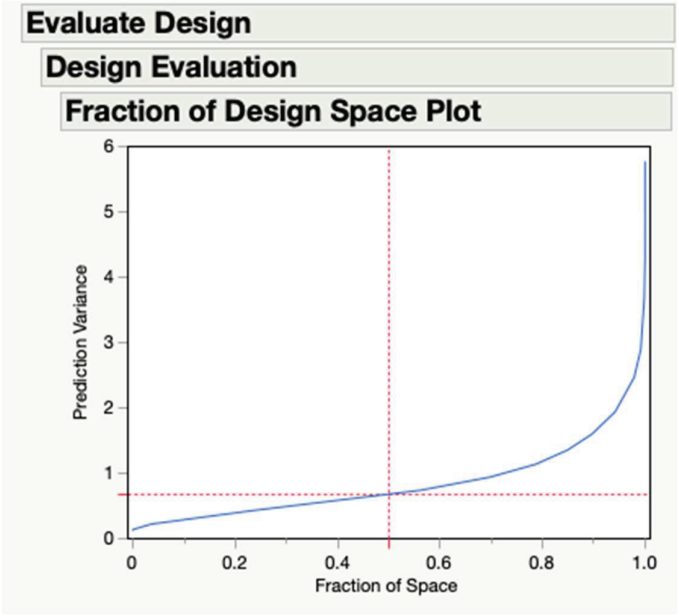

Figure 5. Assessing study design evaluation by a Fraction of Design Space plot. A total of 80% of the fraction of space is less then the prediction variance of 1.

3.3. Maximizing the Cell Count in Lipoaspirate Processing

To forecast the ideal combination of factors for maximizing the cell count, predictive profilers were generated based on the Least Squares and Mixed models. An example of a profiler setting is presented in Figures 6 and 7, respectively. In these figures, the predicted model is represented by the black line, while the blue lines depict the statistical confidence limits. The vertical red dashed line indicates the setting of the factor value that, when considered in conjunction with other factors, shows the predicted cell count shown by the horizontal red dashed line. For example, in Figure 6, the setting of 10 intra-syringe passes, in combination with the other factor settings, predicts a cell count of 76,937 cells per 1 mL of lipoaspirate. Employing the maximize-desirability function, the optimized setup for achieving the maximum cell count per 1 mL of lipoaspirate is summarized in Table 6. Both models agree regarding the optimal factor values. With the ideal combination of factors (Table 6), the Standard Least Squares model predicts a cell count of 158,631 cells per mL of lipoaspirate, compared to the Mixed model, which predicts 167,529 cells per mL of lipoaspirate, a difference of only 5.3%.

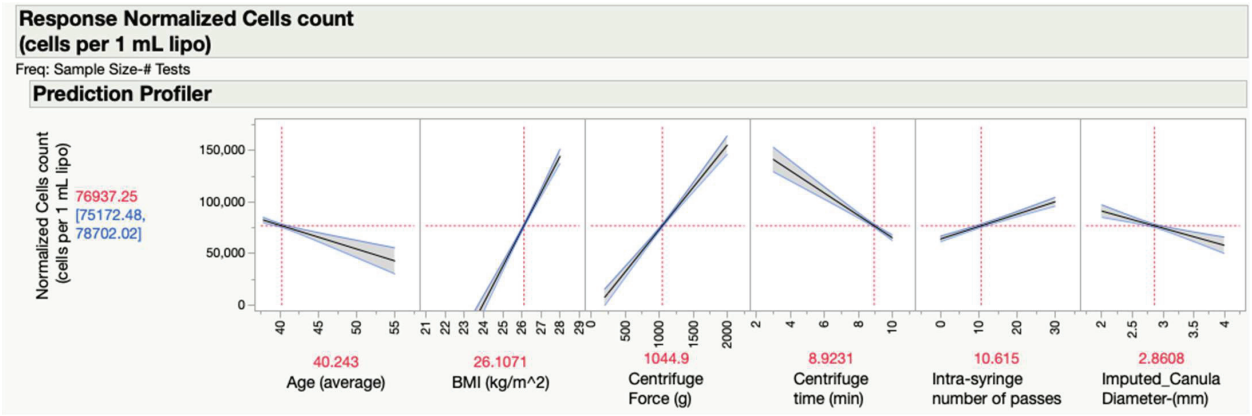

Figure 6. Predictive profiler generated by JMP® software using the fitted least squares model (black curve). The response on the *y*-axis is the normalized cell number per 1 mL of the initial lipoaspirate. The factors affecting the normalized cell number are in the *x*-axis. The blue lines and the grey area are the confidence limits.

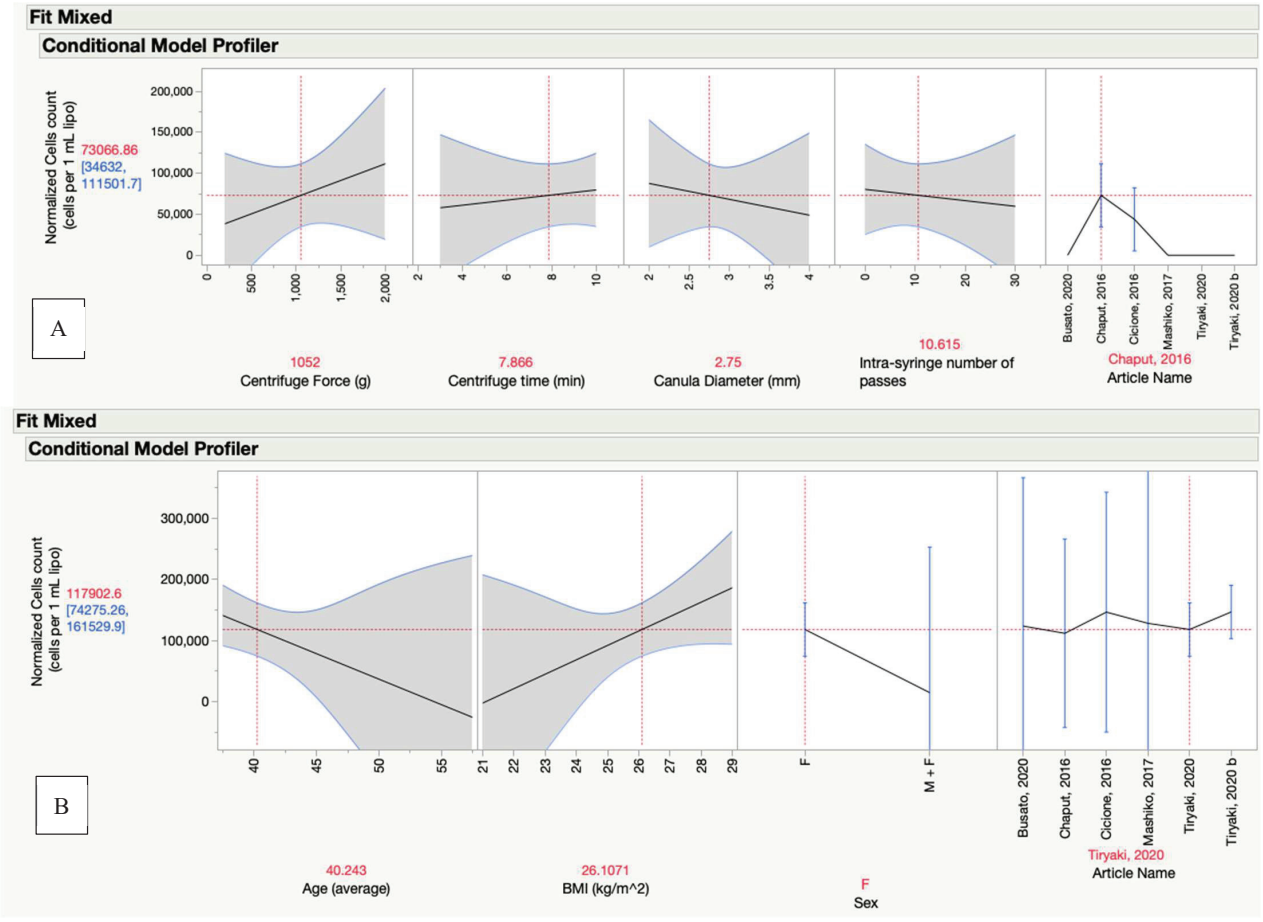

Figure 7. Predictive profiler generated by JMP® software using the fitted Mixed models (black curve) for factors under surgeon control (**A**) and the patient characteristics factors (**B**). The response on the *y*-axis is the normalized cell number per 1 mL of the initial lipoaspirate. The factors affecting the normalized cell number are in the *x*-axis. The blue lines and the grey area are the confidence limits [10–15].

Table 6. The optimized setup for the maximum cell count per 1 mL of lipoaspirate, as predicted by both the Least Squares and Mixed models.

	Centrifuge Force (g)	Centrifuge Time (min)	Canula Diameter (mm)	Intra-Syringe Number of Passes	Predicted Cells per 1 mL of Lipo.
Least Squares model	2000	10	2	30	158,631
Mixed model	2000	10	2	30	167,529

4. Discussion

Mechanical processing offers many advantages over enzymatic methods, including a reduced time and cost and fewer regulatory restrictions. Each of the published articles identified in this systematic review used a different combination of factors for mechanical processing. In this study, a novel method using JMP® software was used to integrate the data from the different studies to create a predictive model that optimizes mechanical processing. The goal for optimization is to maximize the concentration of nucleated cells, an indirect measure of the number of regenerative cells.

The isolation methods of pluripotential mesenchymal cells from adipose tissue at the point of care have direct applications in many fields such as plastic surgery, orthopedic surgery and regenerative medicine. Aronowitz et al. [3] performed a review that compared published articles that used both mechanical and enzymatic methods for processing lipoaspirate. The gold standard remains using proteolytic enzymes to break down the extracellular matrix, releasing the cells into the solution and giving the highest concentration of nucleated cells. In contrast, the stromal vascular fraction (SVF) obtained through mechanical techniques is safe, avoids regulatory restrictions, is more cost-effective, and is less time-consuming. Mechanical methods have some benefits but have a lower yield when compared to enzymatic methods [3]. In this study, we performed a systematic literature review and a multifactorial meta-analysis to identify the best combination of mechanical processing methods to improve the concentration of nucleated cells.

The number of studies that used only mechanical methods of lipoaspirate processing to yield ASCs without the addition of an enzyme is notably scarce. We considered including articles that used mechanical methods for processing but used an enzyme for cell counting but decided that including these studies would give erroneous results. Comparing two mechanical methods where one study used an enzyme for cell counting might theoretically consider one mechanical method as more superior when it was the counting that was more efficient.

This study had two goals. The primary goal was to identify the optimum method of the mechanical processing of lipoaspirate based on the current published data. The second goal was to demonstrate the ability of combining the data from different studies to create a predictive model that would identify this ideal combination. For that purpose, the JMP® statistical software provided a powerful dynamic tool that identified the effect of each factor on the cell count and provided the ideal combination of factors. A similar analysis could be used in a future study to optimize for other outcome measures such as specific phenotypes, cell types, or the differentiation potential. In addition, a similar method could be used to study MSC processing from other sources such as bone marrow.

The initial step in the analysis required determining the important factors to include in the predictive model (Figure 1). Of the 16 factors, only 6 were statistically important. However, the other 12 factors might also have an impact on other outcome measures. For example, although the source of lipoaspirate was not found to be a statistically critical or important factor for maximizing cell count, it might have an impact on the effectiveness of a specific application. For example, some lipoaspirate sources might be more effective at reducing joint inflammation, and other lipoaspirate sources might be more effective at healing diabetic wounds.

The next step after choosing the factors to analyze is to create the predictive model. Other models were considered before choosing the Standards Least Squares and Mixed

models. However, they were not included in the analysis based on a lack of fit using parameters such as R^2, *p*-values, and Bayesian Information Criteria (BIC).

The validation of modeling is essential for the multivariate meta-analysis of multiple factors. When the effect of factors is large compared with the number of collected studies, the estimated variance–covariance matrix using the frequentist method may be inconsistent [21], leading to poor estimates. The plot showed that 80% of the predictive models were accurate, meaning they provided reliable predictions. However, the remaining 20% showed a high level of variability, indicating that they were not consistent or reliable in making predictions. This variability reduces the confidence in the accuracy of these particular predictive models. To improve the accuracy of the predictive model, more data would need to be added to the model. However, we were unable to find additional published studies that met our criteria. In the future, as more studies are published on mechanical processing, data may be added to the study array, which will reduce the setup-related bias in the analysis.

The predictive profiler was instrumental in visualizing the specific effects of each factor concurrently. Since this feature is dynamic, the images seen in Figures 3 and 8 show examples of one combination of factor settings. Table 6 summarizes the predicted setup factors for maximizing the cell yield. Both the Least Squares and Mixed models yielded the same predicted combinations, which increases the confidence in the methodology. The next phase of this investigation will be to test the predicted optimum combination using Quality by Design methodology.

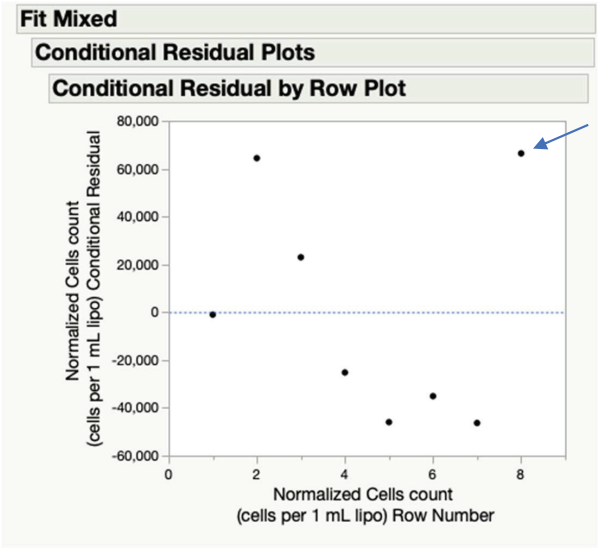

Figure 8. Assessment of unusual points in the Mixed model by a Conditional Residual by Row plot. The blue arrow points to a residual data point that is out of the pattern of the others.

While conducting a meta-analysis on a set of articles, an intriguing anomaly surfaced through the residual plot—a data point that conspicuously deviated from the anticipated pattern of residual distribution (Figure 8). This particular data point has raised questions about its consistency with the rest of the dataset. Notably, this outlier corresponds to a study that advocates for the use of a specific product, a factor that could potentially impact the reliability and integrity of the results. It is imperative to underscore the significance of result reliability when performing a meta-analysis, as the inclusion of data points influenced by external factors may introduce bias and affect the overall robustness of the analysis. In order to enable the generation of the models (minimal data points), it was included. Removing this outlier would have improved the model reliability. However, the improved outcome may be the result of a technical innovation and therefore needed to be included.

One of the limitations of this study was the lack of uniformity in how the different authors presented their data. For example, one study expressed the absolute cell count and

another expressed the concentration. Some studies reported the initial lipoaspirate volume while others reported the volume after decanting. For future comparative analysis, we suggest that specific details are included in future studies (Table 7). This standardization would greatly facilitate the comparison of studies.

Table 7. Factors to include in studies reporting lipoaspirate mechanical processing.

Patient Factors
Sex
Age
BMI
Mechanical Factors
• Initial lipoaspirate volume
• Volume of fat after decantation or centrifugation
• Final cell count per mL of the final product
• Final volume of the final product

In the course of this systematic review, out of a total of 10,000 articles evaluated, only six met the criteria for this study. Although the dataset comprises only six articles, there were 117 volunteers. While this is an admittedly limited number for robust statistical analysis, this scarcity underscores the importance of including specific data factors that would allow for the integration of data.

5. Conclusions

In a traditional meta-analysis, data from different studies are used to analyze the association of a single variable with the outcome measure. The novelty of the method used here was in combining data across different studies to understand the effect of the individual factors and in the optimization of their combination for mechanical lipoaspirate processing. This was carried out by using a powerful program to create predictive models based on least fit criteria. The statistical method revealed which factors are unimportant and identified the crucial factors along with their optimal settings. For achieving a maximum cell count, the following factors are suggested to maximize the nucleated cell count concentration: a centrifuge speed at 2000$\times$ g for 10 min, a 2 mm cannula diameter, and 30 passes through the intra-syringe.

Author Contributions: Conceptualization, G.Z. and R.S.-G.; Overall Methodology, G.Z. and R.S.-G.; Software Methodology and Analysis, R.S.-G. and R.K.; Investigation, N.K., R.S.-G. and G.Z.; Resources, A.P.; Writing—Original Draft Preparation, R.S.-G.; Writing—Review and Editing, G.Z., R.K. and A.P. All authors have read and agreed to the published version of the manuscript.

Funding: This research received no external funding.

Institutional Review Board Statement: Not applicable.

Informed Consent Statement: Not applicable.

Data Availability Statement: Additional data are available upon request.

Conflicts of Interest: The authors declare no conflict of interest. Ron Kenett works in The KPA Group. The KPA Group has made no contributions to the study.

References

1. Mazini, L.; Rochette, L.; Amine, M.; Malka, G. Regenerative Capacity of Adipose Derived Stem Cells (ADSCs), Comparison with Mesenchymal Stem Cells (MSCs). *Int. J. Mol. Sci.* **2019**, *20*, 2523. [CrossRef] [PubMed]
2. Gimble, J.M.; Katz, A.J.; Bunnell, B.A. Adipose-derived stem cells for regenerative medicine. *Circ. Res.* **2007**, *100*, 1249–1260. [CrossRef] [PubMed]

3. Aronowitz, J.A.; Lockhart, R.A.; Hakakian, C.S. Mechanical versus enzymatic isolation of stromal vascular fraction cells from adipose tissue. *Springerplus* **2015**, *4*, 713. [CrossRef]
4. Zhu, Y.; Liu, T.; Song, K.; Fan, X.; Ma, X. Comparison of mechanical and enzymatic methods for the isolation of adipose-derived stem cells. *Biomed. Res. Int.* **2017**, *2017*, 1461704.
5. Glass, G.V. Primary, Secondary, and meta-analysis of research. *Educ. Res.* **1976**, *5*, 3–8. [CrossRef]
6. Egger, M.; Smith, G.D. Misleading meta-analysis. *Br. Med. J.* **1995**, *310*, 752–754. [CrossRef]
7. Fernández-Castilla, B.; Aloe, A.M.; Declercq, L.; Jamshidi, L.; Beretvas, S.N.; Onghena, P.; Van den Noortgate, W. Estimating outcome-specific effects in meta-analyses of multiple outcomes: A simulation study. *Behav. Res.* **2021**, *53*, 702–717. [CrossRef]
8. Lin, L.; Chu, H. Bayesian multivariate meta-analysis of multiple factors. *Res. Synth. Methods* **2018**, *9*, 261–272. [CrossRef]
9. Moher, D.; Liberati, A.; Tetzlaff, J.; Altman, D.G.; PRISMA Group. Preferred reporting items for systematic reviews and meta-analyses: The PRISMA statement. *PLoS Med.* **2009**, *6*, e1000097. [CrossRef]
10. Cicione, C.; Di Taranto, G.; Barba, M.; Isgrò, M.A.; D'Alessio, A.; Cervelli, D.; Sciarretta, F.V.; Pelo, S.; Michetti, F.; Lattanzi, W. In vitro validation of a closed device enabling the purification of the fluid portion of liposuction aspirates. *Plast. Reconstr. Surg.* **2016**, *137*, 1157–1167. [CrossRef] [PubMed]
11. Chaput, B.; Bertheuil, N.; Escubes, M.; Grolleau, J.L.; Garrido, I.; Laloze, J.; Espagnolle, N.; Casteilla, L.; Sensebé, L.; Varin, A. Mechanically isolated stromal vascular fraction provides a valid and useful collagenase-free alternative technique: A comparative study. *Plast. Reconstr. Surg.* **2016**, *138*, 807–819. [CrossRef] [PubMed]
12. Mashiko, T.; Wu, S.H.; Feng, J.; Kanayama, K.; Kinoshita, K.; Sunaga, A.; Narushima, M.; Yoshimura, K. Mechanical micronization of lipoaspirates: Squeeze and emulsification techniques. *Plast. Reconstr. Surg.* **2017**, *139*, 79–90. [CrossRef] [PubMed]
13. Tiryaki, K.T.; Cohen, S.; Kocak, P.; Canikyan Turkay, S.; Hewett, S. In-vitro comparative examination of the effect of stromal vascular fraction isolated by mechanical and enzymatic methods on wound healing. *Aesthetic Surg. J.* **2020**, *40*, 1232–1240. [CrossRef]
14. Busato, A.; De Francesco, F.; Biswas, R.; Mannucci, S.; Conti, G.; Fracasso, G.; Conti, A.; Riccio, V.; Riccio, M.; Sbarbati, A. Simple and Rapid Non-Enzymatic Procedure Allows the Isolation of Structurally Preserved Connective Tissue Micro-Fragments Enriched with SVF. *Cells* **2020**, *10*, 36. [CrossRef] [PubMed]
15. Tiryaki, T.; Condé-Green, A.; Cohen, S.R.; Canikyan, S.; Kocak, P. A 3-step mechanical digestion method to harvest adipose-derived stromal vascular fraction. *Plast. Reconstr. Surg. Glob. Open* **2020**, *8*, e2652. [CrossRef] [PubMed]
16. Abdi, H. The method of least squares. *Encycl. Meas. Stat.* **2007**, *1*, 530–532.
17. Xu, R. Measuring explained variation in linear mixed effects models. *Stat. Med.* **2003**, *22*, 3527–3541. [CrossRef] [PubMed]
18. Kenett, R.S.; Zacks, S. *Modern Industrial Statistics: With Applications in R, MINITAB, and JMP®*, 3rd ed.; Wiley: Hoboken, NJ, USA, 2021.
19. Kenett, R.S.; Nguyen, N.-K. Experimental Learning Generate high information quality by comparing alternative experimental designs. *Qual. Prog.* **2017**, *50*, 40–47.
20. Kenett, R.S.; Zacks, S.; Gedeck, P. *Modern Statistics: A Computer-Based Approach with Python*; Springer: Berlin/Heidelberg, Germany, 2023.
21. Bickel, P.J.; Levina, E. Regularized estimation of large covariance matrices. *Ann. Stat.* **2008**, *36*, 199–227. [CrossRef]

pharmaceutics

MDPI

Article

Assessment of Bioprotect's Biodegradable Balloon System as a Rectal Spacer in Radiotherapy: An Animal Study on Tissue Response and Biocompatibility

Yuval Ramot [1,2], Tal Levin-Harrus [3], Adva Ezratty [3], Michal Steiner [3], Nati Ezov [3], Abraham J. Domb [4], Muhammad Abdel-Haq [4], Shaul Shohat [5], Liron Aperman [5], Lee Adler [5], Oleg Dolkart [6] and Abraham Nyska [7,*]

1 Department of Dermatology, Hadassah Medical Center, Jerusalem 9112001, Israel; yuval.ramot@mail.huji.ac.il
2 Faculty of Medicine, Hebrew University of Jerusalem, Jerusalem 9112001, Israel
3 Envigo CRS Israel Limited, Ness Ziona 7414001, Israel; tal.levinharrus@hbi-cro.com (T.L.-H.); adva.ezratty@hbi-cro.com (A.E.); michal.steiner@hbi-cro.com (M.S.); nati.ezov@hbi-cro.com (N.E.)
4 Institute for Drug Research, School of Pharmacy, Faculty of Medicine, Hebrew University of Jerusalem, Jerusalem 9112001, Israel; avid@ekmd.huji.ac.il (A.J.D.); muhammad.abdel-haq@mail.huji.ac.il (M.A.-H.)
5 BioProtect, Tzur Yigal 4486200, Israel; shaul@bioprotect.com (S.S.); liron@bioprotect.com (L.A.); lee@bioprotect.com (L.A.)
6 Assuta Ashdod University Hospital, Ben-Gurion University of the Negev, Beer Sheba 8410501, Israel; olegdo@assuta.co.il
7 Sackler School of Medicine, Tel Aviv University, Tel Aviv 6200515, Israel
* Correspondence: anyska@nyska.net

Abstract: Prostate cancer is a significant health concern for men, emphasizing the need for effective treatment strategies. Dose-escalated external beam radiotherapy shows promise in improving outcomes but presents challenges due to radiation effects on nearby structures, such as the rectum. Innovative techniques, including rectal spacers, have emerged to mitigate these effects. This study comprehensively assessed tissue responses following the implantation of the Bioprotect biodegradable fillable balloon as a rectal spacer in a rat model. Evaluation occurred at multiple time points (4, 26, and 52 weeks) post-implantation. Results revealed localized tissue responses consistent with the expected reaction to biodegradable materials, characterized by mild to moderate fibrotic reactions and encapsulation, underscoring the safety and biocompatibility of the balloon. Importantly, no other adverse events occurred, and the animals remained healthy throughout the study. These findings support its potential clinical utility in radiotherapy treatments to enhance patient outcomes and minimize long-term implant-related complications, serving as a benchmark for future similar studies and offering valuable insights for researchers in the field. In conclusion, the findings from this study highlight the safety, biocompatibility, and potential clinical applicability of the Bioprotect biodegradable fillable balloon as a promising rectal spacer in mitigating radiation-induced complications during prostate cancer radiotherapy.

Keywords: prostate cancer; rectal spacer; Bioprotect balloon; radiotherapy; biodegradable balloon; tissue response; animal model; radiation therapy; treatment complications; biocompitability

1. Introduction

Prostate cancer ranks as the second-leading cause of mortality in American men following a cancer diagnosis [1]. Remarkably, one in every nine men is anticipated to receive a prostate cancer diagnosis during their lifetime. Consequently, the development of effective treatment regimens for prostate cancer management assumes paramount significance [1]. Dose-escalated external beam radiotherapy (RT) stands out as a compelling strategy for achieving favorable biochemical and clinical outcomes in prostate cancer management [2–8]. Nonetheless, the anatomical proximity of the prostate to the urinary tract and rectum necessitates consideration, as these adjacent structures are susceptible to

the deleterious effects of ionizing radiation. Consequently, while dose escalation is associated with an improved relapse-free survival rate, it also brings about a heightened incidence of adverse effects in the urinary tract and rectum, along with potential complications related to erectile dysfunction [5].

In pursuit of mitigating these undesirable consequences, several innovative technical advancements have emerged. These include the development of intensity-modulated RT (IMRT) [4], the utilization of volume-modulated arc therapy [9,10], and the integration of image-guided RT (IGRT) into clinical practice [7]. Despite the significant strides made in refining these techniques, one challenge endures—the delivery of radiation dose to the rectum, whether through external beam RT or brachytherapy, remains a limiting factor when contemplating dose escalation in prostate cancer treatment.

The occurrence and intensity of rectal adverse events (AEs) can be mitigated by augmenting the separation between the prostate and the rectum. This is achieved through the insertion or injection of spacers composed of either biodegradable materials, such as hyaluronic acid (HA), or non-biodegradable materials, into the perirectal fat. The underlying principle of using a spacer is to introduce a non-biotoxic substance between the posterior surface of the prostate and the anterior surface of the rectum. This strategic placement effectively reduces the volume of the rectum exposed to high radiation doses [1,11]. Notably, the adoption of spacer techniques has been linked to a reduction in the frequency and severity of rectal AEs [5,12–14].

The Bioprotect biodegradable fillable balloon is made of PLCL (poly (L-lactide-co-ε-caprolactone) (BioProtect Ltd., Tzur Yigal, Israel). It serves as a rectal spacer that has demonstrated both safety and efficacy in comprehensive preclinical and clinical investigations [5,15–19]. After positioning the balloon in the intended location, it is filled with sterile saline until it achieves its ultimate configuration. The balloon maintains this inflated state throughout the entirety of the treatment duration [16,17]. The formation of the balloons as well as their degradation process have been described in our previous publications [20,21].

The utilization of biodegradable materials is progressively gaining traction across various medical disciplines [22]. Therefore, it is imperative that biodegradable materials undergo thorough evaluation through preclinical studies, emphasizing the importance of comprehending the anticipated clinical and pathological outcomes stemming from such investigations. While there is a growing body of knowledge regarding the anticipated pathological findings associated with the use of biodegradable materials in suitable animal models [22], our understanding of biodegradable materials for rectal spacers remains relatively limited.

The objective of this investigation was to comprehensively evaluate the localized tissue response subsequent to the implantation of a perirectally positioned balloon in a rat model followed by a course of irradiation consisting of five consecutive days to mimic the clinical scenario expected in humans.

2. Materials and Methods

2.1. Study Design

The study was conducted in Envigo CRS, Israel, following approval by the National Council for Animal Experimentation (Approval No. NPC-En-IL-2111-129-4). Six-week-old male Sprague Dawley [Hsd: Sprague Dawley® SD®] rats were procured from Envigo RMS (Ness-Ziona, Israel) LTD. In this study, 30 animals were implanted with the balloon and categorized into a group denoted as Group 2M (Table 1). This group was further subdivided into three sub-groups, each assigned to specific predetermined observation time points (4 weeks, 26 weeks, and 52 weeks), with each sub-group comprising 10 animals. Additionally, an equally sized control group (and corresponding sub-groups) underwent sham operations and were subjected to identical experimental conditions, constituting Group 1M. At the conclusion of the designated observation time points, the animals underwent urinalysis, blood sampling, and were subsequently euthanized. Selected organs were harvested, fixed, and submitted for processing and histopathological evaluation.

Table 1. Study design.

Group No.	Group Size	Implantation & Iradiation			Scheduled Sacrifice (Post-Implantation)
		Implanted Material	Surgical Procedure	Irradiation Dose and Frequency	
1M	*n* = 10	Not Applicable (Sham-Operated Control)	Creation of perirectal SC "pocket" and placement of 2 sutures on both sides	Irradiation of 2 Gray/animal/day starting 7 days post-implantation × 5 days	4 Weeks
	n = 10				26 Weeks
	n = 10				52 Weeks
2M	*n* = 10	Balloon Spacer (Test Device)	Creation of perirectal SC "pocket" and implantation of 1 TD/animal and suturing the TD with 2 sutures		4 Weeks
	n = 10				26 Weeks
	n = 10				52 Weeks

SC = Subcutaneous; TD = Test Device.

2.2. Surgical Procedure and Irradiation

Delicate surgical scissors were employed to create a horizontal skin incision approximately 2 cm in length, positioned directly below the anus. Blunt dissection was carefully performed with the scissors, separating the perineal muscles in a ventral direction. This dissection aimed to facilitate visualization of the rectal wall and create a deep pocket beneath it. Particular attention was given to ensuring that the pocket was both sufficiently deep and spacious enough to accommodate the entire implant, with unaffected subcutaneous tissue above it. This design allowed for closure without any contact with the implant and minimized the risk of implant extrusion through the skin incision. The balloon was then inserted into the created pocket, adjacent to the rectal wall and positioned as deeply as possible. To secure the balloon in place, it was affixed to the subcutaneous tissue on each lateral side of the implant, utilizing 5-0 non-absorbable suture material (Polypropylene monofilament) with a simple interrupted suture applied on each side. The skin incision was closed using surgical wound clips.

In the sham-operated group, the animals underwent an identical procedure to that described for the balloon-implanted groups. This included the placement of non-absorbable sutures on both lateral sides of the created pocket. However, it is important to note that in the sham-operated group, no implant material was inserted into the pocket.

Each animal underwent a course of irradiation consisting of five consecutive days, commencing seven days after implantation. The irradiation was administered using the Poskom pxr 1 tube series x-ray generator. To deliver a dose of 2 Gray per fraction, the following parameters were employed: four consecutive pulses were generated for each animal, with the animal positioned approximately 0.5 cm from the collimator. The machine settings were configured to 61 kV, 160 mA, and 2 s (320 mAs). The collimator was adjusted to yield an exposure field measuring 0.5–1.0 cm^2, and it was expected that each individual pulse would produce a dose of 0.5 Gray.

2.3. In Life Analysis

The animals underwent observation for a cumulative period spanning 4 weeks, 26 weeks, and 52 weeks post-implantation. Viability assessments, which included monitoring for mortality and overall condition, were conducted once daily throughout the entire 52-week observation period. Additionally, Cage-Side Clinical Observations were performed once daily over the same 52-week period. Comprehensive clinical examinations, encompassing both systemic and local reactions, were conducted on all animals one day after implantation and subsequently once weekly. The determination of individual body weights of animals was initially conducted during the randomization procedure, followed by body weight assessments on the day of implantation and subsequently on a weekly basis. Individual urine samples were collected during the last week prior to each scheduled termination for the animals.

2.4. Terminal Investigations

At designated time points, animals were euthanized via CO_2 asphyxiation. Prior to each termination, hematology and biochemistry parameters were assessed. A comprehensive necropsy, including gross pathological examination of the implantation sites, was conducted on all animals. Specific attention was paid to macroscopic alterations, regional lymph nodes, tissue reactions (such as hematoma, edema, encapsulation), and implant characteristics. For the implantation site near the rectum, adjacent tissues including the anus and surrounding unaffected tissue (2 mm to 5 mm) were excised for histopathological evaluation. In cases where the implant was not visible, additional tissue surrounding the expected implant site was included. Collection of regional lymph nodes, kidneys, and any abnormalities was also performed during necropsy.

2.5. Histopathological Assessment

The following organs/tissues underwent processing and evaluation: the implantation site, regional draining lymph nodes, and kidneys. Tissues were meticulously trimmed, embedded in paraffin, and sectioned to approximately 5-micron thickness. Subsequent staining with Hematoxylin and Eosin (H&E) was performed. Special care was taken to maintain the integrity of the implant/tissue interface during the staining process for the implantation site. Xylene-free reagents were used for deparaffinization to prevent implant displacement.

For the implantation site, three transverse sections were prepared, covering the entire site and adjacent rectum. Each transverse slice was embedded in paraffin to expose the cut surface, resulting in one block per slice and three slides per animal for examination.

Histopathological examination of the implantation site involved assessing various parameters, including necrosis graded on a scale from 0 (none) to 4 (severe). Additionally, evaluations were conducted for neovascularization, fibrosis/fibrous capsule formation, and fatty infiltrate, with scoring according to a specific evaluation system detailed in Table 2.

Table 2. Histological evaluation system—tissue response.

Cell Type/Response	**Score**				
	0	**1**	**2**	**3**	**4**
Neovascularisation	0	Minimal capillary proliferation, focal, 1 to 3 buds	Groups of 4 to 7 capillaries with supporting fibroblastic structures	Broad band of capillaries with supporting fibroblastic structures	Extensive band of capillaries with supporting fibroblastic structures
Fibrosis	0	Narrow band	Moderately thick band	Thick band	Extensive band
Fatty Infiltrate	0	Minimal amount of fat associated with fibrosis	Several layers of fat and fibrosis	Elongated and broad accumulation of fat cells at activation site	Extensive fat completely surrounding the activation site

The histopathological evaluation involved assessing the quantity and dispersion of different inflammatory cell types concerning their proximity to the implantation site/tissue interface. These cell types included polymorphonuclear neutrophilic leukocytes, lymphocytes, plasma cells, eosinophils, macrophages, and multinucleated cells. The assessment of cell types and their responses utilized the evaluation system detailed in Table 3.

Table 3. Histological evaluation system—cell type/response.

Cell Type/Response	**Score**				
	0	**1**	**2**	**3**	**4**
Polymorphonuclear	0				
Lymphocytes	0				
Plasma Cells	0	Rare, 1–5/phf [a]	5–10/phf	Heavy infiltrate	Packed
Macrophages	0				
Giant Cells	0	Rare, 1–2/phf	3–5/phf		Sheets

[a]—phf = per high powered (400×) field.

We calculated the total scores for each parameter in both treatment and control implantation sites. Additionally, we doubled the scores for inflammatory cell infiltrates and necrosis. These combined scores were then averaged for each group. To establish a reactivity grade, we subtracted the average score of the control treatment from that of the test treatment, utilizing the interpretation scale detailed in Table 4.

Table 4. Reactivity grade.

	Score Following Control Subtraction			
	0.0–2.9	**3.0–8.9**	**9.0–15.0**	**>15.1**
Total Reactivity	minimal or no reaction	slight reaction	moderate reaction	severe reaction

At the implantation site, specific parameters were assessed and graded on a severity scale, including:

- Incidents of hemorrhage;
- Granuloma formation;
- Presence of fragmentation and/or debris;
- Presence and location of degraded material remnants;
- Quantity and quality of tissue ingrowth;
- Mineralization.

These parameters were graded on a severity scale ranging from 0 (none) to 4 (severe). Additionally, the quantity of residual implanted material in balloon-implanted sites was evaluated and scored using a specific grading scale [23]:

0 = No apparent degradation.

1 = Minimal degradation of implant, with some minor dissolution on edges, cracks in the implant, and/or small fragments present.

2 = Moderate degradation of implant with cracks in the implant and/or some fragments.

3 = Marked degradation of implant with the presence of several fragments.

4 = Abundant degradation of implant with (almost) complete fragmentation.

Any additional histopathological changes or changes observed in other organs were described and scored. These assessments utilized a semi-quantitative grading system with five grades (0–4), taking into consideration the severity of the changes [24]: Grade 0 = no changes observed; Grade 1 = minimal; Grade 2 = mild; Grade 3 = moderate; Grade 4 = severe.

2.6. Statistical Analysis

2.6.1. Calculations

- MeanSDRelative_01.2.Rnw: this is a validated R-Script used for calculations of mean group, standard deviation, and the number of observations.
- MultiComp.Rnw: this is a validated R-Script used for statistical evaluations involving multiple groups and/or multiple parameters between two groups.

2.6.2. Evaluation Process

Before applying the appropriate statistical method, a normality test was performed to determine if the data followed a Gaussian distribution, for example, using the Shapiro–Wilk normality test with a significance level of $p < 0.01$.

For MultiComp.Rnw, the following steps were taken based on the normality test results:

1. If the normality test passed for all groups:
    - An equal-variance test (e.g., Bartlett test) was performed with a significance level of $p < 0.01$.
    - If the Bartlett test passed, a one-way ANOVA with Dunnett's posttest was performed.
    - If the Bartlett test did not pass, a Kruskal–Wallis test with Mann–Whitney U test was performed.

2. If the normality test did not pass for all groups, a Kruskal–Wallis test with Mann–Whitney U test was performed for further analysis.

3. Results

3.1. Mortality and Clinical Signs

No mortality occurred in any of the animals evaluated during the entire observation period. Throughout the 52-week observation period, no abnormal clinical signs were observed, except for two transient incidents:

1. One incidence of alopecia on the scrotum was noted in a balloon-implanted animal during the second week post-implantation.
2. One incidence of alopecia and crust on the right shoulder and peri-orbital staining was observed in a sham-operated animal during the 39th week post-implantation.

Both of these incidents resolved spontaneously by the following week.

3.2. Body Weight, Clinical Pathology and Urinalysis

The group mean body weight values and gains were largely similar between the two groups and showed the expected gradual increase over time. Results of urinalysis were also comparable between the two test groups, with no clear treatment-related effects observed. The values were within the normal expected range, as anticipated. Additionally, group mean hematology, biochemistry, and coagulation values were mostly comparable between the two test groups. While there were some statistically significant differences, these values were either within the normal range or below the normal range and did not have any biological significance.

3.3. Macroscopic Assessment of the Implantation Site

No alterations in normal structure or enlarged regional lymph nodes were observed in any of the animals at all time points.

At the 4-week time point, no local tissue reaction was recorded in both groups, and the expected location of the implant was confirmed in all animals from the balloon-implanted group.

For animals assigned to the 26-week time point, local tissue reactions included hematoma-like lesions around the operated area, noted in one sham-operated animal, encapsulation around the implant in all balloon-implanted animals, and the presence of adhesions around the operated area was noted in one sham-operated animal.

In animals assigned to the 52-week time point, local tissue reactions were observed, including a round whitish semi-solid mass of approximately 0.5 cm in diameter with a glandular appearance located laterally to the implantation site on the left side, noted in one balloon-implanted animal. Encapsulation around the implant was noted in three balloon-implanted animals, and the presence of adhesions around the operated area was noted in five balloon-implanted animals. The expected location of the implant was confirmed in most animals of the balloon-implanted group through various methods such as visualization of sutures, visualization of the balloon within the encapsulation, and palpation of the balloon.

3.4. Histopathological Evaluation

3.4.1. 4-Week Time Point

In Group 1M (sham-operated control), histopathological analysis of the subcutaneous, perirectal area revealed minimal chronic inflammation, characterized by granulation tissue predominated by fibrosis with limited mixed mononuclear inflammatory cell infiltration (Figure 1).

In Group 2M (balloon-implanted), the presence of the implant was confirmed in 9 out of 10 animals. Histological examination of the subcutaneous, perirectal implantation site revealed a central cavity containing distinct elongated remnants of the balloon (Figure 2). Surrounding this cavity was relatively mature connective tissue classified as Grade 2. The

inner surface of the capsule that enveloped the cavity was lined with a single layer of flattened to cuboidal macrophages, designated as Grade 1. Minimal degradation (Grade 1) of the balloon (implant) was observed, along with minor dissolution at the edges, cracks within the implant, and small fragments present. The calculated Reactivity Score, determined by subtracting the total score of the sham-operated control, fell within the category of "slight reaction" (score: 5) for the balloon (Table 5). No histopathological changes were detected in the kidneys, rectum, regional lymph nodes, or any adjacent tissues included in the sections of the implantation site.

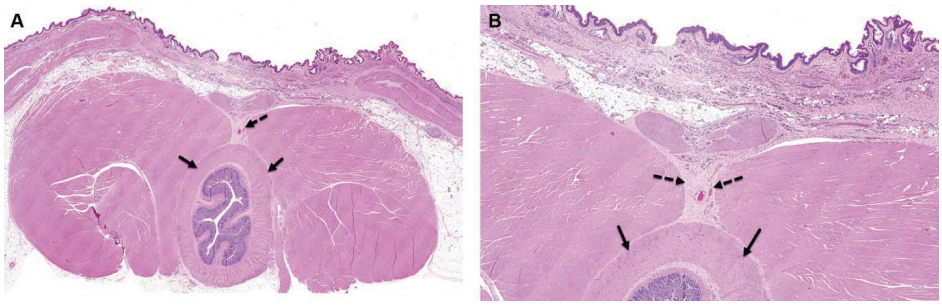

Figure 1. Group 1M (sham-operated control) at the 4-week time point, both low ×1 (**A**) and high ×4 (**B**) magnification views of the implantation site are presented. At this stage, changes are evident at the subcutaneous and perirectal implantation site, characterized by minimal chronic inflammation, which includes granulation tissue. This inflammation is primarily composed of fibrosis with minimal mononuclear inflammatory cells, as indicated by the broken arrows. However, no changes are observed in the rectum, as shown by the arrows in the images. The staining method used is Hematoxylin and Eosin (H&E).

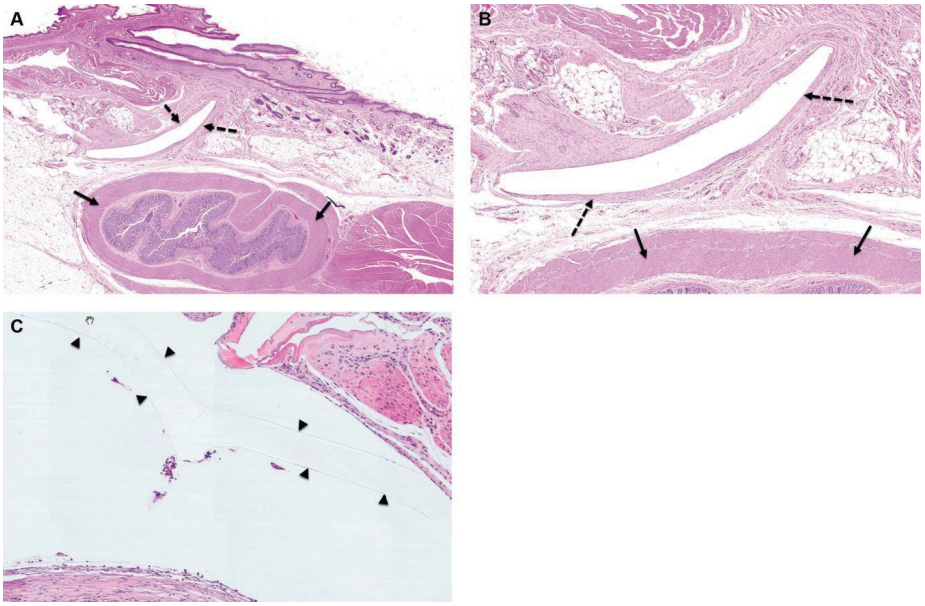

Figure 2. Group 2M (balloon-implanted group) at the 4-week time point, low ×1 (**A**), high ×4 (**B**), and very high (**C**) magnification views of the implantation site are presented. At this stage, changes are observed at the perirectal implantation site, which consist of a central cavity in which clear elongated remnants of the balloon are identified (arrowheads). The cavity is surrounded by relatively mature connective tissue, which has been scored as Grade 2, signifying mild changes (as represented by the broken arrows). Furthermore, a single layer of flattened to cuboidal macrophages is lining the inner surface of the capsule, and this has been scored as Grade 1, indicating minimal changes. Additionally, there are sporadic minimal polymorphonuclear cells and lymphocytes dispersed within the capsule. It is noteworthy that no changes are observed in the rectum, as indicated by the arrows. The staining method used for this image is Hematoxylin and Eosin (H&E).

Table 5. Individual and group reaction scoring (4 weeks post-implantation).

		Histopathology Findings at 4 Weeks Post-Implantation (Group No., Treatment, Animal's No.)																			
		1M									**2M**										
		Sham-Operated Control									**Balloon Spacer (Test Device = TD)**										
		1	**2**	**3**	**4**	**5**	**6**	**7**	**8**	**9**	**10**	**31**	**32**	**33**	**34**	**35**	**36**	**37**	**38**	**39**	**40**
	Parameter	**Sham-Operated Site**									**Implantation Site**										
Cell Type/Response	Polymorphonuclear	0	0	0	0	0	0	0	0	0	0	1	1	1	1	1	1	1	1	1	NA
	Lymphocytes	1	1	1	1	1	1	1	1	1	1	1	1	1	1	1	1	1	1	1	NA
	Plasma Cells	0	0	0	0	0	0	0	0	0	0	0	0	0	0	0	0	0	0	0	NA
	Macrophages	0	0	0	0	0	0	0	0	0	0	1	1	1	1	1	1	1	1	1	NA
	Giant Cells	0	0	0	0	0	0	0	0	0	0	0	0	0	0	0	0	0	0	0	NA
	Necrosis	0	0	0	0	0	0	0	0	0	0	0	0	0	0	0	0	0	0	0	NA
	Sub Total	1	1	1	1	1	1	1	1	1	1	3	3	3	3	3	3	3	3	3	NA
	Sub Total (×2)	2	2	2	2	2	2	2	2	2	2	6	6	6	6	6	6	6	6	6	NA
Tissue Response	Neovascularization	1	1	1	1	1	1	1	1	1	1	1	1	1	1	1	1	1	1	1	NA
	Fibrosis/fibrous capsule	1	1	1	1	1	1	1	1	1	1	2	2	2	2	2	2	2	2	2	NA
	Fatty Infiltrate	0	0	0	0	0	0	0	0	0	0	0	0	0	0	0	0	0	0	0	NA
	Sub Total	2	2	2	2	2	2	2	2	2	2	3	3	3	3	3	3	3	3	3	NA
	Total	4	4	4	4	4	4	4	4	4	4	9	9	9	9	9	9	9	9	9	NA
	Group Total Reactivity	40									81										
	Average Reactivity	4.0									9.0										
	Average TD minus Average Control	5.0																			
	Total Reactivity	Slight Reaction																			
	Hemorrhage	0	0	0	0	0	0	0	0	0	0	0	0	0	0	0	0	0	0	0	NA
	Granuloma	0	0	0	0	0	0	0	0	0	0	0	0	0	0	0	0	0	0	0	NA
	foreign debris	0	0	0	0	0	0	0	0	0	0	0	0	0	0	0	0	0	0	0	NA
	Tissue ingrowth	0	0	0	0	0	0	0	0	0	0	0	0	0	0	0	0	0	0	0	NA
	Mineralization	0	0	0	0	0	0	0	0	0	0	0	0	0	0	0	0	0	0	0	NA
	Residual Material (implant)	NA	NA	NA	NA	NA	NA	NA	NA	NA	NA	NA	1	1	1	1	1	1	1	1	NA

NA—not applicable (since the Test Device could not be detected/was not present in the sham control).

3.4.2. 26-Week Time Point

In the sham-operated control group, no histopathological changes were observed at this time point in the skin, underlying subcutis, or in the rectum (i.e., implantation site) (Figure 3).

In the balloon-implanted group, the implantation site was identifiable in all 10 animals, and remnants of the balloon were still detectable in 6 out of 10 animals. Over time, the implants exhibited gradual fragmentation, resulting in the formation of multiple chambers (Figure 4). Each chamber was surrounded by a fibrotic reaction, primarily graded as minimal to mild (Grade 1 to 2), with occasional instances of moderate (Grade 3) fibrotic reactions. The central cavity housing the implant remnants was encased by relatively mature connective tissue, graded between 2 and 3. Minimal sporadic polymorphonuclear cells and lymphocytic infiltrations were sporadically observed within the capsule. A layer of flattened to columnar macrophages (graded 1 to 2) lined the inner surface of the capsule.

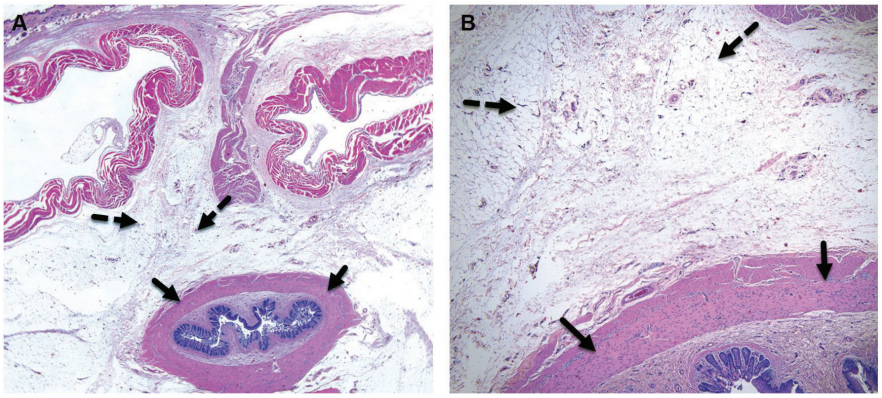

Figure 3. Group 1M (sham-operated control) at the 26-week time point, both low ×1 (**A**) and high ×4 (**B**) magnification views of the implantation site are presented. At this stage, there are no observable changes at the subcutaneous, perirectal implantation site, as indicated by the broken arrows. Additionally, there are no changes seen in the rectum, as indicated by the arrows. The staining method used for this image is Hematoxylin and Eosin (H&E).

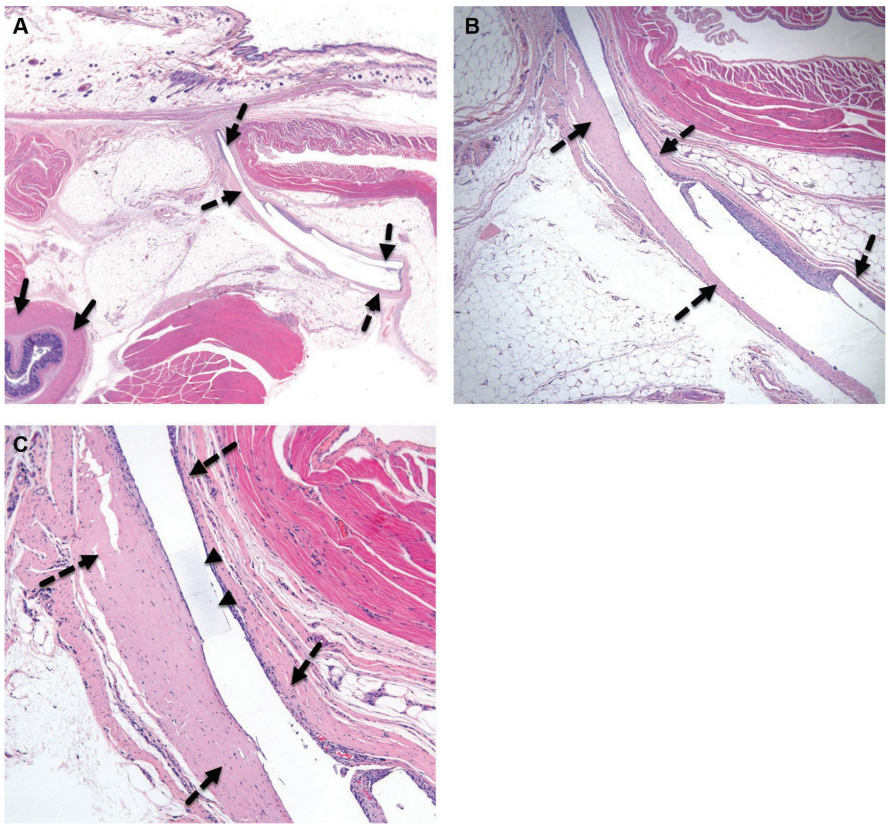

Figure 4. Group 2M (balloon-implanted group) at the 26-week time point, low ×1 (**A**), high ×4 (**B**), and very high (**C**) magnification views of the implantation site are presented. At this stage, changes are observed at the perirectal implantation site, which consist of a central cavity in which clear elongated remnants of the balloon are identified (arrowheads). It appears that the implant has slightly fragmented over time, forming multiple chambers, each surrounded by a fibrotic reaction, which is scored as grade 1. The cavity itself is surrounded by relatively mature connective tissue, scored as grade 2, mild (broken arrows). A single layer of flattened to cuboidal macrophages lines the inner surface of the capsule. Sporadic (minimal) polymorphonuclear cells and lymphocytes are dispersed within the capsule. No changes are observed in the rectum (arrows). H&E staining was used for this evaluation.

The observed changes were consistent with expectations for biodegradable materials and indicated a moderate to abundant degradation (Grade 2 to 4) of the balloon (implant). This ranged from the formation of some fragments, with either no or a moderate amount (Grade 2) of residual material, to abundant degradation with almost complete fragmentation (Grade 4). After subtracting the control data, the reactivity score indicated a "moderate reactivity" (score: 10.2) of the implantation site compared to the non-implanted site (Table 6).

Table 6. Individual and group reaction scoring (26 weeks post-implantation).

		Histopathology Findings at 26 Weeks Post-Implantation (Group No., Treatment, Animal's No.)																			
		1M									**2M**										
		Sham-Operated Control									**Balloon Spacer (Test Device = TD)**										
		11	**13**	**14**	**15**	**16**	**17**	**18**	**19**	**20**	**61**	**41**	**42**	**43**	**44**	**45**	**46**	**47**	**48**	**49**	**50**
Parameter		**Sham-Operated Site**									**Implantation Site**										
Cell Type/Response	Polymorphonuclear	0	0	0	0	0	0	0	0	0	0	0	1	1	1	1	3 *	0	1	0	1
	Lymphocytes	0	0	0	0	0	0	0	0	0	0	1	1	1	1	1	1	1	1	1	1
	Plasma Cells	0	0	0	0	0	0	0	0	0	0	0	0	0	0	0	0	0	0	0	0
	Macrophages	0	0	0	0	0	0	0	0	0	0	2	1	1	1	1	1	1	1	1	1
	Giant Cells	0	0	0	0	0	0	0	0	0	0	0	0	0	0	0	1	0	0	0	0
	Necrosis	0	0	0	0	0	0	0	0	0	0	0	0	0	0	0	0	0	0	0	0
	Sub Total	0	0	0	0	0	0	0	0	0	0	3	3	3	3	3	6	2	3	2	3
	Sub Total (×2)	0	0	0	0	0	0	0	0	0	0	6	6	6	6	6	12	4	6	4	6
Tissue Response	Neovascularization	0	0	0	0	0	0	0	0	0	0	1	1	1	1	1	1	1	1	1	1
	Fibrosis/fibrous capsule	0	0	0	0	0	0	0	0	0	0	2	2	2	3	3	3	2	2	2	2
	Fibrosis/fibrous within the cavity	0	0	0	0	0	0	0	0	0	0	3	1	1	2	1	2	0	2	2	1
	Fatty Infiltrate	0	0	0	0	0	0	0	0	0	0	0	0	0	0	0	0	0	0	0	0
	Sub Total	0	0	0	0	0	0	0	0	0	0	6	4	4	6	5	0	3	5	5	4
Total		0	0	0	0	0	0	0	0	0	0	12	10	10	12	11	18	7	11	9	10
Group Total Reactivity		0									92										
Average Reactivity		0.0									10.2										
Average TD minus Average Control		10.2																			
Total Reactivity		Moderate Reaction																			
Hemorrhage		0	0	0	0	0	0	0	0	0	0	0	0	0	0	0	0	0	0	0	0
Granuloma		0	0	0	0	0	0	0	0	0	0	1	1	0	0	0	0	0	0	0	0
foreign debris		0	0	0	0	0	0	0	0	0	0	1	1	0	0	0	0	2	0	0	0
Tissue ingrowth (fibrosis)		0	0	0	0	0	0	0	0	0	0	0	3	1	1	2	1	2	0	2	2
Mineralization		0	0	0	0	0	0	0	0	0	0	0	0	0	0	0	0	2	0	0	0
Residual Material (implant)		NA	NA	NA	NA	NA	NA	NA	NA	NA	NA	4	2	2	3	4	2	4	3	4	2

NA—not applicable (since the Test Device was not present in the sham control). * Animal #46: The accumulation of polymorphonuclear cells was consistent with the morphological aspect of abscess formation, and was associated with the presence of bacterial colonies, mineralization, and hair shafts. The cavity was partially lined by squamous epithelium. These changes were suggested to occur due to incidental bacterial contamination at the implant site. Consequently, this case was excluded from the average calculation.

No histopathological changes were detected in the kidneys, rectum, regional lymph nodes, or any adjacent tissues included in the sections of the implantation site.

3.4.3. 52-Week Time Point

In the sham-operated control group, there were no histopathological changes observed in the skin, underlying subcutis, or the rectum (i.e., implantation site) (Figure 5).

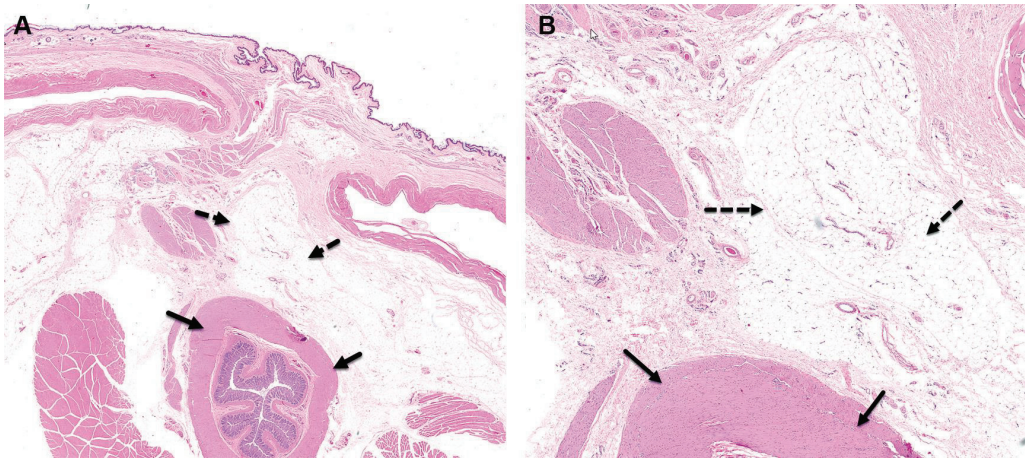

Figure 5. Group 1M (sham-operated control) at the 52-week time point, both low ×1 (**A**) and high ×4 (**B**) magnification views of the implantation site are presented. At this stage, no changes are observed at the subcutaneous, perirectal implantation site (broken arrows). No changes are seen in the rectum (arrows). H&E staining.

In the balloon-implanted animals, the implantation site was identifiable in 9 out of 10 animals. Notably, it appeared that the implant fragmented over time, resulting in the formation of multiple chambers (Figure 6). Each chamber exhibited a minimal fibrotic reaction, scored as Grade 1 (minimal). The entire implantation area was enveloped by relatively mature connective tissue, graded as Grade 2. Within the capsules, minimal sporadic lymphocytic infiltrations were noted. A layer of flattened to cuboidal macrophages (graded as Grade 1) lined the inner surfaces of the cavities where the implant had previously resided and was subsequently resorbed.

Upon calculating the Total Reactivity Score, following the subtraction of values from the sham-operated group, it indicated a "slight reactivity" (score: 8) of the balloon when compared to the non-implanted site (Table 7).

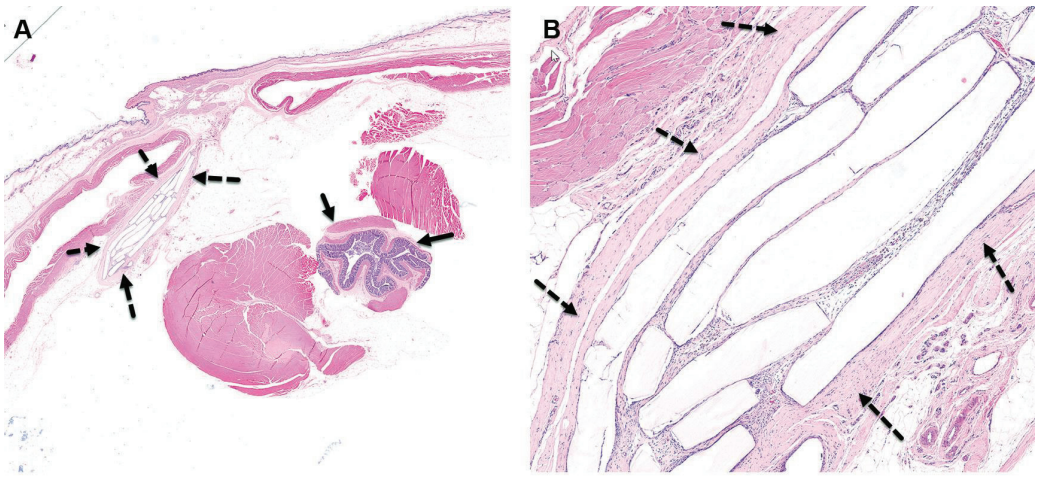

Figure 6. *Cont.*

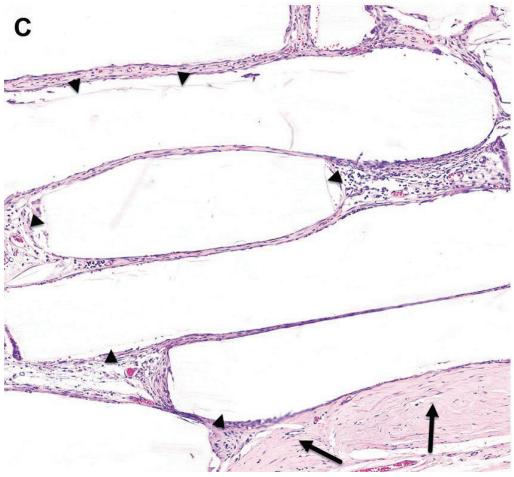

Figure 6. Group 2M (balloon-implanted group) at the 52-week time point, low ×1 (**A**), high ×4 (**B**), and very high (**C**) magnification views of the implantation site are presented. At this stage, histological alterations are observed at the perirectal implantation site, characterized by the presence of a central cavity containing ghost-like elongated remnants of the balloon (indicated by arrowheads). Over time, the implant appears to have fragmented, resulting in the formation of multiple chambers, each surrounded by a fibrotic reaction that is graded as mild (Grade 1). The central cavity is encircled by relatively mature connective tissue, with a mild intensity score of 2 (Grade 2) (indicated by broken arrows). Additionally, a monolayer of flattened to cuboidal macrophages lines the inner surface of these chambers. Scattered polymorphonuclear cells and lymphocytes are sporadically dispersed within the capsule but at minimal levels. Importantly, no discernible changes are observed in the rectal tissue (indicated by arrows). These findings were visualized using Hematoxylin and Eosin (H&E) staining.

Table 7. Individual and group reaction scoring (52 weeks post-implantation).

		Histopathology Findings at 52 Weeks Post-Implantation (Group No., Treatment, Animal's No.)																			
		1M									**2M**										
		Sham-Operated Control									**Balloon Spacer (Test Device = TD)**										
		21	**22**	**23**	**24**	**25**	**26**	**27**	**28**	**29**	**30**	**51**	**52**	**53**	**101**	**55**	**56**	**57**	**58**	**59**	**60**
	Parameter	**Sham-Operated Site**									**Implantation Site**										
Cell Type/Response	Polymorphonuclear	0	0	0	0	0	0	0	0	0	0	0	0	0	0	NA	0	0	0	0	0
	Lymphocytes	0	0	0	0	0	0	0	0	0	0	1	1	1	1	NA	1	1	1	1	1
	Plasma Cells	0	0	0	0	0	0	0	0	0	0	0	0	0	0	NA	0	0	0	0	0
	Macrophages	0	0	0	0	0	0	0	0	0	0	1	1	1	1	NA	1	1	1	1	1
	Giant Cells	0	0	0	0	0	0	0	0	0	0	0	0	0	0	NA	0	0	0	0	0
	Necrosis	0	0	0	0	0	0	0	0	0	0	0	0	0	0	NA	0	0	0	0	0
	Sub Total	0	0	0	0	0	0	0	0	0	0	2	2	2	2	NA	2	2	2	2	2
	Sub Total (×2)	0	0	0	0	0	0	0	0	0	0	4	4	4	4	NA	4	4	4	4	4
Tissue Response	Neovascularization	0	0	0	0	0	0	0	0	0	0	1	1	1	1	NA	1	1	1	1	1
	Fibrosis/fibrous capsule	0	0	0	0	0	0	0	0	0	0	2	2	2	2	NA	2	2	2	2	2
	Fibrosis/fibrous within the cavity	0	0	0	0	0	0	0	0	0	0	1	1	1	1	NA	1	1	1	1	1
	Fatty Infiltrate	0	0	0	0	0	0	0	0	0	0	0	0	0	0	NA	0	0	0	0	0
	Sub Total	0	0	0	0	0	0	0	0	0	0	4	4	4	4	NA	4	4	4	4	4

Table 7. *Cont.*

	Histopathology Findings at 52 Weeks Post-Implantation (Group No., Treatment, Animal's No.)																				
	1M										**2M**										
	Sham-Operated Control										**Balloon Spacer (Test Device = TD)**										
	21	**22**	**23**	**24**	**25**	**26**	**27**	**28**	**29**	**30**	**51**	**52**	**53**	**101**	**55**	**56**	**57**	**58**	**59**	**60**
Parameter	**Sham-Operated Site**										**Implantation Site**									
Total	0	0	0	0	0	0	0	0	0	0	8	8	8	8	NA	8	8	8	8	8
Group Total Reactivity	0										72									
Average Reactivity	0.0										8.0									
Average TD minus Average Control	8.0																			
Total Reactivity	Slight Reaction																			
Hemorrhage	0	0	0	0	0	0	0	0	0	0	0	0	0	0	NA	0	0	0	0	0
Granuloma	0	0	0	0	0	0	0	0	0	0	0	0	0	1	NA	0	0	0	0	1
foreign debris	0	0	0	0	0	0	0	0	0	0	0	0	0	0	NA	0	0	0	0	0
Tissue ingrowth (fibrosis)	0	0	0	0	0	0	0	0	0	0	2	2	2	2	NA	2	2	2	2	2
Mineralization	0	0	0	0	0	0	0	0	0	0	0	0	0	0	NA	0	0	0	0	0
Residual Material (implant)	NA	NA	NA	NA	NA	NA	NA	NA	NA	NA	4 *	4 *	4 *	4 *	NA	4 *	4 *	4 *	4 *	4 *

* Minimal ghost residues, judged to be innocuous, reflecting end-of-process residue in trace amounts.

4. Discussion

The principal findings of this study indicate that balloon implantation led to localized tissue responses characterized by fibrotic reactions and encapsulation, which are consistent with the anticipated foreign body reaction to biodegradable materials [25–27]. Notably, these responses were mild to moderate in nature, suggesting a gradual and expected healing process rather than adverse reactions.

The computation of the total Reactivity Score revealed a notable elevation in reactivity from the 4-week to the 26-week time interval, primarily attributed to heightened fibrotic responses. These responses are recognized as integral facets of the expected and progressive healing process, rather than adverse reactions, culminating in the development of scar tissue. Conversely, an observable decrease in the total Reactivity Score at the 52-week time point in comparison to the 26-week milestone suggests a diminishing inflammatory reaction. Significantly, this decline is construed as a manifestation of ongoing and anticipated healing, devoid of any untoward consequences.

The selection of an appropriate radiation dose for evaluating the impact on the integrity of the balloon implant remains a critical consideration in our study. While conventional prostate radiotherapy typically prescribes doses exceeding 70 Gy, it is essential to note that only a fraction of this dosage directly affects the rectum and the implant area. Thus, our choice to expose the implant to a dose of 10 Gy/5f was a cautious approach aimed at simulating a worst-case scenario specifically targeting the implant site. This decision was made to rigorously assess the potential degradation of the balloon under conditions that closely mimic its real-world application. Furthermore, comprehensive validation tests were conducted, including exposure of the balloon to doses as high as 150 Gy, demonstrating its robustness and resistance to degradation even at significantly elevated radiation levels. These findings reinforce the confidence in the balloon's durability under realistic clinical radiation scenarios, supporting its potential feasibility for long-term use in prostate radiotherapy. Therefore, while acknowledging the discrepancy between our applied dose and the conventional prescription, our study provides valuable insights into the resilience of the implant to radiation exposure relevant to its intended clinical use.

Our histopathological examinations meticulously tracked tissue reactions associated with the implantation of the biodegradable spacer and the effects of ionizing radiation. Importantly, our observations consistently revealed that all identified histological changes were exclusively attributed to the presence and degradation process of the spacer material. Notably, the administered ionizing radiation, within the parameters applied in our study, did not yield any discernible histopathological alterations or reactions in the examined tissues. These findings underscore the specificity of the histological reactions solely to the presence of the spacer and its degradation, reinforcing the notion that the ionizing radiation, as utilized in our experimental design, did not contribute to any observed tissue changes.

These findings underscore the safety and biocompatibility of the balloon as a rectal spacer. The observed tissue responses align with the expected healing process, and the minimal degradation of the implant at the first weeks after implantation suggests its suitability for clinical use. Furthermore, the absence of adverse effects in adjacent tissues highlights the precision and efficacy of this spacer in minimizing radiation exposure to the rectum.

The results of this study have significant implications for the clinical use of balloon implants. The progressive and predictable degradation behavior of these implants underscores their potential utility in clinical settings, particularly in radiotherapy treatments. The absence of significant adverse effects on animal health and the observed tissue responses affirm the biocompatibility of the balloon implants. The findings presented here provide a strong foundation for further investigations and clinical trials. The use of these implants may offer improved patient outcomes and treatment precision while minimizing long-term implant-related complications.

5. Conclusions

Our study demonstrates the safety, biocompatibility, and gradual degradation behavior of the Bioprotect biodegradable fillable balloon as a rectal spacer in a rat model over a 52-week evaluation period. The observed tissue responses, characterized by mild to moderate fibrotic reactions and encapsulation, align with expected healing processes without adverse effects on adjacent tissues. These findings highlight the potential clinical utility of the Bioprotect balloon in minimizing radiation exposure to the rectum during prostate cancer radiotherapy. The predictable degradation pattern and minimal adverse reactions suggest its viability for clinical translation. Our research provides a foundation for future clinical trials, emphasizing improved patient outcomes and reduced long-term complications in prostate cancer treatment.

Author Contributions: Conceptualization, A.J.D., S.S., L.A. (Liron Aperman), L.A. (Lee Adler) and O.D.; Methodology, M.A.-H. and O.D.; Formal analysis, A.N.; Investigation, A.E., M.S. and N.E.; Resources, A.J.D., M.A.-H., S.S., L.A. (Liron Aperman) and L.A. (Lee Adler); Data curation, T.L.-H., A.E., M.S., O.D. and A.N.; Writing—original draft, Y.R.; Writing—review & editing, Y.R., T.L.-H., A.E., M.S., N.E., A.J.D., M.A.-H., S.S., L.A. (Liron Aperman), L.A. (Lee Adler), O.D. and A.N. All authors have read and agreed to the published version of the manuscript.

Funding: This research was funded by BioProtect Ltd., Tzur Yigal, Israel.

Institutional Review Board Statement: The study was approved by the National Council for Animal Experimentation (Approval No. NPC-En-IL-2111-129-4).

Data Availability Statement: The data presented in this study are available on request from Shaul Shohat.

Conflicts of Interest: Shaul Shohat, Liron Aperman, and Lee Adler are employees of BioProtect. The study described in this manuscript received funding support from Bioprotect. Although representatives of Bioprotect participated in the writing and approved the decision to publish the results, they had no involvement in the design of the study, data collection, analyses, or interpretation of the findings. Tal Levin-Harrus, Adva Ezratty, Michal Steiner and Nati Ezov are employees of Envigo CRS Israel Ltd. Envigo team members were involved in planning the study, gathering and analyzing data, and writing the manuscript. However, they don't own shares or have any financial stake in

Bioprotect. Envigo CRS Israel Ltd had no role in the design of the study; in the collection, analyses, or interpretation of data; in the writing of the manuscript, or in the decision to publish the results.

References

1. Su, Z.; Henderson, R.; Nichols, R.; Bryant, C.; Hoppe, B.; Mendenhall, W.; Mendenhall, N. A comparative study of prostate PTV margins for patients using hydrogel spacer or rectal balloon in proton therapy. *Phys. Med.* **2021**, *81*, 47–51. [CrossRef]
2. Beckendorf, V.; Guerif, S.; Le Prise, E.; Cosset, J.M.; Bougnoux, A.; Chauvet, B.; Salem, N.; Chapet, O.; Bourdain, S.; Bachaud, J.M.; et al. 70 Gy versus 80 Gy in localized prostate cancer: 5-year results of GETUG 06 randomized trial. *Int. J. Radiat. Oncol. Biol. Phys.* **2011**, *80*, 1056–1063. [CrossRef]
3. Cahlon, O.; Hunt, M.; Zelefsky, M.J. Intensity-modulated radiation therapy: Supportive data for prostate cancer. *Semin. Radiat. Oncol.* **2008**, *18*, 48–57. [CrossRef] [PubMed]
4. Dearnaley, D.P.; Jovic, G.; Syndikus, I.; Khoo, V.; Cowan, R.A.; Graham, J.D.; Aird, E.G.; Bottomley, D.; Huddart, R.A.; Jose, C.C.; et al. Escalated-dose versus control-dose conformal radiotherapy for prostate cancer: Long-term results from the MRC RT01 randomised controlled trial. *Lancet Oncol.* **2014**, *15*, 464–473. [CrossRef] [PubMed]
5. Latorzeff, I.; Bruguiere, E.; Bogart, E.; Le Deley, M.C.; Lartigau, E.; Marre, D.; Pasquier, D. Use of a Biodegradable, Contrast-Filled Rectal Spacer Balloon in Intensity-Modulated Radiotherapy for Intermediate-Risk Prostate Cancer Patients: Dosimetric Gains in the BioPro-RCMI-1505 Study. *Front. Oncol.* **2021**, *11*, 701998. [CrossRef]
6. Peeters, S.T.; Heemsbergen, W.D.; Koper, P.C.; van Putten, W.L.; Slot, A.; Dielwart, M.F.; Bonfrer, J.M.; Incrocci, L.; Lebesque, J.V. Dose-response in radiotherapy for localized prostate cancer: Results of the Dutch multicenter randomized phase III trial comparing 68 Gy of radiotherapy with 78 Gy. *J. Clin. Oncol.* **2006**, *24*, 1990–1996. [CrossRef] [PubMed]
7. Zelefsky, M.J.; Kollmeier, M.; Cox, B.; Fidaleo, A.; Sperling, D.; Pei, X.; Carver, B.; Coleman, J.; Lovelock, M.; Hunt, M. Improved clinical outcomes with high-dose image guided radiotherapy compared with non-IGRT for the treatment of clinically localized prostate cancer. *Int. J. Radiat. Oncol. Biol. Phys.* **2012**, *84*, 125–129. [CrossRef] [PubMed]
8. Zelefsky, M.J.; Pei, X.; Chou, J.F.; Schechter, M.; Kollmeier, M.; Cox, B.; Yamada, Y.; Fidaleo, A.; Sperling, D.; Happersett, L.; et al. Dose escalation for prostate cancer radiotherapy: Predictors of long-term biochemical tumor control and distant metastases-free survival outcomes. *Eur. Urol.* **2011**, *60*, 1133–1139. [CrossRef] [PubMed]
9. Hall, W.A.; Fox, T.H.; Jiang, X.; Prabhu, R.S.; Rossi, P.J.; Godette, K.; Jani, A.B. Treatment efficiency of volumetric modulated arc therapy in comparison with intensity-modulated radiotherapy in the treatment of prostate cancer. *J. Am. Coll. Radiol.* **2013**, *10*, 128–134. [CrossRef]
10. Khan, M.I.; Jiang, R.; Kiciak, A.; Ur Rehman, J.; Afzal, M.; Chow, J.C. Dosimetric and radiobiological characterizations of prostate intensity-modulated radiotherapy and volumetric-modulated arc therapy: A single-institution review of ninety cases. *J. Med. Phys.* **2016**, *41*, 162–168. [CrossRef]
11. Susil, R.C.; McNutt, T.R.; DeWeese, T.L.; Song, D. Effects of prostate-rectum separation on rectal dose from external beam radiotherapy. *Int. J. Radiat. Oncol. Biol. Phys.* **2010**, *76*, 1251–1258. [CrossRef] [PubMed]
12. Leiker, A.J.; Desai, N.B.; Folkert, M.R. Rectal radiation dose-reduction techniques in prostate cancer: A focus on the rectal spacer. *Future Oncol.* **2018**, *14*, 2773–2788. [CrossRef] [PubMed]
13. Mok, G.; Benz, E.; Vallee, J.P.; Miralbell, R.; Zilli, T. Optimization of radiation therapy techniques for prostate cancer with prostate-rectum spacers: A systematic review. *Int. J. Radiat. Oncol. Biol. Phys.* **2014**, *90*, 278–288. [CrossRef] [PubMed]
14. Vaggers, S.; Rai, B.P.; Chedgy, E.C.P.; de la Taille, A.; Somani, B.K. Polyethylene glycol-based hydrogel rectal spacers for prostate brachytherapy: A systematic review with a focus on technique. *World J. Urol.* **2021**, *39*, 1769–1780. [CrossRef] [PubMed]
15. Melchert, C.; Gez, E.; Bohlen, G.; Scarzello, G.; Koziol, I.; Anscher, M.; Cytron, S.; Paz, A.; Torre, T.; Bassignani, M.; et al. Interstitial biodegradable balloon for reduced rectal dose during prostate radiotherapy: Results of a virtual planning investigation based on the pre- and post-implant imaging data of an international multicenter study. *Radiother. Oncol.* **2013**, *106*, 210–214. [CrossRef] [PubMed]
16. Pasquier, D.; Bogart, E.; Bonodeau, F.; Lacornerie, T.; Lartigau, E.; Latorzeff, I. BioPro-RCMI-1505 trial: Multicenter study evaluating the use of a biodegradable balloon for the treatment of intermediate risk prostate cancer by intensity modulated radiotherapy; study protocol. *BMC Cancer* **2018**, *18*, 566. [CrossRef] [PubMed]
17. Schorghofer, A.; Drerup, M.; Kunit, T.; Lusuardi, L.; Holzinger, J.; Karner, J.; Groher, M.; Zoubek, C.; Forstner, R.; Sedlmayer, F.; et al. Rectum-spacer related acute toxicity—Endoscopy results of 403 prostate cancer patients after implantation of gel or balloon spacers. *Radiat. Oncol.* **2019**, *14*, 47. [CrossRef]
18. Vanneste, B.G.L.; van De Beek, K.; Lutgens, L.; Lambin, P. Implantation of a biodegradable rectum balloon implant: Tips, Tricks and Pitfalls. *Int. Braz. J. Urol.* **2017**, *43*, 1033–1042. [CrossRef]
19. Vanneste, B.G.L.; van Wijk, Y.; Lutgens, L.C.; Van Limbergen, E.J.; van Lin, E.N.; van de Beek, K.; Lambin, P.; Hoffmann, A.L. Dynamics of rectal balloon implant shrinkage in prostate VMAT: Influence on anorectal dose and late rectal complication risk. *Strahlenther. Onkol.* **2018**, *194*, 31–40. [CrossRef]
20. Basu, A.; Haim-Zada, M.; Domb, A.J. Biodegradable inflatable balloons for tissue separation. *Biomaterials* **2016**, *105*, 109–116. [CrossRef]
21. Haim Zada, M.; Kumar, A.; Elmalak, O.; Markovitz, E.; Icekson, R.; Domb, A.J. In vitro and in vivo degradation behavior and the long-term performance of biodegradable PLCL balloon implants. *Int. J. Pharm.* **2020**, *574*, 118870. [CrossRef] [PubMed]

22. Ramot, Y.; Steiner, M.; Lavie, Y.; Ezov, N.; Laub, O.; Cohen, E.; Schwartz, Y.; Nyska, A. Safety and efficacy of sFilm-FS, a novel biodegradable fibrin sealant, in Gottingen minipigs. *J. Toxicol. Pathol.* **2021**, *34*, 319–330. [CrossRef] [PubMed]
23. De Jong, W.H.; Eelco Bergsma, J.; Robinson, J.E.; Bos, R.R. Tissue response to partially in vitro predegraded poly-L-lactide implants. *Biomaterials* **2005**, *26*, 1781–1791. [CrossRef] [PubMed]
24. Schafer, K.A.; Eighmy, J.; Fikes, J.D.; Halpern, W.G.; Hukkanen, R.R.; Long, G.G.; Meseck, E.K.; Patrick, D.J.; Thibodeau, M.S.; Wood, C.E.; et al. Use of Severity Grades to Characterize Histopathologic Changes. *Toxicol. Pathol.* **2018**, *46*, 256–265. [CrossRef] [PubMed]
25. Onuki, Y.; Bhardwaj, U.; Papadimitrakopoulos, F.; Burgess, D.J. A review of the biocompatibility of implantable devices: Current challenges to overcome foreign body response. *J. Diabetes Sci. Technol.* **2008**, *2*, 1003–1015. [CrossRef] [PubMed]
26. Ramot, Y.; Nyska, A.; Markovitz, E.; Dekel, A.; Klaiman, G.; Zada, M.H.; Domb, A.J.; Maronpot, R.R. Long-term Local and Systemic Safety of Poly(L-lactide-co-epsilon-caprolactone) after Subcutaneous and Intra-articular Implantation in Rats. *Toxicol. Pathol.* **2015**, *43*, 1127–1140. [CrossRef] [PubMed]
27. Schuh, J.C. Medical device regulations and testing for toxicologic pathologists. *Toxicol. Pathol.* **2008**, *36*, 63–69. [CrossRef]

pharmaceutics

MDPI

Article

The Complexity of Bariatric Patient's Pharmacotherapy: Sildenafil Biopharmaceutics and Pharmacokinetics before vs. after Gastric Sleeve/Bypass

Daniel Porat [1], Oleg Dukhno [2], Sandra Cvijić [3] and Arik Dahan [1,*]

[1] Department of Clinical Pharmacology, School of Pharmacy, Faculty of Health Sciences, Ben-Gurion University of the Negev, P.O. Box 653, Beer-Sheva 8410501, Israel; poratdan@post.bgu.ac.il
[2] Department of Surgery B, Soroka University Medical Center, Beer-Sheva 8410101, Israel; dukhnoo@bgu.ac.il
[3] Department of Pharmaceutical Technology and Cosmetology, Faculty of Pharmacy, University of Belgrade, Vojvode Stepe 450, 11221 Belgrade, Serbia; sandra.cvijic@pharmacy.bg.ac.rs
* Correspondence: arikd@bgu.ac.il; Tel.: +972-8-6479483; Fax: +972-8-6479303

Abstract: Postbariatric altered gastrointestinal (GI) anatomy/physiology may significantly harm oral drug absorption and overall bioavailability. In this work, sildenafil, the first phosphodiesterase-5 (PDE5) inhibitor, was investigated for impaired postbariatric solubility/dissolution and absorption; this research question is of particular relevance since erectile dysfunction (ED) is associated with higher body mass index (BMI). Sildenafil solubility was determined both in vitro and ex vivo, using pre- vs. postsurgery gastric contents aspirated from patients. Dissolution tests were done in conditions mimicking the stomach before surgery, after sleeve gastrectomy (post-SG, pH 5), and after one anastomosis gastric bypass (post-OAGB, pH 7). Finally, these data were included in physiologically based pharmacokinetic (PBPK) modelling (GastroPlus®) to simulate sildenafil PK before vs. after surgery. pH-dependent solubility was demonstrated with low solubility (0.3 mg/mL) at pH 7 vs. high solubility at pH 1–5, which was also confirmed ex vivo with much lower solubility values in postbariatric gastric samples. Hampered dissolution of all sildenafil doses was obtained under post-OAGB conditions compared with complete (100%) dissolution under both presurgery and post-SG conditions. PBPK simulations revealed delayed sildenafil absorption in postbariatric patients (increased t_{max}) and reduced C_{max}, especially in post-OAGB patients, relative to a presurgery state. Hence, the effect of bariatric surgery on sildenafil PK is unpredictable and may depend on the specific bariatric procedure. This mechanistically based analysis suggests a potentially undesirable delayed onset of action of sildenafil following gastric bypass surgery.

Keywords: bariatric surgery; oral absorption; gastric pH; ex vivo solubility; postbariatric dissolution; delayed onset; phosphodiesterase-5 inhibitors; physiologically based pharmacokinetic modeling; erectile dysfunction

1. Introduction

Obesity is a major factor contributing to the development of serious medical conditions, including diabetes, hyperlipidemia, and cardiovascular disease. Obesity is also associated with other medical issues such as erectile dysfunction (ED). The prevalence of ED is higher in men with a body mass index (BMI) of 25–30 kg/m^2, compared to men with a BMI below 25 kg/m^2, and higher still in men with a BMI over 30 kg/m^2 [1]. This association is related to both pathophysiological and psychological factors. Pathophysiological factors include reduced synthesis of nitric oxide (NO), lower plasma testosterone levels, endothelial dysfunction, and dyslipidaemia [2]. Psychological factors include low self esteem, stress, and anxiety associated with excessive weight.

Bariatric surgery is a highly effective approach towards the treatment of patients with severe obesity. Significant and long-lasting weight loss is achieved in many cases, as well

as the resolution of related comorbidities. As of 2023, there are several bariatric surgery procedures commonly performed, including sleeve gastrectomy (SG), one-anastomosis gastric bypass (OAGB), and Roux-en-Y gastric bypass (RYGB). Bariatric surgery was also shown to have a positive effect on sexual satisfaction and erectile function [3–6]. This may be related to weight loss [7,8] and overall improved body image [9,10]. However, in many cases, erectile dysfunction may still be a problem after these surgeries.

The first line and most common treatment of erectile dysfunction nowadays is oral phosphodiesterase-5 inhibitors (PDE5i), with attributes of high safety, rapid efficacy and noninvasiveness [11,12]. Following sexual stimulation, NO is released from endothelial cells. NO interacts with guanylyl cyclase in smooth muscle cells, resulting in the synthesis of cGMP from GMP. PDE5i prevents the hydrolysis of cGMP by PDE5, thus allowing penile smooth muscle relaxation, leading to increased arterial blood flow and erection [13]. However, to be effective, these drugs require satisfactory absorption from the gastrointestinal tract (GIT) into the bloodstream, a process dependent upon various factors related to the drug properties, the drug product (formulation, excipients), and the GIT physiology [14,15].

Following bariatric surgery, the GIT anatomy/physiology is significantly altered. 80–90% of the stomach is excised, resulting in decreased gastric volume, acidity, contractility, and residence time [16,17]. These changes may severely hamper the dissolution of the drug dose, a prerequisite for drug absorption [18,19]. Some drugs, including those with limited water solubility, high dose, and a weakly basic nature, are more prone and may be more sensitive to these postbariatric changes than others [20,21].

Sildenafil is the first and main PDE5i, approved for ED treatment, as well as for pulmonary arterial hypertension. It has a weakly basic, pH-dependent solubility nature [22]. Sildenafil is among the 200 most commonly prescribed medications in the US (2020) and the 1st among all ED drugs, with ~3 million prescriptions annually (ClinCalc.com (accesses on 15 December 2023); therefore, it is clinically relevant and significant to study the use of this drug in the growing population of bariatric patients (∼700,000 surgeries annually worldwide). The pH-dependent solubility of sildenafil was studied in vitro, as well as ex vivo, in aspirated gastric contents obtained from patients pre- vs. postbariatric surgery. Then, a recently developed biorelevant in vitro dissolution technique was used to mimic the post-SG/OAGB gastric conditions and study the sildenafil product (Viagra®) dissolution pre- vs. postbariatric surgery. Finally, advanced physiologically based pharmacokinetic (PBPK) models were developed to simulate the absorption and pharmacokinetic changes in sildenafil pre- vs. postbariatric surgery. Altogether, this mechanistic research reveals the complexity involved in pharmacotherapy management after bariatric surgery, attempting to predict potential postbariatric treatment failure in advance for the benefit of this growing patient population.

2. Materials and Methods

2.1. Materials

Sildenafil citrate powder (Carbosynth Limited, Berkshire, UK) was used for the solubility studies. Sildenafil citrate (Viagra®, Pfizer Inc., New York, NY, USA) tablets of 25, 50 and 100 mg were used in the dissolution tests. The following materials from Sigma-Aldrich (Chemie GmbH, Steinheim, Germany) were used for buffer preparation: acetic acid, maleic acid, sodium phosphate monobasic, sodium dodecyl sulfate (SDS), hydrochloric acid, sodium hydroxide, and sodium chloride. Water and acetonitrile of ultraperformance liquid chromatography (UPLC)-grade were purchased from Bio-Lab Ltd. (Ashkelon, Israel).

2.2. In Vitro Solubility

The equilibrium solubility of sildenafil was determined using the shake-flask method, described previously [23,24]. pH 1 and pH 3 (maleate 0.2 M), pH 5 (acetate 0.2 M), and pH 7 (phosphate 0.2 M) buffers were used. Quadruplets (n = 4) for each pH were produced by excess drug powder added to vials containing 500 µL of the solution medium. Vials were incubated for 24 h at 37 °C and shaken at 200 rpm (Orbital Shaker Incubator, MRC

Laboratory Instruments, Holon, Israel). Next, the samples were then moved to Eppendorf tubes and centrifuged (Centrifuge 5430 R, Eppendorf®, Hamburg, Germany) at 20,817× *g* and 37 °C for 10 min. Then, supernatants were diluted as needed (by a factor of 10 or 40, depending on solubility) and immediately analyzed by UPLC-PDA.

2.3. Ex Vivo Solubility

The solubility of sildenafil in gastric fluid was determined using the above-mentioned shake-flask method. Excess drug powder was added to glass vials containing gastric fluid at a fasted state, aspirated from three bariatric patients (one SG, one RYGB, and one OAGB) in the perioperative time through the nasogastric tube, before and one day after surgery. The study protocol was approved by the institutional review board of the Ben-Gurion University School of Medicine (institutional board request number 0248-18-SOR) and informed consent was obtained presurgery from all patients. pH measurements and recording were done immediately after gastric content collection; the content was vortexed, and 2 mL of gastric fluid were centrifuged for 10 min at 20,817× *g* and 25 °C; 400 µL of supernatant fluid was used in the solubility experiment [20,21]. Samples with appropriate pH [16] and sufficient gastric fluid volume were chosen for the solubility study. The experimental process and conditions were similar to the solubility study in vitro (Section 2.2) with the additional step of sample filtering prior to UPLC analysis. Dilutions were made with an acidic buffer after the removal of any undissolved drug.

2.4. In Vitro Dissolution

The dissolution of sildenafil, 25, 50 and 100 mg whole tablets, was studied in three different conditions: (1) pH 1 maleate, 250 mL medium, using USP dissolution apparatus II (Premiere 5100, Distek®, North Brunswick, NJ, USA), and with a paddle rotated at 100 rpm [25,26]; (2) pH 5 acetate, 50 mL (+0.05% SDS) medium; and (3) pH 7 phosphate, 50 mL (+0.05% SDS) medium, using 50 mL round-bottom flask inside a water bath with a minipaddle rotated at 153 rpm. This rotation-speed calculation was previously described [20,21,27]. SDS was used to prevent precipitation of the dissolved drug. A temperature of 37 ± 0.5 °C was maintained throughout the dissolution study. These conditions mimic the intragastric parameters before and after bariatric surgery, including pH, fluid volume, temperature, and gastric contractility. Samples of 300 µL were drawn at 5, 10, 15, 20, 30, 40, 50, 60, 75, and 90 min, filtered, and centrifuged for 12 min at 20,817× *g* (37 °C) before UPLC analysis.

2.5. Analytical Method

Sample analysis was performed using UPLC with Waters Acquity H-Class system equipped with a PDA detector and controlled by Empower software (EMP 2 Feature release 5, Built 2154). The analytical method followed the previous publication [28], and it is detailed in Table 1. The ambient temperature of the column and samples was used. Linear (R^2 = 0.999) calibration curves were obtained for each pH in the relevant drug-concentration ranges. Inter- and intraday coefficients of variation were lower than 1%. The stability of sildenafil over the experimental course was verified.

Table 1. UPLC-PDA analytic method for solubility/dissolution studies of sildenafil.

Drug	Column	Mobile Phase	Flow Rate (mL/min)	Injection Volume (µL)	Total Run Time (min)	Retention Time (min)	Detection Wavelength (nm)
Sildenafil	Waters XBridge C8, 3.5 µm, 4.6 × 150 mm	Water:Acetonitrile (+0.1% trifluoroacetic acid), 90:10 to 15:85 (*v*/*v*), gradient	1.0	5	5.0	4.0	294

2.6. Physiologically Based Pharmacokinetic (PBPK) Modeling

Drug-specific PBPK models were constructed using GastroPlus® software (version 9.8.3012; Simulations Plus Inc., Lancaster, CA, USA). The software predicts the dissolution, absorption, and disposition of a drug based on its physicochemical and PK properties, in conjunction with the parameters describing the physiological characteristics of the human gastrointestinal (GI) tract. These physiological parameters are integrated into the software-specific advanced compartmental absorption and transit (ACAT) model of the GI tract and accounted for in a series of differential equations used to simulate the dynamic processes a drug undergoes in the body after peroral administration [29,30]. Physiological parameters describing a healthy human representative in the fasted state were kept at the software default values, except for the % fluid volumes in the small intestine (23%) and colon (0.5%), which were decreased from the default 40% and 10% to 23% and 0.5% [31], respectively, to account for the much smaller GI volumes in vivo [32–34]. To account for postbariatric surgery changes in physiological conditions, the ACAT model parameters were manually adjusted, i.e., gastric volume was decreased from default 50 to 10 mL, corresponding to 20% of the presurgery gastric volume [35,36], and gastric transit time was decreased from default 0.25 to 0.12 h [37,38]. The simulations were also performed for bypassed duodenum and jejunum physiology in post-OAGB patients, setting the volume, length, and transit time for the duodenum and jejunum 1 and 2 segments to zero [20,36]. Moreover, stomach pH was increased from default pH 1.3 to pH 5.0 (post-SG) and pH 7.0 (post-OAGB) to account for the influence of the different bariatric procedures and gastric pH on drug dissolution and absorption [16,39]. Intestinal pH was not altered [39].

The input values regarding properties of sildenafil were taken from the literature, in silico predicted (ADMET Predictor® module, version 10.4.0.0; Simulations Plus Inc., Lancaster, CA, USA) based on the structure of the drug or experimentally determined, as depicted in Table 2. Drug dissolution throughout the GI tract was calculated using the software default Johnson equation [40] that accounts for a drug's solubility and particle size. In the absence of data on drug particle size in the commercial products, an approximate value of 100 μm was used for all simulations. Considering the poor aqueous solubility, the models also accounted for the effect of bile salts on drug solubility and dissolution.

Pharmacokinetic parameters describing the distribution and elimination of the tested drug were estimated from the in vivo data on drug plasma concentration over time following intravenous (i.v.) and/or peroral drug dosing, using the software integrated PKPlus™ module and, if needed, further optimized, while keeping the final values within the range reported in literature Table 2.

The predictive power of the designed models was assessed by comparing the predicted with the in vivo observed values for the maximum plasma concentration (C_{max}), time to reach C_{max} (t_{max}) and area under the plasma concentration time curve (AUC_{0-inf}) for different drug doses given to healthy human subjects in the fasted state. The predicted values referred to a healthy human representative, and the in vivo values were digitized (DigIt software, version 1.0.4; Simulations Plus, Inc., Lancaster, CA, USA) from the mean profiles observed in clinical studies and published in the literature [41–43]. A comparison was performed by calculating fold errors between the observed and predicted data, whereas the fold error represents the ratio between the predicted and observed values. According to the commonly applied criteria, a 2-fold error can be considered acceptable for most drugs, although tighter boundaries in the 1.5-fold range could be more appropriate for drugs with, e.g., low variable pharmacokinetics and vice versa, less stringent 2.5-fold criterium may apply for drugs with high pharmacokinetic variability [44,45]. Additionally, the coefficient of determination (R^2) was used to evaluate linearity between the observed and predicted values.

Table 2. Input parameters for sildenafil PBPK models.

	Value	Source/Ref
Molecular weight (g/mol)	474.59	/
LogP/LogD	2.7 (pH 7.4)	[46]
Solubility at 37 °C (mg/mL)	30 (pH 1); 2 (pH 3); 3.1 (pH 5); 0.3 (pH 7)	Experimental
pKa(s)	1.72 (base); 6.03 (base); 8.74 (acid)	predicted using ADMET Predictor® module, then fitted (software integrated option) to the experimental pH solubility profile
Human effective permeability, Peff (cm/s)	4.48×10^{-4}	[47]
Diffusion coefficient (cm^2/s)	0.6006×10^{-5}	software calculated (based on drug molecular weight)
Particle diameter (μm)	100	Approximated
Mean precipitation time (s)	900	software default
Drug dose (mg) (dosage form)	20 [a], 25, 100 (tablet); 50 (tablet, capsule [a])	/
Volume of fluid taken with drug (mL)	250 (presurgery); 50 (postsurgery)	software default or decreased by 80% to comply with the smaller gastric volume [35] and limited volume of fluid the bariatric patient can ingest
Blood/plasma concentration ratio	0.81	predicted using ADMET Predictor® module
Plasma fraction unbound (%)	4	[46,48]
First pass effect, FPE (%)	60	optimized to comply with the literature's reported values [46,49,50]
Clearance, CL (L/h/kg)	0.556	estimated using PKPlus™ module, based on the in vivo data for i.v. drug dose [42]; comply with the reported data [41]
Volume of distribution, Vd (L/kg)	1.112	
Distribution constant k_{12} (1/h)	0.049	
Distribution constant k_{21} (1/h)	0.292	
Elimination half life, $t_{1/2}$ (h)	2.83	software calculated; complies with the reported data [46,49]

[a] solely for the model validation.

3. Results

3.1. Sildenafil Solubility

The in vitro solubility of sildenafil decreased with the increasing pH. At pH 1, the solubility was over 30 mg/mL; however, at pH 7, sildenafil had low solubility, 0.3 mg/mL, representing an over 100-fold decrease. The ex vivo solubility in intragastric contents from pre- vs. postbariatric patients (Table 3) was consistent with the in vitro solubility results showing a >100-fold decreased solubility for sildenafil postsurgery (Figure 1; Table 4).

Table 3. Patient characteristics include measured intragastric pH before vs. day after bariatric surgery. RYGB, Roux-en-Y gastric bypass; OAGB, one-anastomosis gastric bypass; SG, sleeve gastrectomy.

Patient	Age	Gender	BMI	Procedure	Presurg pH	Postsurg pH
1	49	male	43	RYGB	2.7	6.8
2	51	female	39	OAGB	1.5	7.2
3	25	male	71	SG	2.0	7.0

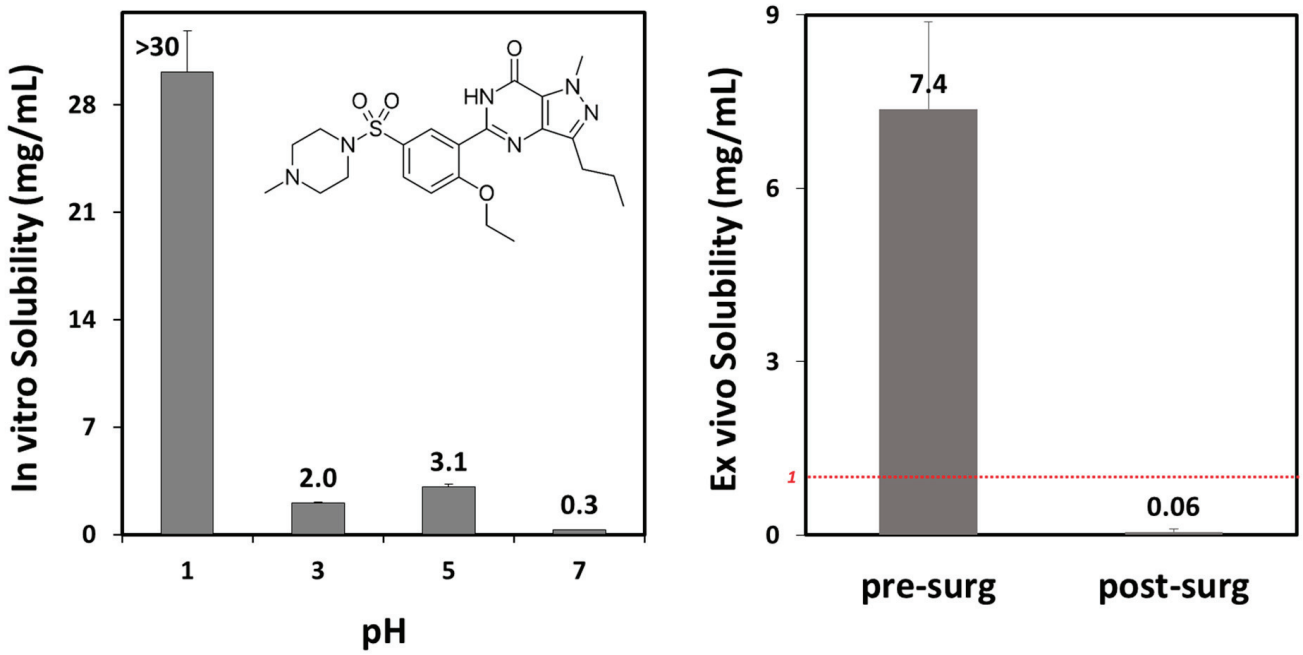

Figure 1. Sildenafil in vitro solubility as a function of pH ((**left**) panel) and ex vivo solubility in gastric fluid aspirated from three patients before ((**left**) column; mean pH 2.0) vs. after ((**right**) column; mean pH 7.0) bariatric surgery. The red dashed line represents the solubility threshold for complete postbariatric dose dissolution. Data presented as mean (SD); $n = 4$ for each pH; $n = 3$ for each experimental group.

Table 4. In vitro and ex vivo saturation solubility of sildenafil. Data presented as mean (SD); in vitro, $n = 4$; ex vivo, $n = 3$.

		In Vitro				Ex Vivo	
Conditions	**Medium**	**Maleate Buffer**	**Maleate Buffer**	**Acetate Buffer**	**Phosphate Buffer**	**Presurgery Stomach Content**	**Postsurgery Stomach Content**
	pH	1	3	5	7	2.1 (0.6)	7.0 (0.2)
Solubility (mg/mL)		>30	2.0 (0.09)	3.1 (0.2)	0.3 (0.03)	7.4 (1.5)	0.06 (0.05)

3.2. In Vitro Dissolution

The dissolution of sildenafil was complete (100%) in presurgery, pH 1 conditions and in post-SG, pH 5 conditions. However, in post-OAGB, pH 7 conditions, sildenafil dissolution was severely hampered, with less than 10% of the sildenafil dissolved from its drug products (Figure 2). In other words, while in presurgery conditions, the dissolution of sildenafil is complete, in postsurgery conditions, sildenafil dissolution depends on the pH.

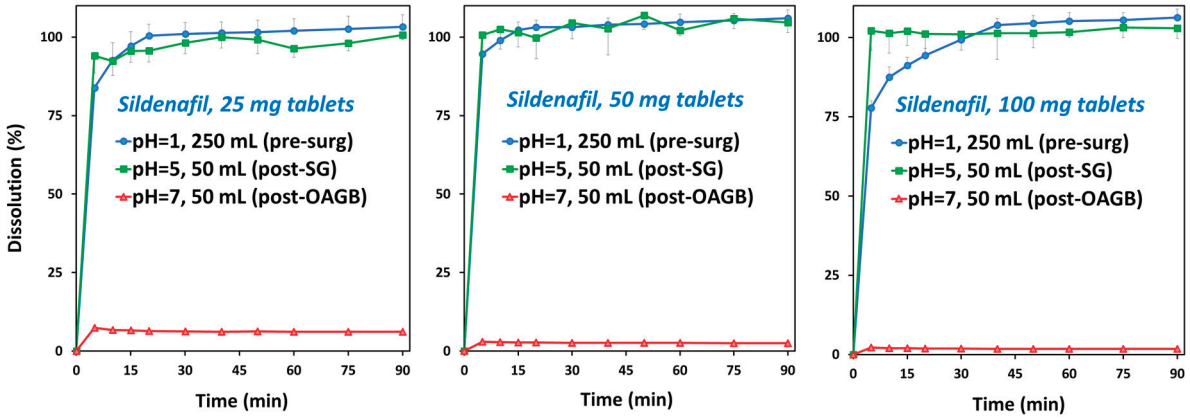

Figure 2. Sildenafil in vitro dissolution of commercially available Viagra® tablets of 25 mg ((**left**) panel), 50 mg ((**middle**) panel) and 100 mg ((**right**) panel). The 250 mL at pH 1 medium (blue circles) represents presurgery stomach state, 50 mL at pH 5 medium (green squares) represents post-SG conditions, and 50 mL at pH 7 medium (red triangles) represents post-OAGB gastric scenario. Average (SD); n = 4 for each experimental group.

3.3. Physiologically Based Pharmacokinetic (PBPK) Simulations

The simulated pharmacokinetic parameters (C_{max}, t_{max}, AUC_{0-inf}) for different oral doses of sildenafil coincide well with the mean data observed in clinical studies (Supplementary Table S1), demonstrating the acceptable prediction power of the designed PBPK models. The presurgery simulated plasma concentrations relate well with the available data from human studies, both for 50 mg and 100 mg sildenafil doses (Figure 3). According to the calculated R^2 values (Supplementary Table S1), there is a linear relationship between the simulated and observed data. The predictions for sildenafil are within the 1.5-fold range (0.67–1.50), except for AUC_{0-inf} for 100 mg sildenafil dose (fold error 0.66) which complies with the two-fold criterion (range between 0.5 and 2.0). A larger deviation of the predicted AUC_{0-inf} from the mean in vivo data in the case of 100 mg sildenafil dose can be explained by a slightly nonproportional increase in systemic drug exposure with an increased drug dose, which was attributed to the saturation of elimination pathways [51]. However, the degree of nonproportionality for doses up to 200 mg is considered small and not clinically significant [49,51]. Moreover, sildenafil exhibits pronounced interindividual pharmacokinetic variability [50] implying that a two-fold prediction error is acceptable for this compound.

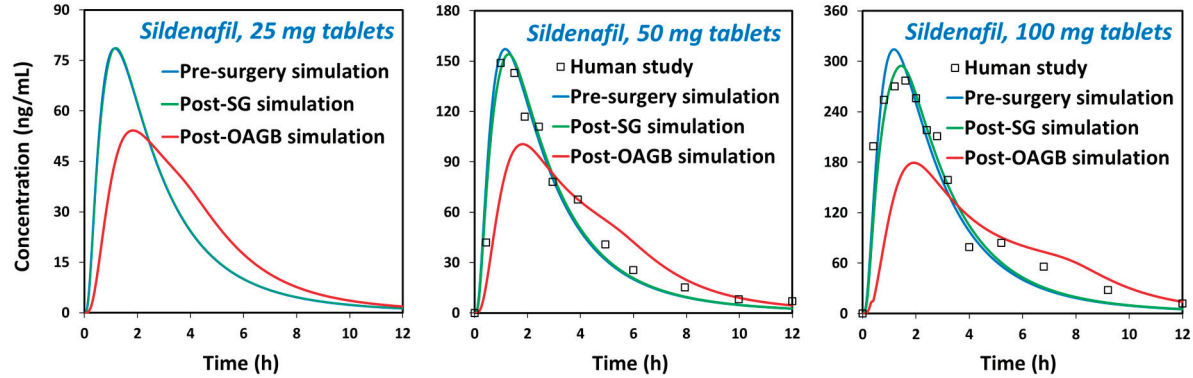

Figure 3. The predicted plasma concentration time profiles under presurgery, post-SG, and post-OAGB states for sildenafil 25 mg ((**left**) panel), 50 mg ((**middle**) panel), and 100 mg ((**right**) panel). Square markers represent the mean values observed in human studies (50 mg, Nichols et al.; 100 mg, Alwhaibi et al.) [41,49].

The designed drug-specific PBPK models were eventually used to estimate in vivo dissolution and absorption of sildenafil in postbariatric vs. nonoperated subjects and to mechanistically explain the combined influence of drug physicochemical and physiological factors on its systemic exposure.

The prediction results for sildenafil (Figure 3, Supplementary Table S2) indicate delayed drug absorption in postbariatric patients (increased t_{max}) and reduced C_{max} values, especially in post-OAGB patients in comparison to a presurgery state. Moreover, the reduction in C_{max} was more pronounced with an increasing drug dose, reaching a 43% reduction in a post-OAGB state for a 100 mg sildenafil dose. Another observation regarding sildenafil plasma exposure is that the increase in stomach pH from pH 5 to pH 7 reduces C_{max} and prolonges t_{max}, which can be explained by delayed overall drug dissolution in cases of less acidic stomach pH (Figure 4, left panel). These results are in line with the experimental data showing a notable decline in drug solubility and postsurgery gastric dissolution when the pH changes from pH 5 to pH 7 (Figures 1 and 2). As a consequence of reduced gastric dissolution, there is a marked drop in sildenafil absorption from the subsequent GI compartment (duodenum in post-SG patients and ileum 1 in post-OAGB patients), as visible from the simulated regional absorption distribution (Figure 4, right panel). However, the overall sildenafil plasma exposure (total percent absorbed in Figure 3 and AUC in Supplementary Table S2) does not seem to be affected by the altered GI conditions after bariatric surgery. Namely, according to the simulation results, even a 100 mg drug dose will eventually dissolve in the GI tract, and high drug permeability will enable sufficient drug absorption from the subsequent GI compartments (Figures 3 and 4, right panel).

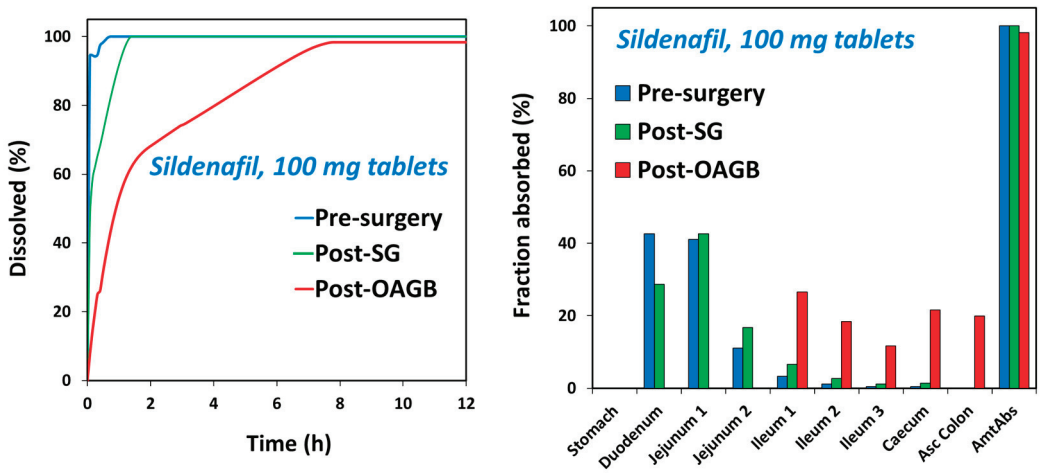

Figure 4. The predicted in vivo dissolution ((**left**) panel) and the predicted GI tract regional absorption ((**right**) panel) profiles under presurgery, post-SG, and post-OAGB states for sildenafil 100 mg tablets.

4. Discussion

This work shows that the solubility of sildenafil may be significantly lower in postbariatric conditions, resulting in potentially hampered dissolution of the drug dose. For sildenafil, the postoperative gastric pH is a crucial factor. This observation is attributed to its pKa value of ~6.7 [52], so that highly increased intragastric pH, such as that measured for some postbariatric patients (especially those undergoing bypass procedures) may result in dramatically lower solubility [16]. In fact, low solubility was observed in high pH (~7) gastric fluids from patients after different bariatric procedures. This indicates that, while some patients may have unaltered sildenafil pharmacokinetics after bariatric surgery, others may experience treatment failure related to insufficient drug absorption and exposure [20,53].

Bariatric surgery may prolong the absorption half life, especially in bypass procedures. For many orally administered drugs, absorption occurs from the upper part of the small intestine [54,55], and, when bypassed, the full drug dose may only be absorbed later, as dis-

tally as the large intestine [20,56]. It should be highlighted that, particularly with sildenafil, the onset of action is desired to be as immediate as possible, and, hence, altered/delayed absorption (with lower C_{max} and longer T_{max}) following gastric bypass is detrimental to treatment success, even with an unaffected AUC.

Sildenafil is increasingly popular, and, in the US as of 2020, sildenafil had ~3 million prescriptions [57]. As mentioned, people with obesity are even more likely to experience ED and be treated with PDE5i. Bariatric surgery may improve sexual function among people with obesity; however, no data is available on changes in PDE5i use after surgery [58]. It is likely that many people will still require PDE5i after bariatric surgery. For one, weight loss along with its beneficial effects is not immediate, so continuation is expected for at least the first few months [59]. Second, when the underlying cause of ED is unrelated to weight, then the surgery itself is unlikely to solve the problem. Third, drugs taken by the patients may cause ED, e.g., in psychiatry; a high percentage of people undergoing bariatric surgery have a psychiatric background [60]. In fact, one year after bariatric surgery, the prevalence of psychiatric conditions is even higher than prior to surgery [61]. Many of the most commonly prescribed psychotropic drugs are likely to cause ED, so for these patients, erectile problems may well persist [62]. Fourth, while long-term weight loss is achieved in many cases, the phenomenon of weight regain is well known and quite common [63]. For all these reasons, PDE5i use, and in particular sildenafil, is expected to be highly relevant among patients who underwent bariatric surgery.

Previous studies predicted hampered dissolution, resulting in decreased blood levels for weakly basic drugs with particularly low pKa. These drugs were lamotrigine [21] (pKa = 5.7), loratadine [20] (pKa = 4.5), and etoricoxib (pKa = 4.6) [56]. Here, we showed that a basic drug with pKa in the upper limit of the physiological range (pKa ~6.7) is also sensitive to increased intragastric pH after bariatric surgery, suggesting that multiple other drugs with similar pKa values may also have altered dissolution and absorption following these procedures. One such drug is vardenafil, another important PDE5i; given the high structural similarity and common basic nature, the postbariatric predictions for sildenafil may apply to vardenafil, as well. In this context, no reported interactions between sildenafil/vardenafil and proton pump inhibitors (PPIs) can be found in the literature. This may be so, given that bariatric surgery also involved the removal of at least 80% of the stomach volume, further contributing to the limited solubility/dissolution. This is not the case in patients not having bariatric surgery who use PPIs.

Other mechanisms involved in the pharmacokinetics of these drugs may also be affected by bariatric surgery [64–68]. For example, the activity of CYP3A enzymes is increased with weight loss [69–71], and since sildenafil is mainly metabolized by CYP3A4, its postbariatric plasma levels may be further decreased.

It is worth mentioning that another drug in this class, udenafil, is currently available in Korea, Russia, and the Philippines and is yet to be approved for use in the USA by the FDA. It is structurally close to sildenafil and vardenafil but is a stronger base and also contains a weakly acidic group. Thus, it is expected to be far less affected by altered intragastric pH after bariatric surgery. It was also found to be weight negative in mice studies [72], implying suitability for this patient population.

5. Conclusions

Delayed absorption of sildenafil after gastric bypass surgery may suggest that ingestion of this drug shortly before intercourse, as normally indicated, may fail to produce the desired effects. In fact, after gastric bypass, patients using sildenafil may need to take this drug hours in advance, which is suboptimal and impractical, to say the least. Time to effect may change from patient to patient, so predicting the proper timing for taking it may not be possible. Indeed, when PDE5i is considered, the absorption rate is as important as its extent.

The issues addressed in this work should be further elucidated in human studies of the pharmacokinetics and pharmacodynamics of the different PDE5i among patients un-

dergoing bariatric surgery, with special emphasis on the comparison between the different bariatric procedures, most specifically sleeve gastrectomy vs. gastric bypass.

Supplementary Materials: The following supporting information can be downloaded at: https://www.mdpi.com/article/10.3390/pharmaceutics15122795/s1, Table S1: Comparison of the simulated and observed pharmacokinetic parameters for sildenafil; Table S2: Percent decrease/increasea in the simulated values of pharmacokinetic parameters for sildenafil before and after bariatric surgery in comparison to pre-surgery state.

Author Contributions: Conceptualization, D.P., S.C. and A.D.; methodology, D.P., O.D., S.C. and A.D.; software, S.C.; validation, D.P., O.D. and S.C.; formal analysis, D.P., S.C. and A.D.; investigation, D.P. and S.C.; resources, S.C. and A.D.; data curation, D.P. and S.C.; writing—original draft preparation, D.P. and S.C.; writing—review and editing, O.D. and A.D.; supervision, A.D.; All authors have read and agreed to the published version of the manuscript.

Funding: This work received no external funding.

Institutional Review Board Statement: The study protocol was approved by the institutional review board of the Ben-Gurion University School of Medicine: Request Number 0248-18-SOR.

Informed Consent Statement: Informed consent was obtained presurgery from all patients.

Data Availability Statement: Data will be made available upon reasonable request.

Conflicts of Interest: The authors have no conflict of interest to declare.

References

1. Chitaley, K.; Kupelian, V.; Subak, L.; Wessells, H. Diabetes, obesity and erectile dysfunction: Field overview and research priorities. *J. Urol.* **2009**, *182*, S45–S50. [CrossRef] [PubMed]
2. Akdemir, A.O.; Karabakan, M.; Aktas, B.K.; Bozkurt, A.; Ozgur, E.G.; Akdogan, N.; Yaris, M. Visceral adiposity index is useful for evaluating obesity effect on erectile dysfunction. *Andrologia* **2019**, *51*, e13282. [CrossRef] [PubMed]
3. Minambres, I.; Sarda, H.; Urgell, E.; Genua, I.; Ramos, A.; Fernandez-Ananin, S.; Balague, C.; Sanchez-Quesada, J.L.; Bassas, L.; Perez, A. Obesity Surgery Improves Hypogonadism and Sexual Function in Men without Effects in Sperm Quality. *J. Clin. Med.* **2022**, *11*, 5126. [CrossRef] [PubMed]
4. Chen, G.; Sun, L.; Jiang, S.; Chen, X.; Zhu, J.; Zhao, X.; Yu, S.; Dong, Z.; Chen, Y.; Zhang, W.; et al. Effects of bariatric surgery on testosterone level and sexual function in men with obesity: A retrospective study. *Front. Endocrinol.* **2022**, *13*, 1036243. [CrossRef] [PubMed]
5. El-Tholoth, H.S.; Bedaiwi, A.K.; Binjawhar, A.; Almulhem, A.A.; Bedaiwi, K.K.; Alshurafa, H.; Alzahrani, T.; Alhussein, R.K.; Alhussein, A.K.; Alnumi, M. Male sexual function after weight-loss surgeries in a group of Saudi population. *Urol. Ann.* **2021**, *13*, 125–129. [CrossRef] [PubMed]
6. Machado, F.P.; Rhoden, E.L.; Pioner, S.R.; Halmenschlager, G.; de Souza, L.V.B.; Lisot, B.C.; Drachler, I.P. Weight Loss Through Bariatric Surgery in Men Presents Beneficial Effects on Sexual Function, Symptoms of Testosterone Deficiency, and Hormonal Profile. *Sex. Med.* **2021**, *9*, 100400. [CrossRef] [PubMed]
7. Li, H.; Xu, W.; Wang, T.; Wang, S.; Liu, J.; Jiang, H. Effect of weight loss on erectile function in men with overweight or obesity: A meta-analysis of randomised controlled trials. *Andrologia* **2022**, *54*, e14250. [CrossRef]
8. Mora, M.; Aranda, G.B.; de Hollanda, A.; Flores, L.; Puig-Domingo, M.; Vidal, J. Weight loss is a major contributor to improved sexual function after bariatric surgery. *Surg. Endosc.* **2013**, *27*, 3197–3204. [CrossRef]
9. Fahmy, A.; Abdeldaiem, H.; Abdelsattar, M.; Aboyoussif, T.; Assem, A.; Zahran, A.; Elgebaly, O. Impact of Bariatric Surgery on Sexual Dysfunction in Obese Men. *Sex. Med.* **2021**, *9*, 100322. [CrossRef]
10. Nimbi, F.M.; Virginia, C.; Cinzia, D.M.; Michela, D.T.; Gianfranco, S.; Emanuela, P. The relation between sexuality and obesity: The role of psychological factors in a sample of obese men undergoing bariatric surgery. *Int. J. Impot. Res.* **2022**, *34*, 203–214. [CrossRef]
11. Wang, C.M.; Wu, B.R.; Xiang, P.; Xiao, J.; Hu, X.C. Management of male erectile dysfunction: From the past to the future. *Front. Endocrinol.* **2023**, *14*, 1148834. [CrossRef] [PubMed]
12. Mykoniatis, I.; Pyrgidis, N.; Sokolakis, I.; Ouranidis, A.; Sountoulides, P.; Haidich, A.B.; van Renterghem, K.; Hatzichristodoulou, G.; Hatzichristou, D. Assessment of Combination Therapies vs Monotherapy for Erectile Dysfunction: A Systematic Review and Meta-analysis. *JAMA Netw. Open* **2021**, *4*, e2036337. [CrossRef] [PubMed]
13. Moncada, I.; Martinez-Salamanca, J.; Ruiz-Castane, E.; Romero, J. Combination therapy for erectile dysfunction involving a PDE5 inhibitor and alprostadil. *Int. J. Impot. Res.* **2018**, *30*, 203–208. [CrossRef] [PubMed]
14. Dahan, A.; Beig, A.; Lindley, D.; Miller, J.M. The solubility-permeability interplay and oral drug formulation design: Two heads are better than one. *Adv. Drug Deliv. Rev.* **2016**, *101*, 99–107. [CrossRef] [PubMed]

15. Martinez, M.N.; Amidon, G.L. A mechanistic approach to understanding the factors affecting drug absorption: A review of fundamentals. *J. Clin. Pharmacol.* **2002**, *42*, 620–643. [CrossRef]
16. Porat, D.; Vaynshtein, J.; Gibori, R.; Avramoff, O.; Shaked, G.; Dukhno, O.; Czeiger, D.; Sebbag, G.; Dahan, A. Stomach pH before vs. after different bariatric surgery procedures: Clinical implications for drug delivery. *Eur. J. Pharm. Biopharm.* **2021**, *160*, 152–157. [CrossRef]
17. Steenackers, N.; Vanuytsel, T.; Augustijns, P.; Tack, J.; Mertens, A.; Lannoo, M.; Van der Schueren, B.; Matthys, C. Adaptations in gastrointestinal physiology after sleeve gastrectomy and Roux-en-Y gastric bypass. *Lancet Gastroenterol. Hepatol.* **2021**, *6*, 225–237. [CrossRef]
18. Azran, C.; Wolk, O.; Zur, M.; Fine-Shamir, N.; Shaked, G.; Czeiger, D.; Sebbag, G.; Kister, O.; Langguth, P.; Dahan, A. Oral drug therapy following bariatric surgery: An overview of fundamentals, literature and clinical recommendations. *Obes. Rev.* **2016**, *17*, 1050–1066. [CrossRef]
19. Porat, D.; Dahan, A. Medication Management after Bariatric Surgery: Providing Optimal Patient Care. *J. Clin. Med.* **2020**, *9*, 1511. [CrossRef]
20. Porat, D.; Dukhno, O.; Vainer, E.; Cvijic, S.; Dahan, A. Antiallergic Treatment of Bariatric Patients: Potentially Hampered Solubility/Dissolution and Bioavailability of Loratadine, but Not Desloratadine, Post-Bariatric Surgery. *Mol. Pharm.* **2022**, *19*, 2922–2936. [CrossRef]
21. Porat, D.; Azran, C.; Mualem, Y.; Vainer, E.; Gibori, R.; Vaynshtein, J.; Dukhno, O.; Dahan, A. Lamotrigine therapy in patients after bariatric surgery: Potentially hampered solubility and dissolution. *Int. J. Pharm.* **2022**, *612*, 121298. [CrossRef] [PubMed]
22. Zucchi, A.; Costantini, E.; Scroppo, F.I.; Silvani, M.; Kopa, Z.; Illiano, E.; Petrillo, M.G.; Cari, L.; Nocentini, G. The first-generation phosphodiesterase 5 inhibitors and their pharmacokinetic issue. *Andrology* **2019**, *7*, 804–817. [CrossRef] [PubMed]
23. Beig, A.; Miller, J.M.; Dahan, A. The interaction of nifedipine with selected cyclodextrins and the subsequent solubility-permeability trade-off. *Eur. J. Pharm. Biopharm.* **2013**, *85*, 1293–1299. [CrossRef] [PubMed]
24. Beig, A.; Agbaria, R.; Dahan, A. The use of captisol (SBE7-beta-CD) in oral solubility-enabling formulations: Comparison to HPbetaCD and the solubility-permeability interplay. *Eur. J. Pharm. Sci.* **2015**, *77*, 73–78. [CrossRef]
25. Fassihi, A.R.; Munday, D.L. Dissolution of theophylline from film-coated slow release mini-tablets in various dissolution media. *J. Pharm. Pharmacol.* **1989**, *41*, 369–372. [CrossRef]
26. Silva, O.S.; Souza, C.R.; Oliveira, W.P.; Rocha, S.C. In vitro dissolution studies of sodium diclofenac granules coated with Eudragit L-30D-55 by fluidized-bed system. *Drug Dev. Ind. Pharm.* **2006**, *32*, 661–667. [CrossRef]
27. Sugano, K. *Biopharmaceutics Modeling and Simulations: Theory, Practice, Methods, and Applications*; Wiley: Hoboken, NJ, USA, 2012.
28. Beig, A.; Dahan, A. Quantification of carbamazepine and its 10,11-epoxide metabolite in rat plasma by UPLC-UV and application to pharmacokinetic study. *Biomed. Chromatogr.* **2014**, *28*, 934–938. [CrossRef]
29. Agoram, B.; Woltosz, W.S.; Bolger, M.B. Predicting the impact of physiological and biochemical processes on oral drug bioavailability. *Adv. Drug Deliv. Rev.* **2001**, *50* (Suppl. 1), S41–S67. [CrossRef]
30. Lin, L.; Wong, H. Predicting Oral Drug Absorption: Mini Review on Physiologically-Based Pharmacokinetic Models. *Pharmaceutics* **2017**, *9*, 41. [CrossRef]
31. Jereb, R.; Opara, J.; Bajc, A.; Petek, B. Evaluating the Impact of Physiological Properties of the Gastrointestinal Tract On Drug In Vivo Performance Using Physiologically Based Biopharmaceutics Modeling and Virtual Clinical Trials. *J. Pharm. Sci.* **2021**, *110*, 3069–3081. [CrossRef]
32. Mudie, D.M.; Murray, K.; Hoad, C.L.; Pritchard, S.E.; Garnett, M.C.; Amidon, G.L.; Gowland, P.A.; Spiller, R.C.; Amidon, G.E.; Marciani, L. Quantification of gastrointestinal liquid volumes and distribution following a 240 mL dose of water in the fasted state. *Mol. Pharm.* **2014**, *11*, 3039–3047. [CrossRef] [PubMed]
33. Murray, K.; Hoad, C.L.; Mudie, D.M.; Wright, J.; Heissam, K.; Abrehart, N.; Pritchard, S.E.; Al Atwah, S.; Gowland, P.A.; Garnett, M.C.; et al. Magnetic Resonance Imaging Quantification of Fasted State Colonic Liquid Pockets in Healthy Humans. *Mol. Pharm.* **2017**, *14*, 2629–2638. [CrossRef] [PubMed]
34. Schiller, C.; Frohlich, C.P.; Giessmann, T.; Siegmund, W.; Monnikes, H.; Hosten, N.; Weitschies, W. Intestinal fluid volumes and transit of dosage forms as assessed by magnetic resonance imaging. *Aliment. Pharmacol. Ther.* **2005**, *22*, 971–979. [CrossRef] [PubMed]
35. Elbanna, H.; Emile, S.; El-Hawary, G.E.; Abdelsalam, N.; Zaytoun, H.A.; Elkaffas, H.; Ghanem, A. Assessment of the Correlation Between Preoperative and Immediate Postoperative Gastric Volume and Weight Loss After Sleeve Gastrectomy Using Computed Tomography Volumetry. *World J. Surg.* **2019**, *43*, 199–206. [CrossRef] [PubMed]
36. Almukainzi, M.; Lukacova, V.; Löbenberg, R. Modelling the Absorption of Metformin with Patients Post Gastric Bypass Surgery. *J. Diabetes Metab.* **2014**, *5*, 1000353. [CrossRef]
37. Dahan, A.; Porat, D.; Markovic, M.; Zur, M.; Kister, O.; Langguth, P. Optimized In Silico Modeling of Drug Absorption after Gastric Bypass: The Case of Metformin. *Pharmaceutics* **2021**, *13*, 1873. [CrossRef]
38. Darwich, A.S.; Pade, D.; Rowland-Yeo, K.; Jamei, M.; Asberg, A.; Christensen, H.; Ashcroft, D.M.; Rostami-Hodjegan, A. Evaluation of an In Silico PBPK Post-Bariatric Surgery Model through Simulating Oral Drug Bioavailability of Atorvastatin and Cyclosporine. *CPT Pharmacomet. Syst. Pharmacol.* **2013**, *2*, e47. [CrossRef]

39. Steenackers, N.; Vanuytsel, T.; Augustijns, P.; Deleus, E.; Deckers, W.; Deroose, C.M.; Falony, G.; Lannoo, M.; Mertens, A.; Mols, R.; et al. Effect of sleeve gastrectomy and Roux-en-Y gastric bypass on gastrointestinal physiology. *Eur. J. Pharm. Biopharm.* **2023**, *183*, 92–101. [CrossRef]
40. Lu, A.T.; Frisella, M.E.; Johnson, K.C. Dissolution modeling: Factors affecting the dissolution rates of polydisperse powders. *Pharm. Res.* **1993**, *10*, 1308–1314. [CrossRef]
41. Alwhaibi, A.; Alsanea, S.; Alrabiah, Z.; Alanazi, F.K.; Al-Hadiya, B.M.; Abou-Auda, H.S. Pharmacokinetic profile of sildenafil citrate in healthy Middle Eastern Males: Comparison with other ethnicities. *Saudi Pharm. J.* **2021**, *29*, 1498–1505. [CrossRef]
42. Food and Drug Administration, Center for Drug Evaluation and Research. Viagra (Sildenafil) "Joint Clinical Review" for NDA-20-895. Available online: https://www.accessdata.fda.gov/drugsatfda_docs/NDA/98/viagra/sect7.PDF (accessed on 15 December 2023).
43. Gao, X.; O'Gorman, M.; Cook, J.; Shi, H.; LaBadie, R.R. A Randomized, Open-Label, 3-Way Crossover Study to Demonstrate Bioequivalence of Sildenafil Powder for Oral Suspension With Tablets Used Commercially and in Clinical Studies for the Treatment of Pulmonary Arterial Hypertension. *Clin. Pharmacol. Drug Dev.* **2012**, *1*, 152–157. [CrossRef] [PubMed]
44. Abduljalil, K.; Cain, T.; Humphries, H.; Rostami-Hodjegan, A. Deciding on success criteria for predictability of pharmacokinetic parameters from in vitro studies: An analysis based on in vivo observations. *Drug Metab. Dispos.* **2014**, *42*, 1478–1484. [CrossRef] [PubMed]
45. Puttrevu, S.K.; Arora, S.; Polak, S.; Patel, N.K. Physiologically Based Pharmacokinetic Modeling of Transdermal Selegiline and Its Metabolites for the Evaluation of Disposition Differences between Healthy and Special Populations. *Pharmaceutics* **2020**, *12*, 942. [CrossRef] [PubMed]
46. Walker, D.K.; Ackland, M.J.; James, G.C.; Muirhead, G.J.; Rance, D.J.; Wastall, P.; Wright, P.A. Pharmacokinetics and metabolism of sildenafil in mouse, rat, rabbit, dog and man. *Xenobiotica* **1999**, *29*, 297–310. [CrossRef] [PubMed]
47. Macente, J.; Nauwelaerts, N.; Russo, F.M.; Deprest, J.; Allegaert, K.; Lammens, B.; Hernandes Bonan, R.; Turner, J.M.; Kumar, S.; Diniz, A.; et al. PBPK-based dose finding for sildenafil in pregnant women for antenatal treatment of congenital diaphragmatic hernia. *Front. Pharmacol.* **2023**, *14*, 1068153. [CrossRef] [PubMed]
48. Salerno, S.N.; Edginton, A.; Gerhart, J.G.; Laughon, M.M.; Ambalavanan, N.; Sokol, G.M.; Hornik, C.D.; Stewart, D.; Mills, M.; Martz, K.; et al. Physiologically-Based Pharmacokinetic Modeling Characterizes the CYP3A-Mediated Drug-Drug Interaction Between Fluconazole and Sildenafil in Infants. *Clin. Pharmacol. Ther.* **2021**, *109*, 253–262. [CrossRef]
49. Nichols, D.J.; Muirhead, G.J.; Harness, J.A. Pharmacokinetics of sildenafil after single oral doses in healthy male subjects: Absolute bioavailability, food effects and dose proportionality. *Br. J. Clin. Pharmacol.* **2002**, *53* (Suppl. 1), 5S–12S. [CrossRef]
50. Jetter, A.; Kinzig-Schippers, M.; Walchner-Bonjean, M.; Hering, U.; Bulitta, J.; Schreiner, P.; Sorgel, F.; Fuhr, U. Effects of grapefruit juice on the pharmacokinetics of sildenafil. *Clin. Pharmacol. Ther.* **2002**, *71*, 21–29. [CrossRef]
51. Gupta, M.; Kovar, A.; Meibohm, B. The clinical pharmacokinetics of phosphodiesterase-5 inhibitors for erectile dysfunction. *J. Clin. Pharmacol.* **2005**, *45*, 987–1003. [CrossRef]
52. Barbas, R.; Llinas, A.; Prohens, R. The Solid State Landscape of the Sildenafil Drug. *J. Pharm. Sci.* **2022**, *111*, 1104–1109. [CrossRef]
53. Mitra, A.; Kesisoglou, F. Impaired drug absorption due to high stomach pH: A review of strategies for mitigation of such effect to enable pharmaceutical product development. *Mol. Pharm.* **2013**, *10*, 3970–3979. [CrossRef] [PubMed]
54. Masaoka, Y.; Tanaka, Y.; Kataoka, M.; Sakuma, S.; Yamashita, S. Site of drug absorption after oral administration: Assessment of membrane permeability and luminal concentration of drugs in each segment of gastrointestinal tract. *Eur. J. Pharm. Sci.* **2006**, *29*, 240–250. [CrossRef] [PubMed]
55. Abuhelwa, A.Y.; Foster, D.J.R.; Upton, R.N. A Quantitative Review and Meta-models of the Variability and Factors Affecting Oral Drug Absorption-Part II: Gastrointestinal Transit Time. *AAPS J.* **2016**, *18*, 1322–1333. [CrossRef] [PubMed]
56. Porat, D.; Dukhno, O.; Partook-Maccabi, M.; Vainer, E.; Cvijic, S.; Dahan, A. Selective COX-2 inhibitors after bariatric surgery: Celecoxib, etoricoxib and etodolac post-bariatric solubility/dissolution and pharmacokinetics. *Int. J. Pharm.* **2023**, *645*, 123347. [CrossRef] [PubMed]
57. ClinCalc.com. The Top 300 Drugs of 2020. Available online: https://clincalc.com/DrugStats/Top300Drugs.aspx (accessed on 15 December 2023).
58. Liu, S.; Cao, D.; Ren, Z.; Li, J.; Peng, L.; Zhang, Q.; Cheng, B.; Cheng, Z.; Ai, J.; Zheng, X.; et al. The relationships between bariatric surgery and sexual function: Current evidence based medicine. *BMC Urol.* **2020**, *20*, 150. [CrossRef] [PubMed]
59. Tenhagen, M.; van Ramshorst, G.H.; Demirkiran, A.; Hunfeld, M.A.; Cense, H.A. Perioperative Online Weight Monitoring in Bariatric Surgery with a Digital Internet-Connected Scale. *Obes. Surg.* **2016**, *26*, 1120–1126. [CrossRef] [PubMed]
60. Sockalingam, S.; Leung, S.E.; Wnuk, S.; Cassin, S.E.; Yanofsky, R.; Hawa, R. Psychiatric Management of Bariatric Surgery Patients: A Review of Psychopharmacological and Psychological Treatments and Their Impact on Postoperative Mental Health and Weight Outcomes. *Psychosomatics* **2020**, *61*, 498–507. [CrossRef] [PubMed]
61. Becerra, A.Z.; Khalid, S.I.; Morgenstern, A.S.; Rembert, E.A.; Carroll, M.M.; Omotosho, P.A.; Torquati, A. The Association Between Bariatric Surgery and Psychiatric Disorders: A National Cohort Study. *Obes. Surg.* **2022**, *32*, 1110–1118. [CrossRef]
62. Trinchieri, M.; Trinchieri, M.; Perletti, G.; Magri, V.; Stamatiou, K.; Cai, T.; Montanari, E.; Trinchieri, A. Erectile and Ejaculatory Dysfunction Associated with Use of Psychotropic Drugs: A Systematic Review. *J. Sex. Med.* **2021**, *18*, 1354–1363. [CrossRef]

63. El Ansari, W.; Elhag, W. Weight Regain and Insufficient Weight Loss After Bariatric Surgery: Definitions, Prevalence, Mechanisms, Predictors, Prevention and Management Strategies, and Knowledge Gaps-a Scoping Review. *Obes. Surg.* **2021**, *31*, 1755–1766. [CrossRef]
64. Porat, D.; Markovic, M.; Zur, M.; Fine-Shamir, N.; Azran, C.; Shaked, G.; Czeiger, D.; Vaynshtein, J.; Replyanski, I.; Sebbag, G.; et al. Increased Paracetamol Bioavailability after Sleeve Gastrectomy: A Crossover Pre- vs. Post-Operative Clinical Trial. *J. Clin. Med.* **2019**, *8*, 1949. [CrossRef] [PubMed]
65. Dahan, A.; Porat, D.; Azran, C.; Mualem, Y.; Sakran, N.; Abu-Abeid, S. Lithium Toxicity with Severe Bradycardia Post Sleeve Gastrectomy: A Case Report and Review of the Literature. *Obes. Surg.* **2019**, *29*, 735–738. [CrossRef] [PubMed]
66. Margolin, N.; Porat, D.; Dahan, A.; Lavon, O. Influence of Bariatric Surgery on Levetiracetam Clinical Effectiveness: Case Series. *Obes. Surg.* **2022**, *32*, 2795–2796. [CrossRef] [PubMed]
67. Azran, C.; Porat, D.; Fine-Shamir, N.; Hanhan, N.; Dahan, A. Oral levothyroxine therapy postbariatric surgery: Biopharmaceutical aspects and clinical effects. *Surg. Obes. Relat. Dis.* **2019**, *15*, 333–341. [CrossRef]
68. Porat, D.; Azran, C.; Kais, H.; Dahan, A. Managing the Unpredictable: Mechanistic Analysis and Clinical Recommendations for Lamotrigine Treatment after Bariatric Surgery. *J. Clin. Med.* **2021**, *10*, 5627. [CrossRef]
69. Kvitne, K.E.; Robertsen, I.; Skovlund, E.; Christensen, H.; Krogstad, V.; Wegler, C.; Angeles, P.C.; Wollmann, B.M.; Hole, K.; Johnson, L.K.; et al. Short- and long-term effects of body weight loss following calorie restriction and gastric bypass on CYP3A-activity—A non-randomized three-armed controlled trial. *Clin. Transl. Sci.* **2022**, *15*, 221–233. [CrossRef]
70. Zarezadeh, M.; Saedisomeolia, A.; Shekarabi, M.; Khorshidi, M.; Emami, M.R.; Muller, D.J. The effect of obesity, macronutrients, fasting and nutritional status on drug-metabolizing cytochrome P450s: A systematic review of current evidence on human studies. *Eur. J. Nutr.* **2021**, *60*, 2905–2921. [CrossRef]
71. Porat, D.; Margolin, N.; Lavon, O.; Dahan, A. Carbamazepine Therapy After Bariatric Surgery: Eight Sleeve Gastrectomy Cases and Review of the Literature. *Obes. Surg.* **2022**, *32*, 3481–3486. [CrossRef]
72. Ryu, S.Y.; Choi, Y.J.; Park, S.Y.; Kim, J.Y.; Kim, Y.D.; Kim, Y.W. Udenafil, a Phosphodiesterase 5 Inhibitor, Reduces Body Weight in High-Fat-Fed Mice. *World J. Mens. Health* **2018**, *36*, 41–49. [CrossRef]

pharmaceutics

MDPI

Communication

Safety of Repeated Administration of Xenogeneic Human Apoptotic State (Allocetra-OTS) in Sprague Dawley Rats

Chen Ankri [1], Oren Hershkovitz [1], Liat Hershkovitz [2], Meital Brami [3], Ronnie Levy [3], Hadar Sarig [3], Einat Souli [3], Barak Reicher [1], Veronique Amor-Baroukh [1], Dror Mevorach [1] and Abraham Nyska [4,*]

[1] Enlivex Therapeutics Ltd., Ness Ziona 7403618, Israel; chen@enlivexpharm.com (C.A.); oren@enlivexpharm.com (O.H.); barak@enlivexpharm.com (B.R.); veronique@enlivexpharm.com (V.A.-B.); mevorachd@enlivexpharm.com (D.M.)
[2] Independent Researcher, Revadim 798200, Israel; liatorenh@gmail.com
[3] Pharmaseed Ltd., Ness Ziona 7404709, Israel; meital@pharmaseedltd.com (M.B.); ronnie@pharmaseedltd.com (R.L.); hadars@pharmaseedltd.com (H.S.); einat@pharmaseedltd.com (E.S.)
[4] Sackler School of Medicine, Tel Aviv University, Tel Aviv 6139001, Israel
* Correspondence: anyska@nyska.net; Tel.: +972-54-3003447

Abstract: Apoptotic cells possess immunomodulatory effects that can be utilized to treat imbalanced immune conditions. Information on the preclinical safety of such treatment is sparse. In this study, the safety of apoptotic cells (Allocetra-OTS) was assessed in a GLP toxicological study on Sprague Dawley rats. Three doses of Allocetra-OTS or vehicle were administered intravenously (IV) for 3 consecutive days. Animals in the main study were sacrificed on day 4, while animals from the recovery groups were kept for 14 or 28 days. Allocetra-OTS was well tolerated, and no adverse effects were observed in terms of body weight, clinical signs, food consumption, or ophthalmologic observation. Thus, the No Observed Adverse Effect Level (NOAEL) dose was determined as the highest dose administered. An observed elevation in immune cells was suspected to be due to Allocetra-OTS, similarly to other clinical chemistry parameters; however, it was resolved in the recovery phases. Splenomegaly and dose-related extramedullary hematopoiesis (EMH) in the red pulp were observed, with no adverse events, and were considered to be a normal and expected reaction following the IV administration of cell-based therapies. In conclusion, under the conditions of this study, Allocetra-OTS was concluded to be safe, further supporting its potential candidacy for clinical studies.

Keywords: cell-based therapies; human apoptotic cells; PBMC; safety

1. Introduction

The therapeutic use of apoptotic cells is an emerging modality and is currently being assessed in clinical studies [1–3]. Apoptotic cells exert immunomodulatory effects [4] by physically interacting with macrophages and dendritic cells and by secreting several paracrine factors; the clearance process of these cells drives an immune homeostasis state [1,5–11]. Apoptosis, or programmed cell death, is a natural and critical process in tissue homeostasis and results in the immediate removal of a dying cell by macrophages and dendritic cells (DCs). DCs are professional antigen-presenting cells (APCs) in mammals; they mature from highly phagocytic precursors in response to 'danger' signals that are present in damaged or infected tissue. At the same time, immature DCs are capable of the large-scale phagocytosis of apoptotic cells and mature alternatively into a homeostatic state [12]. In a similar way, macrophages may produce a large variety of inflammatory cytokines in response to danger signals. However, the removal of apoptotic cells often occurs by macrophages downregulated by NF-Kb [13] and inflammatory responses in macrophages [14,15]. This combined effect was shown to induce several changes and functional activities in the engulfing APCs involving the regulation of immune responses. The clearance of apoptotic cells allows

immune homeostasis, which can lead to a non-inflammatory state for both macrophages and DCs and contribute to the maintenance of peripheral homeostasis and tolerance in some clinical settings [11,16]. Conversely, under certain conditions, such as the killing of tumor cells by specific cell death inducers, the recognition of apoptotic tumor cells can promote an immunogenic response and anti-tumor immunity. Complex factors, such as cell type, the conditions leading to apoptosis, the apoptotic stage of the cells, and others, may lead to various pro-homeostatic effects mediated by macrophages and other APCs. Thus, apoptotic cells may deliver complex information that regulates different immunological responses in a context-dependent manner. The cell type, the cause of cell death, the microenvironment, quantity, and other factors may result in different immunomodulating signals, thus allowing for the modulation of immune processes in different clinical settings [9]. As many as 3×10^8 cells undergo apoptosis every hour in our bodies, and one of the primary "eat me" signals expressed by apoptotic cells is phosphatidylserine (PtdSer). Apoptotic cells themselves are major contributors to the "non-inflammatory" nature of the engulfment process, some by secreting thrombospondin-1 (TSP-1) or adenosine monophosphate and possibly other immune-modulating "calm-down" signals that interact with macrophages and DCs. Apoptotic cells also produce "find me" and "tolerate me" signals to attract and immune modulate macrophages and DCs that express specific receptors for some of these signals [17,18]. Among emerging cell-based therapies, the use of dying cells defined as apoptotic cells as novel therapeutic strategies appears to hold significant promise. These apoptotic-cell-based therapies may be limited not only to transplantation settings, but also to other inflammatory diseases. The immunomodulatory mechanisms associated with physiological apoptotic cell removal (called efferocytosis) were reported in different experimental models of inflammatory diseases or transplantation settings using apoptotic cell infusion [19–24]. Apoptotic cells have been suggested as a clinical therapeutic modality in a variety of immune-mediated disorders [10,25–28], including autoimmune and autoinflammatory conditions (e.g., arthritis [29], colitis [15]), graft rejection [23], post-ischemic injury, and conditions characterized by a cytokine storm, such as septic shock [30] and COVID-19 [31]. The properties of apoptotic cells may promote an immunogenic response and anti-tumor activity by restoring organ macrophage homeostasis [32].

Cell-based human products may contain cells that are autologous, or allogeneic, and may or may not include cells that have been genetically modified, or which may or may not be combined with a device, scaffold, or mesh. Cell-based human products are aimed at repairing, restoring, replacing, or regenerating the structure and function of a damaged organ in order to ameliorate or cure previously untreatable injury or disease. Although there has been an increase and rapid progression in recent years in the development of new cellular therapies, more particularly the development of apoptotic cells, for clinical use, very limited data are available regarding their toxicity and tolerability in preclinical studies, and few guidelines have been published to assist in the design of appropriate preclinical studies [33].

Enlivex Therapeutics Ltd. (Ness-Ziona, Israel) is developing Allocetra-OTS, an off-the-shelf macrophage reprogramming cell therapy produced by the induction and stabilization of apoptotic cells derived from the peripheral blood mononuclear cells (PBMCs) of healthy donors. The stable apoptotic state of these cells is verified by staining with annexin V and propidium iodide, thus avoiding potential adverse effects from necrotic cells (Figure 1).

The robust manufacturing process of Allocetra-OTS enables the production of stable apoptotic cells with a predefined quality attribute profile. A comprehensive nonclinical Good Laboratory Practice (GLP) biodistribution and persistence study demonstrated that the Allocetra-OTS levels in the blood, lungs, liver, spleen, and additional organs peaked 10–60 min following the injection, with the rapid clearance of Allocetra-OTS cells from most of the organs within 24 h (Supplementary Figure S1). The Allocetra-OTS cell suspension is transfused intravenously (IV) for systemic indications such as sepsis and COVID-19, intraperitoneally (IP) for the treatment of peritoneal metastasis, and intra-articularly for the treatment of osteoarthritis. It has shown a favorable safety profile in solid tumors

(ClinicalTrials.gov identifiers NCT05431907 and NCT05581719). In addition, Allocetra-OTS has shown promising safety and preliminary efficacy in phase 1 [3] and phase 2 studies of sepsis (NCT03925857 and NCT04612413, respectively), as well as in COVID-19 in humans (NCT04922957) [2]. In addition, a previously conducted preclinical toxicology study in rats (using the liquid formulation of the product) showed that Allocetra-OTS was well tolerated, and that no serious adverse effects were observed.

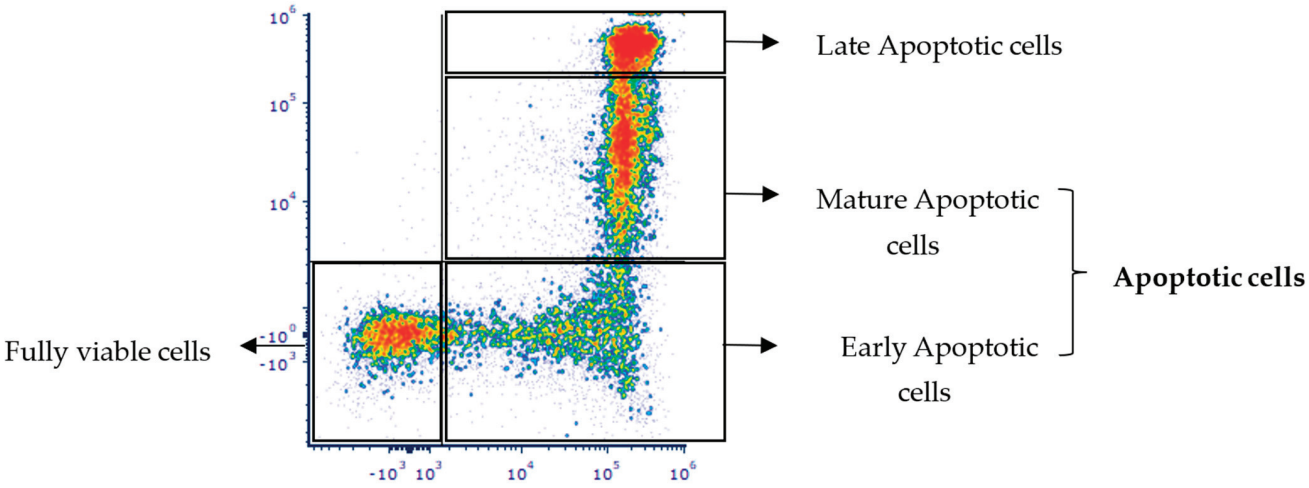

Figure 1. Apoptosis process analysis in Allocetra-OTS cells following annexin V and propidium iodide (PI) staining. Cells of Allocetra-OTS FDP were stained with annexin V (X axis) and propidium iodide (Y axis) to assess the prevalence of these apoptotic cells immediately following product thawing (representative Allocetra-OTS batch).

To extend the shelf life of Allocetra-OTS, Enlivex Therapeutics Ltd. has developed a new cryopreserved formulation for the product. Here we present a recently conducted toxicology study aimed at establishing the safety of repeated IV administrations of the newly formulated Allocetra-OTS in Sprague Dawley (SD) rats. Allocetra-OTS was shown to be safe and well tolerated, with a major finding of spleen enlargement. These data, by showing similar safety profiles for both formulations, strengthen the safety profile of Allocetra-OTS. This finding is expected to be of significant importance for future clinical studies performed with similar treatment modalities.

2. Materials and Methods

2.1. Investigational Product

Allocetra-OTS (Enlivex Therapeutics, Ness Ziona, Israel) is manufactured from a mononuclear-enriched cell fraction collected from the peripheral blood of healthy unrelated donors via leukapheresis. Cells and plasma are transported to Enlivex's manufacturing facility under temperature-controlled conditions. Upon arrival, the cells are processed and cryopreserved according to common practice for the cryopreservation of donor lymphocyte infusion (DLI) cells. Following thawing and the removal of the freezing medium, the cells are resuspended and incubated in apoptosis induction medium containing methylprednisolone, which is subsequently removed using an automated process of media replacement and volume reduction. The apoptotic cells are suspended in Plasma-Lyte, irradiated (X-ray, 4000 cGy), diluted 1:1 with CryoStor® CS5 (BioLife Solutions Inc., Bothell, WA, USA) to a final targeted concentration in a solution containing 2.5% DMSO, and stored in liquid nitrogen. On each dosing day, the vehicle (Allocetra-OTS suspension medium) is thawed in a 37 ± 1 °C water bath for up to 5 min, transferred to a sterile bottle under aseptic conditions, and kept at ambient conditions. Allocetra-OTS cells are thawed (37 ± 1 °C water bath for approx. 2 min), centrifuged (300× *g*, 10 min at 2–8 °C), and resuspended using the vehicle. The final cell concentration is adjusted using the vehicle, according to the required injected dose. Cells are readministered no later than 2 h after thawing.

2.2. Animal Husbandry and Maintenance

SD rats were chosen as the animal species since they are commonly used in safety studies in accordance with international recommendations and the published literature. The SD strain is a well-known laboratory model with adequate historical data. A total of 120 SD rats (60 males (M) and 60 females (F)), aged 8 weeks at study initiation, were obtained from Envigo CRS Ltd. (Ness-Ziona, Israel) and were housed and treated at Pharmaseed Ltd. (Ness-Ziona, Israel). Animals were provided with a commercial rodent diet ad libitum and allowed free access to drinking water. Temperature was maintained at 18–24 °C with 30–70% relative humidity and a 12 h light/dark cycle. The study was performed in compliance with the Israel Animal Welfare Act and was approved by the Israel Board for Animal Experiments Ethics Committee (#NPC-Ph-IL-2111-113-5).

2.3. Experimental Design

Allocetra-OTS was studied at three doses (140×10^6 [group 2M/2F], 700×10^6 [group 3M/3F] and 1260×10^6 Allocetra-OTS cells/kg [group 4M/4F]) and compared to the vehicle group (in suspension media; group 1M/1F). Allocetra-OTS or vehicle was administered IV (tail vain) via three consecutive administrations (days 1–3). The animals of the main study were sacrificed on day 4, and the animals of the recovery groups (Allocetra-OTS high dose and vehicle) were kept for two or four weeks of recovery after the last dosing day (see Table 1). Allocetra-OTS or the vehicle were administered to 5–10 animals per group at a rate of 2 mL/min at a dose volume of 10 mL/kg (Table 1). The study was conducted in compliance with the principles of Good Laboratory Practice (GLP). The details regarding the design of the experiment, the groups' allocation across the study phases (main study, 14 days recovery phase, and 28 days recovery phase), and the treatment doses are described in Table 1.

Table 1. Experimental design.

	Group	Animal No. (Total No.)		IV Treatment	Dose (Cells $\times 10^6$/kg)	Dose Volume (mL/kg)
		M	F			
Main Study	1M/1F	10	10	Vehicle	NA	10
	2M/2F	10	10	Allocetra-OTS	140	
	3M/3F	10	10		700	
	4M/4F	10	10		1260	
Recovery Phase—14 days	1M/1F	5	5	Vehicle	NA	10
	4M/4F	5	5	Allocetra-OTS	1260	
Recovery Phase—28 days	1M/1F	5	5	Vehicle	NA	10
	4M/4F	5	5	Allocetra-OTS	1260	

M, male; F, female; NA, not applicable; IV, intravenous.

2.4. Observations and Examinations

All animals were observed for clinical signs prior to each dose for the first 3 h post first dosing, for 1 h post the second and the third doses, and twice a week thereafter for the recovery phases before termination. Body weight and food consumption were monitored, along with ophthalmic examinations. Prior to termination, urine was collected from the animals of both the main and recovery phases, and analyzed for pH, glucose, specific gravity, bilirubin, urine total protein, ketones, urobilinogen, and microscopic sediment. Upon termination, and following at least 2 h of food restriction, blood was drawn from all animals for the following analyses:

Hematology: A total of 300 µL of whole blood in K3 EDTA-containing tubes was run on an Advia 2120i blood analyzer (automatic differential count) (Siemens HealthCare Ltd.,

Rosh Haayin, Israel) or 50 µL of whole blood using the Sysmex blood analyzer (manual differential count).

Clinical Chemistry: Approx. 0.5 mL of whole blood per animal was collected into cup tubes with clotting activator gel. The tubes were kept at room temperature for at least 30 min for clotting and then centrifuged at 4 °C for 10 min at 1790× *g*. Separated serum (180 µL) was analyzed with a Cobas 6000 chemistry analyzer.

Coagulation: Citrated blood (approx. 450 µL of blood + 50 µL of sodium citrate or approx. 900 µL of blood + 100 µL of sodium citrate) per animal was collected into sodium citrate tubes. The samples were centrifuged at 4 °C for 10 min at 1790× *g* for the separation of plasma. Citrated plasma (300 µL) was analyzed for prothrombin time (PT), activated partial thromboplastin time (aPTT), and fibrinogen (FIB) using a Sysmex CS2500 analyzer (Sysmex, Singapore). Group mean values were compared to the normal references (strain- and sex-related values) provided by the clinical pathology laboratory and analyzed by *t*-test for statistical differences from the relevant vehicle control group.

Urine Analysis: Prior to termination, urine was collected from both the main and recovery phases during 14 ± 2 h using metabolic cages. The urine samples were analyzed for the following parameters: pH, glucose, specific gravity, bilirubin, urine total protein, ketones, urobilinogen—qualitative determination, and microscopic examination of sediment.

Gross Pathology: Gross pathology was thoroughly examined, and organs were wet weighed. All groups were subjected to histopathology analysis of the following tissues: adrenals, aorta, brain, cecum, colon, ileum with Peyer's patches, prostate, seminal vesicles and coagulating glands, duodenum, stomach, epididymides, esophagus, thyroid with parathyroids, trachea, eyes, femoral muscle with sciatic nerve, femur with joint, heart, jejunum, kidneys, liver, lung including main bronchi, skin with mammary glands, mandibular lymph nodes, ovaries and oviducts, pituitary, pancreas, rectum, urinary bladder, salivary glands, spinal cord, spleen, sternum with marrow, testes, thymus, uterus with cervix, vagina, mesentery, and tail (injection site).

Histopathological Assessment: Histology slide preparation included tissue decalcification (as applicable), trimming, dehydration, and embedding. The resulting blocks were sectioned to a thickness of approx. 4 microns, mounted, and stained with hematoxylin and eosin. Histopathology changes were described and scored using a semi-quantitative grading (0 = normal, 1 = minimal, 2 = mild, 3 = moderate, 4 = severe) [34].

3. Results

3.1. Morbidity and Mortality, Clinical Signs, and Body Weights

No animal died or was found in morbid condition during the study, and no significant differences in food consumption were observed between the tested groups. No differences in average body weight were observed between the vehicle- (1F) and the Allocetra-OTS-treated groups (2F, 3F, and 4F) in female rats of the main and recovery phases. However, on days 2 and 3 in male rats in both the main and the 14-day recovery phase studies, a slight (<3%) but statistically significant decrease was observed in the relative average body weight (% of day 1 weight) of group 4M compared to the vehicle group (1M). This decrease was also observed on day 3 in group 3M of the main study. Full recovery of body weight was seen in the 28-day recovery phase.

All animals in both the main and the recovery phases of the study demonstrated piloerection, swelling of the feet and face, edema, and cyanosis during the first 3 h after the initial administration of both the vehicle and Allocetra-OTS. These phenomena were also observed after the second and third administrations. Most animals demonstrated full recovery from all symptoms by 24 h post-administration. These clinical signs had disappeared by the end of the injection days (on day 4) in all cases, both in the main and in the recovery studies. As was seen in the vehicle as well, these clinical signs were not all considered to be Allocetra-OTS-related. Furthermore, no Allocetra-OTS-related ophthalmologic symptoms were observed in any of the animals.

3.2. Clinical Pathology

The comprehensive findings from the hematology, clinical chemistry, and coagulation analysis are summarized in tables presented in the Supplementary information (Tables S1–S15) as values of the averages per group. A distinct table is provided for the treatment groups categorized by gender (male or female groups) and for both the main study and recovery phases for each clinical pathology analysis. For each treatment group, *t*-test analyses were used to compare the result to the normal range of each parameter, as well as to the vehicle-treated group.

3.2.1. Hematology

White blood cells (WBCs): Among the male rat groups in the main study, a significant dose-related increase in WBC concentration was observed in all the treated groups (2M, $p < 0.01$; 3M and 4M, $p < 0.001$) compared to the vehicle group (1M), although WBC values remained within the normal range for all groups. This increase was not observed in any of the recovery phases.

Lymphocytes: Among the male rats in the main study, a significant dose-related increase in the absolute lymphocyte count was observed in all the treated groups (2M, $p < 0.01$; 3M and 4M, $p < 0.001$) compared to the vehicle group (1M). A significant increase ($p < 0.05$) was also observed in the female group (3F) of the main study compared to the vehicle group (1F). This increase was not observed in any of the recovery phases. All of the increased values were within their normal ranges.

Monocytes: Among the female rat groups in the main study, both the absolute count and the average percentage of monocyte values were significantly increased in groups 3F ($p < 0.05$) and 4F ($p < 0.01$) compared to the vehicle group (1F). A significant increase in the absolute monocyte count was also observed in the male rat groups (3M, $p < 0.01$ and 4M, $p < 0.001$), whereas an increase in the monocyte percentage values was observed only in group 4M ($p < 0.05$). Both the absolute and percentage values of the monocytes in all groups remained within normal ranges. No such increases in monocyte values were observed in any of the recovery phases.

Basophils: In both the males and females in the treated groups (2M/2F, 3M/3F, and 4M/4F) of the main study, a significant dose-related increase in both the absolute counts and the percentage values of basophils was observed compared to the vehicle group (1M/1F). Moreover, basophil percentage values were higher than the normal range in both the male and female groups of the main study. This increase was not observed in any of the recovery phases.

All of the abovementioned changes in hematology were related to Allocetra-OTS and were already resolved by the end of the 14-day recovery phase. Most remained within their normal ranges and were therefore not considered to be adverse events (see Supplementary Information).

3.2.2. Clinical Chemistry

Albumin and globulin: In both the male and the female groups of the main study, a significant dose-related decrease in the albumin concentration, all within the normal range, was observed in all the treated groups (2M/2F, 3M/3F, and 4M/4F) compared to the vehicle groups (1M/1F). No such decrease was observed in any of the recovery phases. Among female rats in the main study, a significant dose-related increase in the globulin concentration was observed in all the treated groups (2F, 3F, and 4F) compared to the vehicle group (1F). All observed changes remained within the normal range. A similar increase, again within the normal range, was also observed in the male rat group 4M of the main study compared to the vehicle group (1M) and was not observed in any of the recovery phases. Among female rat groups of the main study, the dose-related albumin/globulin ratio was significantly decreased in all the treated groups (2F, 3F, 4F) compared to the vehicle group (1F). This decrease was also observed in the male rat group (4M) of the main study compared to the vehicle group (1M), but not in any of the recovery phases.

LDH: Among the female rat groups within the main study, the LDH concentration was significantly decreased (within normal range) in two groups (2F, $p < 0.05$; 4F, $p < 0.01$) compared to the vehicle group (1F). A similar decrease (within normal range) was also observed in the treated female 14-day recovery group (4F) but not in the 28-day recovery phase.

SGOT and SGPT: Among the female rat groups within the main study, a significant decrease in the serum glutamic-oxaloacetic transaminase (SGOT) concentration (though within its normal ranges) was observed in groups 2F and 3F compared to the vehicle group (1F). This decrease was not observed in any of the recovery phases. In group 3F of the main study, the serum glutamate pyruvate transaminase (SGPT) concentration was also significantly decreased (also within its normal range) compared to the vehicle group (1F), but no such decrease was seen in any of the recovery phases. In addition, in the recovery phase, the SGPT values among treated female rats (4F) were higher than their normal range, but they did not differ statistically from values in the vehicle group.

Calcium, phosphorus, and potassium: In group 3M of the main study, a slight but significant increase (within its normal range) in the calcium concentration was observed compared to the vehicle group (1M). This increase was not observed in any of the recovery phases. In group 4M of the main study, a significant increase (within normal range) in the phosphorus concentration was observed compared to the vehicle group (1M). No such increase was observed in any of the recovery phases. In group 3M of the main study, the potassium concentration was significantly decreased (within normal range) in comparison to the vehicle group (1M). A similar decrease was observed in treated males (4) in the 14-day recovery group (4M).

Creatinine: In the female vehicle group of the main study, creatinine values were slightly lower than their normal range. In group 3F of the main study, the creatinine concentration was slightly (within normal range) but significantly increased compared to the vehicle group (1F). This slight increase was not observed in any of the recovery phases.

Total protein: Among the male rat groups of the main study, a significant dose-related decrease, within its normal range, in the total protein concentration was observed in all the treated groups (2M, 3M, 4M) compared to the vehicle group (1M). This decrease was not observed in any of the recovery phases.

3.2.3. Coagulation

Fibrinogen: Among the male rat groups (3M and 4M) of the main study, the fibrinogen concentration was significantly increased compared to the vehicle group (1M), with full recovery attained by day 14.

aPTT: In the male rat high-dose treatment group (4M), both in the main study and in the 28-day recovery phase, a slight (within normal range) but significant increase in aPTT was observed in comparison to the vehicle group (1M).

In general, some significant differences in clinical chemistry parameters were observed in both male and female rat groups of the main study. No such differences were observed in either the 14-day or the 28-day recovery phases, except for the decrease in the LDH concentration observed in the 14-day (but not in the 28-day) recovery phase in female rats, and the decrease in the potassium concentration that was also observed in the males of the 14-day recovery phase, but not in the 28-day recovery phase. In general, male rats seemed to be more susceptible to the transient recorded effects than females.

3.3. Urinalysis

There was no difference in urine parameters between the vehicle- and the drug-treated groups in the main study and the recovery phases.

3.4. Organ Weight

A significant dose-related increase ($p < 0.001$) in absolute and relative spleen weights was observed in all the treated groups of the main study compared to the vehicle groups.

A significant increase in absolute and in relative spleen weight was also observed in male treated rats (4M) of the 28-day recovery phase ($p < 0.05$). The relative spleen weights were calculated as a percent (%) of the total body weight of each animal. The average of the relative spleen weight results across all the treatment groups during both the main study and the recovery phases is presented in Table 2.

Table 2. Relative spleen weight analysis.

Relative Organ Weight (% of BW)	Vehicle (1M/1F)			Allocetra-OTS 140 × 10^6 cells/kg (2M/2F)			Allocetra-OTS 700 × 10^6 cells/kg (3M/3F)			Allocetra-OTS 1260 × 10^6 cells/kg (4M/4F)		
	AVG	SEM	N	AVG	SEM	N	AVG	SEM	N	AVG	SEM	N
Males, main study												
Spleen	0.263	0.010	10	0.395 ***	0.012	10	0.449 ***	0.013	10	0.456 ***	0.010	10
Females, main study												
Spleen	0.292	0.014	10	0.430 ***	0.017	10	0.468 ***	0.013	10	0.489 ***	0.017	10
Relative Organ Weight (% of BW)	**Vehicle (1M/1F)**			**Allocetra-OTS 1260 × 10^6 cells/kg (4M/4F)**								
	AVG	**SEM**	**N**	**AVG**	**SEM**	**N**						
Males, recovery, 14 days												
Spleen	0.260	0.013	5	0.294	0.008	5						
Females, recovery, 14 days												
Spleen	0.296	0.017	5	0.332	0.005	5						
Males, recovery, 28 days												
Spleen	0.223	0.004	5	0.265 *	0.013	5						
Females, recovery, 28 days												
Spleen	0.265	0.012	5	0.302	0.012	5						

* $p < 0.05$; *** $p < 0.001$ compared to vehicle (1M) using *t*-test. BW = body weight; F = female; M = male; N = number of animals; AVG = average; SEM = standard error of the mean.

3.5. Gross Pathology

The most prominent abnormality was the enlarged spleen observed in most of the treated male and female rat groups of the main study, including those in the vehicle groups. This phenomenon was not observed in the 28-day recovery phase.

3.6. Histopathological Evaluation

The histopathological individual findings are presented in the Supplementary Tables as follows: Tables S16–S19, group 1M–4M (male), respectively, main study. Tables S20–S23, group 1F–4F, respectively (female), main study. Table S24, 1M and 4M (male), recovery phase 14 days. Table S25, 1F and 4F (female), recovery phase 14 days. Table S26, 1M and 4M (male), recovery phase 28 days. Table S27, 1F and 4F (female), recovery phase 28 days.

Treatment-related changes were observed only in the red pulp of the spleen. These changes included the presence of round, relatively small hyperchromatic dark blue nuclear remnants, and/or round empty cavities with or without remaining nuclear and cell eosinophilic ghosts (dead cells) (Figure 2A–F and Tables S16–S27). These changes were consistent with a diagnosis of apoptotic cells [35]. The degree of change was mild in groups 3 and 4, and minimal in group 2. In addition, extramedullary hematopoiesis (EMH), manifested as a diffuse increase in the number of cells with a large irregular nucleus, prominent nucleoli, and scant cytoplasm (compared to controls), was observed in the Allocetra-OTS-treated rats. The degree of change was usually moderate in groups 3 and 4 and mild in group 2, and minimal in the vehicle groups (Figure 2A–F and Tables S16–S27). Extramedullary hematopoiesis (EMH) was observed in the red pulp of the spleen, with no adverse events, and was considered to be a normal and expected reaction for the removal of degenerated cells following the IV administration of cell-based therapies [36]. No treatment-related changes were seen in the recovery phases of the study.

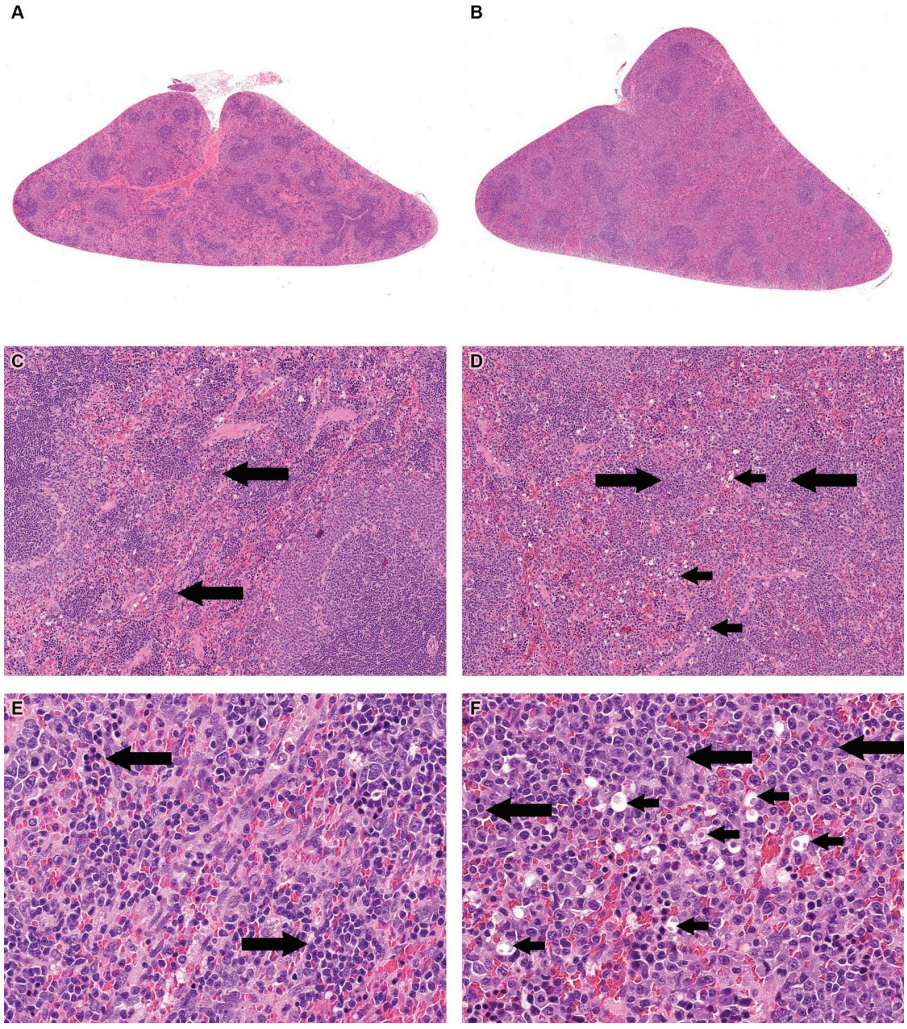

Figure 2. Histopathology analysis of spleen. (**A**). Histopathology section of the spleen from a rat from the vehicle group (1M). Original magnification ×1. (**B**) Spleen from the high-dose Allocetra-OTS-treated animal group (4M). Original magnification ×1. (**C**) Spleen from the vehicle group (1M). Long arrows indicate minimal extramedullary hematopoiesis (EMH) in the red pulp. Original magnification ×10. (**D**) Spleen from the high-dose Allocetra-OTS group (4M). Short arrows indicate the presence of apoptotic cells. Long arrows indicate EMH. Original magnification ×10. (**E**) Spleen from the vehicle group (1M). Long arrows indicate EMH in the red pulp. Original magnification ×10. (**F**) Spleen from the high-dose Allocetra-OTS group (4M). Short arrows indicate the presence of apoptotic cells, and long arrows indicate EMH.

4. Discussion

Here we present the results of a detailed safety evaluation of three repeated doses of Allocetra-OTS (140×10^6, 700×10^6, and 1260×10^6 cells/kg) administered IV in SD rats and compared to a control vehicle group. The dosages used in this toxicology study were at least nine-fold higher than those of the equivalent human doses administered in a previously conducted phase 1b clinical study of Allocetra-OTS in sepsis [3], as well as in an ongoing sepsis phase 2 study.

All dose levels were well tolerated, and no serious adverse or toxicologically meaningful effects were observed with regard to body weight, clinical signs, food consumption, urinalysis, or ophthalmologic evaluation.

Piloerection, swelling, edema, and cyanosis were observed in all animals during the first 3 h after the dosage administration in both the vehicle- and Allocetra-OTS-treated groups. These changes were fully resolved in all cases. These changes were considered to

be vehicle-related, as also confirmed in a follow-up experiment, and were probably caused by the hypersensitivity of rats to dextran, a component of the media formulation. This reaction is well known in rats and is not expected in humans [37–40].

Some significant differences in the hematology analysis parameters were observed in both the male and female rat groups of the main and recovery phases, found while comparing the treated and vehicle groups. Since most of these differences were not related to dosage, or disappeared during recovery phases, they were not considered to be toxicologically adverse events. The high WBC levels observed in the male groups in the main study are an expected phenomenon since -OTS consists of foreign (human) cells that lead to leukocyte proliferation as part of the physiological immune response [41]. Significant differences were observed in several of the clinical chemistry parameters in both the male and female rat groups of the main study. These differences were not considered to be clinically relevant, as well as the decreases in the LDH concentration and potassium that were not seen in the 28-day recovery phase.

Significant dose-related increases in absolute and relative spleen weights were observed in all the drug-treated groups of the main study compared to vehicle-treated groups, including in the 28-day recovery phase in male rats. These findings correlated with enlarged spleens, with the most prominent abnormality being observed during the evaluation of gross pathology in most of the Allocetra-OTS-treated groups of the main study. Notably, differences in recovery phases between the treated and vehicle groups were substantially smaller and were not observed during the gross pathology evaluation after 28 days of recovery. IV-injected cells have a well-known tendency to become trapped in the spleen. This organ serves as a common homing location for immune cells when infused systemically [42–44] and was shown to be the major target for the accumulation of PBMCs following IV injection in rats [45]. This phenomenon is also observed in other cell-based treatments such as stem cell therapies [46,47]. It is, therefore, not surprising to observe the presence of PBMC-derived apoptotic cells in the spleen in this study. Nevertheless, other than the expected splenomegaly, this did not lead to any observed adverse events in the spleen.

This phenomenon was further investigated, moreover, in an in vivo study in mice, aimed at determining whether the observed splenomegaly is restricted to the xenogeneic source of apoptotic cells (namely, human cells injected into BALB/c mouse). That study compared the impact of repeated injections of apoptotic cells using xenogeneic, allogeneic (C57BL/6 cells to BALB/c mice, reflecting the clinical administration of allogeneic Allocetra-OTS to humans), and syngeneic (BALB/c cells to BALB/c mice) apoptotic cells. The results demonstrated splenomegaly in the human Allocetra-OTS-treated mice, but not in the syngeneic- or allogeneic-treated mice. Despite several differences in the immune response between Wistar rats and BALB/c mice to foreign antigens (human cells), the central 'eat me' signal pathways for apoptotic cell engulfment from C. elegans to humans are well conserved [48,49]. We therefore believe that the findings of that in vivo mouse study adequately support our splenomegaly finding obtained in this toxicology study.

Since the injection of Allocetra-OTS into humans in a clinical setting is the equivalent of an allogeneic apoptotic cell injection into mice, it can be hypothesized that the changes observed in the spleens of Allocetra-OTS-treated mice are related to their xenogeneic origin and are not expected in an allogeneic clinical setting.

An additional observed finding is EMH, i.e., the presence of hematopoiesis in locations other than the bone marrow [50–52], which has been observed in all animals in this study and was more pronounced in the Allocetra-OTS-treated rats. EMH is an additional factor contributing to the splenomegaly and the changes seen in the WBC counts observed here in the Allocetra-OTS-treated animals. Commonly observed in rats [53], EMH is not limited to hematotoxic insults and can also occur in various conditions such as general stress, inflammation, and systemic anemia. In all the animals in our study, including those receiving the highest dose of Allocetra-OTS and experiencing the highest degree of EMH and accumulation of apoptotic cells, the findings were completely resolved during

the 14-day recovery phase. Together with the fact that EMH was also observed in the vehicle group, the observed EMH was not regarded as related to Allocetra-OTS treatment. This conclusion is in line with the results from a previous GLP toxicology study in which Allocetra-OTS was administered at the same doses and with the dose regimen applied in the current study to SD rats with a former (liquid) formulation. In that study, the spleens of animals in both the control and high-dose groups (1260 cells $\times$ 10^6/kg) demonstrated the presence of apoptotic cells and EMH, which were both more pronounced in Allocetra-OTS-treated rats. Based on those previous results, it can be concluded that the EMH observed in all animals in the present study indeed reflects the presence of Allocetra-OTS cells in the spleen.

Given that the spleen was the only target organ, and that the changes noted in this organ are considered to reflect the expected pharmacological accumulation of IV-administered Allocetra-OTS cells (associated with reactive EMH, which recovered completely following the 14 days of drug withdrawal), the observed changes are judged to be not adverse according to the criteria of the Society of Toxicologic Pathology [54–59].

In general, Allocetra-OTS was well tolerated in our SD rat model, and no serious adverse or toxicologically meaningful effects were observed. It was therefore concluded that Allocetra-OTS is safe, with the highest dose administered determined as No Observed Adverse Effect Level (NOAEL). This safety profile is comparable to a previously conducted GLP toxicology study evaluating the safety of a liquid formulation of Allocetra-OTS in SD rats using identical doses and the same dose regimen used here, in which the highest administered dose was also determined as NOAEL. Since this toxicity preclinical examination revealed no signs of abnormal cell proliferation in any organ, and no threshold for adverse effects on the host was detected [33,60], we believe that the present study confirms the favorable safety profile of Allocetra-OTS as a possible treatment modality for humans in clinical trial settings. It also provides critical information on the expected changes in animal models when injected IV with PBMC-derived apoptotic cells, thus facilitating the interpretation of histopathology findings in future studies of such treatments.

Supplementary Materials: The following supporting information can be downloaded at: https://www.mdpi.com/article/10.3390/pharmaceutics16030426/s1, Figure S1: Average Allocetra-OTS concentration vs. time data following IV administration, linear scale; Table S1: Hematology analysis, Male, Main Study; Table S2: Hematology analysis, Female, Main Study; Table S3: Hematology analysis, Male, Recovery Phase 14 Days; Table S4: Hematology analysis, Female, Recovery Phase 14 Days; Table S5: Hematology analysis, Male, Recovery Phase 28 Days; Table S6: Hematology analysis, Female, Recovery Phase 28 Days; Table S7: Clinical chemistry, Male, Main Study; Table S8: Clinical chemistry, Female, Main Study; Table S9: Clinical chemistry, Male, Recovery 14 Days Phase; Table S10: Clinical chemistry, Female, Recovery 14 Days Phase; Table S11: Clinical chemistry, Male, Recovery 28 Days Phase; Table S12: Clinical chemistry, Female, Recovery 28 Days Phase; Table S13: Coagulation, Males and Females, Main study; Table S14: Coagulation, Males and Females, Recovery 14 Days Phase; Table S15: Coagulation, Males and Females, Recovery 28 Days Phase; Table S16: Individual histopathological findings-Male Main Study (Group 1M); Table S17: Individual histopathological findings-Male Main study (Group 2M); Table S18: Individual histopathological findings-Male Main study (Group 3M); Table S19: Individual histopathological findings-Male Main Study (Group 4M); Table S20: Individual histopathological findings-Female Main Study (Group 1F); Table S21: Individual histopathological findings-Female Main study (Group 2F); Table S22: Individual histopathological findings-Female Main study (Group 3F); Table S23: Individual histopathological findings-Female Main Study (Group 4F); Table S24: Individual histopathological findings-14 days Recovery Phase, Groups 1M and 4M; Table S25: Individual histopathological findings-14 days Recovery Phase, Groups 1F and 4F; Table S26: Individual histopathological findings-28 days Recovery phase, Group 1M and 4M; Table S27: Individual histopathological findings-28 days Recovery phase, Group 1F and 4F.

Author Contributions: Conceptualization, C.A., O.H., V.A.-B. and L.H.; methodology, M.B., H.S., R.L. and E.S.; formal analysis, M.B., H.S. and A.N.; investigation, C.A., D.M., B.R. and V.A.-B.; resources, C.A., M.B., H.S, R.L., V.A.-B., B.R. and D.M.; data curation, M.B., H.S., R.L., A.N., B.R. and C.A.;

writing—original draft preparation, C.A., M.B., H.S. and A.N.; writing—review and editing, O.H., L.H., D.M. and E.S.; supervision, C.A. and O.H. All authors have read and agreed to the published version of the manuscript.

Funding: This study was funded by Enlivex Therapeutics Ltd. Ness-Ziona, Israel.

Institutional Review Board Statement: The animal study protocol was approved by the Israel Board for Animal Experiments Ethics Committee (#NPC-Ph-IL-2111-113-5, date of approval 22 December 2021).

Informed Consent Statement: Not applicable.

Data Availability Statement: The raw data supporting the conclusions of this article will be made available by the authors on request.

Conflicts of Interest: C.A., O.H., B.R., V.A.-B. and D.M. are employees of Enlivex Therapeutics Ltd. The study described in this manuscript received funding support from Enlivex Therapeutics Ltd. Although representatives of Enlivex Therapeutics Ltd. Participated in the principal design of the study, writing, and approving the decision to publish the results, they had no involvement in the study execution, data collection, analyses, or interpretation of the findings. Also, in this study, L.H. served as a toxicology and preclinical safety consultant for Enlivex; she had no involvement in the study execution, data collection, analyses, or interpretation of the findings or approving the decision to publish the results. M.B., R.L., H.S., E.S. and A.N. served as service providers; they were involved in planning the study, gathering and analyzing data, and writing the manuscript. However, none of the above own shares or have any financial stake in Enlivex Therapeutics Ltd.

References

1. Mevorach, D.; Zuckerman, T.; Reiner, I.; Shimoni, A.; Samuel, S.; Nagler, A.; Rowe, J.M.; Or, R. Single Infusion of Donor Mononuclear Early Apoptotic Cells as Prophylaxis for Graft-versus-Host Disease in Myeloablative HLA-Matched Allogeneic Bone Marrow Transplantation: A Phase I/IIa Clinical Trial. *Biol. Blood Marrow Transplant.* **2014**, *20*, 58–65. [CrossRef]
2. Mevorach, D. Immunotherapy: Treatment with Allocetra-Ots Apoptotic Cells In 21 Severely/Critically Ill Patients with COVID-19. *Cytotherapy* **2022**, *24*, S121–S122. [CrossRef]
3. van Heerden, P.V.; Abutbul, A.; Sviri, S.; Zlotnick, E.; Nama, A.; Zimro, S.; El-Amore, R.; Shabat, Y.; Reicher, B.; Falah, B.; et al. Apoptotic Cells for Therapeutic Use in Cytokine Storm Associated with Sepsis—A Phase Ib Clinical Trial. *Front. Immunol.* **2021**, *12*, 718191. [CrossRef]
4. James, H.; Alberto, B. Extracorporeal Photopheresis Suppresses Transplant Fibrosis by Inducing Decorin Expression in Alveolar Macrophages. *Transplantation* **2023**, *107*, 1010–1012.
5. Beer, L.; Mildner, M.; Gyöngyösi, M.; Ankersmit, H.J. Peripheral blood mononuclear cell secretome for tissue repair. *Apoptosis* **2016**, *21*, 1336–1353. [CrossRef] [PubMed]
6. Bonnefoy, F.; Gauthier, T.; Vallion, R.; Martin-Rodriguez, O.; Missey, A.; Daoui, A.; Valmary-Degano, S.; Saas, P.; Couturier, M.; Perruche, S. Factors produced by macrophages eliminating apoptotic cells demonstrate pro-resolutive properties and terminate ongoing inflammation. *Front. Immunol.* **2018**, *9*, 2586. [CrossRef]
7. Elliott, M.R.; Ravichandran, K.S. Clearance of apoptotic cells: Implications in health and disease. *J. Cell Biol.* **2010**, *189*, 1059–1070. [CrossRef] [PubMed]
8. Krispin, A.; Bledi, Y.; Atallah, M.; Trahtemberg, U.; Verbovetski, I.; Nahari, E.; Zelig, O.; Linial, M.; Mevorach, D. Apoptotic cell thrombospondin-1 and heparin-binding domain lead to dendritic-cell phagocytic and tolerizing states. *Blood* **2006**, *108*, 3580–3589. [CrossRef] [PubMed]
9. Poon, I.K.H.; Lucas, C.D.; Rossi, A.G.; Ravichandran, K.S. Apoptotic cell clearance: Basic biology and therapeutic potential. *Nat. Rev. Immunol.* **2014**, *14*, 166–180. [CrossRef] [PubMed]
10. Saas, P.; Daguindau, E.; Perruche, S. Concise Review: Apoptotic Cell-Based Therapies-Rationale, Preclinical Results and Future Clinical Developments. *Stem Cells* **2016**, *34*, 1464–1473. [CrossRef] [PubMed]
11. Trahtemberg, U.; Mevorach, D. Apoptotic cells induced signaling for immune homeostasis in macrophages and dendritic cells. *Front. Immunol.* **2017**, *8*, 1356. [CrossRef]
12. Inna, V.; Bychkov, H.; Trahtemberg, U.; Shapira, I.; Hareuveni, M.; Ben-Tal, O.; Kutikov, I.; Gill, O.; Mevorach, D. Opsonization of Apoptotic Cells by Autologous IC3b Facilitates Clearance by Immature Dendritic Cells, down-Regulates DR and CD86, and up-Regulates CC Chemokine Receptor 7. *J. Exp. Med.* **2002**, *196*, 1553–1561.
13. Gordon, S.; Plüddemann, A. Macrophage clearance of apoptotic cells: A critical assessment. *Front. Immunol.* **2018**, *9*, 127. [CrossRef] [PubMed]
14. Elliott, M.R.; Koster, K.M.; Murphy, P.S. Efferocytosis Signaling in the Regulation of Macrophage Inflammatory Responses. *J. Immunol.* **2017**, *198*, 1387–1394. [CrossRef]

15. An, Y.; Zhang, H.; Wang, C.; Jiao, F.; Xu, H.; Wang, X.; Luan, W.; Ma, F.; Ni, L.; Tang, X.; et al. Activation of ROS/MAPKs/NF-κB/NLRP3 and inhibition of efferocytosis in osteoclast-mediated diabetic osteoporosis. *FASEB J.* **2019**, *33*, 12515–12527. [CrossRef]
16. Das, A.; Ganesh, K.; Khanna, S.; Sen, C.K.; Roy, S. Engulfment of apoptotic cells by macrophages: A role of microRNA-21 in the resolution of wound inflammation. *J. Immunol.* **2014**, *192*, 1120–1129. [CrossRef] [PubMed]
17. Arandjelovic, S.; Ravichandran, K. Phagocytosis of apoptotic cells in homeostasis. *Nat. Immunol.* **2015**, *16*, 907–917. [CrossRef]
18. Fadok, V.A.; Voelker, D.R.; Campbell, P.A.; Cohen, J.J.; Bratton, D.L.; Henson, P.M. Exposure of phosphatidylserine on the surface of apoptotic lymphocytes triggers specific recognition and removal by macrophages. *J. Immunol.* **1992**, *148*, 2207–2216. [CrossRef] [PubMed]
19. Perruche, S.; Saas, P.; Chen, W. Apoptotic cell-mediated suppression of streptococcal cell wall-induced arthritis is associated with alteration of macrophage function and local regulatory T-cell increase: A potential cell-based therapy? *Arthritis Res. Ther.* **2009**, *11*, R104. [CrossRef]
20. Huynh, M.L.; Fadok, V.A.; Henson, P.M. Phosphatidylserine-dependent ingestion of apoptotic cells promotes TGF-beta1 secretion and the resolution of inflammation. *J. Clin. Investig.* **2002**, *109*, 41–50. [CrossRef]
21. Kushwah, R.; Oliver, J.R.; Zhang, J.; Siminovitch, K.A.; Hu, J. Apoptotic dendritic cells induce tolerance in mice through suppression of dendritic cell maturation and induction of antigen-specific regulatory T cells. *J. Immunol.* **2009**, *183*, 7104–7118. [CrossRef] [PubMed]
22. Sun, E.; Gao, Y.; Chen, J.; Roberts, A.; Wang, X.; Chen, Z.; Shi, Y. Allograft tolerance induced by donor apoptotic lymphocytes requires phagocytosis in the recipient. *Cell Death Differ.* **2004**, *11*, 1258–1264. [CrossRef] [PubMed]
23. Kleinclauss, F.; Perruche, S.; Masson, E.; de Carvalho Bittencourt, M.; Biichle, S.; Remy-Martin, J.P.; Ferrand, C.; Martin, M.; Bittard, H.; Chalopin, J.M.; et al. Intravenous apoptotic spleen cell infusion induces a TGF-beta-dependent regulatory T-cell expansion. *Cell Death Differ.* **2006**, *13*, 41–52. [CrossRef] [PubMed]
24. Lichtenauer, M.; Mildner, M.; Baumgartner, A.; Hasun, M.; Werba, G.; Beer, L.; Altmann, P.; Roth, G.; Gyöngyösi, M.; Podesser, B.K.; et al. Intravenous and intramyocardial injection of apoptotic white blood cell suspensions prevents ventricular remodelling by increasing elastin expression in cardiac scar tissue after myocardial infarction. *Basic Res. Cardiol.* **2011**, *106*, 645–655. [CrossRef] [PubMed]
25. Barten, M.J.; Sax, B.; Schopka, S.; Amarelli, C.; Epailly, E.; Natali, B.; Teszák, T.; Gökler, J.; Borchert, K.; Theil, J.; et al. European multicenter study on the real-world use and clinical impact of extracorporeal photopheresis after heart transplantation. *J. Heart Lung Transpl.* **2023**, *42*, 1131–1139. [CrossRef] [PubMed]
26. Gregorini, M.; Del Fante, C.; Pattonieri, E.F.; Avanzini, M.A.; Grignano, M.A.; Cassaniti, I.; Baldanti, F.; Comolli, G.; Nocco, A.; Ramondetta, M.; et al. Photopheresis Abates the Anti-HLA Antibody Titer and Renal Failure Progression in Chronic Antibody-Mediated Rejection. *Biology* **2021**, *10*, 547. [CrossRef] [PubMed]
27. Delbrück, C.; Gambichler, T.; Susok, L.; Peinemann, F. Extracorporeal photopheresis for systemic sclerosis: A meta-analysis of randomized clinical trials. *Derm. Ther.* **2022**, *35*, e15530. [CrossRef] [PubMed]
28. Gandelman, J.S.; Song, D.J.; Chen, H.; Engelhardt, B.G.; Chen, Y.B.; Clark, W.B.; Giver, C.R.; Waller, E.K.; Jung, D.K.; Jagasia, M. A Prospective Trial of Extracorporeal Photopheresis for Chronic Graft-versus-Host Disease Reveals Significant Disease Response and No Association with Frequency of Regulatory T Cells. *Biol. Blood Marrow Transpl.* **2018**, *24*, 2373–2380. [CrossRef]
29. Toussirot, E.; Bonnefoy, F.; Vauchy, C.; Perruche, S.; Saas, P. Mini-Review: The Administration of Apoptotic Cells for Treating Rheumatoid Arthritis: Current Knowledge and Clinical Perspectives. *Front. Immunol.* **2021**, *12*, 630170. [CrossRef]
30. Karbian, N.; Abutbul, A.; El-Amore, R.; Eliaz, R.; Beeri, R.; Reicher, B.; Mevorach, D. Apoptotic cell therapy for cytokine storm associated with acute severe sepsis. *Cell Death Dis.* **2020**, *11*, 535. [CrossRef]
31. Michalski, A.; Wójcicka, P.; Bielawska-Drózd, A.; Bartoszcze, M. Review of studies on SARS-CoV-2 infection inhibitors. *Ann. Agric. Environ. Med.* **2021**, *28*, 541–550. [CrossRef] [PubMed]
32. Shin, S.A.; Moon, S.Y.; Park, D.; Park, J.B.; Lee, C.S. Apoptotic cell clearance in the tumor microenvironment: A potential cancer therapeutic target. *Arch. Pharm. Res.* **2019**, *42*, 658–671. [CrossRef] [PubMed]
33. Bradley, A.E.; Black, L. Evaluation of Stem Cell-Derived Cellular Therapy Products. *Toxicol. Pathol.* **2021**, *49*, 1288–1293. [CrossRef]
34. Schafer, K.A.; Eighmy, J.; Fikes, J.D.; Halpern, W.G.; Hukkanen, R.R.; Long, G.G.; Meseck, E.K.; Patrick, D.J.; Thibodeau, M.S.; Wood, C.E.; et al. Use of Severity Grades to Characterize Histopathologic Changes. *Toxicol. Pathol.* **2018**, *46*, 256–265. [CrossRef]
35. Elmore, S.A.; Dixon, D.; Hailey, J.R.; Harada, T.; Herbert, R.A.; Maronpot, R.R.; Nolte, T.; Rehg, J.E.; Rittinghausen, S.; Rosol, T.J.; et al. Recommendations from the INHAND Apoptosis/Necrosis Working Group. *Toxicol. Pathol.* **2016**, *44*, 173–188. [CrossRef] [PubMed]
36. Suttie, A.W. Histopathology of the spleen. *Toxicol. Pathol.* **2006**, *34*, 466–503. [CrossRef]
37. Blazsó, G.; Koltai, M.; Ottlecz, A.; Minker, E. Dextran anaphylactoid reaction in Sprague-Dawley CFY rats. *Acta Physiol. Acad. Sci. Hung* **1979**, *54*, 281–286.
38. De Brito, F.B.; Hanahoe, T.H.P.; Shah, P.; West, G.B. Delayed Hypersensitivity Reactions in Rats and Their Response to Clinical Dextran. *Arch. Allergy Appl. Immunol.* **1982**, *69*, 109–112. [CrossRef]
39. Delitheos, A.; Nanahoe, T.; West, G. A Comparison of the Anaphylactoid Actions of a Synthetic Linear Dextran and a Natural Branched Dextran. *Arch. Allergy Appl. Immunol.* **1976**, *50*, 436–445. [CrossRef] [PubMed]
40. Edlund, T.; Lofgren, B.; Vali, L. Toxicity of dextran in rats. *Nature* **1952**, *170*, 125. [CrossRef]
41. Ashton, N. Physiology of red and white blood cells. *Anaesth. Intensive Care Med.* **2013**, *14*, 261–266. [CrossRef]

42. Patel, S.S.; Thiagarajan, R.; Willerson, J.T.; Yeh, E.T.H. Inhibition of 4 Integrin and ICAM-1 Markedly Attenuate Macrophage Homing to Atherosclerotic Plaques in ApoE-Deficient Mice. *Circulation* **1998**, *97*, 75–81. [CrossRef]
43. Iezzi, G.; Scheidegger, D.; Lanzavecchia, A. Brief Definitive Report Migration and Function of Antigen-primed Nonpolarized T Lymphocytes In Vivo. *J. Exp. Med.* **2001**, *193*, 987–993. [CrossRef]
44. Hendrikx, P.; Martens, C.; Hagenbeek, A.; Keij, J.; Visser, J. Homing of fluorescently labeled murine hematopoietic stem cells. *Exp. Hematol.* **1996**, *24*, 129–140.
45. Ankersmit, H.J.; Hoetzenecker, K.; Dietl, W.; Soleiman, A.; Horvat, R.; Wolfsberger, M.; Gerner, C.; Hacker, S.; Mildner, M.; Moser, B.; et al. Irradiated cultured apoptotic peripheral blood mononuclear cells regenerate infarcted myocardium. *Eur. J. Clin. Investig.* **2009**, *39*, 445–456. [CrossRef]
46. Kurpisz, M.; Czepczyński, R.; Grygielska, B.; Majewski, M.; Fiszer, D.; Jerzykowska, O.; Sowiński, J.; Siminiak, T. Bone marrow stem cell imaging after intracoronary administration. *Int. J. Cardiol.* **2007**, *121*, 194–195. [CrossRef]
47. Aicher, A.; Brenner, W.; Zuhayra, M.; Badorff, C.; Massoudi, S.; Assmus, B.; Eckey, T.; Henze, E.; Zeiher, A.M.; Dimmeler, S.; et al. Assessment of the tissue distribution of transplanted human endothelial progenitor cells by radioactive labeling. *Circulation* **2003**, *107*, 2134–2139. [CrossRef] [PubMed]
48. Elliott, M.R.; Ravichandran, K.S. The Dynamics of Apoptotic Cell Clearance. *Dev. Cell* **2016**, *38*, 147–160. [CrossRef] [PubMed]
49. Nagata, S. Apoptosis and Clearance of Apoptotic Cells. *Annu. Rev. Immunol.* **2018**, *36*, 489–517. [CrossRef] [PubMed]
50. Kumari, D.; Nair, N.; Bedwal, R.S. Morphological changes in spleen after dietary zinc deficiency and supplementation in Wistar rats. *Pharmacol. Rep.* **2019**, *71*, 206–217. [CrossRef] [PubMed]
51. Kim, C. Homeostatic and pathogenic extramedullary hematopoiesis. *J. Blood Med.* **2010**, *1*, 13–19. [CrossRef] [PubMed]
52. Zhang, H.Z.; Li, Y.; Liu, X.; Chen, B.R.; Yao, G.H.; Peng, Y.N. Extramedullary hematopoiesis: A report of two cases. *Exp. Ther. Med.* **2016**, *12*, 3859–3862. [CrossRef] [PubMed]
53. Raval, S.H.; Joshi, D.V.; Patel, B.J.; Patel, J.G.; Patel, P. Extramedullary haematopoiesis in spleen of Wistar rat: A case report. *Indian J. Vet. Pathol.* **2014**, *38*, 131. [CrossRef]
54. Palazzi, X.; Burkhardt, J.E.; Caplain, H.; Dellarco, V.; Fant, P.; Foster, J.R.; Francke, S.; Germann, P.; Gröters, S.; Harada, T.; et al. Characterizing "adversity" of Pathology Findings in Nonclinical Toxicity Studies: Results from the 4th ESTP International Expert Workshop. *Toxicol. Pathol.* **2016**, *44*, 810–824. [CrossRef]
55. Kerlin, R.; Bolon, B.; Burkhardt, J.; Francke, S.; Greaves, P.; Meador, V.; Popp, J. Scientific and Regulatory Policy Committee: Recommended ("Best") Practices for Determining, Communicating, and Using Adverse Effect Data from Nonclinical Studies. *Toxicol. Pathol.* **2016**, *44*, 147–162. [CrossRef] [PubMed]
56. Baldrick, P.; Cosenza, M.E.; Alapatt, T.; Bolon, B.; Rhodes, M.; Waterson, I. Toxicology Paradise: Sorting Out Adverse and Non-adverse Findings in Animal Toxicity Studies. *Int. J. Toxicol.* **2020**, *39*, 365–378. [CrossRef] [PubMed]
57. Pandiri, A.R.; Kerlin, R.L.; Mann, P.C.; Everds, N.E.; Sharma, A.K.; Myers, L.P.; Steinbach, T.J. Is It Adverse, Nonadverse, Adaptive, or Artifact? *Toxicol. Pathol.* **2017**, *45*, 238–247. [CrossRef]
58. Lewis, R.W.; Billington, R.; Debryune, E.; Gamer, A.; Lang, B.; Carpanini, F. Recognition of Adverse and Nonadverse Effects in Toxicity Studies. *Toxicol. Pathol.* **2002**, *30*, 66–74. [CrossRef]
59. Engelhardt, J.A.; Dorato, M.A. Perspective on Adversity in Toxicology Evaluations. *Toxicol. Pathol.* **2021**, *49*, 408–410. [CrossRef]
60. Jensen, N.K.; Ingvorsen, C.; Petersen, D.R.; Pereira, M.J.; Lu, T.T.H.; Alsted, T.J.; Kirkegaard, J.S.; Keane, K.A. Characterization of the Nonendocrine Cell Populations in Human Embryonic Stem Cell-Derived (hESC) Islet-Like Clusters Posttransplantation. *Toxicol. Pathol.* **2021**, *49*, 1269–1287. [CrossRef]

pharmaceutics

MDPI

Article

Development of Clarstatin, a Novel Drug Lead for the Therapy of Autoimmune Uveitis

Shira Merzbach [1], Amnon Hoffman [1,*], Philip Lazarovici [1], Chaim Gilon [2] and Radgonde Amer [3]

[1] Institute for Drug Research, School of Pharmacy, Faculty of Medicine, The Hebrew University of Jerusalem, Jerusalem 9112001, Israel; shira.zuriya@mail.huji.ac.il (S.M.); philipl@ekmd.huji.ac.il (P.L.)
[2] Institute of Chemistry, The Hebrew University of Jerusalem, Jerusalem 9190401, Israel; chaimgilon@gmail.com
[3] Department of Ophthalmology, Hadassah Medical Center, Faculty of Medicine, Hebrew University of Jerusalem, Jerusalem 9112001, Israel; radgonde@gmail.com
* Correspondence: amnonh@ekmd.huji.ac.il; Tel.: +972-2-6720259

Abstract: We describe the design, synthesis, and activity of a potent thiourea-bridged backbone cyclic peptidomimetic known as Clarstatin, comprising a 5-amino acid sequence (Q/D)^1-(R/K)^2-X^3-X^4-A^5-(Gln/Asp)^1-(Arg/Lys)^2-AA^3-AA^4-Ala^5-based on a motif called "shared epitope (SE)", specifically present in specific alleles of the *HLA-DRB1* gene. This SE binds to a particular site within the proline reach domain (P-domain) of the cell surface-calreticulin (CS-CRT). CS-CRT is a multifunctional endoplasmic reticulum (ER) calcium-binding protein that is located on the cell surface of T cells and triggers innate immune signaling, leading to the development of inflammatory autoimmune diseases. The development of Clarstatin was based on the parent peptide W-G-D^1-K^2-S^3-G^4-A^5- derived from the active region of the SE. Following the design based on the cycloscan method, the synthesis of Clarstatin was performed by the Fmoc solid phase peptide synthesis (SPPS) method, purified by HPLC to 96% homogeneity, and its structure was confirmed by LC-MS. Clarstatin reduced calcium levels in Jurkat lymphocyte cultures, ameliorated uveitis in vivo in the experimental autoimmune uveitis (EAU) mice model, and was safe upon acute toxicity evaluation. These findings identify Clarstatin as a promising lead compound for future drug development as a novel class of therapeutic agents in the therapy of uveitis.

Keywords: backbone cyclization; thiourea-bridged; peptomer; calreticulin; experimental autoimmune uveoretinitis; inflammatory autoimmune diseases; peptidomimetic; uveitis

1. Introduction

Uveitis is an ocular sight-threatening inflammation that affects the uveal tract (iris, choroid, and ciliary body) and may also affect the adjacent structures (including the sclera, cornea, vitreous humor, retina, and optic nerve head). Some uveitic entities may be chronic or recurrent, thus causing transient or permanent visual impairment and ocular complications. Uveitis can occur either as a co-manifestation of various autoimmune disorders and infections or it can arise as purely idiopathic ocular inflammation [1]. The management of uveitis remains a challenge for clinicians, in particular, because of the paucity of specific eye-targeted anti-inflammatory drugs. Despite the multitude of adverse effects, corticosteroids remain the first-line and the mainstay of therapy for patients with active uveitis [2]. Therapeutics targeting common inflammatory pathways are also used. These treatments include steroid-sparing immunomodulatory agents. Although often effective, these agents can be associated with potentially severe adverse events [3]. Therefore, there is an unmet clinical need to develop new, safe, and effective drugs for uveitis.

Population stratification investigations have linked autoimmune diseases with polymorphism and mutations of alleles of the major histocompatibility complex (MHC) system called the human leukocyte antigen (HLA). HLA isotypes belonging to MHC class II are HLA-DP, HLA-DM, HLA-DOA, HLA-DOB, HLA-DQ, and HLA-DR [4]. Despite the highly polymorphic nature of the human leukocyte antigens (HLAs) class II genes, the majority of autoimmune diseases are linked

to a limited set of class *II-DR* or -*DQ* gene alleles polymorphism and/or mutations such as the *DRB1*, *DQB1*, and *DPB1* [5]. Genetic studies have linked uveitis to certain MHC class II alleles such as *HLA-DR4* [6]. HLA genes show a strong association with both Vogt–Koyanagi–Harada (VKH) (*HLA-DR4*, *DRB1/DQA1*) and Behcet's disease (BD) (*HLA-B51*), which are two multi-systemic diseases that may present with non-infectious uveitis [7]. These alleles bear a similar amino acid sequence within the DRB1 molecule, generating the "shared-epitope (SE)" hypothesis [8]. This hypothesis claims that possession of the common, five-residue sequence motif in the DR1β-chain may confer an increased risk for autoimmune diseases, including uveitis [9]. For this reason, the $(Q/D)^1$-$(R/K)^2$-X^3-X^4-A^5 five-amino acid SE consensus motif was proposed as essential and sufficient to confer susceptibility to an autoimmune disease, as exemplified in the therapy of rheumatoid arthritis [10]. The native conformation of this sequence is an α-helix and therefore, using cyclic peptides to stabilize this conformation, may produce a potent SE peptidomimetic with drug-like properties. Indeed, several studies developed potent peptidomimetics bearing the SE pharmacophores DKCLA, QKCLA, and DERAA for the therapy of rheumatoid arthritis [10–12], but no studies were directed for the development of a cyclic peptide drug for the therapy of uveitis.

Calreticulin (CRT) is a highly conserved calcium-binding protein in hematopoietic cells. In various autoimmune diseases, CRT migrates and binds to the cell surface (CS-CRT) [13] being expressed on human T lymphocytes where it is physically associated with a pool of different molecules such as the MHC [14,15]. The HLA-DR 'shared epitope' sequence represents a signal transduction target that binds to CS-CRT [16], activating the innate immune signaling and thus contributing to T lymphocyte activation and inflammatory autoimmunity [17]. The presentation of peptide antigens to T cells by MHC class II proteins is a central process in cellular and humoral immune responses. Among the most highly upregulated proteins in uveitis are calreticulin (CRT) and the HLAs [18]. Therefore, inhibition of the interaction between the disease-associated HLAs (such as DR1 and DR4) and CS-CRT may be useful for the treatment of various autoimmune diseases, including uveitis. In addition, it was suggested that there are reciprocal functional interactions between CS-CRT, integrins, and calcium channels on the cell surface of T cells [19,20], and therefore, inhibition of the signal transduction of CS-CRT may block a wide array of cellular responses critical in immune response [21], thereby providing therapy to a wide range of inflammatory autoimmune diseases. However, peptidomimetic inhibitors of the HLA SE motif-CS-CRT interaction that are effective in the therapy of uveitis were not yet reported, and therefore, these were developed in the present study.

Here we describe the use of a urea-bridged backbone cyclic SE peptidomimetic to design and develop a thiourea-bridged backbone cyclic peptidomimetic analog called Clarstatin (Figure 1). The thiourea bond in thiourea-bridged cyclic peptides was previously used to generate a plethora of guanidine and substituted guanidine's containing bridges to test the influence of the bridge chemistry on the activity and selectivity of cyclic peptides [22]. A cyclized enkephalin with a thiourea bridge and methyl guanidine bridge showed good biological activity [23]. We hypothesized, therefore, that thiourea-bridged Clarstatin will also be biologically active and represent a pragmatic novel therapeutic strategy for uveitis. We found that Clarstatin reduced calcium levels in Jurkat lymphocyte cultures, ameliorated uveitis-induced eye pathology in an in vivo experimental autoimmune uveitis (EAU) mice model, and was well tolerated upon acute systemic delivery, representing a novel lead compound for the therapy of uveitis.

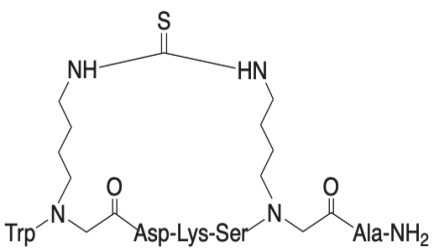

Figure 1. Structure of Clarstatin.

2. Experimental Method

2.1. Fluorescent Ca^{2+} Imaging

Jurkat cells were attached to polylysine-coated glass coverslips for Ca^{2+} imaging conducted in Ringer's solution composed of 126 mM NaCl, 5.4 mM KCl, 0.8 mM $MgCl_2$, 20 mM HEPES, 1.8 mM $CaCl_2$, and 15 mM glucose. The pH of the solution was adjusted to 7.4 using NaOH. Prior to imaging, the cells were loaded with Fura 2 AM from Teflabs, Jackson Springs, NC, USA. Intracellular Ca^{2+} responses were observed in the presence of 2 mM EGTA. Illumination of cells was accomplished using a 175 W xenon arc lamp, and the excitation wavelengths of 340/380 nm were selected via a Lambda DG-4 monochromatic wavelength changer from Sutter Instrument, Novato, CA, USA. The intracellular Ca^{2+} concentration was quantified using digital video microfluorometry employing a front-illuminated interline CCD camera (Exi Blue; QImaging, Surrey, BC, Canada) alongside MetaFluor Fluorescence Ratio Imaging Software (Meta Imaging Series 6.1) from Molecular Devices, Sunnyvale, CA, USA. Dual images (340 and 380 nm excitation, 510 nm emission) were captured, and pseudocolor ratio-metric images were recorded every 2 s throughout the experiment, all performed at room temperature [24].

2.2. Experimental Autoimmune Uveitis Model

2.2.1. Experimental Autoimmune Uveitis Induction

To evaluate the therapeutic effect of Clarstatin, we performed experiments on C57BL/6J mice in an experimental autoimmune uveitis (EAU) mice model. Female, 6- to 8-week-old C57BL/6J mice were maintained in the specific pathogen-free unit of our Faculty of Medicine, and all experiments were approved by the Hebrew University–Hadassah Institutional Animal Care and Use Committee. The mice were immunized subcutaneously (SC) with 500 μg interphotoreceptor retinoid-binding protein ($IRBP_{1–20}$, GPTHLFQPSLVLD-MAKVLLD) (Adar Biotech, Rehovot, Israel) emulsified with an equal volume of complete Freund's adjuvant (CFA) (Sigma, St. Louis, MO, USA) in a total volume of 200 μL. The mixture contained 2.5 mg/mL *Mycobacterium tuberculosis* H37RA (BD, Bethesda, MD, USA). An additional intraperitoneal injection of 1 μg of purified Bordetella pertussis toxin (PTX) (List biological laboratories, Campbell, CA, USA) was also applied to each animal. The control mice were immunized with the same volume of PBS instead of IRBP in CFA and PTX. The mice were sacrificed at day 36 after primary immunization.

2.2.2. Treatment with Clarstatin

Each mouse in the treatment group received 3.6, 36, or 360 μg/kg of Clarstatin in a volume of 50 μL once or twice per week by an intraperitoneal (i.p.) injection (n = 4, 8, 5, respectively). The first dose was administered concurrently with EAU induction. The mice in the control group received PBS i.p. at the same volume. In each mouse, one eye was collected and embedded in paraffin for histopathological analysis.

2.2.3. Histological Evaluation of Eye Slices

To analyze the histopathology results after immunization for 36 days, eyes were collected immediately after exitus and prefixed for 24 h in Davidson solution. Next, the fixed eyes were dehydrated in alcohol with concentration gradients and embedded in paraffin. Then, tissue sections (3–6 μm) were stained with hematoxylin and eosin. The severity of uveitis was evaluated histologically and graded in a masked fashion. This grading system permitted a semi-quantitative assessment of the severity and extent of both infiltrative and structural/morphologic changes of the uveitis at various points throughout the course of EAU. Histological changes were evaluated and graded on a scale from 0 to 4 according to the previously described criteria [25].

2.3. Cell Death Assay

Cell death of Jurkat cells was measured by the release of lactate dehydrogenase (LDH) into the medium, in the absence and presence of different concentrations of Clarstatin after 48 h of treatment, using the LDH reagent. H_2O_2-treated cells were used as a positive

control. LDH activity was determined spectrophotometrically at 340 nm by following the rate of conversion of oxidized NAD to the reduced form of NAD (NADH). LDH release was expressed as the optical density units and calculated as a percentage of total LDH. Each experiment was performed three times in six replicates (n = 18) [26].

2.4. Acute Toxicity Evaluation of Clarstatin in Mice

Female ICR mice (n = 5) were injected intravenously with 0.2 mL Clarstatin at a dose of 10 mg/kg. Untreated mice (n = 5) were the control. The brain, liver, kidneys, spleen, heart, lungs, small and large intestines, stomach, and thymus from the mice were harvested after 48 h and fixed in 4% formaldehyde. Then, the tissues were trimmed, placed in embedding cassettes, and processed routinely for paraffin embedding. Six cassettes were prepared per animal (8 organs). Paraffin sections (4 microns thick) were cut, placed on glass slides, and stained with haematoxylin and eosin (H&E) for histological evaluation. Pictures were taken with an Olympus microscope (BX60, serial NO. 7D04032) (Olympus, Tokyo, Japan) using the microscope's camera (Olympus DP73, serial No. OH05504) at an objective magnification of ×10 and ×4. The H&E-stained slides were examined and scored by the study's pathologist, using a semi-quantitative 5-point grading scale, for the severity of the histopathological changes: Grade 0—the tissue appears normal, without any changes at all; Grade 1—minimal pathological findings; Grade 2—mild pathological findings; Grade 3—moderate pathological findings; Grade 4—severe pathological findings. The histopathological evaluation included a comparison between treated and naïve animals.

2.5. Statistics

Data are presented as the mean ± standard error of the mean (SEM) and were considered significant when the p-value was <0.05. Statistical analysis was performed using one-way ANOVA followed by Dunnett's multiple comparisons by using GraphPad Prism 5.0 (GraphPad Software, San Diego, CA, USA).

3. Results

3.1. SPPS of Clarstatin

The solid phase peptide synthesis of Clarstatin is shown in Scheme 1.

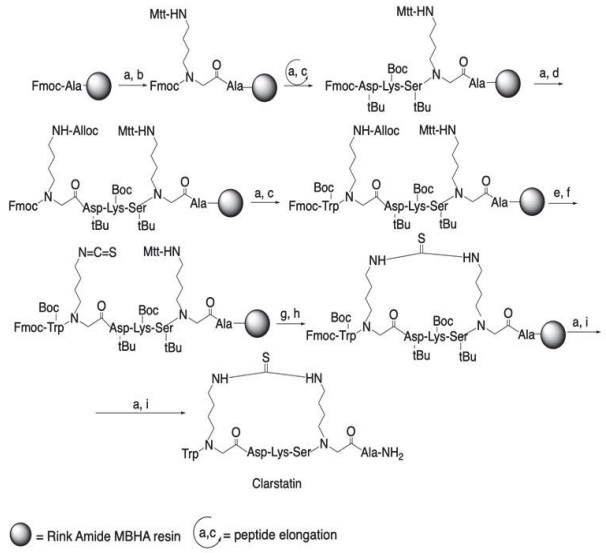

Scheme 1. Solid phase synthesis of Clarstatin. Reagents: (a) piperidine/DMF 20%; (b) coupling of Fmoc-[N-(Mtt)δ-aminobutyl]glycine building unit: TBTU/DIEA/DMF; (c) FmocAA + TBTU/DIEA/DMF; (d) coupling of Fmoc-[N-(alloc)δ-aminobutyl]glycine building unit: TBTU/DIEA/DMF; (e) (PPh3)4Pd(0)/N-methylmorpholine/AcOH; (f) isothiocyanate formation: CS_2/HBTU/DIEA/DMF; (g) DCM/TFE/AcOH (7/2/1); (h) DIEA/DMF; (i) TFA/TIS/H2O (95/2.5/2.5).

After synthesis, the crude Clarstatin was purified to 96% homogeneity using preparative HPLC (Figure 2). The molecular structure was then verified by mass spectrometry (Figure 3). In the analytical HPLC, the main peak corresponded to Clarstatin with a molecular weight of 903.1, which matched the calculated value of 903.

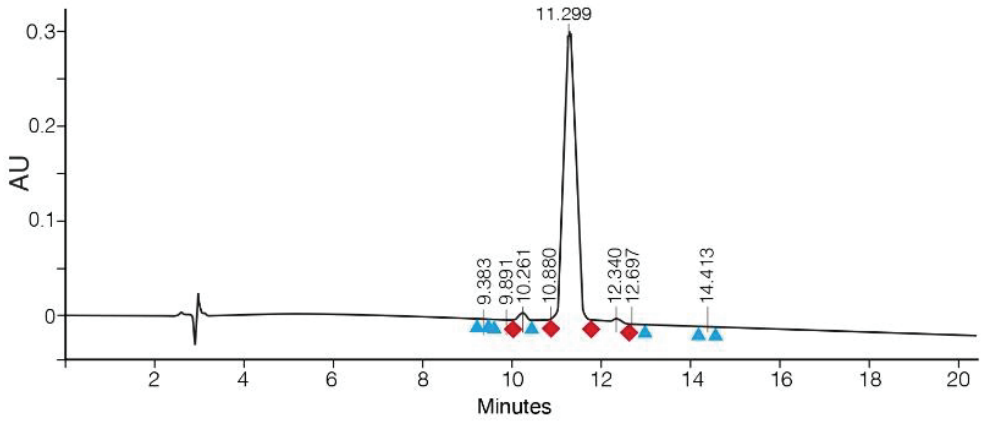

Figure 2. Analytical HPLC of Clarstatin.

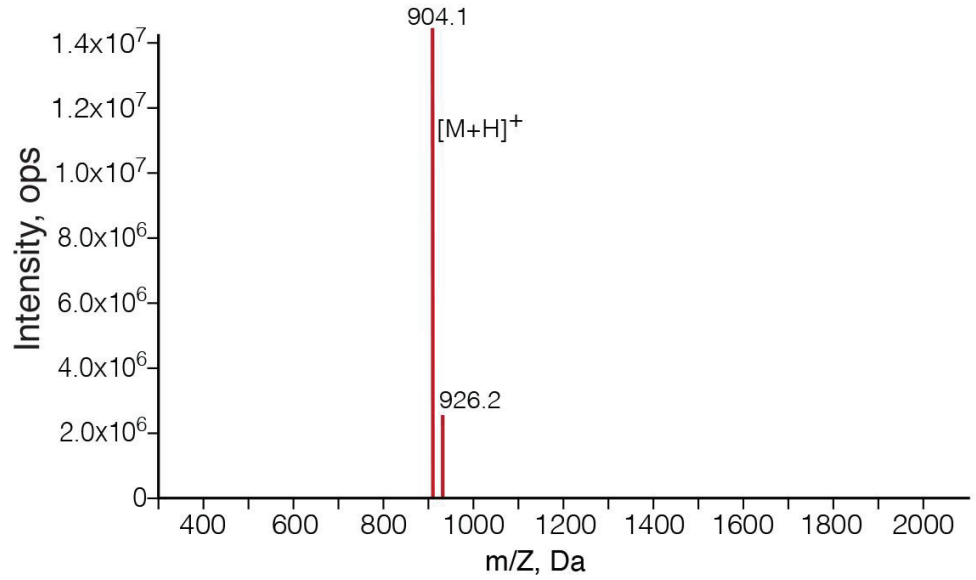

Figure 3. Mass spectrum of Clarstatin.

3.2. Ca^{2+} Signaling Was Reduced in Jurkat Cells upon Clarstatin Treatment

Multiple inflammatory stimuli converge on Ca^{2+} signaling in immune cells. We sought to characterize the effect of Clarstatin on Ca^{2+} signaling in Jurkat cells in vitro by comparing it to the inflammatory lipopolysaccharide bacterial endotoxin (LPS). Cytosolic intracellular Ca^{2+} content was measured in Jurkat cells loaded with Fura-2AM in the presence of EGTA to prevent extracellular influx by calcium channels. As expected, intracellular Ca^{2+} levels significantly decreased upon LPS treatment (Figure 4A). In the presence of Clarstatin, intracellular Ca^{2+} content was also significantly attenuated (Figure 4B). The overall calcium level, calculated as the area under the curve (AUC), was reduced by 65% in LPS-treated cells and by 15% in Clarstatin-treated cells (orange traces) compared to control-untreated cells (blue traces). Overall, the reduced calcium levels remained significantly decreased for about 500 s. To evaluate a potential cytotoxic effect, Jurkat cells were incubated with 0.3, 36, and 100 µg/mL Clarstatin for 48 h and thereafter the necrotic cell death was measured by the release of LDH. Figure 4C indicates that at in all concentrations, Clarstatin did not significantly increase cell death compared to control-untreated cells, stressing the cellular

safety of the Jurkat cells treated with Clarstatin and indicating that the effect of Clarstatin on the intracellular Ca^{2+} content was not due to cytotoxicity.

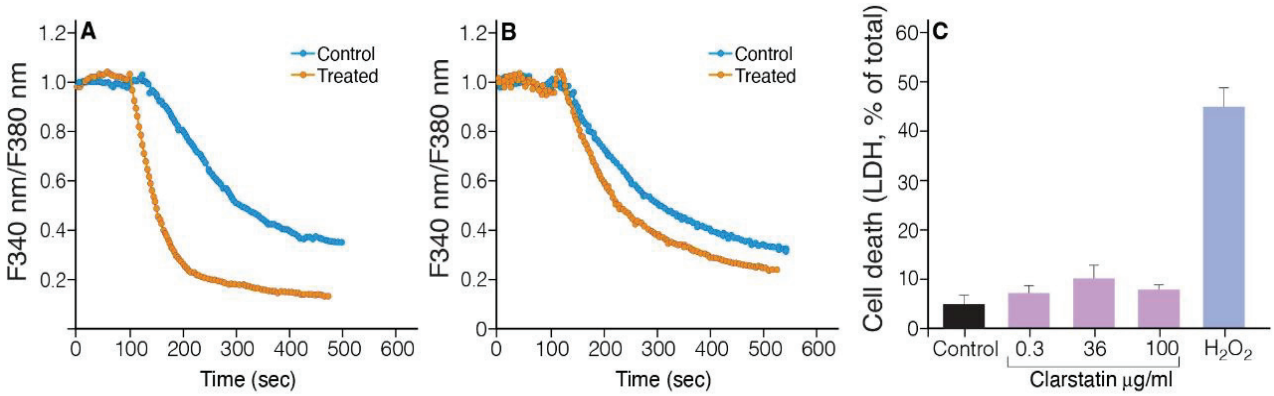

Figure 4. Ca^{2+} signaling was reduced in Jurkat cells upon Clarstatin treatment in the absence of cytotoxic effects. Changes with time of Ca^{2+} signaling in Jurkat cells in response to (**A**) LPS (50 µg/mL) and (**B**) Clarstatin (36 µg/mL); (**C**) necrotic cell death measured by LDH release in Jurkat cells exposed for 48 h to different Clarstatin concentrations; H_2O_2 treatment was used as a positive cytotoxic control. Values expressed as mean ± SEM (n = 18). $p \leq 0.05$ for H_2O_2 vs. control are percent of LDH released in the medium out of the total culture LDH. No significance was found for Clarstatin concentrations compared to control (ANOVA test).

3.3. The Severity of EAU Was Reduced in Mice upon Clarstatin Treatment

To evaluate the therapeutic effect of Clarstatin, we performed experiments on C57BL/6J mice in the EAU mice model. The mice were immunized subcutaneously with the interphotoreceptor retinoid-binding protein (IRBP) to induce uveitis, treated or untreated with Clarstatin, and sacrificed. To analyze the eye histopathology, the eyes were collected, fixed, and eye sections were stained with hematoxylin and eosin. The intensity of eye uveitis was evaluated histologically permitting a semi-quantitative assessment of the severity and extent of the inflammation and pathological changes of the eye. The EAU histopathological score (a scale from 0–4 according to the extent of inflammation and tissue damage) was used for grading the severity of uveitis disease. Score 0—few (1–2) very small, peripheral, focal, chorioretinal lesions and minimal vasculitis; score 1—mild vasculitis, small focal chorioretinal lesions (no more than five), linear chorioretinal lesion (no more than one); score 2—multiple (more than five) chorioretinal lesions and/or inflammatory infiltrates severe vasculitis (large, thick infiltrates), linear chorioretinal lesions (more than five); score 3—pattern of linear chorioretinal lesions, large, confluent chorioretinal lesions, subretinal neovascularization, hemorrhages; score 4—large retinal detachment, retinal atrophy.

The histology sections of the eyes in the treatment group with Clarstatin (3.6 µg/kg, i.p) showed reduced signs of active uveitis (Figure 5C). However, EAU mice that were not treated showed signs of active disease like vitreous cells and several foci of retinal infiltrates and vasculitis (Figure 5B). The wild-type mouse, which was not immunized with IRBP, showed a normal retinal structure (Figure 5A). Quantitation of the therapeutic effect of Clarstatin based on the EAU score from histopathological sections showed that untreated mice developed EAU at an average score of 1.4. Control mice that were not immunized with IRBP (WT) did not develop EAU (score 0). Mice treated with 3.6 µg/kg Clarstatin developed EAU at an average score of 0.7. Mice treated with 36 µg/kg Clarstatin developed EAU at an average score of 0.8. Mice treated with 360 µg/kg Clarstatin developed EAU at an average score of 0.3. In the treatment group which received a dose of 3.6 µg/kg Clarstatin, the EAU score was reduced from 1.4 to 0.7 (p = 0.06). In the treatment group which received a dose of 36 µg/kg Clarstatin, the EAU score was reduced from 1.4 to 0.8 ($p < 0.05$). In the treatment group which received a dose of 360 µg/kg Clarstatin, the EAU score was reduced from 1.4 to 0.3 ($p < 0.01$) (Figure 5D).

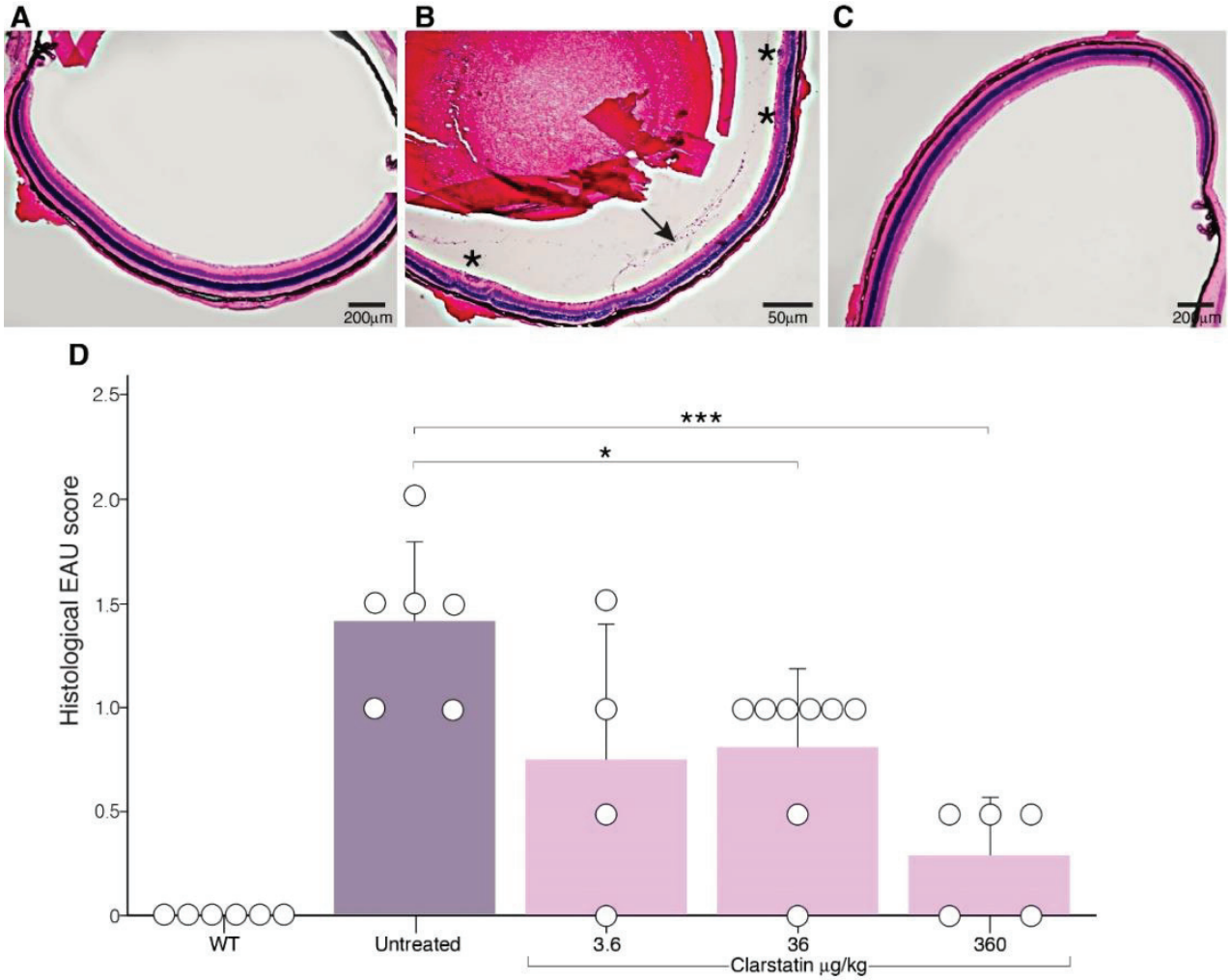

Figure 5. Examination of the therapeutic effect of the cyclic peptide, Clarstatin, in the EAU mice model by histopathology analysis. Representative photographs of the histopathology of retinal sections of C57BL/6J mice 36 days after EAU induction. (**A**) The wild-type mouse, which was not immunized with IRBP, showed normal retinal structure. (**B**) The EAU mouse which was immunized with IRBP showed active uveitis with vitreous cells (arrow) and several foci of retinal infiltrates and vasculitis (star). (**C**) The EAU mouse which was immunized with IRBP and treated with Clarstatin (3.6 µg/kg mice, 50 µL, i.p., twice per week) showed no signs of active uveitis. (**D**) Quantitation by dose response of the therapeutic effect of Clarstatin based on the EAU score from histopathological sections. EAU scores were assigned on a scale from 0 to 4 according to the extent of inflammation and tissue damage. Each point represents one mouse. The ocular inflammatory response was ameliorated in mice treated with Clarstatin compared to untreated mice. * $p < 0.05$ *** $p < 0.001$ (ANOVA test).

3.4. Acute Tolerability of Clarstatin in Mice without Short-Term Adverse Pathological Effects on Major Organs

We conducted an acute, single-dose toxicity study to determine the short-term adverse pathological effects of Clarstatin on major mice organs when administered in mice in a single high dose. One group of five mice received a dose of 0.25 mg/mice (10 mg/kg) Clarstatin by intravenous (i.v.) injection, in a volume of 0.2 mL/mouse. The second group of five naïve mice did not receive Clarstatin and were considered as the control. Before Clarstatin administration, the body weight of each animal was determined, and the dose was calculated according to the body weight. The mice were observed for any toxic effect for the first 4 h after Clarstatin injection and for the entire period of the two days. They did not display any changes in behavior, breathing, skin effects, body weight, urinations, food

and water intake, temperature, and changes in eye and skin colors. There were no signs of constipation, sedation, convulsion, tremor, lethargy, drowsiness, coma, or death. After 48 h of exposure and follow up, the animals were sacrificed, and organs were harvested for pathology analyses. By comparing the organs from Clarstatin-treated mice to the control, no pathological changes were observed, as evidenced from Figure 6. The tested organs, including the brain, kidneys, spleen, heart, lungs, small intestine and large intestine, stomach, and thymus looked normal, without any microscopically pathological changes. The absence of pathological findings indicates acute tolerability at 48 h after i.v. injection of 10 mg/kg Clarstatin in mice.

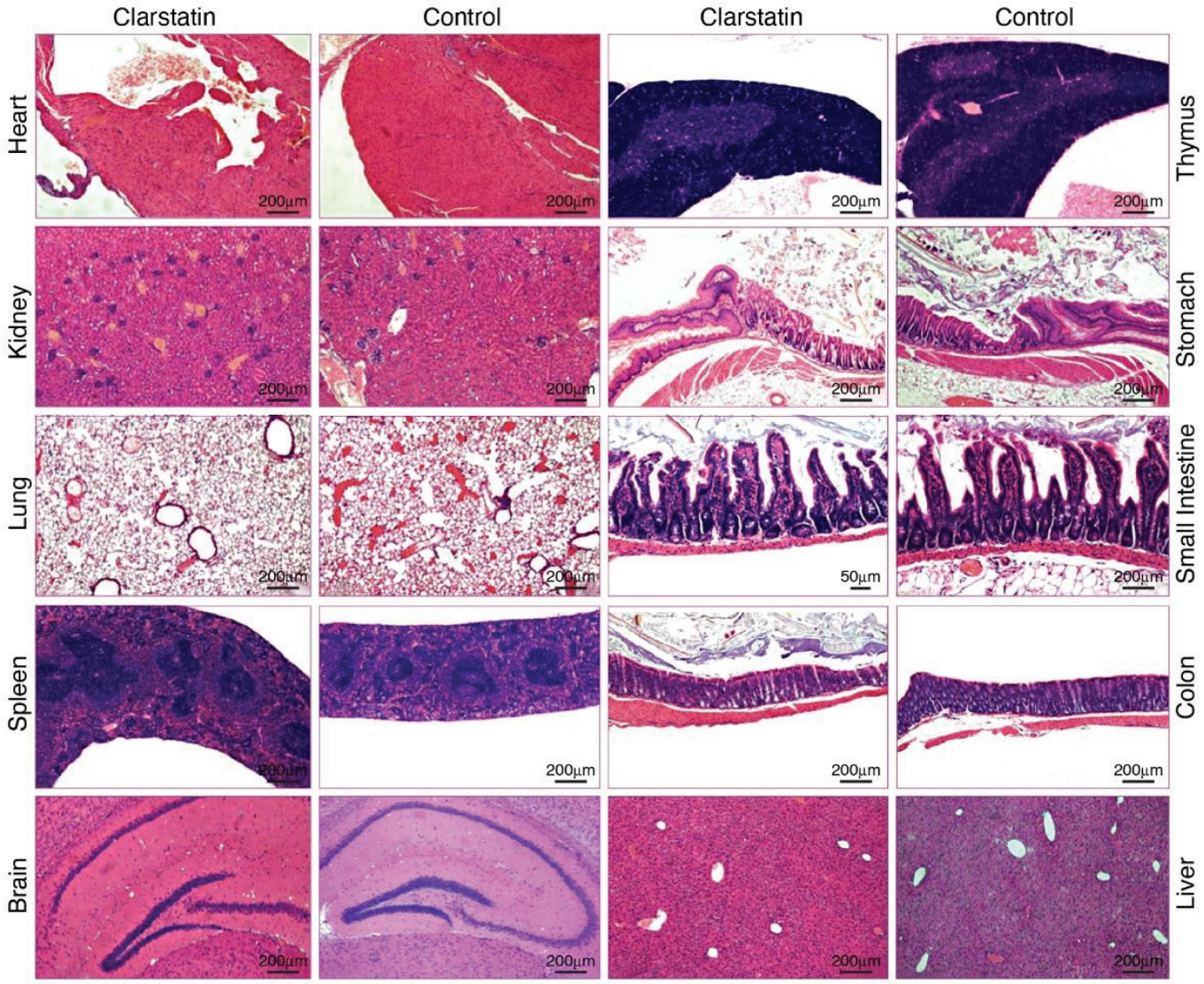

Figure 6. Representative histological images of organ slices stained with hematoxylin and eosin in an acute toxicity test of female ICR mice after administration of Clarstatin (10 mg/kg) by i.v. injection for 48 h.

4. Discussion

We have previously [27] applied the cycloscan method to the shared epitope (SE) sequence -Gly-Gln-Lys-Cys-Gly-Ala-NH_2 bridging the amide nitrogens of the two Gly residues with a urea-bridged, aliphatic bridge of various sizes and found a highly potent cyclic peptide with a ring size of 24 atoms. Moreover, we characterized a small SE-mimetic c(HS4-4), containing the SE primary sequence motif QKRAA, which was synthesized using a backbone cyclization method. The SE-peptidomimetic c(HS4-4) interacted strongly with the SE receptor

calreticulin (CRT) [11]. The docking of c(HS4-4) to the CS-CRT:HLA-DRB1 complex revealed the importance of Gln70. We speculated, therefore, that replacing Gln in the SE-mimetic with Asp will lead to an effective inhibitor of HLA-CRT interaction. Indeed, bridging the amide nitrogens of the two Gly residues in the sequence -Gly-Asp-Lys-Cys-Gly-Ala-NH_2 with a urea-bridged aliphatic ring of 11 atoms yielded a backbone cyclic peptide with a ring size of 24 atoms that potently abolished arthritis in mice [12]. With this background, in the present study, we designed, synthesized, and characterized another novel shared epitope (SE), thiourea-bridged backbone cyclic peptide, named Clarstatin, that reduced calcium levels in Jurkat lymphocyte cultures, was well tolerated in cell cultures upon acute toxicity testing, and ameliorated uveitis in vivo in an EAU mice model. To our knowledge, this is the first description of the SPPS of a backbone cyclic peptide with a thiourea bridge. We used the same strategy described by Touati-Jallabe et al. [22] for the SPPS, namely, we incorporated two building units having the Mtt and Alloc orthogonal protection on the N-alkyl amino groups. We found out that the on-resin generation of the isothiocyanate, after the removal of the Alloc protecting group, was best performed by the procedure described by Boas et al. [28] rather than the procedure described by Touati-Jallabe et al. [22]. Apparently, CS2 + HBTU gave better yields than di-2-pyridylthionocarbonate (DPT) for the generation of the isothiocyanate. Using these procedures, we obtained, after purification with prep. HPLC, a highly pure, biologically active peptidomimetic named Clarstatin.

Beyond offering new insights into the drug development of novel peptide biologics for uveitis, the present findings illustrate the therapeutic target ability of the HLA-DR 'shared epitope' sequence–calreticulin signaling pathway by a specific, rationally designed backbone cyclic peptide. Clarstatin showed potent activity both in vitro and in vivo. This finding could facilitate future optimization efforts of Clarstatin. From the medicinal chemistry perspective, it is also worth noting that the thiourea bridge and the introduction of two glycines did not appear to play a functional role in the compounds' biological effects.

The main significance of the findings reported here relates to the fact that they propose Clarstatin as a novel biologic lead compound for the treatment of uveitis. To date, novel treatment modalities in uveitis such as monoclonal antibodies have targeted cytokines, their receptors, or other players in the immune-activated final common pathway [29]. Due to their involvement in the final steps of uveitis pathogenesis, the current treatment with biologics is less effective than steroids but safer [30]. The advantage of the Clarstatin approach over current or emerging drugs is that it addresses an unmet need by offering a potent intervention strategy that specifically targets the early important event in the lymphocyte pathologic autoimmune inflammatory cascade by targeting and inhibiting the interaction between the HLA-DR 'shared epitope' sequence and calreticulin. Calreticulin, in addition to being localized in the endoplasmic reticulum, is also expressed in other subcellular compartments such as the nucleus, the nuclear envelope, the cytosol, and the cell surface of the cells. Therefore, Clarstatin's ability to reduce cytosol calcium levels can be attributed to its ability to antagonize calreticulin activity in one of these cellular compartments. A decreased calreticulin level will decrease the lymphocyte's cytosol calcium levels as well as Ca^{2+} storage capacity and Ca^{2+} sequestering ability, thus causing increased sensitivity of cells toward the intracellular Ca^{2+} level and signaling [31]. This hypothesis is supported by findings indicating that treatment of cells with antisense nucleotides decreases calreticulin expression and lowers the Ca^{2+} response [32]. A decrease in cytosolic calcium in leukocytes may affect the cellular compartment distribution of calreticulin and may have implications for cytokine production and innate inflammatory purposes [33]. The present results clearly and indirectly indicate that the synthetic Clarstatin is active in vitro, most probably by functionally antagonizing the calcium-buffering ability of cellular calreticulin.

Experimental autoimmune uveoretinitis (EAU) is thought to be a representative model for the study of therapeutic approaches to human posterior uveitis [34]. EAU can be induced in animals through systemic immunization with retinal proteins, initiating an immune response that results in tissue damage. This process is orchestrated by CD4(+) T cells specific to autoantigens, whose activation triggers the infiltration of various other

leukocytes into the retina. Throughout EAU, immune cells penetrate the eye's parenchyma, causing pathological processes on both the retina and choroid. In the present study, it was found that treatment with Clarstatin reduces the severity of EAU, most probably reflecting reduced inflammatory cell recruitment and infiltration into the eye. Therefore, it is reasonable to propose that Clarstatin inhibited the process of inflammatory cell recruitment to the eye that involves their activation by elevation of the intracellular calcium [35], as evident from the present experiments with the Jurkat cells. The possibility that Clarstatin also inhibited adhesion, and/or migration, and eye infiltration, preventing focal retinal tissue damage, is under investigation in our laboratories.

5. Conclusions

This study suggests that Clarstatin could be a useful thiourea-bridged backbone cyclic SE peptidomimetic lead compound and tool for studying the mechanisms governing uveitis. Furthermore, the results of this study provide a rationale and early preclinical information that could pave the way for the development of specific, potent, safe, and inexpensive drugs for uveitis.

6. Patents

Gilon C, Hoffman A, Lazarovici P, Radgonde A. Calreticulin peptidomimetic inhibitors and prodrugs. U.S. provisional patent application No. 63/477,201 filed on 26 December 2022 and refiled 26 December 2023. Assigned to YISSUM research and development Co. of the Hebrew University of Jerusalem LTD., and HADASIT Medical Research services and development LTD.

Author Contributions: The authors contributed to this work as follows: conceptualization, C.G., A.H., P.L. and R.A.; methodology, S.M., C.G., A.H., P.L. and R.A.; investigation, S.M., C.G., A.H., P.L. and R.A.; data curation, S.M., C.G., A.H., P.L. and R.A.; validation, S.M., C.G., A.H., P.L. and R.A.; formal analysis, S.M., C.G., A.H., P.L. and R.A.; writing the original draft preparation, manuscript review, and editing, S.M., C.G., A.H., P.L. and R.A.; funding acquisition, A.H. and R.A.; project administration, A.H. and R.A. All authors contributed to the writing of the manuscript. All authors have read and agreed to the published version of the manuscript.

Funding: This work was supported in part by the Hebrew University of Jerusalem—Yissum Intramural Research Funds, and by a Kamin grant (67970) from the Israel Innovation Authority.

Institutional Review Board Statement: The acute toxicity experiment was approved by the Institutional Animal Care and Use Committee and performed according to OECD guidelines for chemical testing—PathoLogica study number: HEB-1023-PRJ approved 4 November 2020. The uveitis animal study protocol was approved by the Institutional Ethics Committee of the Faculty of Medicine, the Hebrew University of Jerusalem, code MD-20-16345-2, approved 17 August 2020, and the experiments were performed in strict accordance with the Guide for the Care and Use of Laboratory Animals published by the US National Institutes of Health (NIH approval number: OPRR-A01-5011).

Informed Consent Statement: Not applicable.

Data Availability Statement: The data presented in this study are available in this article.

Acknowledgments: P.L. holds the Jacob Gitlin Chair in Physiology and is affiliated and supported in part by the David R. Bloom Center for Pharmacy, Adolf and Klara Brettler Center for Research in Molecular Pharmacology and Therapeutics, and the Grass Center for Drug Design and Synthesis of Novel Therapeutics at the Hebrew University of Jerusalem, Israel. We would like to thank Zehava Cohen for help with the artwork, Matan Geron for the assistance with the calcium experiments, and the expert pathologist Loeb Emanuel for the help with the toxicity experiment.

Conflicts of Interest: The authors declare no conflicts of interest.

References

1. Barisani-Asenbauer, T.; MacA, S.M.; Mejdoubi, L.; Emminger, W.; MacHold, K.; Auer, H. Uveitis—A Rare Disease Often Associated with Systemic Diseases and Infections—A Systematic Review of 2619 Patients. *Orphanet. J. Rare Dis.* **2012**, *7*, 57. [CrossRef]
2. Valdes, L.M.; Sobrin, L. Uveitis Therapy: The Corticosteroid Options. *Drugs* **2020**, *80*, 765–773. [CrossRef] [PubMed]
3. Rosenbaum, J.T.; Bodaghi, B.; Couto, C.; Zierhut, M.; Acharya, N.; Pavesio, C.; Tay-Kearney, M.L.; Neri, P.; Douglas, K.; Pathai, S.; et al. New Observations and Emerging Ideas in Diagnosis and Management of Non-Infectious Uveitis: A Review. *Semin. Arthritis Rheum.* **2019**, *49*, 438–445. [CrossRef] [PubMed]
4. Jones, E.Y.; Fugger, L.; Strominger, J.L.; Siebold, C. MHC Class II Proteins and Disease: A Structural Perspective. *Nat. Rev. Immunol.* **2006**, *6*, 271–282. [CrossRef] [PubMed]
5. Mangalam, A.K.; Rajagopalan, G.; Taneja, V.; David, C.S. HLA Class II Transgenic Mice Mimic Human Inflammatory Diseases. *Adv. Immunol.* **2008**, *97*, 65–147. [PubMed]
6. Li, S.; Yan, L.; Li, M.; Fan, N. Analysis of HLA Profiles in 390 Uveitis Cases: Insights into Clinical Presentations. *Altern. Ther. Health Med.* **2023**, *29*, 717–721. [PubMed]
7. Hou, S.; Li, N.; Liao, X.; Kijlstra, A.; Yang, P. Uveitis Genetics. *Exp. Eye Res.* **2020**, *190*, 107853. [CrossRef] [PubMed]
8. Gregersen, P.K.; Silver, J.; Winchester, R.J. The Shared Epitope Hypothesis. An Approach to Understanding the Molecular Genetics of Susceptibility to Rheumatoid Arthritis. *Arthritis Rheum.* **1987**, *30*, 1205–1213. [CrossRef] [PubMed]
9. Guarene, M.; Capittini, C.; De Silvestri, A.; Pasi, A.; Badulli, C.; Sbarsi, I.; Cremaschi, A.L.; Garlaschelli, F.; Pizzochero, C.; Monti, M.C.; et al. Targeting the Immunogenetic Diseases with the Appropriate HLA Molecular Typing: Critical Appraisal on 2666 Patients Typed in One Single Centre. *Biomed. Res. Int.* **2013**, *2013*, 904247. [CrossRef]
10. Naveh, S.; Tal-Gan, Y.; Ling, S.; Hoffman, A.; Holoshitz, J.; Gilon, C. Developing Potent Backbone Cyclic Peptides Bearing the Shared Epitope Sequence as Rheumatoid Arthritis Drug-Leads. *Bioorganic Med. Chem. Lett.* **2012**, *22*, 493–496. [CrossRef]
11. Fu, J.; Ling, S.; Liu, Y.; Yang, J.; Naveh, S.; Hannah, M.; Gilon, C.; Zhang, Y.; Holoshitz, J. A Small Shared Epitope-Mimetic Compound Potently Accelerates Osteoclast-Mediated Bone Damage in Autoimmune Arthritis. *J. Immunol.* **2013**, *191*, 2096–2103. [CrossRef] [PubMed]
12. Ling, S.; Liu, Y.; Fu, J.; Colletta, A.; Gilon, C.; Holoshitz, J. Shared Epitope-Antagonistic Ligands: A New Therapeutic Strategy in Mice with Erosive Arthritis. *Arthritis Rheumatol.* **2015**, *67*, 2061–2070. [CrossRef] [PubMed]
13. Wiersma, V.R.; Michalak, M.; Abdullah, T.M.; Bremer, E.; Eggleton, P. Mechanisms of Translocation of ER Chaperones to the Cell Surface and Immunomodulatory Roles in Cancer and Autoimmunity. *Front. Oncol.* **2015**, *5*, 7. [CrossRef] [PubMed]
14. Solheim, J.C. Class I MHC Molecules: Assembly and Antigen Presentation. *Immunol. Rev.* **1999**, *172*, 11–19. [CrossRef] [PubMed]
15. Adibzadeh, M.; Friccius, H.; Bornhak, S.; Max, H.; Hambrecht, A.; Sansom, D.; Kalbacher, H.; Schenk, A.; Pohla, H.; Pawelec, G. Role of Three Quantitatively Dominant Endogenous Peptides from HLA-DRB1*0401 Molecules in Class II Specific Alloreactivity. *Transpl. Immunol.* **1994**, *2*, 293–299. [CrossRef] [PubMed]
16. Ling, S.; Cheng, A.; Pumpens, P.; Michalak, M.; Holoshitz, J. Identification of the Rheumatoid Arthritis Shared Epitope Binding Site on Calreticulin. *PLoS ONE* **2010**, *5*, e11703. [CrossRef] [PubMed]
17. Onuora, S. Pharmacotherapy: Going Upstream: Peptidomimetics Block Shared-Epitope Signalling. *Nat. Rev. Rheumatol.* **2015**, *11*, 320. [CrossRef] [PubMed]
18. Cresswell, P.; Ackerman, A.L.; Giodini, A.; Peaper, D.R.; Wearsch, P.A. Mechanisms of MHC Class I-Restricted Antigen Processing and Cross-Presentation. *Immunol. Rev.* **2005**, *207*, 145–157. [CrossRef] [PubMed]
19. Ohkuro, M.; Kim, J.D.; Kuboi, Y.; Hayashi, Y.; Mizukami, H.; Kobayashi-Kuramochi, H.; Muramoto, K.; Shirato, M.; Michikawa-Tanaka, F.; Moriya, J.; et al. Calreticulin and Integrin Alpha Dissociation Induces Anti-Inflammatory Programming in Animal Models of Inflammatory Bowel Disease. *Nat. Commun.* **2018**, *9*, 1982. [CrossRef]
20. Liu, C.-C.; Leclair, P.; Yap, S.Q.; Lim, C.J. The Membrane-Proximal KXGFFKR Motif of α-Integrin Mediates Chemoresistance. *Mol. Cell. Biol.* **2013**, *33*, 4334–4345. [CrossRef]
21. Gold, L.I.; Eggleton, P.; Sweetwyne, M.T.; Van Duyn, L.B.; Greives, M.R.; Naylor, S.; Michalak, M.; Murphy-Ullrich, J.E. Calreticulin: Non-Endoplasmic Reticulum Functions in Physiology and Disease. *FASEB J.* **2010**, *24*, 665–683. [CrossRef] [PubMed]
22. Touati-Jallabe, Y.; Bojnik, E.; Legrand, B.; Mauchauffée, E.; Chung, N.N.; Schiller, P.W.; Benyhe, S.; Averlant-Petit, M.C.; Martinez, J.; Hernandez, J.F. Cyclic Enkephalins with a Diversely Substituted Guanidine Bridge or a Thiourea Bridge: Synthesis, Biological and Structural Evaluations. *J. Med. Chem.* **2013**, *56*, 5964–5973. [CrossRef] [PubMed]
23. Verbeken, M.; Wynendaele, E.; Mauchauffée, E.; Bracke, N.; Stalmans, S.; Bojnik, E.; Benyhe, S.; Peremans, K.; Polis, I.; Burvenich, C.; et al. Blood-Brain Transfer and Antinociception of Linear and Cyclic N-Methyl-Guanidine and Thiourea-Enkephalins. *Peptides* **2015**, *63*, 10–21. [CrossRef] [PubMed]
24. Geron, M.; Kumar, R.; Matzner, H.; Lahiani, A.; Gincberg, G.; Cohen, G.; Lazarovici, P.; Priel, A. Protein Toxins of the Echis Coloratus Viper Venom Directly Activate TRPV1. *Biochim. Biophys. Acta Gen. Subj.* **2017**, *1861*, 615–623. [CrossRef] [PubMed]
25. Thurau, S.R.; Chan, C.C.; Nussenblatt, R.B.; Caspi, R.R. Oral Tolerance in a Murine Model of Relapsing Experimental Autoimmune Uveoretinitis (EAU): Induction of Protective Tolerance in Primed Animals. *Clin. Exp. Immunol.* **1997**, *109*, 370–376. [CrossRef] [PubMed]

26. Lahiani, A.; Hidmi, A.; Katzhendler, J.; Yavin, E.; Lazarovici, P. Novel Synthetic PEGylated Conjugate of α-Lipoic Acid and Tempol Reduces Cell Death in a Neuronal PC12 Clonal Line Subjected to Ischemia. *ACS Chem. Neurosci.* **2016**, *7*, 1452–1462. [CrossRef]
27. Naveh, S. *Development of Chemical Tools for Studying Protein-Protein Interactions*; The Hebrew University of Jerusalem: Jerusalem, Israel, 2012.
28. Boas, U.; Gertz, H.; Christensen, B.; Heegaard, P.M.H. Facile Synthesis of Aliphatic Isothiocyanates and Thioureas on Solid Phase Using Peptide Coupling Reagents Q. *Tetrahedron Lett.* **2004**, *45*, 269–272. [CrossRef]
29. Weinstein, J.E.; Pepple, K.L. Cytokines in Uveitis. *Curr. Opin. Ophthalmol.* **2018**, *29*, 267–274. [CrossRef]
30. Gupta, S.; Shyamsundar, K.; Agrawal, M.; Vichare, N.; Biswas, J. Current Knowledge of Biologics in Treatment of Noninfectious Uveitis. *J. Ocul. Pharmacol. Ther.* **2022**, *38*, 203–222. [CrossRef]
31. Michalak, M.; Corbett, E.F.; Mesaeli, N.; Nakamura, K.; Opas, M. Calreticulin: One Protein, One Gene, Many Functions. *Biochem. J.* **1999**, *344 Pt 2*, 281–292. [CrossRef]
32. Liu, N.; Fine, R.E.; Simons, E.; Johnson, R.J. Decreasing Calreticulin Expression Lowers the Ca^{2+} Response to Bradykinin and Increases Sensitivity to Ionomycin in NG-108-15 Cells. *J. Biol. Chem.* **1994**, *269*, 28635–28639. [CrossRef] [PubMed]
33. Peters, L.R.; Raghavan, M. Endoplasmic Reticulum Calcium Depletion Impacts Chaperone Secretion, Innate Immunity, and Phagocytic Uptake of Cells. *J. Immunol.* **2011**, *187*, 919–931. [CrossRef] [PubMed]
34. Klaska, I.; Forrester, J. Mouse Models of Autoimmune Uveitis. *Curr. Pharm. Des.* **2015**, *21*, 2453–2467. [CrossRef] [PubMed]
35. Gardner, P. Calcium and T Lymphocyte Activation. *Cell* **1989**, *59*, 15–20. [CrossRef] [PubMed]

pharmaceutics

MDPI

Communication

Differential Effect of Simulated Microgravity on the Cellular Uptake of Small Molecules

Odelia Tepper-Shimshon [1], Nino Tetro [1], Roa'a Hamed [1], Natalia Erenburg [1], Emmanuelle Merquiol [1], Gourab Dey [1], Agam Haim [2], Tali Dee [2], Noa Duvdevani [2], Talin Kevorkian [2], Galia Blum [1], Eylon Yavin [1] and Sara Eyal [1,*]

[1] Institute for Drug Research, School of Pharmacy, Faculty of Medicine, The Hebrew University of Jerusalem, Jerusalem 9112002, Israel; odelis1@gmail.com (O.T.-S.); ntetro@gmail.com (N.T.); roua.hamed@mail.huji.ac.il (R.H.); natalia.erenburg@mail.huji.ac.il (N.E.); emmanuellem@savion.huji.ac.il (E.M.); gourab.dey@mail.huji.ac.il (G.D.); galiabl@ekmd.huji.ac.il (G.B.); eylony@ekmd.huji.ac.il (E.Y.)

[2] School of Space Science, Hebrew University Youth Division, The Hebrew University of Jerusalem, Jerusalem 9112002, Israel; noaduv123@gmail.com (N.D.)

* Correspondence: sara.eyal@mail.huji.ac.il; Tel.: +972-2-675-8667

Abstract: The space environment can affect the function of all physiological systems, including the properties of cell membranes. Our goal in this study was to explore the effect of simulated microgravity (SMG) on the cellular uptake of small molecules based on reported microgravity-induced changes in membrane properties. SMG was applied to cultured cells using a random-positioning machine for up to three hours. We assessed the cellular accumulation of compounds representing substrates of uptake and efflux transporters, and of compounds not shown to be transported by membrane carriers. Exposure to SMG led to an increase of up to 60% ($p < 0.01$) in the cellular uptake of efflux transporter substrates, whereas a glucose transporter substrate showed a decrease of 20% ($p < 0.05$). The uptake of the cathepsin activity-based probe GB123 (MW, 1198 g/mol) was also enhanced (1.3-fold, $p < 0.05$). Cellular emission of molecules larger than ~3000 g/mol was reduced by up to 50% in SMG ($p < 0.05$). Our findings suggest that short-term exposure to SMG could differentially affect drug distribution across membranes. Longer exposure to microgravity, e.g., during spaceflight, may have distinct effects on the cellular uptake of small molecules.

Keywords: microgravity; multidrug resistance–associated proteins; MRP1; P-glycoprotein; MDR1; breast cancer resistance protein; BCRP; GB123; glucose transporters; pharmacokinetics

1. Introduction

Microgravity, defined as the condition of experiencing very low or negligible gravitational forces, is a crucial aspect of the space environment. The microgravity of space can considerably alter human physiology, affecting almost every system of the body. Examples include fluid shifts toward the head and chest, an approximately 20-fold faster increase in carotid artery stiffness as compared to healthy aging, and accelerated bone and muscle mass loss [1].

The physiological changes that occur during spaceflight can result in medical conditions that require drug treatment and can affect the pharmacokinetics and pharmacodynamics of medications taken in space [1]. One factor that may contribute to altered pharmacokinetics and pharmacodynamics is an increase in membrane fluidity, which was observed during a parabolic flight mission and in simulated microgravity (SMG). In a study conducted onboard a sounding rocket, altered fluidity was shown to affect lidocaine integration into membranes. Microgravity was also associated with reduced transmembranal transport activity of the multidrug resistance–associated transporter (MRP) 2 [1].

Based on the changes in membrane properties, we hypothesized that microgravity could affect the distribution of small molecules into cells, due to changes in passive diffusion, carrier-mediated transport, or both. In this pilot study, we tested our hypothesis using SMG. We focused on the activity of the efflux transporters P-glycoprotein (P-gp), the breast cancer resistance protein (BCRP), and MRP1. We used selective transporter inhibitors and cell lines that overexpress these carriers to isolate the effects of SMG on distinct transporters. We also assessed the distribution into cells of an uptake transporter substrate, a compound which is not a P-gp/BCRP substrate, and several compounds of larger molecular weights. Our preferred probes were molecules trapped within cells (Table 1), which helped combat the reversibility of SMG effects when cells are removed from the microgravity simulator.

Table 1. Physicochemical properties of the studied compounds.[1]

Compound	MW (g/mol)	xLogP	HBD	HBA	TPSA	Comments
2-NBDG	342	−1.4	5	11	195	A fluorescently labeled deoxyglucose analog; a probe of glucose carrier activity that becomes trapped in cells (hence results should not be affected by SMG reversal)
Hoechst 33342	453	4.6	2	5	73	A DNA fluorescent stain; a P-gp and BCRP substrate
Doxorubicin	543	1.3	6	12	206	A fluorescent chemotherapeutic agent that intercalates into DNA and inhibits topoisomerase II; a substrate of P-gp, BCRP, and MRP1
BODIPY prazosin	563	N/A	1	10	111	A fluorescent probe of BCRP activity
Calcein AM	995	2.9	0	25	305	A non-fluorescent precursor of calcein
Calcein	623	−3.1	6	15	232	A fluorescent probe of P-gp activity; also an MRP1 substrate
GB123	1198	N/A	N/A	N/A	N/A	A fluorescently quenched activity-based probe of cysteine cathepsin activity; not a P-gp or BCRP substrate
NLS-PNA-FITC	6254					An 18-mer peptide nucleic acid (PNA) conjugated to FITC fluorophore and to the NLS peptide, which was previously reported as a nuclear targeting agent

[1] Data for compounds other than GB123 and NLS-PNA-FITC are based on PubChem (https://pubchem.ncbi.nlm.nih.gov/; accessed on 26 August 2024). The molecular weights of dextrans were 4000 g/mol (neutral), 3000–6000 g/mol (positively charged), and 4000 g/mol (negatively charged). BCRP, breast cancer resistance protein; Calcein AM, calcein acetoxymethyl ester; FITC, fluorescein isothiocyanate; HBA, hydrogen bond acceptor count; HBD, hydrogen bond donor count; MRP, multidrug resistance–associated protein; N/A, not available; 2-NBDG, 2-Deoxy-2-[(7-nitro-2,1,3-benzoxadiazol-4-yl)amino]-D-glucose; NLS, nuclear localization sequence; P-gp, P-glycoprotein; xLogP; calculated logarithm of the predicted n-octanol: water partition coefficient; TPSA, topological polar surface area. References for the table are available upon request.

2. Materials and Methods

2.1. Materials

GB123 [2] and the FITC-labeled nuclear localization sequence (NLS)-peptide nucleic acid (PNA) [3] were synthesized as previously described. Bovine serum albumin (BSA), Biotechnology Grade, was obtained from Tamar laboratory supplies (Mevaseret Zion, Israel). The other cell culture reagents, phosphate-buffered saline (PBS), trypsin EDTA Solution C (0.05%), and 2,3-Bis(2-methoxy-4-nitro-5-sulfophenyl)-2H-tetrazolium-5-carboxanilide (XTT) were purchased from Biological Industries Ltd. (Beit Haemek, Israel). Dimethyl sulfoxide (extra dry 99.7% DMSO) was obtained from Acros Organics (Geel, Belgium). Calcein AM and boron-dipyrromethene (BODIPY) prazosin were obtained from Thermo Fisher Scientific (Waltham, MA USA). Hoechst 33342 was obtained from Abcam (Cambridge, UK). 2-Deoxy-2-[(7-nitro-2,1,3-benzoxadiazol-4-yl)amino]-D-glucose (2-NBDG) was obtained from Cayman Chemical (Ann Arbor, MI, USA). 4′,6-Diamidino-2-phenylindole (DAPI) was obtained from Fluoromount G (SouthernBiotech, Birmingham, AL, USA). Valspodar (PSC-833) was obtained from Tocris Bioscience (Bristol, UK). All other reagents were obtained from Sigma-Aldrich (Rehovot, Israel).

2.2. Cell Lines and Cell Culture

The cell lines were selected based on their profile of efflux transporter expression. Several species were chosen in order to enhance extrapolation potential. The RAW 264.7

line is derived from murine macrophages and has been commonly utilized in microgravity research [4]. These cells express functional P-gp [5]. Madin–Darby canine kidney (MDCK) II cells transfected with cDNA coding for the human P-gp (MDCK-MDR1 cells) are a well-characterized in vitro model for assessment of P-gp activity [6–8]. U87 human glioblastoma cells were selected based on their low level of P-gp expression [9].

RAW 264.7 cells (from Prof. Boaz Tirosh, The Hebrew University) were grown in RPMI 1640 medium supplemented with 10% fetal bovine serum, L-glutamine (2 mM), sodium pyruvate (1 mM), non-essential amino acids, penicillin (100 Units/mL), and streptomycin (100 μg/mL). U87-MG cells (from Prof. Ofra Benny, The Hebrew University) were cultured in Eagle's MEM medium supplemented with 10% fetal calf serum, L-glutamine (2 mM), sodium pyruvate (1 mM), and 1% penicillin/streptomycin. MDCK-MDR1 cells were provided by Prof. Alfred Schinkel (The Netherlands Cancer Institute). Cells were maintained in Dulbecco's modified Eagle's phenol-free low-glucose medium (DMEM) supplemented with 10% fetal bovine serum, 2 mM L-glutamine, 100 units/mL penicillin, and 100 μg/mL streptomycin at 37 °C in a 5% CO_2 incubator. The cells were harvested after achieving 70–80% confluence. The transmembranal transfer studies were all conducted using suspended cells. Cell viability was analyzed using the XTT assay kit according to the manufacturer's instructions.

2.3. Tested Compounds

Calcein AM and Hoechst 33342 were used at 0.25 μM [10,11] and 60 μM (determined after several preliminary experiments), respectively. Doxorubicin was used at 5 μM, based on preliminary XTT experiments showing that at this concentration, it does not affect the viability of the studied cells. The concentration of BODIPY prazosin was 1 μM (based on preliminary experiments) and that of 2-NBDG was 100 μM [12]. Valspodar (a P-gp inhibitor [13]) was used at 1.65 μM [14] and fumitremorgin C (FTC; a BCRP inhibitor [13]) at 10 μM [14,15]. FITC-labeled dextrans were used at 2 mg/mL [16,17] (molar values are only an approximation, see Table 1) and NLS-PNA-FITC was used at 5 μM [3].

2.4. Experiments in Simulated Microgravity

Microgravity conditions were simulated by a random positioning machine (RPM) 2.0 (purchased from Yuri GmbH, Meckenbeuren, Germany; originally from DutchSpace Airbus, Leiden, The Netherlands). The RPM continuously and randomly changes the orientation of the accommodated experiments relative to the Earth gravity vector. Objects cannot adjust or react to the gravitational pull due to rapid and continuous changes in orientation. This simulates a microgravity environment by neutralizing the net effect of gravity on the objects, allowing gravity levels that replicate those of the Moon (0.16 g) and of Mars (0.38 g), with a minimum of 10^{-3} g. The RPM was maintained within a cell culture incubator (3 °C, 5% CO_2).

Cells were removed from the culture plates according to the instructions from the American Type Culture Collection (ATCC) website; 0.05% trypsin for MDCK cells, 0.25% trypsin for U87 cells, and scraping for RAW 264.7 cells. Cells in media containing the fluorescent probe were transferred to 0.5 mL Eppendorf tubes placed at the center of the simulator (Appendix A, Figure A1) or on a shelf within the same incubator. Potential effects of the stationary position were excluded based on comparison to samples placed on a shaker (Appendix B, Figure A2). To enable the placement of all tubes on the central part of the RPM, all experiments were conducted using up to six tubes per treatment group. Incubation in the RPM or under control conditions was for the duration of one hour unless otherwise stated (due to slow uptake kinetics). In experiments with transporter inhibitors, the cells were preincubated with the inhibitor for one hour under Earth conditions. The inhibitor was also present throughout the experiment. The RPM was set at Partial G, Loop path, and No Motion mode.

At the end of the experiments, all tubes were immediately placed on ice and the remaining procedures were carried out at 4 °C. The cells were washed with PBS, filtered

using a 40 μm nylon mesh filter, and fluorescence was measured by flow cytometry using a Fortessa FACS Analyzer (BD LSRFortessa™ Flow Cytometer, BD Biosciences, San Jose, CA, USA). The results were analyzed using FlowJo™ v10.7 analysis software (https://www.flowjo.com; accessed on 1 August 2024).

For the analyses with GB123, RAW 264.7 cells were divided into four groups. Two groups were incubated with 0.25 μM GB123 for two hours, washed three times, and incubated with PBS for an additional two hours. The other two groups were incubated with the medium over the first two hours, then with 0.25 μM GB123 under Earth conditions for the next two hours. In the cellular uptake experiments, the chambers were washed with phosphate-buffered saline (PBS) three times and stained with DAPI (1:1000) diluted in PBS. The cells were then imaged by a Nikon motorized Ti2E confocal fluorescent microscope with a Yokogawa W1 Spinning Disk (Olympus, Tokyo, Japan). The cathepsin binding analysis was conducted after the cells were lysed in RIPA buffer. Equal amounts of protein (100 μg per sample) were loaded onto the gel and separated on a 12.5% SDS PAGE (Appendix D, Figure A3). Instead of transferring the proteins to a membrane and using a loading control, we scanned the gel for Cy5 using a Typhoon laser scanner and compared the fluorescence intensity of GB123 between the groups. This method allowed direct assessment and comparison of cathepsin expression levels [14].

Statistical Analysis

Two-way ANOVA, the Mann–Whitney test or the Kruskal–Wallis test, as appropriate, were used for comparisons across treatment groups (Prism 10.2.3; GraphPad, La Jolla, CA, USA). Flow cytometry results are expressed as the medians of the fluorescence signal obtained in 10,000 cells. Results are reported as individual values with group medians. A p value ≤ 0.05 was considered significant.

3. Results

3.1. Simulated Microgravity Can Enhance the Cellular Uptake of Efflux Transporter Substrates

Exposure to SMG increased the cellular uptake of calcein AM (Figure 1a–c). The effect was highest in U87 cells (a median 60% increase in emission; Figure 1b). Overall, the magnitude of change in calcein AM emission did not reflect P-gp abundance. However, in MDCK-MDR1 cells, the SMG-inhibition interaction was significant, implying that both efflux transport and diffusion were affected (Figure 1c). In the doxorubicin experiment, only the effect of gravity was statistically significant (Figure 1d). The fold change in doxorubicin (Figure 1d) and BODIPY prazosin uptake (Figure 1e) was similar to that of calcein AM. Hoechst 33342 emission was not significantly affected by SMG (Figure 1f). We did not pursue the experiments with BODIPY prazosin in MDCK-MDR1 and U87 cells any further because these cells have no functional BCRP activity [18] or express low BCRP levels [9].

3.2. Glucose Transporter Activity/Metabolism Is Reduced in Simulated Microgravity

Unlike the efflux transporter substrates, the emission intensity of the glucose analog 2-NBDG was 20% lower under SMG conditions targeting 0.001 g ($p < 0.01$; Appendix E, Figure A4). Similar results were obtained at 0.16 g.

3.3. Simulated Microgravity Can Enhance the Cellular Uptake of a Molecule Larger Than 1000 g/mol

GB123, a cathepsin activity-based probe, is larger than the transporter substrates described above (Table 1). Under simulated Moon gravity (0.16 g), the cellular accumulation of this compound was also enhanced by 30% (Appendix F, Figure A5a–c). The experiments were conducted at higher gravity as compared to the others in order to minimize the potential of cathepsin activation. Indeed, the change in GB123 uptake was not due to increased cathepsin activity (which tended to decrease and not increase under SMG conditions; Appendix F, Figure A5d,e).

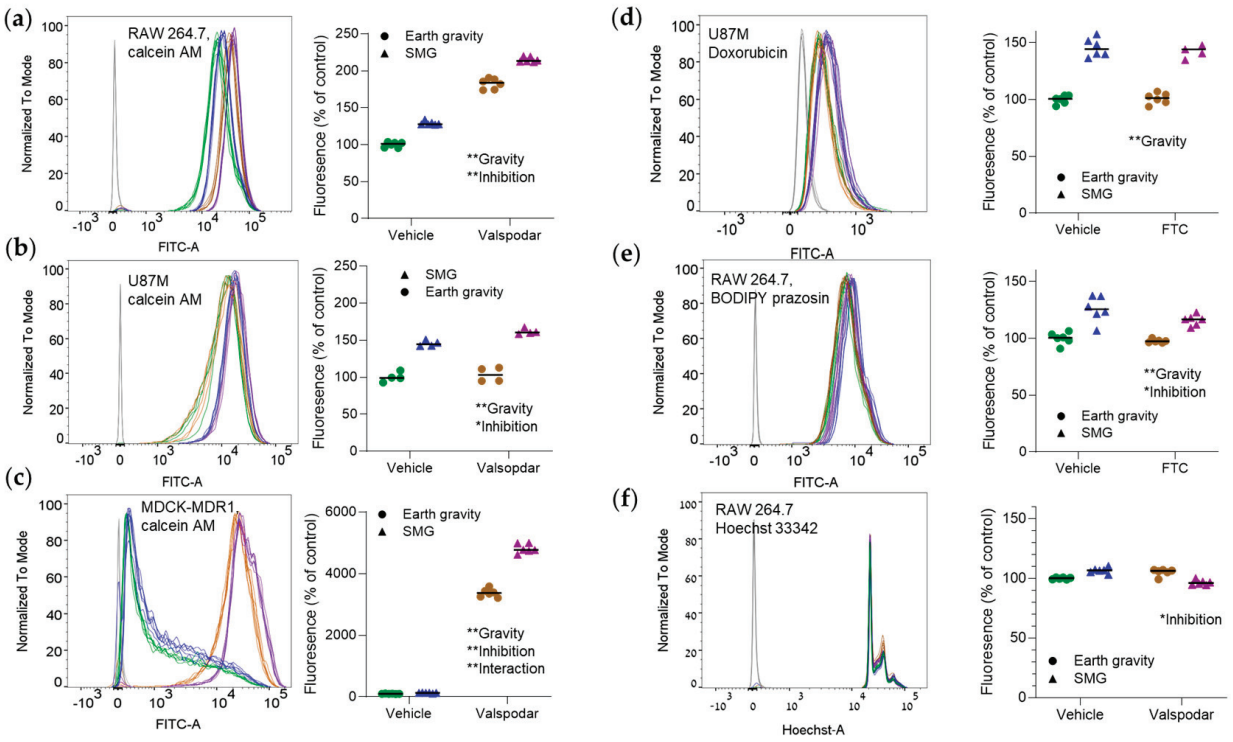

Figure 1. The uptake of efflux transporter substrates can be increased in simulated microgravity (SMG). Cells were incubated at Earth gravity or SMG (target: 0.001 g; Appendix C) with efflux transporter substrates in the presence or the absence of transporter inhibitors. Emission intensity was measured by flow cytometry. The left part of each panel shows a representative emission distribution curve. The right part is a quantitative analysis of the results. Shifts to the right indicate a higher uptake of the fluorescent probe by the cells. (**a**–**c**) Raw 264.7 (n = 6/group) (**a**), U87 (n = 4/group) (**b**), or MDCK-MDR1 (n = 6/group) (**c**) cells, incubated with 0.25 μM calcein AM with or without 1.65 μM valspodar (a P-gp inhibitor) [13]). (**d**) U877 cells incubated with 5 μM doxorubicin with or without 1.65 μM valspodar (n = 6/group). (**e**) RAW 264.7 cells incubated with 1 μM BODIPY prazosin with or without 10 μM fumitremorgin C (FTC; a BCRP inhibitor [13]; n = 6/group). (**f**) RAW 264.7 cells incubated with 60 μM Hoechst 33342 with or without 1.65 μM valspodar (n = 6/group, except for n = 5 in the SMG + valspodar group). Dark gray lines in the distribution curves denote non-stained cells. * $p < 0.05$; ** $p < 0.01$; 2-way ANOVA. The test assesses whether the emission is significantly affected by SMG, the inhibitor, and their interaction. The figures are labeled accordingly. Experiments were repeated thrice with similar results. The numbers of replicates per group denote biological replicates (samples cultured separately). Heights are normalized ("to mode") to highlight shifts to the right or the left. Green, vehicle and Earth gravity; blue, vehicle and SMG; brown, transporter inhibitor and Earth gravity; purple, transporter inhibitor and SMG.

3.4. The Cellular Distribution of Molecules that Weigh 3000 g/mol or More Is Reduced in Simulated Microgravity

To assess the effect of size and charge on cellular uptake in SMG, we used positively charged, negatively charged, and neutral FITC-labeled dextrans. The signal from neutral dextran was similar to that of non-treated cells and we did not further explore this compound. Positive dextran yielded a considerably higher signal than negative dextran. The emission of both dextrans was approximately half in SMG (Figure 2a,b).

The effect of SMG on large, positively charged molecules was confirmed with NLS-PNA-FITC, [6253.70 g/mol] whose fluorescence intensity at SMG was lower as well (Figure 2c,d).

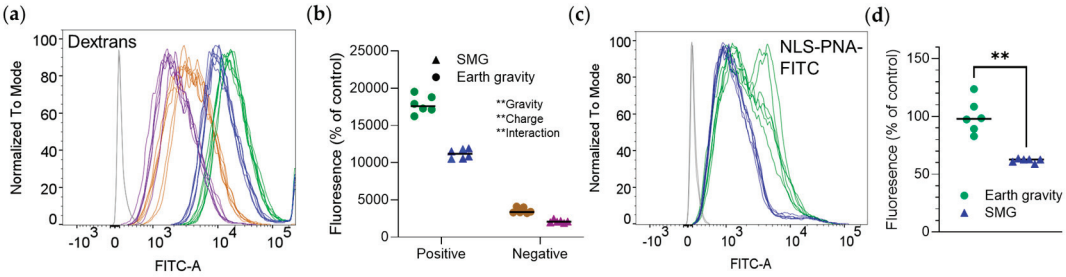

Figure 2. Simulated Moon gravity reduces the uptake of molecules larger than 3000 g/mol into RAW 264.7 cells. Cells were incubated at Earth gravity or SMG with positively charged, negatively charged, or neutral dextrans (Table 1) for one hour, or with NLS−PNA−FITC for three hours. Emission intensity was measured by flow cytometry. Shown are representative distribution curves of emission intensity obtained by flow cytometry (**a**,**c**) and quantitative analyses of the results (**b**,**d**). (**a**,**b**) Fluorescently labeled dextrans. (**b**,**c**) NLS−PNA−FITC. ** $p < 0.01$, two−way ANOVA (**b**) or Mann—Whitney test (**d**). Experiments were repeated thrice (n = 6 biological replicates per group in each experiment), with similar results. (**a**,**b**) Green, positively-charged dextran and Earth gravity; blue, positively-charged dextran and SMG; brown, negatively-charged dextran and Earth gravity; purple, negatively-charged and SMG.

4. Discussion

Since the beginning of human spaceflight, significant time, resources, and effort have been devoted to the study of space physiology, whereas space pharmacology was far less thoroughly explored. Few pharmacokinetic studies have been conducted in astronauts and cosmonauts, with conflicting findings. The relatively consistent delayed absorption and other pharmacokinetic changes were mostly attributed to fluid shifts and changes in gastrointestinal function [1]. However, the microgravity of space might also affect membrane permeability, as was previously demonstrated in isolated vesicles [19]. This prompted us to explore the transmembranal distribution of smaller and larger molecules. We investigated small molecule (<1000 g/mol) efflux transporter substrates, an uptake transporter substrate, and larger molecules to rule out globally enhanced diffusion into cells. To avoid altered gene expression as a confounder, we limited our analyses to one hour (except for the GB123 and NLS-PNA-FITC studies).

This analysis is a pilot study, yet we could identify several physicochemical properties of the tested compounds that could affect their behavior in SMG. To our knowledge, such an analysis has not yet been reported. One notable observation was the higher cellular uptake of efflux transporter substrates in SMG. The magnitude of change was modest but statistically significant. The SMG effect on calcein AM kinetics was independent of P-gp abundance (Figure 1a–c; low, moderate, and high in U87 [9], RAW 264.7 [5], and MDCK-MDR1 cells, respectively). It was likely related to both enhanced diffusion and reduced P-gp activity (Figure 1c). The altered P-gp function could reflect changes in substrate or ATP binding, altered internalization, or cytoskeletal changes. The reduced 2-NBDG accumulation coupled with the lack of SMG effect on Hoechst 33342 suggest that the higher distribution of small molecules into cells in SMG is not a global phenomenon.

The SMG effect on a larger molecule, GB123, was similar to those observed with the efflux transporter substrates (although GB123 is not a P-gp or BCRP substrate [14]). Our analysis excluded enhanced cathepsin activity as the cause because activity tended to be lower when the cells were exposed to SMG. The enhanced GB123 uptake did not extend to larger molecules, at least not to those with the molecular properties described above.

This pilot study has several limitations. First, lower gravity (0.001 g) is achieved only after prolonged incubation (e.g., 24 h) and the one-hour exposure did not suffice. Yet, gravity was 0.01 g at 10 min and 0.006 g at 30 min after the onset of the experiment (Appendix C). This issue was less pronounced with lunar gravity, because the target value (0.16 g) was obtained within 30 min. Second, the closed Eppendorf tubes minimized exposure to CO_2,

which could potentially affect the results However, preliminary experiments with Falcon flasks that allow gas exchange yielded similar results, probably because the incubation was relatively short. Third, we took all available steps in order to remove bubbles, but their presence in the vials (and consequent shear forces) cannot be completely ruled out. Therefore, our findings might misinterpret the magnitude of the SMG effect. Additionally, this study assessed only short-time exposure and only transcellular transport. Longer exposure to microgravity has been shown to affect transporter gene expression [1] and could change the magnitude or reverse the direction of the changes observed in the current study. Altered paracellular transport (e.g., tight junction opening) might potentially also affect the transfer of small and large molecules across biological barriers in space. Finally, the cells were cultured in 2D. A study in cardiomyocytes demonstrated similar cellular responses to pharmacological agents in 2D and 3D under SMG conditions [20]. Hence dimensionality is not necessarily expected to affect our results, but further experiments should be performed to ensure that this is the case.

If our findings are applied to humans, membrane permeability to small- and large-molecule drugs could be altered. This could result in enhanced absorption, reduced systemic elimination, and enhanced distribution across the BBB, which may require dosing adjustment. One example is apixaban, a small molecule, P-gp substrate oral anticoagulant [21].

5. Conclusions

SMG selectively affects the uptake of small molecules into cells, but the direction of change varies across molecules. The changes were observed across several cell lines of various origins, suggesting that this phenomenon is not cell-type specific. In space, this could alter drug absorption, distribution, and elimination, and potentially also drug effects. Future research may shed light on the clinical implications of altered transmembranal transport of small molecules during spaceflight.

Author Contributions: Conceptualization, O.T.-S. and S.E.; methodology, O.T.-S., N.T., R.H., N.E., G.D., E.M. and S.E.; validation, R.H. and N.T.; formal analysis, O.T.-S.; investigation, O.T.-S., N.T., R.H., N.E., G.D., E.M., A.H., T.D., N.D. and T.K.; resources, G.B. and E.Y.; data curation, O.T.-S.; writing—original draft preparation, O.T.-S.; writing—review and editing, O.T.-S., N.T., R.H., N.E., G.D., E.M., E.Y., G.B. and S.E.; visualization, G.B., E.Y. and S.E.; project administration, O.T.-S.; funding acquisition, S.E. and E.Y. All authors have read and agreed to the published version of the manuscript.

Funding: This research was funded by the Israel Space Agency, grant numbers 0004079 and 0006055, and by the Israel Science Foundation, grant number 1366/23.

Institutional Review Board Statement: Not applicable.

Informed Consent Statement: Not applicable.

Data Availability Statement: Data are available from S.E. upon request.

Acknowledgments: We are grateful to Boaz Tirosh from the Hebrew University for providing RAW 264.7 cells; Ofra Benny from the Hebrew University for the U87 cell line; and Alfred Schinkel from The Netherlands Cancer Institute for MDCK-MDR1 cells. We thank Omer Eyal for language editing. Sara Eyal is affiliated with the David R. Bloom Centre for Pharmacy and Adolf and Klara Brettler Center for Research in Molecular Pharmacology and Therapeutics at The Hebrew University of Jerusalem, Israel, and is holding a Dame Susan Garth Chair of Cancer Research.

Conflicts of Interest: S.E. has served as an advisor to SpacePharma, Israel. The other authors have no conflicts of interest. The funders had no role in the design of this study; in the collection, analyses, or interpretation of data; in the writing of the manuscript; or in the decision to publish the results.

Appendix A

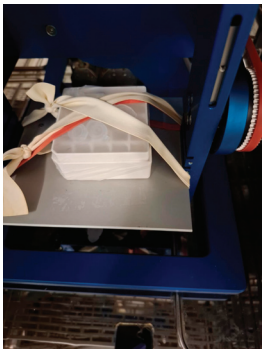

Figure A1. Placement of vials within the RPM.

Appendix B

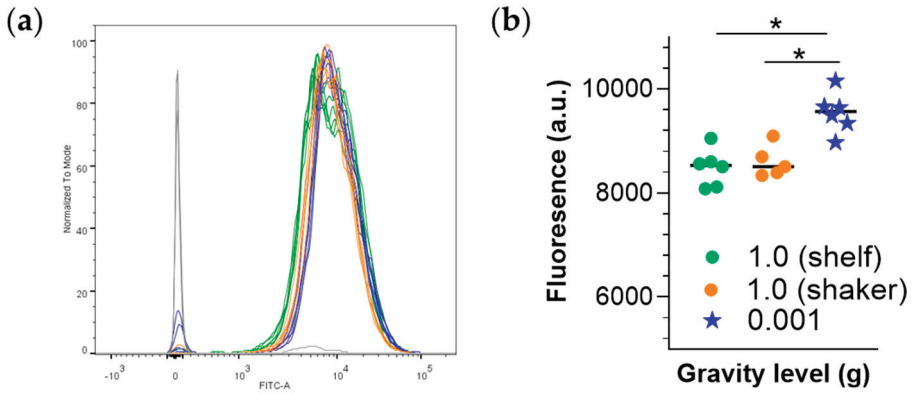

Figure A2. Comparison of shelf- versus shaker placement of samples. (**a**) Histograms showing the distribution of cells by emission intensity within each treatment group. (**b**) quantitative analysis of emission intensity by group. In this experiment, calcein AM uptake into RAW 264.7 cells was assessed as described above, with additional control of "ground" samples placed on a shaker. No difference was observed between the two "ground controls" (Figure). * $p < 0.05$, Kruskal–Wallis test.

Appendix C

Table A1. Mean Gravity throughout a One-Hour Experiments That Target 0.16 g or 0.001 g.

Time (min)	Gravity	
	Setting: 0.16 g	**Setting: 0.001 g**
10	0.17	0.011
20	0.163	0.008
30	0.155	0.006
40	0.155	0.005
50	0.156	0.005
60	0.157	0.003

Appendix D

Figure A3. Protein loading in the cathepsin activity analysis.

Appendix E

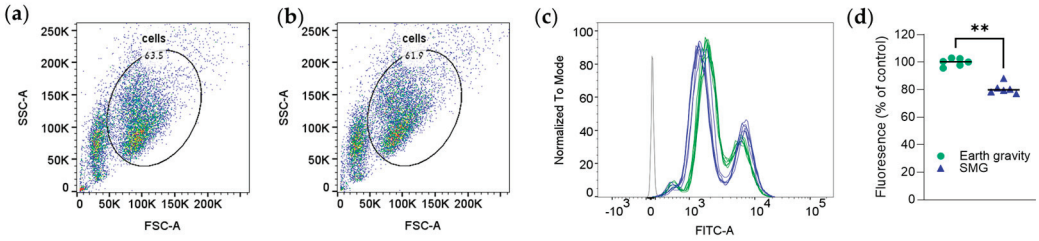

Figure A4. Simulated microgravity reduces the cellular accumulation of the glucose transporter substrate 2-NBDG. RAW 264.7 cells were incubated in Earth gravity or SMG (target, 0.001 g; Appendix C) with 2-NBDG for one hour. Emission intensity was measured by flow cytometry. (**a**,**b**) Gating for the cells exposed to Earth (**a**) or SMG (**b**) conditions. (**c**). A representative distribution curve of emission intensity obtained by flow cytometry. Dark gray lines in the distribution curves denote non-stained cells. (**d**) Quantitative analyses of the results. n = 6/group (biological replicates); ** $p < 0.01$, Mann–Whitney test. Experiments were repeated twice at target 0.001 and thrice at 0.16 g with similar results.

Appendix F

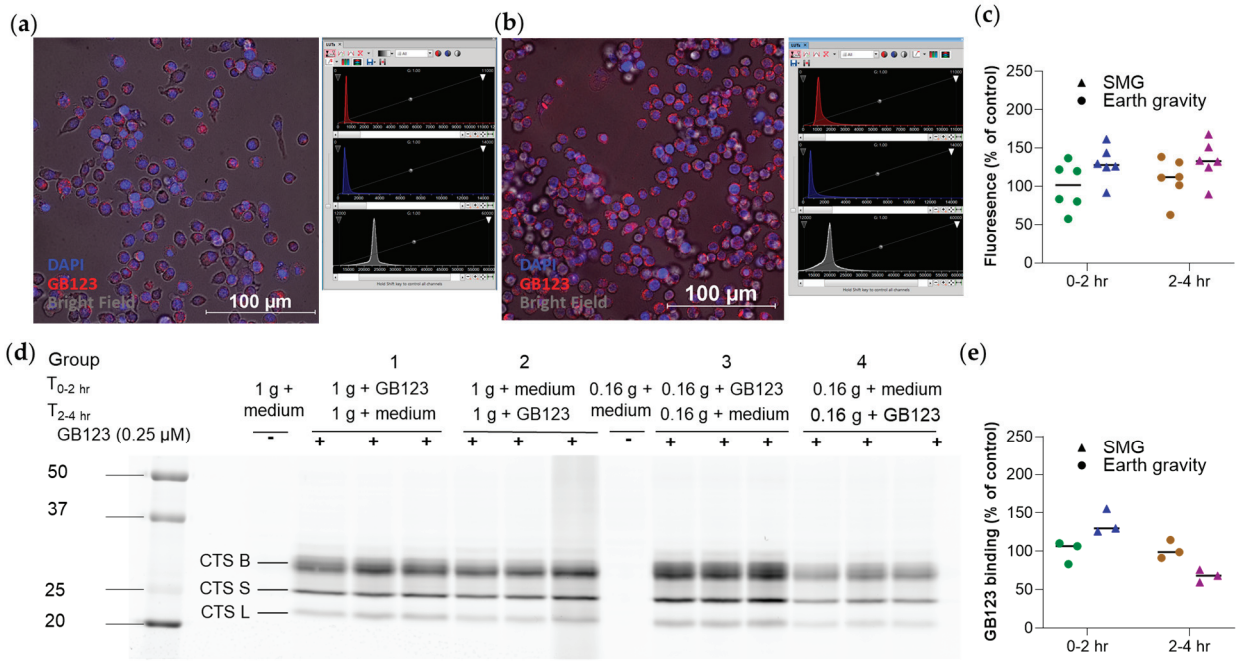

Figure A5. Simulated Moon gravity modestly increases GB123 uptake into RAW 264.7 cells. Cells were divided into four groups, n = 6/group: two groups (1—Earth and 3—Moon) were incubated

with GB123 at 0–2 h under simulated Earth or Moon conditions, washed three times, and incubated with PBS for an additional two hours (under the same respective conditions). The other groups (2—Earth and 4—Moon) were treated similarly, except that the first two hours were with the medium only (without GB123), to assess the effect of SMG on cathepsin activity. Cells were either imaged by confocal microscopy or lysed in RIPA buffer and subjected to Western blot analysis. Experiments were repeated twice, with similar results. (**a**,**b**) Confocal microscopy images of RAW 264.7 cells treated with the medium (**a**) or GB123 (**b**) for two hours. Red, GB123. Blue, DAPI. Also shown are the imaging settings. For both the Earth and the Moon images, ranges were set as 0–11,000 for the red channel, 0–14,000 for the blue channel, and 12,000–60,000 for the bright field. (**c**) Quantitative analysis of the GB123 signal. (**d**) Images of cathepsin-bound GB123 following separation on a gel. (**e**) Quantitative analysis of the respective GB123 emission, n = 3/group (biological replicates). The bands represent cathepsins (CTS) B, S, and L.

References

1. Eyal, S.; Derendorf, H. Medications in Space: In Search of a Pharmacologist's Guide to the Galaxy. *Pharm. Res.* **2019**, *36*, 148. [CrossRef] [PubMed]
2. Blum, G.; von Degenfeld, G.; Merchant, M.J.; Blau, H.M.; Bogyo, M. Noninvasive optical imaging of cysteine protease activity using fluorescently quenched activity-based probes. *Nat. Chem. Biol.* **2007**, *3*, 668–677. [CrossRef] [PubMed]
3. Soudah, T.; Mogilevsky, M.; Karni, R.; Yavin, E. CLIP6-PNA-Peptide Conjugates: Non-Endosomal Delivery of Splice Switching Oligonucleotides. *Bioconjug. Chem.* **2017**, *28*, 3036–3042. [CrossRef] [PubMed]
4. Ludtka, C.; Silberman, J.; Moore, E.; Allen, J.B. Macrophages in microgravity: The impact of space on immune cells. *NPJ Microgravity* **2021**, *7*, 13. [CrossRef] [PubMed]
5. Zha, W.; Wang, G.; Xu, W.; Liu, X.; Wang, Y.; Zha, B.S.; Shi, J.; Zhao, Q.; Gerk, P.M.; Studer, E.; et al. Inhibition of P-glycoprotein by HIV protease inhibitors increases intracellular accumulation of berberine in murine and human macrophages. *PLoS ONE* **2013**, *8*, e54349. [CrossRef] [PubMed]
6. FDA. In Vitro Drug Interaction Studies—Cytochrome P450 Enzyme- and Transporter-Mediated Drug Interactions. Guidance for Industry. Available online: https://www.fda.gov/media/134582/download (accessed on 23 June 2023).
7. Irvine, J.D.; Takahashi, L.; Lockhart, K.; Cheong, J.; Tolan, J.W.; Selick, H.E.; Grove, J.R. MDCK (Madin-Darby canine kidney) cells: A tool for membrane permeability screening. *J. Pharm. Sci.* **1999**, *88*, 28–33. [CrossRef] [PubMed]
8. Sato, S.; Tohyama, K.; Kosugi, Y. Investigation of MDR1-overexpressing cell lines to derive a quantitative prediction approach for brain disposition using in vitro efflux activities. *Eur. J. Pharm. Sci.* **2020**, *142*, 105119. [CrossRef] [PubMed]
9. Schulz, J.A.; Rodgers, L.T.; Kryscio, R.J.; Hartz, A.M.; Bauer, B. Characterization and comparison of human glioblastoma models. *BMC Cancer* **2022**, *22*, 844. [CrossRef] [PubMed]
10. Portnoy, E.; Gurina, M.; Magdassi, S.; Eyal, S. Evaluation of the near infrared compound indocyanine green as a probe substrate of P-glycoprotein. *Mol. Pharm.* **2012**, *9*, 3595–3601. [CrossRef] [PubMed]
11. Guberović, I.; Marjanović, M.; Mioč, M.; Ester, K.; Martin-Kleiner, I.; Ramljak, T.; Mlinarić-Majerski, K.; Kralj, M. Crown ethers reverse P-glycoprotein-mediated multidrug resistance in cancer cells. *Sci. Rep.* **2018**, *8*, 14467. [CrossRef] [PubMed]
12. Ogawa, T.; Sasaki, A.; Ono, K.; Ohshika, S.; Ishibashi, Y.; Yamada, K. Uptake of fluorescent D- and L-glucose analogues, 2-NBDG and 2-NBDLG, into human osteosarcoma U2OS cells in a phloretin-inhibitable manner. *Hum. Cell* **2021**, *34*, 634–643. [CrossRef] [PubMed]
13. FDA. Drug Development and Drug Interactions | Table of Substrates, Inhibitors and Inducers. Available online: https://www.fda.gov/drugs/drug-interactions-labeling/drug-development-and-drug-interactions-table-substrates-inhibitors-and-inducers (accessed on 25 July 2024).
14. Hamed, R.; Merquiol, E.; Zlotver, I.; Blum, G.; Eyal, S.; Ekstein, D. Challenges in Batch-to-Bed Translation Involving Inflammation-Targeting Compounds in Chronic Epilepsy: The Case of Cathepsin Activity-Based Probes. *ACS Omega* **2024**, *9*, 6965–6975. [CrossRef] [PubMed]
15. Rubinchik-Stern, M.; Shmuel, M.; Eyal, S. Antiepileptic drugs alter the expression of placental carriers: An in vitro study in a human placental cell line. *Epilepsia* **2015**, *56*, 1023–1032. [CrossRef] [PubMed]
16. Nevo, N.; Chossat, N.; Gosgnach, W.; Logeart, D.; Mercadier, J.-J.; Michel, J.-B. Increasing endothelial cell permeability improves the efficiency of myocyte adenoviral vector infection. *J. Gene Med.* **2001**, *3*, 42–50. [CrossRef] [PubMed]
17. Martin, C.; Marino, N.; Curran, C.; McHale, A.P.; Callan, J.F.; Callan, B. Cholesteryl to improve the cellular uptake of polymersomes within HeLa cells. *Int. J. Pharm.* **2016**, *511*, 570–578. [CrossRef] [PubMed]
18. Wang, Q.; Strab, R.; Kardos, P.; Ferguson, C.; Li, J.; Owen, A.; Hidalgo, I.J. Application and limitation of inhibitors in drug-transporter interactions studies. *Int. J. Pharm.* **2008**, *356*, 12–18. [CrossRef] [PubMed]
19. Vaquer, S.; Cuyàs, E.; Rabadán, A.; González, A.; Fenollosa, F.; de la Torre, R. Active transmembrane drug transport in microgravity: A validation study using an ABC transporter model [version 1; peer review: 2 approved]. *F1000Research* **2014**, *3*, 201. [CrossRef] [PubMed]

20. Jha, R.; Wu, Q.; Singh, M.; Preininger, M.K.; Han, P.; Ding, G.; Cho, H.C.; Jo, H.; Maher, K.O.; Wagner, M.B.; et al. Simulated Microgravity and 3D Culture Enhance Induction, Viability, Proliferation and Differentiation of Cardiac Progenitors from Human Pluripotent Stem Cells. *Sci. Rep.* **2016**, *6*, 30956. [CrossRef] [PubMed]
21. FDA (USA Food and Drug Administration). Eliquis (Apixaban). Available online: https://www.accessdata.fda.gov/drugsatfda_docs/label/2021/202155s034lbl.pdf (accessed on 22 June 2024).

pharmaceutics

MDPI

Article

Targeted Polymer–Peptide Conjugates for E-Selectin Blockade in Renal Injury

Nenad Milošević, Marie Rütter, Yvonne Ventura, Valeria Feinshtein and Ayelet David *

Department of Clinical Biochemistry and Pharmacology, Faculty of Health Sciences, Ben-Gurion University of the Negev, Beer-Sheva 84105, Israel

* Correspondence: ayeletda@bgu.ac.il; Tel: +972-8-6477364

Abstract: Background/Objectives: Leukocytes play a significant role in both acute kidney injury (AKI) and chronic kidney disease (CKD), contributing to pathogenesis and tissue damage. The process of leukocyte infiltration into the inflamed tissues is mediated by the interactions between the leukocytes and cell adhesion molecules (CAMs, i.e., E-selectin, P-selectin, and VCAM-1) present on the inner surface of the inflamed vasculature. Directly interfering with these interactions is a viable strategy to limit the extent of excessive inflammation; however, several small-molecule drug candidates failed during clinical translation. We hypothesized that a synthetic polymer presenting multiple copies of the high-affinity E-selecting binding peptide (P-Esbp) could block E-selectin-mediated functions and decrease leukocytes infiltration, thus reducing the extent of inflammatory kidney injury. Methods: P-Esbp was synthesized by conjugating E-selecting binding peptide (Esbp) to N-(2-hydroxypropyl)methacrylamide (HPMA) copolymer with reactive ester groups via aminolysis. The effects of P-Esbp treatment on kidney injury were investigated in two different models: AKI model (renal ischemia—reperfusion injury—RIRI) and CKD model (adenine-induced kidney injury). Results: We found that the mRNA levels of E-selectin were up-regulated in the kidney following acute and chronic tissue injury. P-Esbp demonstrated an extended half-life time in the bloodstream, and the polymer accumulated significantly in the liver, lungs, and kidneys within 4 h post injection. Treatment with P-Esbp suppressed the up-regulation of E-selectin in mice with RIRI and attenuated the inflammatory process. In the adenine-induced CKD model, the use of the E-selectin blocking copolymer had little impact on the progression of kidney injury, owing to the compensating function of P-selectin and VCAM-1. Conclusion: Our findings provide valuable insights into the interconnection between CAMs and compensatory mechanisms in controlling leukocyte migration in AKI and CKD. The combination of multiple CAM blockers, given simultaneously, may provide protective effects for preventing excessive leukocyte infiltration and control renal injury.

Keywords: cell adhesion molecules; E-selectin; VCAM-1; P-selectin; "drug-free" macromolecular therapeutics; HPMA; kidney inflammation; nanomedicines

1. Introduction

The development of effective pharmacological treatments for acute kidney injury (AKI) and chronic kidney disease (CKD) remains a significant challenge in global health [1]. Despite ongoing research efforts, there are currently no approved drugs specifically designed to prevent, treat, or enhance recovery from kidney injury, and the current strategies primarily focus on preventing the further deterioration of renal function [2]. Leukocytes

play an important role in renal inflammation, contributing to both harmful and protective effects [3]. Leukocyte trafficking into the inflamed tissue is a crucial component of the inflammatory response; however, when dysregulated or excessive, it can further contribute to pathological development [4–6]. The entry of leukocytes into inflamed tissues is regulated by their interactions with endothelial cells, specifically with the cell adhesion molecules (CAMs) expressed on the endothelium surface. The major endothelial-expressed CAMs can be divided into integrins, selectins (E-, L-, and P-selectin), and immunoglobulin superfamily members (ICAM-1 and VCAM-1), each of them mediating different stages of leukocyte trafficking [7]. Due to their role, CAMs have been recognized as viable targets for reducing leukocyte influx and inhibiting excessive inflammation [6,8] with the aim of reducing tissue injury. Several CAM inhibitors have been employed so far in preclinical development, including recombinant ligands [8], mAbs against selectins [9,10] and small molecular inhibitors (glycomimetics) [11,12]. However, their clinical translation has stagnated due to a combination of factors including insufficient binding affinity (glycomimetics), unfavorable pharmacokinetics (PK), or, in most cases, due to a lack of efficacy.

Some of these challenges could be overcome by designing CAM-targeted nanomedicines decorated with multiple high-affinity ligands for increased binding avidity to CAMs. Due to their large size, targeted nanomedicines (such as nanoparticles, liposomes, and polymer–drug conjugates) exhibit significantly longer half-life times in circulation compared to free small-molecule drugs [13]. Although such nanomedicines are usually intended as drug delivery platforms, a more recent approach aims to develop systems that exert biological activity without the need to add low-molecular-weight drugs. These systems, termed drug-free macromolecular therapeutics (DFMTs), exert their effects through strong binding to their intended targets and blocking their function [14,15].

We previously reported the synthesis of an HPMA-based polymer bearing multiple copies of the high-affinity E-selectin binding peptide (Esbp; primary sequence DITWDQLWDLMK) intended to target E-selectin on activated endothelium. This polymer (designated P-Esbp) was, at first, utilized as a drug delivery platform for a cytotoxic drug (doxorubicin) payload to the tumor vasculature [16–18]. The "drug-free" version of the polymer, without any drug attached, was shown to inhibit the metastatic spread of melanoma by blocking E-selectin (in this case, the E-selectin blockade interfered with the attachment of circulating cancer cells to the inflamed endothelium) [17]. Moreover, P-Esbp was shown to inhibit leukocyte recruitment to inflamed vasculature and reduce atherosclerotic lesion development in atherosclerotic mice [19] and was further demonstrated to attenuate neutrophil-mediated liver injury in a mice model of alcohol-related liver disease [20].

In this work, we investigated the ability of P-Esbp to attenuate kidney inflammation in mice models. Kidney inflammation was chosen as P-Esbp accumulates at high concentration in the kidneys of mice (in addition to liver tissue) [20]. The renal ischemia–reperfusion injury model (RIRI) is a surgical model representing a more acute type of kidney inflammation, with pronounced neutrophil infiltration that is mediated, in part, by E-selectin [21]. The second kidney inflammation model that we chose mimics several aspects of CKD and is induced by feeding mice food that is high in adenine [22]. The consumption of adenine-enriched food leads to the formation of an adenine metabolite—2,8-dihydroxyadenine—which forms crystals within renal tubules and induces renal injury and inflammation, followed by the loss of kidney function [23].

We tested whether the E-selectin blockade by P-Esbp could inhibit leukocyte infiltration into the inflamed kidneys, restrict inflammation, and exert beneficial effects on overall kidney function in these mice models.

2. Materials and Methods

2.1. Chemical Synthesis and Characterization of Polymers P-Esbp

All chemicals were of reagent grade and were obtained from Sigma-Aldrich (Rehovot, Israel) unless stated otherwise. The N-terminal Lysine-harboring E-selectin-binding peptide (Esbp, KDITWDQLWDLMR) and the control peptide with a scrambled Esbp sequence (EsbpScrm, KRMIDWTWLQLDD) were purchased from GL Biochem Ltd. (Shanghai, China). HPMA monomer was purchased from Polysciences (Warrington, PA, USA). The monomers methacryloyl-glycylglycine p-nitrophenyl ester (MA-GG-ONp) and methacryloyl-aminopropyl fluorescein-5-isothiocyanate (MAP–FITC) were synthesized as described previously [16].

P-Esbp was synthesized by coupling the N-terminal lysine-harboring Esbp or Esbp-Scrm to an HPMA-based precursor copolymer with reactive ester (O-nirtophenyl—ONp) groups (P-(GG-ONp)-FITC) via ONp aminolysis, as described previously [17]. The conjugates were isolated and purified on a PD-10 column using double-distilled water as the eluent. The content of conjugated peptides was estimated via ^{1}H-NMR, at 500 Hz, using the Tryptophan (Typ, W) proton chemical shift (δ 6.9–7.6, m, 10 H for Esbp/EsbpScrm). P-Esbp-IR783 was synthesized as described previously [17].

2.2. Pharmacokinetic and Biodistribution Analysis of P-(Esbp)-IR783

The PK parameters of P-Esbp were analyzed in healthy BABL/c mice to provide a baseline for understanding how the polymer distributes throughout the body without the influence of kidney injury. P-(Esbp)-IR783 (Mw: 46.7 kDa; P_I: 1.19; 3 mol% Esbp; 5 mol% IR783) was administered to 8-week-old female BALB/c mice (1 mg polymer/mice; n = 3) via tail vein injection. Animals were euthanized at designated time points (1 min, 5 min, 15 min, 30 min, 1 h, 2 h, 4 h, 8 h, 24 h, and 48 h). Blood and other major organs/tissues including hearts, lungs, kidneys, livers, and spleens were isolated following euthanasia. Serum sample fluorescent intensity was measured using the Infinite M-200 microplate fluorescence reader (Tecan, Männedorf, Switzerland). Corresponding serum concentrations were calculated using a previously constructed calibration curve prepared with known concentrations of the same polymer in human plasma. Major organs were imaged individually, and regions of interest (ROIs) were analyzed using the IVIS-Lumina imaging system without perfusion. The PK parameters, such as total clearance (CL), volume of distribution (Vd), and biological half-life ($t_{1/2}$), were determined using the bolus intravenous input non-compartmental and two-compartmental analysis of WinNonlin. The area under the curve (AUC) was calculated using the trapezoidal rule.

2.3. Animal Models of Kidney Inflammation

All animal experiments were approved and performed in compliance with the standards of the Ben-Gurion University of the Negev (BGU) Institutional Animal Care and Use Committee (IACUC), protocol code IL-56–08-2019 (C), period of authorization from 09/12/2019 through 09/11/2022. Male C57BL/6 mice and female BALB/c mice were obtained from Harlan Biotech Israel (HBI), (Rehovot, Israel) and housed in the animal facility of the Ben-Gurion University of the Negev.

2.3.1. In Vivo Model of Acute Kidney Inflammation—Renal Ischemia–Reperfusion Injury Model (RIRI)

The surgical procedure was based on the adapted protocol from a publication by Singbartl and Ley [24,25]. During initial experiments, high mortality was observed with 32 min bilateral RIRI. In an attempt to reduce the mortality, 25 min of bilateral RIRI was

performed in the following experiments. According to Wei et al. [25], the rise in the blood urea nitrogen (BUN) levels is similar with both 25 and 30 min ischemia.

C57BL/6 mice (age: 8–10 weeks; male; bodyweight more than 20 g) were anesthetized with i.p. injection of ketamine and xylazine (100 mg/kg, 10 mg/kg). After confirming the depth of surgical anesthesia, mice were shaved, and the operating area was disinfected. Mice body temperature was measured using the thermostatic station with a rectal probe, and mice were left to stabilize their body temperature to 37 °C. During the surgery, body temperature was monitored and kept at 37 ± 0.4 °C, as this is crucial for the reproducible kidney injury [26]. Mice skin and muscles were cut to expose renal pedicle first on the left and subsequently on the right side, as shown in Supplementary Figure S1A. The left renal artery was clamped with a Micro Serrefines clamp (Fine Scientific Tools—Supplementary Figure S1B); after confirmation of the color change in the kidney tissue following blood occlusion, the muscle layer was closed with one suture. The right renal artery was also clamped (the time difference between left and right clamping was less than 2 min) and the skin was closed with one suture. Following 25 min of ischemia time, the sutures were opened, the Micro Serrefines clips were removed, and the kidneys were inspected for color change (from dark red to a physiological, light brown color), which is an indicator of successful reperfusion. After closing the muscle layer and skin, mice received 1 mL of heated saline and Buprenorphine (dose: 50 μg/kg subcutaneously). Mice were randomized into groups, as follows: A—only RIRI; B—RIRI and i.p. 1 mg of P-Esbp in saline after reperfusion and another dose of 1 mg of P-Esbp in saline the following morning; and C—sham-operated mice (group C underwent all the procedures as A except for the clamping of the renal arteries). Animals were given thermal support by IR lamps and were followed until regaining full consciousness. All the procedures and time points were recorded for each mouse to exclude any mice where some deviations from the protocol occurred (using surgery logbook—Supplementary Figure S1C). Mice were euthanized exactly 24 h after reperfusion time. Upon euthanasia, blood samples and kidney tissue samples were collected for biochemical analysis and tissue mRNA expression via qRT-PCR, as described below.

2.3.2. In Vivo Model of Adenine-Induced Chronic Kidney Disease (CKD)

Experimental Design of Adenine-Induced CKD Murine Model

A casein-based diet with adenine (TD.130900–Adenine Diet (0.2% adenine, total phosphate content 0.9%, and total calcium content 0.6%), purchased from Harlan Biotech Israel (HBI), Rehovot, Israel) was formulated to have similarities to the diet described by Jia et al. [22]. The vitamin mix was increased by 50% and 2 ppm additional vitamin K and 10 ppm additional thiamin HCl were added to make the diet more suitable for irradiation sterilization. The control diet was also purchased from the same vendor and was identical in formulation to the adenine diet, apart from lacking adenine.

For the calibration experiments, 8-week-old male C57BL/6 mice were randomized into groups receiving either the adenine diet 0.2% for 5 days (n = 4), 14 days (n = 3), and 25 days (n = 6) or the control diet (n = 9; euthanized on days 14 and 25). Three mice were housed per cage. Every second day, mice body weight (BW) was determined as well as average food intake. On the designated days, mice were euthanized, and serum and kidney tissue samples were obtained and processed for further biochemical, histological, and mRNA expression analyses.

In the interventional experiment, C57BL/6 male mice were randomized into groups receiving the 0.2% adenine diet for 25 days and i.p. injections of either P-Esbp, P-EsbpScrm, or saline; the control group received the control diet and saline injections. Treatments

were administered every second day from day 6 in the form of 1 mg of the corresponding polymer dissolved in 200 µL of saline.

Tissue and Serum Processing and Analysis

Total RNA was extracted from kidney samples with TRIzol reagent and was transcribed into cDNA using a High-Capacity cDNA Reverse Transcription Kit. RT-PCR was performed using Taqman probes for E-selectin, TNF-α, and IL-1β, which were normalized to the expression levels of GAPDH (Supplementary Table S1). The results are expressed as fold induction relative to the control-fed groups. Upon blood collection, full blood was let to clot for 15–30 min at room temperature. Following centrifugation at 2000× *g* for 10 min, serum was collected and kept at 4 °C. Serum creatinine and serum urea levels were determined using a clinical chemistry analyzer Beckman Coulter AU5800 (Soroka Medical Center, Beer Sheva, Israel).

3. Results

3.1. Targeted Polymer Synthesis

A polymer precursor for Esbp conjugation (P-(GGONp)-FITC) was synthesized, purified, and characterized as previously reported [16,17,20]. The molecular weight of P-(GGONp)-FITC was 34 kDa (determined via size-exclusion chromatography on an ACTA-FPLC), which is below the renal glomerular filtration threshold, allowing for the polymer to be renally excreted. The content of the reactive group for peptide conjugation—ONp—was 7.5 mol% (determined spectrophotometrically). P-Esbp was synthesized and characterized as previously described [20]. The structure of the FITC-labeled, E-selectin-binding polymer (P-(Esbp)-FITC) is shown in Figure 1. The characteristics of the synthesized polymer and control (P-(EsbpScrm)-FITC) are shown in Table 1. The content of conjugated peptides was estimated via NMR using the ratio of signal intensities of tryptophan present in the peptide sequence (δ 6.9–7.6, m, 10H) and the signal of HPMA (δ 0.9–1.1, m, 6H). The content of Esbp/EsbpScrm in P-Esbp/P-EsbpScrm was estimated close to the theoretical maximum (the content of ONp groups), indicating the full conversion of reactive ONp groups (Table 1).

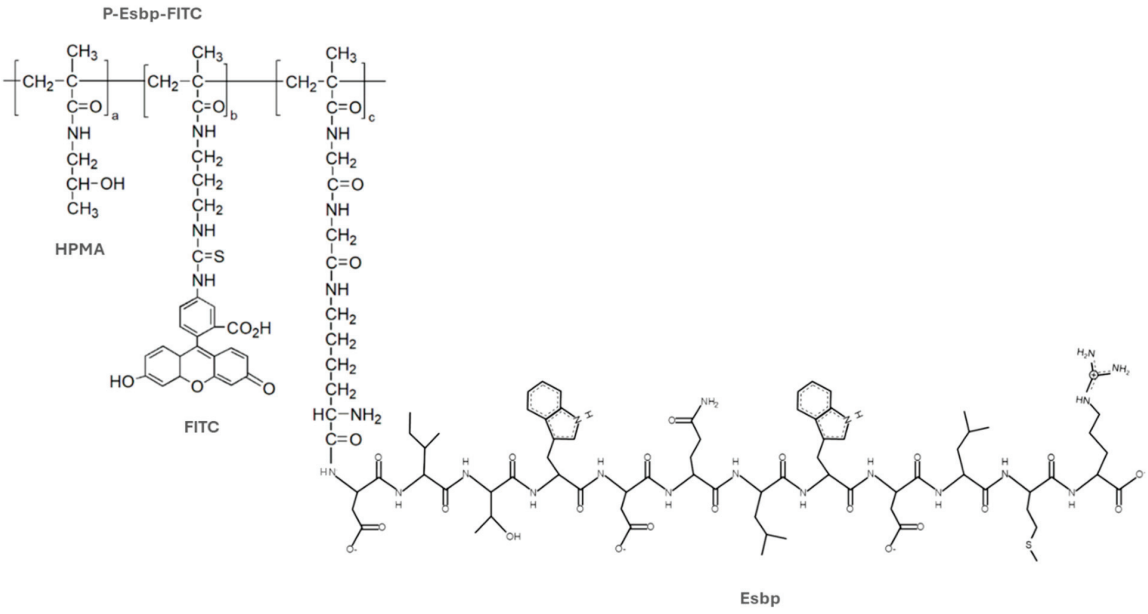

Figure 1. Structure of the FITC-labeled E-selectin-binding polymer (P-(Esbp)-FITC). HPMA indicates N–(2–hydroxypropyl)methacrylamide; Esbp—E-selectin-binding peptide. FITC—fluorescein isothiocyanate.

Table 1. Characteristics of synthesized polymers and precursor copolymers.

HPMA Copolymer	Mw [kDa] [a]	Polydispersity [b]	%mol FITC or IR783 [c]	%mol ONp/Peptide/Scrm [d]
P-(GGONp)-FITC	34.0	1.42	1.8	7.50
P-(Esbp)-FITC	34.1	1.35	1.8	7.49
P-(EsbpScrm)-FITC	33.2	1.2	1.8	7.35

[a,b] Weight-average molecular weight (Mw) and polydispersity (PI) of precursors and copolymer peptide conjugates were estimated via size-exclusion chromatography on an ACTA-FPLC system, using a Sephacryl 16/60 S-400 column (GE Healthcare) calibrated with fractions of known-molecular-weight HPMA homopolymers or by using the GPC/ HPLC Shimadzu system equipped with UV-VIS, refractive index, and multiangle light scattering DAWN 8 EOS (Wyatt Technology Corp., Santa Barbara, CA) detectors using a TSK 3000 SWXL column (Tosoh Bioscience, Japan). [c] The contents of FITC residues were determined by measuring the UV absorbance at 492 nm (ε = 82,000 M^{-1} cm^{-1}). [d] The contents of peptide-targeting moieties were estimated via ^{1}H-NMR at 500 Hz using the Tryptophan (Typ, W) chemical shift of aromatic amino acids (δ 6.9–7.6, m, 10H).

3.2. Pharmacokinetics (PK) and Biodistribution (BD) Analysis of P-(Esbp)-IR783

We first analyzed the PK and BD characteristics of P-Esbp in healthy BALB/c female 8-week-old mice using near-infrared (NIR) optical imaging. The half-life time of HPMA-based copolymers in circulation can vary significantly, depending on the molecular weight and the specific composition of the polymer [27]. P-Esbp-IR783 (Mw~47 kDa) has a distribution ($t_{1/2}$ alpha) of approximately 1 minute and an elimination half-life ($t_{1/2}$ beta) of 8.94 h. The blood data were fitted with a two-compartmental model (Figure 2), consistent with other examples of HPMA-based copolymer conjugates.

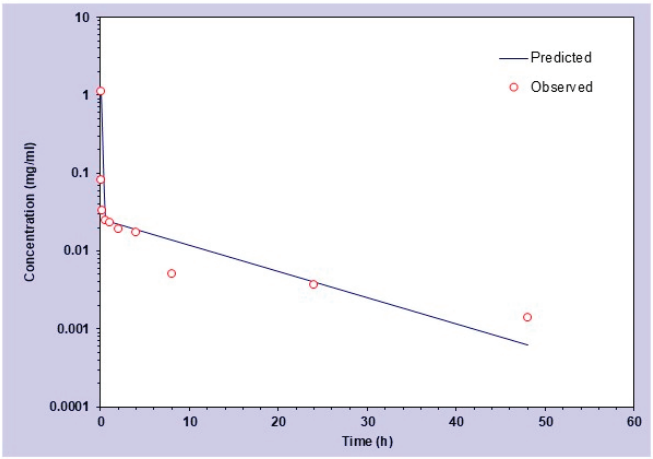

Parameter	Unit	Value
k_{10}	1/h	6.06
k_{12}	1/h	37.82
k_{21}	1/h	0.57
$t_{1/2\alpha}$	h	0.016
$t_{1/2\beta}$	h	8.94
C_0	mg/ml	2.30
V	mL	0.44
CL	mL/h	2.64
V_2	mL	29.01
CL_2	mL/h	16.48
AUC_{0-t}	(mg/ml)xh	0.37
AUC_{0-inf}	(mg/ml)xh	0.38
AUMC	(mg/ml)xh^2	4.23
MRT	h	11.16
V_{ss}	mL	29.45

Figure 2. Compartmental analysis and pharmacokinetic data of P-(Esbp)-IR783 in healthy mice after intravenous bolus injection.

P-(Esbp)-IR783 accumulated significantly in the liver of healthy mice, and a substantial amount of polymer was also detected at the first 4 h in the lungs and kidneys (Figure 3). Detectable levels were observed in the liver and kidneys even 48 hours post-injection. The liver, lungs, and kidneys are characterized by high tissue perfusion and discontinuous vascular walls (these fenestrae are generally between 50 and 100 nanometers in diameter) that allow substances circulating in the plasma to extravasate. These results align with other examples of polymer–drug conjugates or nano-sized formulations, such as liposomes, polymeric micelles, and nanoparticles [28]. The significant perfusion and accumulation of P-Esbp in the kidneys highlight its potential use for treating kidney diseases by targeting the E-selectin that is present at the luminal aspect of inflamed blood vessels. Since E-selectin expression levels are significantly up-regulated in response to inflammatory stimuli, P-Esbp may substantially accumulate in the blood vessels of the injured kidney and the renal localization is expected to be higher.

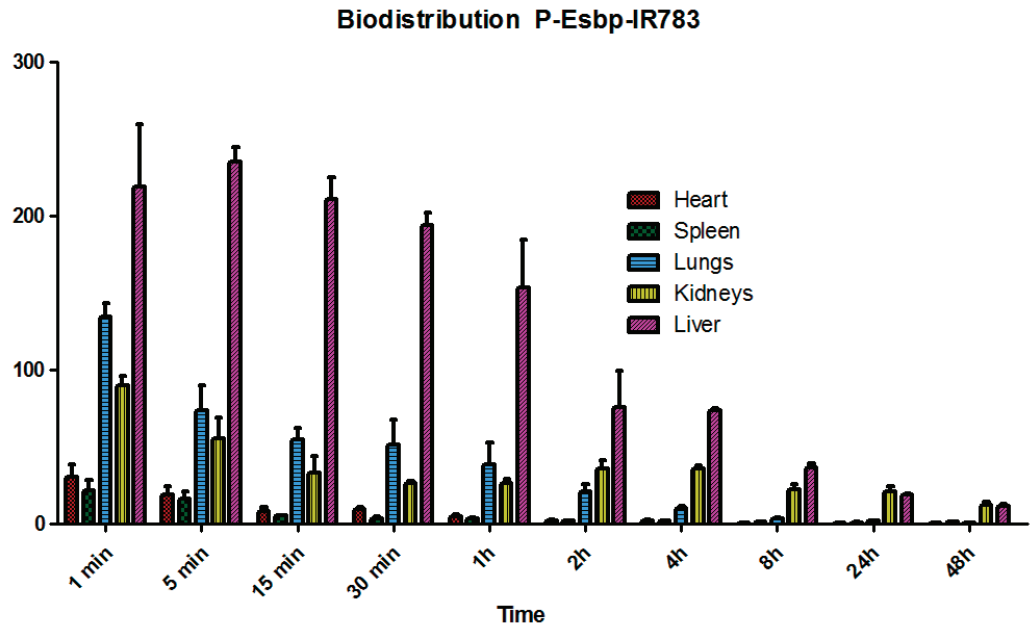

Figure 3. The biodistribution profile of P-Esbp-IR783 in heathy mice.

3.3. P-Esbp Reduced Kidney Damage in Acute Kidney Inflammation—Renal Ischemia–Reperfusion Injury (RIRI) Model

Renal ischemia–reperfusion injury (RIRI) is a model of acute renal damage, and some reports have suggested the important role of E-selectin in mediating the inflammatory response following reperfusion [24]. In a series of experiments, we investigated the effects of P-Esbp on renal injury parameters and the renal expression of E-selectin to determine if it can influence AKI.

In this experimental setting, kidney injury parameters (i.e., urea and creatinine) were elevated after the procedure compared to sham-operated mice. P-Esbp treatment reduced the level of kidney damage, in accordance with Singbartl [24], yet the effects were not statistically significant (Figure 4A,B). Further analysis of renal tissue expression of E-selectin revealed that E-selectin mRNA levels were up-regulated by about 8-fold in the kidney of RIRI mice relative to sham-control mice. This marked up-regulation of E-selectin is crucial in initiating the inflammatory cascade and plays a pivotal role in facilitating neutrophil recruitment to the injured tissue. P-Esbp treatment significantly suppressed the up-regulation of E-selectin in RIRI mice (Figure 4C). The expression levels of pro-inflammatory cytokines—TNFα and IL-1β (Figure 4D,E)—were lower in the P-Esbp-treated group relative to untreated RIRI group, indicating that P-Esbp therapy attenuates inflammatory processes in the acute experimental setting of renal injury.

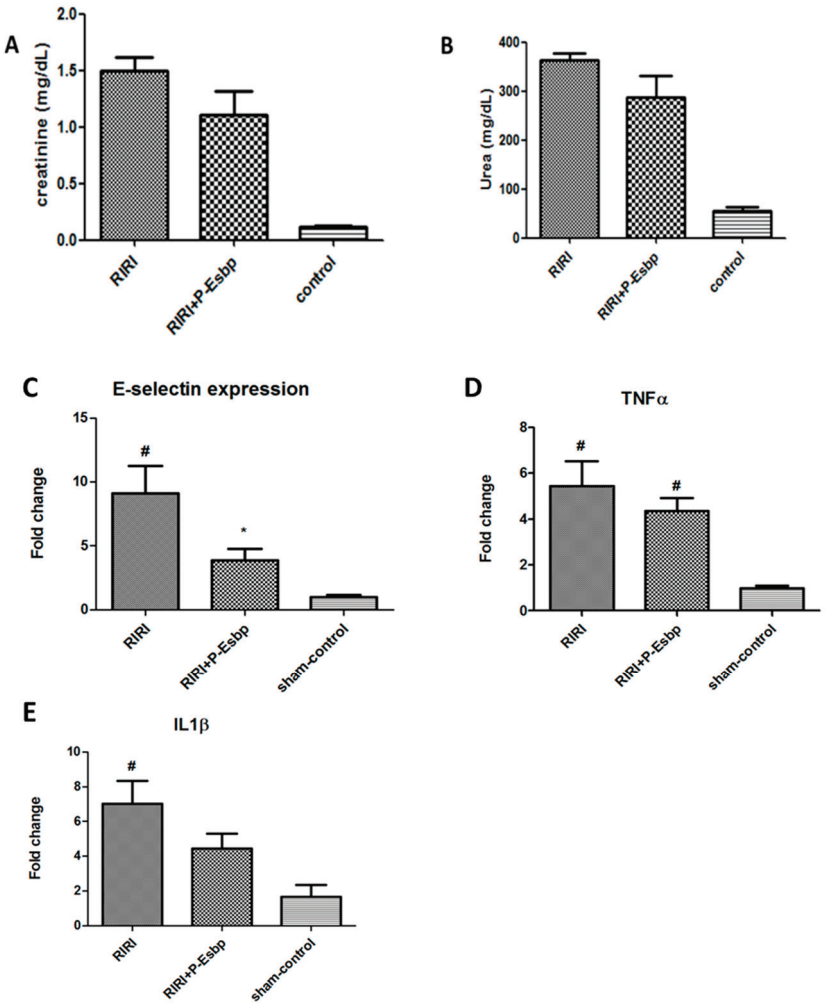

Figure 4. Effects of P-Esbp treatment (1 mg in 200 µL of saline at the time of reperfusion and 1 mg the following morning) on kidney function biochemical parameters—creatinine (**A**) and urea (**B**) 24 h after 25 min RIRI. Renal tissue expression levels of E-selectin (**C**), TNFα (**D**), and IL-1β (**E**) 24 h after 25 min RIRI. #—statistically significant difference compared to the sham-control group, $p < 0.05$; *—statistically significant difference compared to the RIRI group, $p < 0.05$.

3.4. Continuous P-Esbp Treatment Did Not Affect Chronic Kidney Injury in Adenine-Induced CKD Model

Previous studies indicated the development of chronic kidney injury in mice fed with an adenine-rich 0.2% diet [29–31]. In the first experiment, we investigated the effects of an adenine-rich diet on biochemical, and inflammatory cytokine parameters, especially on the expression patterns of CAMs in renal tissues on days 5, 14, and 25 after starting the diet.

Adenine-fed C57BL/6 mice experienced a reduction in BW, which was more pronounced in the first week of feeding and stabilized in the following weeks (Figure 5A,B—individual profiles). This reduction in BW was comparable with that reported in the literature, and, on average, it was around 10% of the original weight [29,32]. The average food intake was 3.2 g of food per mouse per day in the control group and 2.2 g per mouse per day in the adenine group. Kidney injury was confirmed by elevated serum levels of creatinine and serum urea (Figure 5C,D) and their levels gradually increased throughout the course of the experiment.

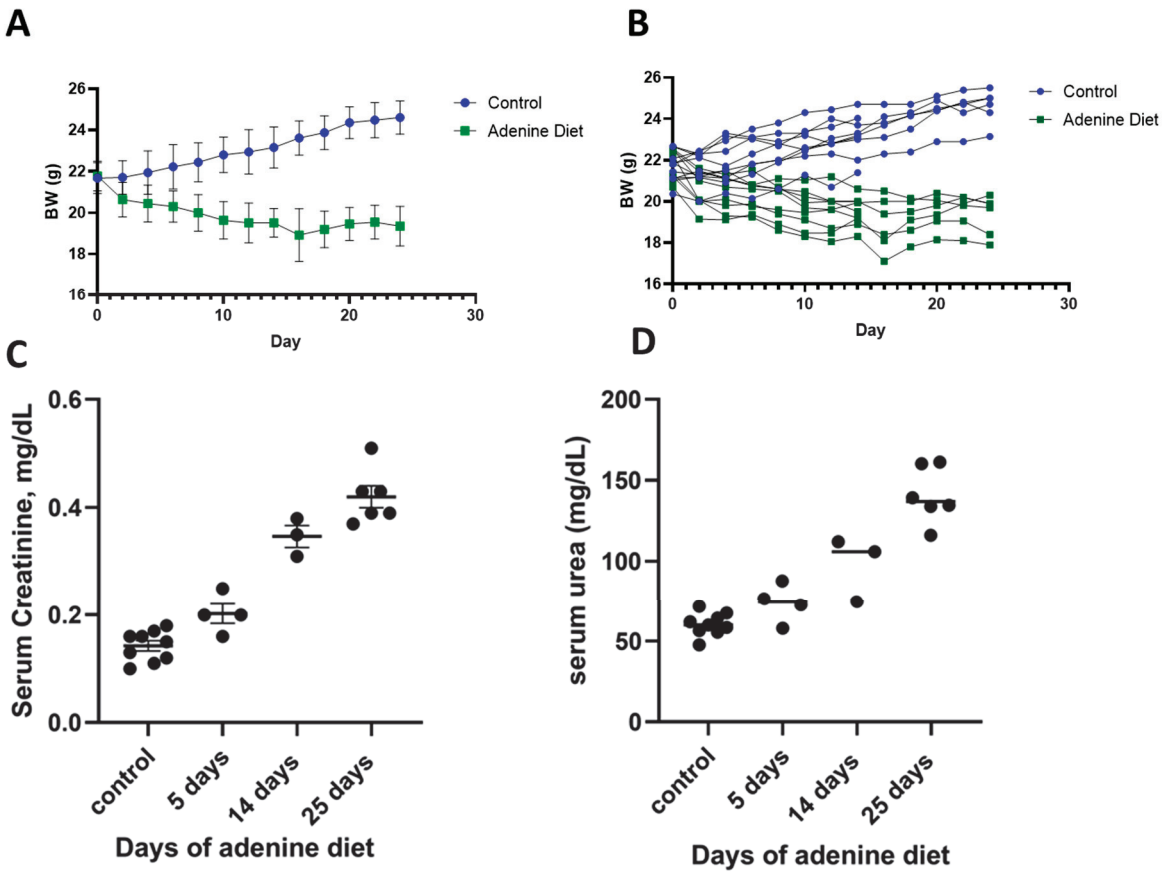

Figure 5. Induction of CKD by adenine diet (0.2%). Mice body weight as group average (**A**) and individual weight (**B**). Biochemical parameters of serum creatinine (**C**) and serum urea (**D**) at different time points from the initiation of the adenine diet.

The inflammatory cytokines TNFα and IL-1β also showed a rising trend in mRNA expression (Figure 6A,B), with a gradual increase in their levels from day 5 to day 25. Endothelial CAMs are overexpressed in response to inflammation and signaling by cytokines. Our results showed that the CAMs E-selectin, VCAM-1, and P-selectin were up-regulated in kidney tissues of adenine-fed mice. The E-selectin levels were elevated at the earliest time point of 5 days and this trend continued for time points at 14 days and 25 days (Figure 6C), demonstrating the highest folds at the last time point (4.6-fold average). Both P-selectin (Figure 6D) and VCAM-1 (Figure 6E) expression levels were enhanced during the course of the experiment, and the fold increase in their mRNA levels was about 5–10-times higher than that of E-selectin.

To investigate the effects of E-selectin blockage with P-Esbp, adenine-fed mice received 10 i.p. injections of P-Esbp or the polymer with the scrambled version of the peptide—P-EsbpScrm. Since the half-life time of P-Esbp is approximately 9 h in circulation, and it takes about 4 to 5 half-lives for an almost complete clearance from the body, P-Esbp was injected once every two days to ensure a continuous dose of the polymer conjugate in circulation, and to ensure that it was available for endothelial E-selectin blockade under chronic conditions. In line with previously described results, biochemistry parameters, serum creatinine, and serum urea (Figure 7A,B) were profoundly higher in mice fed with an adenine diet throughout the experiment (from day 5 to day 25). However, treatment with P-Esbp did not inhibit the rise in serum creatinine and urea levels. The lack of therapeutic efficacy may be attributed to the complementary roles of CAMs. The level of P-selectin was significantly up-regulated in adenine-fed mice. E- and P-selectin function

cooperatively and can compensate each other in various biological processes. We thus assume that targeting and blocking all the three CAMs (E-selectin, P-selectin, and VCAM-1), simultaneously, might provide therapeutic benefits. A suboptimal dosing regimen of P-Esbp can also explain the results. Overall, in the chosen animal model, feeding protocol, and dosing regimen, E-selectin blockade cannot substantially inhibit chronic kidney injury and inflammation caused by adenine diet.

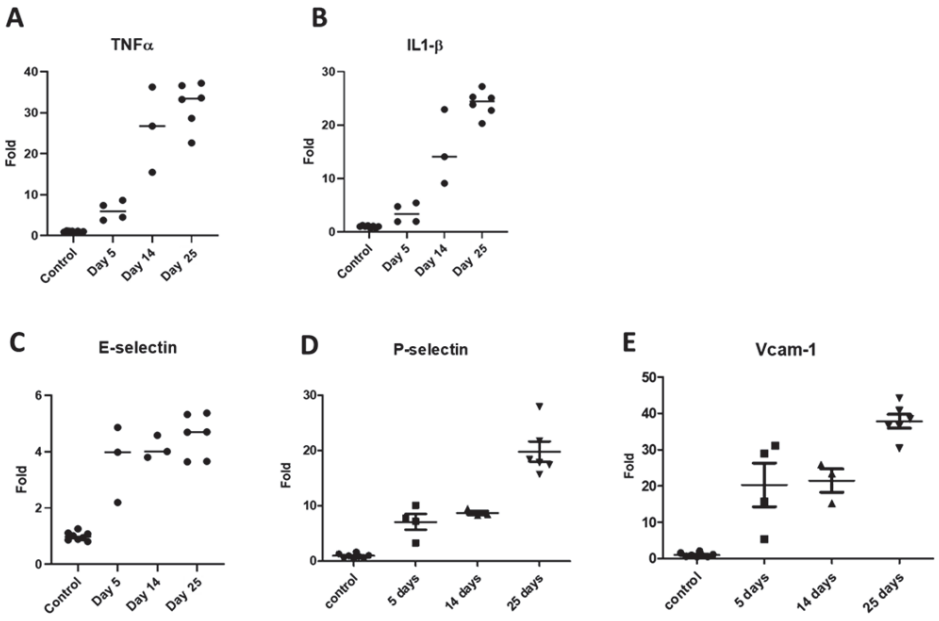

Figure 6. mRNA expression patterns of inflammatory markers in renal tissues of adenine-rich diet-fed mice. TNFα (**A**); IL-1β (**B**); E-selectin (**C**); P-selectin (**D**); and VCAM-1 (**E**).

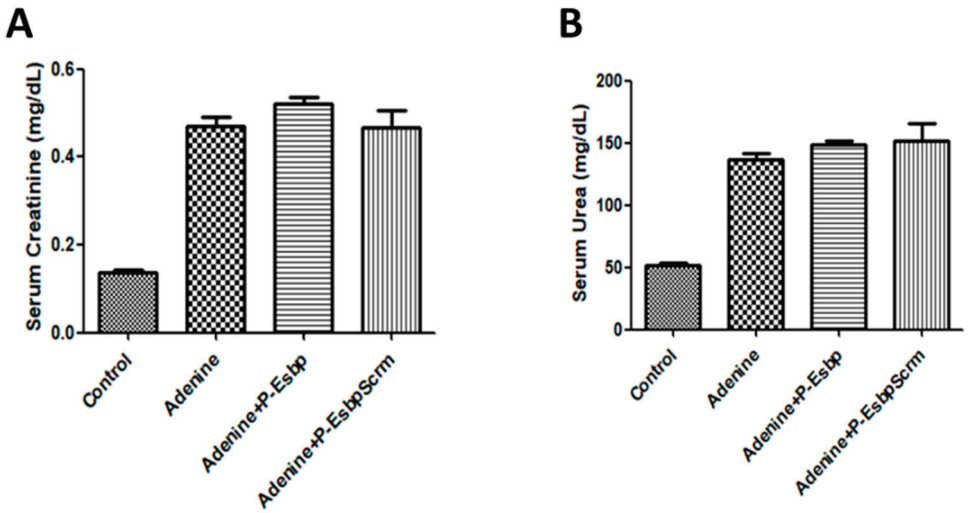

Figure 7. Effects of P-Esbp treatment (1 mg in 200 µL of saline i.p. every second day from day 6 of the experiment; total of ten doses) on kidney function biochemical parameters from the interventional experiment. Serum creatinine (**A**) and serum urea (**B**) upon animal euthanasia on day 28.

4. Discussion

In this study, we investigated different models of kidney inflammation and identified those with a clear involvement of CAMs. In the RIRI model of rapid and acute inflammation, E-selectin mRNA was about eight times higher 24 after ischemia and reperfusion, indicating that E-selectin plays a significant role in the early inflammatory response following AKI.

Treatment with P-Esbp attenuated inflammatory processes in RIRI mice by significantly suppressing the up-regulation of E-selectin expression. This is in line with previous studies showing that the blockade of E-selectin or P-selectin (by a monoclonal antibody or small-molecule selectin ligand) decreases neutrophil recruitment into the kidney and preserves organ morphology and function and in sepsis-induced AKI [33–35]. Yet, polymer treatment only mildly influenced kidney injury parameters (i.e., urea and creatinine). In a model of more gradual, chronic kidney inflammation, we confirmed the up-regulation of all three CAMs (E-selectin, P-selectin, and VCAM-1) in kidney samples from adenine-fed animals. While E-selectin expression was up-regulated approximately 8-fold in RIRI after 24 h, its levels increased only 2-fold in CKD at the initial time point (day 5) and reached 4–5-fold on day 25. P-selectin and VCAM-1 have reached higher folds of up-regulation compared to E-selectin (8-fold and 20-fold, respectively, on day 5, and 20–35 fold of increase on day 25). This indicates that P-selectin and VCAM-1 play a more substantial role in the progression of CKD than E-selectin. Multiple i.p. injections of P-Esbp in the adenine-diet-induced CKD model did not protect mice from kidney injury. The physiological role of P-selectin is to work synergistically with E-selectin in the mediation of initial leukocyte adhesion to activated endothelium during acute and chronic inflammation. It is possible that due to the overlapping and mutually compensating functions of selectins, the blockade of only one selectin family member was not sufficient for inhibiting chronic inflammation and renal injury. For comparison, in an inflammatory model of alcohol-induced liver injury (the NIAAA model), where E-selectin is the sole CAM that was up-regulated to a significant extent [20,36], E-selectin blockade by P-Esbp showed a profound anti-inflammatory efficacy. The increase in P-selectin and VCAM-1 expression in RIRI was less pronounced after 24 h when compared to CKD after 5 days. Specifically, the upregulation was approximately six times higher for P-selectin and twelve times higher for VCAM-1 in RIRI [37–39], which is ~ three times lower relative to their up-regulation in CKD. This might explain the beneficial effects of P-Esbp observed in RIRI but not in CKD. Future experiments with the combination of E-selectin, P-selectin, and VCAM-1 blockers given simultaneously might attenuate the manifestation of adenine-diet-induced kidney injury. Our results show that therapeutic success in treating one disease is not a guarantee for benefit across different pathologies. This is evident in several other drug candidates (i.e., Inclacumab, a monoclonal antibody against P-selectin, was dropped for cardiovascular diseases treatment and is now in trials for the treatment of sickle cell disease [40]). Effectively blocking a single CAM might be beneficial in one inflammatory setting, but might provide limited efficacy in others [41,42].

Taken together, the results from this study give several insights on the process of developing a polymer–peptide conjugate specifically designed to target and block E-selectin to prevent renal injury. E-selectin has a more significant and immediate role in the inflammatory processes in acute compared to chronic renal injury. The upregulation of E-selectin in response to inflammatory stimuli was more pronounced in AKI than CKD. Treatment with P-Esbp suppressed the up-regulation of E-selectin in mice with AKI. The mild protective effects in the models of kidney inflammation highlight the interconnected nature of CAMs and their different individual contributions to the specific pathological process. Careful monitoring of potential compensatory increases in other CAMs is crucial when targeting E-selectin. Overall, more effort should be invested in precisely characterizing different inflammatory diseases and/or animal models to pinpoint those where the blockage of one or several CAMs would provide the most therapeutic benefits.

Supplementary Materials: The following supporting information can be downloaded at: https://www.mdpi.com/article/10.3390/pharmaceutics17010082/s1, Figure S1: The incision locations for left and right kidney clamping-adapted from Ref. [25]; Table S1: Primer sequences for real-time PCR.

Author Contributions: N.M. synthesized the polymers, designed the experiments, developed the animal models, performed the experiments, and analyzed the data. M.R. assisted with polymer synthesis and characterization, as well as manuscript preparation. M.R., Y.V. and V.F. helped to plan and carry out the experiments on mice. A.D. and N.M. wrote the manuscript. AD was involved in planning and supervised the work. All authors have read and agreed to the published version of the manuscript.

Funding: This research was funded by the Israel Science Foundation (grant # 1115/19) and by the LEDUCQ Foundation, as part of the PRIMA (Preventing Rheumatic Injury BioMarker Alliance) Network (grant #22ARF02).

Institutional Review Board Statement: The study protocol was approved by the IACUC of the Ben-Gurion University of the Negev, Authorization number: IL-56-08-2019 (C).

Data Availability Statement: Data will be made available upon reasonable request.

Acknowledgments: We would like to acknowledge Kreitman School of Advanced Graduate Studies (Ben-Gurion University of the Negev, Israel) for supporting N.M and M.R. with Ph.D. and short term post-doctoral scholarship.

Conflicts of Interest: The authors declare no conflict of interest.

References

1. Chawla, L.S.; Eggers, P.W.; Star, R.A.; Kimmel, P.L. Acute kidney injury and chronic kidney disease as interconnected syndromes. *N. Engl. J. Med.* **2014**, *371*, 58–66. [CrossRef]
2. Pickkers, P.; Murray, P.T.; Ostermann, M. New drugs for acute kidney injury. *Intensive Care Med.* **2022**, *48*, 1796–1798. [CrossRef]
3. Kinsey, G.R.; Okusa, M.D. Role of leukocytes in the pathogenesis of acute kidney injury. *Crit. Care* **2012**, *16*, 214. [CrossRef] [PubMed]
4. Hopkin, S.J.; Lewis, J.W.; Krautter, F.; Chimen, M.; McGettrick, H.M. Triggering the resolution of immune mediated inflammatory diseases: Can targeting leukocyte migration be the answer? *Front. Pharmacol.* **2019**, *10*, 184. [CrossRef] [PubMed]
5. Moreira, M.B.; Garcia-Cardeña, G.; Saffi, M.A.L.; Libby, P. Endothelium: A coordinator of acute and chronic inflammation. In *Endothelium and Cardiovascular Diseases*; Protasio, L.D.L., Libby, P., Chagas, A.C.P., Laurindo, F.R.M., Eds.; Academic Press: Cambridge, MA, USA, 2018; pp. 485–491.
6. Kreuger, J.; Phillipson, M. Targeting vascular and leukocyte communication in angiogenesis, inflammation and fibrosis. *Nat. Rev. Drug Discov.* **2016**, *15*, 125–142. [CrossRef]
7. Smith, C.W. 3. Adhesion molecules and receptors. *J. Allergy Clin. Immunol.* **2008**, *121*, S375–S379. [CrossRef] [PubMed]
8. Peres, R.S.; Menezes, G.B.; Teixeira, M.M.; Cunha, F.Q. Pharmacological opportunities to control inflammatory diseases through inhibition of the leukocyte recruitment. *Pharmacol. Res.* **2016**, *112*, 37–48. [CrossRef] [PubMed]
9. Rymer, J.A.; Newby, L.K. Failure to launch: Targeting inflammation in acute coronary syndromes. *Basic. Transl. Sci.* **2017**, *2*, 484–497.
10. Seekamp, A.; van Griensven, M.; Rusu, C.; König, J.; Khan-Boluki, J.; Redl, H. The effect of anti-L-selectin (Aselizumab) on the posttraumatic inflammatory response in multiply traumatized patients. *Eur. J. Trauma* **2005**, *31*, 557–567. [CrossRef]
11. Romano, S.J. Selectin antagonists. *Treat. Respir. Med.* **2005**, *4*, 85–94. [CrossRef]
12. Beeh, K.M.; Beier, J.; Meyer, M.; Buhl, R.; Zahlten, R.; Wolff, G. Bimosiamose, an inhaled small-molecule pan-selectin antagonist, attenuates late asthmatic reactions following allergen challenge in mild asthmatics: A randomized, double-blind, placebo-controlled clinical cross-over-trial. *Pulm. Pharmacol. Ther.* **2006**, *19*, 233–241. [CrossRef] [PubMed]
13. Mitchell, M.J.; Billingsley, M.M.; Haley, R.M.; Wechsler, M.E.; Peppas, N.A.; Langer, R. Engineering precision nanoparticles for drug delivery. *Nat. Rev. Drug Discov.* **2021**, *20*, 101–124. [CrossRef] [PubMed]
14. Rütter, M.; Milošević, N.; David, A. Say no to drugs: Bioactive macromolecular therapeutics without conventional drugs. *J. Control. Release* **2021**, *330*, 1191–1207. [CrossRef]
15. Milošević, N.; Rütter, M.; David, A. Endothelial cell adhesion molecules-(un) Attainable targets for nanomedicines. *Front. Med. Technol.* **2022**, *4*, 846065. [CrossRef] [PubMed]
16. Shamay, Y.; Paulin, D.; Ashkenasy, G.; David, A. E-selectin binding peptide–polymer–drug conjugates and their selective cytotoxicity against vascular endothelial cells. *Biomaterials* **2009**, *30*, 6460–6468. [CrossRef] [PubMed]
17. Shamay, Y.; Raviv, L.; Golan, M.; Voronov, E.; Apte, R.N.; David, A. Inhibition of primary and metastatic tumors in mice by E-selectin-targeted polymer–drug conjugates. *J. Control. Release* **2015**, *217*, 102–112. [CrossRef]

18. Rütter, M.; Milošević, N.; Ventura, Y.; Feinshtein, V.; David, A. E-selectin-targeted polymer-doxorubicin conjugate induces regression of established colorectal liver metastases and improves mice survival. *Nano Today* **2024**, *55*, 102182. [CrossRef]
19. Tsoref, O.; Tyomkin, D.; Amit, U.; Landa, N.; Cohen-Rosenboim, O.; Kain, D.; Golan, M.; Naftali-Shani, N.; David, A.; Leor, J. E-selectin-targeted copolymer reduces atherosclerotic lesions, adverse cardiac remodeling, and dysfunction. *J. Control. Release* **2018**, *288*, 136–147. [CrossRef] [PubMed]
20. Milošević, N.; Rütter, M.; Ventura, Y.; Kezerle, Y.; Feinshtein, V.; David, A. Attenuation of neutrophil-mediated liver injury in mice by drug-free E-selectin binding polymer. *J. Control. Release* **2020**, *319*, 475–486. [CrossRef] [PubMed]
21. Kato, N.; Yuzawa, Y.; Kosugi, T.; Hobo, A.; Sato, W.; Miwa, Y.; Sakamoto, K.; Matsuo, S.; Kadomatsu, K. The E-selectin ligand basigin/CD147 is responsible for neutrophil recruitment in renal ischemia/reperfusion. *J. Am. Soc. Nephrol.* **2009**, *20*, 1565–1576. [CrossRef]
22. Jia, T.; Olauson, H.; Lindberg, K.; Amin, R.; Edvardsson, K.; Lindholm, B.; Andersson, G.; Wernerson, A.; Sabbagh, Y.; Schiavi, S. A novel model of adenine-induced tubulointerstitial nephropathy in mice. *BMC Nephrol.* **2013**, *14*, 116. [CrossRef] [PubMed]
23. Klinkhammer, B.M.; Djudjaj, S.; Kunter, U.; Palsson, R.; Edvardsson, V.O.; Wiech, T.; Thorsteinsdottir, M.; Hardarson, S.; Foresto-Neto, O.; Mulay, S.R.; et al. Cellular and molecular mechanisms of kidney injury in 2,8-dihydroxyadenine nephropathy. *J. Am. Soc. Nephrol. JASN* **2020**, *31*, 799. [CrossRef] [PubMed]
24. Singbartl, K.; Ley, K. Protection from ischemia-reperfusion induced severe acute renal failure by blocking E-selectin. *Crit. Care Med.* **2000**, *28*, 2507–2514. [CrossRef] [PubMed]
25. Wei, Q.; Dong, Z. Mouse model of ischemic acute kidney injury: Technical notes and tricks. *Am. J. Physiol. Ren. Physiol.* **2012**, *303*, F1487–F1494. [CrossRef] [PubMed]
26. Hesketh, E.E.; Czopek, A.; Clay, M.; Borthwick, G.; Ferenbach, D.; Kluth, D.; Hughes, J. Renal ischaemia reperfusion injury: A mouse model of injury and regeneration. *J. Vis. Exp.* **2014**, *88*, e51816. [CrossRef]
27. Shiah, J.-G.; Dvořák, M.; Kopečková, P.; Sun, Y.; Peterson, C.; Kopeček, J. Biodistribution and antitumour efficacy of long-circulating N-(2-hydroxypropyl) methacrylamide copolymer–doxorubicin conjugates in nude mice. *Eur. J. Cancer* **2001**, *37*, 131–139. [CrossRef] [PubMed]
28. Blanco, E.; Shen, H.; Ferrari, M. Principles of nanoparticle design for overcoming biological barriers to drug delivery. *Nat. Biotechnol.* **2015**, *33*, 941–951. [CrossRef]
29. Santana, A.C.; Degaspari, S.; Catanozi, S.; Dellê, H.; de Sá Lima, L.; Silva, C.; Blanco, P.; Solez, K.; Scavone, C.; Noronha, I.L. Thalidomide suppresses inflammation in adenine-induced CKD with uraemia in mice. *Nephrol. Dial. Transplant.* **2013**, *28*, 1140–1149. [CrossRef] [PubMed]
30. de Frutos, S.; Luengo, A.; Garcia-Jerez, A.; Hatem-Vaquero, M.; Griera, M.; O'Valle, F.; Rodríguez–Puyol, M.; Rodríguez–Puyol, D.; Calleros, L. Chronic kidney disease induced by an adenine rich diet upregulates integrin linked kinase (ILK) and its depletion prevents the disease progression. *Biochim. Biophys. Acta BBA Mol. Basis Dis.* **2019**, *1865*, 1284–1297. [CrossRef]
31. Ludwig-Portugall, I.; Bartok, E.; Dhana, E.; Evers, B.D.; Primiano, M.J.; Hall, J.P.; Franklin, B.S.; Knolle, P.A.; Hornung, V.; Hartmann, G.; et al. An NLRP3-specific inflammasome inhibitor attenuates crystal-induced kidney fibrosis in mice. *Kidney Int.* **2016**, *90*, 525–539. [CrossRef] [PubMed]
32. Tamura, M.; Aizawa, R.; Hori, M.; Ozaki, H. Progressive renal dysfunction and macrophage infiltration in interstitial fibrosis in an adenine-induced tubulointerstitial nephritis mouse model. *Histochem. Cell Biol.* **2009**, *131*, 483–490. [CrossRef] [PubMed]
33. Herter, J.M.; Rossaint, J.; Spieker, T.; Zarbock, A. Adhesion molecules involved in neutrophil recruitment during sepsis-induced acute kidney injury. *J. Innate Immun.* **2014**, *6*, 597–606. [CrossRef] [PubMed]
34. Singbartl, K.; Green, S.A. LEYK Blocking P-selectin protects from ischemia/reperfusion-induced acute renal failure. *FASEB J.* **2000**, *14*, 48–54. [CrossRef]
35. Nemoto, T.; Burne, M.J.; Daniels, F.; O'Donnell, M.P.; Crosson, J.; Berens, K.; Issekutz, A.; Kasiske, B.L.; Keane, W.F.; Rabb, H. Small molecule selectin ligand inhibition improves outcome in ischemic acute renal failure. *Kidney Int.* **2001**, *60*, 2205–2214. [CrossRef]
36. Bertola, A.; Park, O.; Gao, B. Chronic plus binge ethanol feeding synergistically induces neutrophil infiltration and liver injury in mice: A critical role for E-selectin. *Hepatology* **2013**, *58*, 1814–1823. [CrossRef]
37. Akhtar, A.M.; Schneider, J.E.; Chapman, S.J.; Jefferson, A.; Digby, J.E.; Mankia, K.; Chen, Y.; McAteer, M.A.; Wood, K.J.; Choudhury, R.P. In vivo quantification of VCAM-1 expression in renal ischemia reperfusion injury using non-invasive magnetic resonance molecular imaging. *PLoS ONE* **2010**, *5*, e12800. [CrossRef] [PubMed]
38. Zhang, K.; Li, R.; Chen, X.; Yan, H.; Li, H.; Zhao, X.; Chen, Y.; McAteer, M.A.; Wood, K.J.; Choudhury, R.P. Renal Endothelial Cell-Targeted Extracellular Vesicles Protect the Kidney from Ischemic Injury. *Adv. Sci.* **2023**, *10*, e2204626. [CrossRef] [PubMed]
39. Boesen, E.I.; Crislip, G.R.; Sullivan, J.C. Use of ultrasound to assess renal reperfusion and P-selectin expression following unilateral renal ischemia. *Am. J. Physiol. Ren. Physiol.* **2012**, *303*, F1333–F1340. [CrossRef] [PubMed]

40. Mayer, C.L.; Koeck, K.; Hottmann, M.; Redfern, A.; Davis, M.; Barth, A.; Geng, X.; Hoppe, C.; Yue, P. A phase 1 study in healthy participants to characterize the safety and pharmacology of inclacumab, a fully human anti-P-selectin antibody, in development for treatment of sickle cell disease. *Eur. J. Clin. Pharmacol.* **2023**, *79*, 1219–1228. [CrossRef] [PubMed]
41. Ailuno, G.; Baldassari, S.; Zuccari, G.; Schlich, M.; Caviglioli, G. Peptide-based nanosystems for vascular cell adhesion molecule-1 targeting: A real opportunity for therapeutic and diagnostic agents in inflammation associated disorders. *J. Drug Deliv. Sci. Technol.* **2020**, *55*, 101461. [CrossRef]
42. Xu, J.; Zhou, J.; Zhong, Y.; Zhang, Y.; Ye, M.; Hou, J.; Wang, Z.; Ran, H.; Liu, J.; Guo, D. EWVDV-Mediated Platelet-Targeting Nanoparticles for the Multimodal Imaging of Thrombi at Different Blood Flow Velocities. *Int. J. Nanomed.* **2020**, *15*, 1759. [CrossRef] [PubMed]

MDPI AG
Grosspeteranlage 5
4052 Basel
Switzerland
Tel.: +41 61 683 77 34

Pharmaceutics Editorial Office
E-mail: pharmaceutics@mdpi.com
www.mdpi.com/journal/pharmaceutics

Academic Open
Access Publishing

mdpi.com

ISBN 978-3-7258-4774-7